Imperial College London

Coherent, Ultrashort IR, UV and X-Ray Sources for Ultrafast Spectroscopies

Timur Bora Avni

London, June 2024

Thesis submitted for the degree of Doctor of Philosophy

Laser Consortium

Quantum Optics and Laser Science Group

Department of Physics

Imperial College London

SW7 2BW

United Kingdom

Declaration of Originality

Unless otherwise stated, the work presented in this thesis is my own.

Timur Bora Avni

Copyright

The copyright of this thesis rests with the author. Unless otherwise indicated, its contents are licensed under a Creative Commons Attribution-Non Commercial-No Derivatives 4.0 International Licence (CC BY-NC-ND). Under this licence, you may copy and redistribute the material in any medium or format on the condition that; you credit the author, do not use it for commercial purposes and do not distribute modified versions of the work. When reusing or sharing this work, ensure you make the licence terms clear to others by naming the licence and linking to the licence text. Please seek permission from the copyright holder for uses of this work that are not included in this licence or permitted under UK Copyright Law.

Acronyms

Acronym	Definition
ADK	Ammosov-Delone-Krainov
AR	Anti-reflection
AR	Anti-reflection
CEP	Carrier Envelope Phase
FME	Forward Maxwell Equation
FROG	Frequency Resolved Optical Gating
FTL	Fourier Transform Limit
FWHM	Full Width at Half Maximum
FWM	Four Wave Mixing
GDD	Group Display Dispersion
GVD	Group Velocity Dispersion
HCF	Hollow Core Fibre / Hollow Capillary Fibre
HHG	High Harmonic Generation
HWP	Half Wave Plate
MCP	Micro-channel Plate
MPI	Multiphoton Ionisation
NLSE	Nonlinear Schröndinger Equation
OPA	Optical Parametric Amplifier
PPT	Perelmov-Popov-Terentev
RDW	Resonant Dispersive Wave
SWIR	Short Wave Infrared
SXR	Soft X-Ray
TOD	Third Order Dispersion
XFEL	X-Ray Free Electron Laser
ZDW	Zero Dispersion Wavelength

Abstract

In this thesis I present development of experimental and computational tools for the enhancement of UV pump, X-Ray probe transient absorption spectroscopy (TAS) experiments. Tunable, optimised and well characterised pump and probe pulse sources are critical for these spectroscopies. For the pump pulse, a 60 fs, 1.5 mJ, 1400 nm pulse is broadened in a tensioned flexible hollow core fibre and characterised with an SHG-FROG. This is used to generate tunable pump pulses in the 250 - 450 nm range using resonant dispersive wave (RDW) emission in a hollow core fibre, with additional apparatus outlined to spectrally filter and characterise the pulses.

Additionally a variable-length cell is constructed to optimise high harmonic generation (HHG) flux. The anticipated harmonic flux from the source is calculated using a (3+1)D SFA code, and a simplified modelling schema is presented for running large parametric scans without the need for costly simulations. These results are put in the context of other recent work in the literature for scaling HHG with pulse energy, gas pressure and interaction length.

The interaction of high peak intensity laser pulses with a liquid jet is also explored, and HHG in the liquid phase is modelled with comparison to recent experimental results. Both investigations here extend the SFA code used for simulating gas phase HHG to account for the effects of a high density medium on both the driving laser and the emitted harmonics.

The ionisation dynamics in the liquid phase are examined, electron scattering rates are found to agree well with literature, and we characterise the formation of a plasma mirror at the jet's surface. Good agreement is also found between the modelled and experimental HHG in the liquid phase, giving new insight into scattering cross-sections for low energy electrons in liquids, and adding to the limited literature on the mechanics of liquid HHG.

"*That might cause a pillar of flame to come out from the roof of the building, but at least the lab will be safe* "

Jacob Lee, on priorities in experimental design

"*If you have no stuff it won't change* "

Dr Mary Matthews, on the fundamentals of non-linear optics

"*Maths is just a game! It's fun once you learn the rules*"

Bora Avni

Acknowledgements

No PhD is achieved alone, and this was certainly no exception. While most attempt to have the writing of their thesis be a concise affair, I was not awarded such luxuries, and so this list will be scaled accordingly. Unlike the writing of this thesis, you dear reader have the option to skip this (and all other) sections, so do as you will.

Thank you to my supervisor Jon Marangos for your support, patience and advice- my PhD has been more kinds of nonlinear than either of us expected. Thanks to Esben Larsen for easing me into ultrafast science and teaching me the many ways to use spanners and fine adjustment tools. Thanks also to Mary for putting up with a million ridiculous idea for experiments, and helping me filter them down to the few that were feasible while sat on the floor. Also for chocolate.

Many thanks to all those who were students in the Laser Consortium through my rather protracted tenure. Thanks to Toby for helping keep me distracted; to Oliver for good ideas and keeping snacks in his drawer; to Clement for keeping the lab running and me grounded; to Jacob for keeping my head in the clouds; and to Kasia for giving me someone to complain to. In particular, many thanks to Bruce Weaver and Ruth Ayers — I could not have asked for better travel buddies, and the joy and sanity you both provided me was invaluable.

Thanks to the wider AttoLab and the Laser Consortium technicians for their help. Without the dedicated work of Andy and Conor much of this project certainly could not have been possible. A further thanks to Susan, whose support and regular chats helped keep me both on my toes and very much sane. Thanks to all those who I have collaborated with through my PhD, including the groups on Antonio Picon, Zhenghu Chang and John Travers. In particular, thank you to Chris Brahms for your support- I certainly couldn't have got all the data I did without your guidance!

Beyond the world of work, thank you to the Kempo (and associated games) crew for all your help, a regular (voluntary) battering certainly keeps you sane in the most stressful of times. Being surrounded by real adults also help keep you sane, and your support over the last few years has been invaluable. Beyond these, thank you to Matteo Tabaro, who's friendship and slow encroachment into every aspect of my life helped make lockdown and it's associated stresses more palatable.

Many thanks to those who have put up with me beyond some well defined groups, including: Myat, for some solidarity through the suffering, Dariusz for respite in well-built houses, as well as Moni, Ozan, Alexis and the rest of our rag-tag gaming bunch; Viktoria, Helen and the Bristol lot for your cheerful spirits; Young for a sense of zen and chaos; Danny for being a very, very sensible person; and Ciara for care and friendship at great distance.

More recently, thanks you to all those at RAL who have supported me through the last few months. In particular Greg, whose support and understanding I could not have managed without, and Chris for sassing me until this became readable. I, for one, hope that this, in its final state, was more palatable (for you). Many thanks to Alasdair and Emma for forming a postdoc support bubble around me, and reminding me that all progress is progress.

A thanks beyond words to Ashleigh Cheyne. You have been my everything these last few years, and I literally couldn't have made it here without you.

Many thanks to my family. The last few years have been trying, and the last couple unimaginable. We have been through it together, and I will love you all eternally for it. Thank you to my mother who has kept supporting and moving me on even when I couldn't myself. Thank you to my siblings for helping me remember what's important and keeping me together. Thank you to my anneanne and dede for your support and care- your support and love have helped me keep going and brought me

constant comfort. Thank you to my babaanne for you love and encouragement, which have nourished me in the darkest times. To all the innumerable others — including every Avni, Alsancak, Aytaçoğlu, Yağcıoğlu, Ersin, Nabi and everyone else I could possibly have forgotten — I will never forget your kindnesses nor stop counting my blessings for having you in my life.

Finally, I'd like to thank my father, Bora Avni, who passed away during my PhD. You made me the man I am today, and taught me everything I needed to know to want to do science. You nurtured my curiosity and sense of fun, taught me and taught me to teach, taught me the value of learning, and I loved you to your very last days. I can never thank you enough. Seni çok seviyorum.

Contents

1 Introduction **14**

1.1 Tunable Ultrafast UV Sources 17

1.2 Optimising High Harmonic Generation for TAS Experiments 19

1.3 Developing Pump-Probe Spectroscopies to allow for Control 20

1.4 Overview of Works in This Thesis 23

1.5 Contributions 24

1.6 Publications arising from works in this thesis 26

2 Theory of Non-linear Optics **27**

2.1 Fundamentals of Ultrashort Pulses 27

2.2 Non-linear Optics and Refractive Indices 31

2.2.1 Frequency Mixing and Phase Matching 42

2.3 Wave Guiding and Hollow Core Fibres 45

2.3.1 Optical Capillary Dynamics and Solitons 50

2.3.2 Dispersive Wave Emission 55

3 Interaction of High Intensity Laser Fields with Matter **62**

3.1 High Harmonic Generation 66

3.1.1 The 3-Step Model 66

3.1.2 The Strong Field Approximation 73

3.1.3 HHG Beyond Monatomic Gasses 80

3.1.4 High Harmonics and Phase-matching 81

3.2 Scaling Laws for Non-linear Optics 84

4 Experimental Apparatus and Methods **85**

4.1 Titanium:Sapphire Chirped Pulse Amplifier 85

4.2 Optical Parametric Amplifier 87

4.3 Spectral Broadening in Hollow Core Fibres 91

4.4 Characterisation of Femtosecond Pulses 93

4.4.1 FROG 94

4.4.2 Second Harmonic FROG 96
4.4.3 Self-Diffraction FROG 98
4.4.4 SPIDER 100
4.5 HHG Apparatus 101

5 Implementations of Flexible Hollow Core Fibres for Ultrafast Beamlines 106
5.1 Flexible Fibres for IR Compression 108
5.1.1 Implementation of Flexible Fibre Stretching 112
5.1.2 Broadening Near-IR Pulses using HCFs 117
5.1.3 Optimisation of Fibre Coupling 123
5.2 Resonant Dispersive Waves: A Tunable UV Source for Pump-Probe Experiments 129
5.2.1 Data Collected with Heriot-Watt's Laser System 129
5.2.2 Construction of a Vacuum-Coupled RDW Source 135

6 Development and Modelling of Optimised High Harmonic Generation in the Gas Phase 144
6.1 Development of a Variable-Length Target for High Harmonic Generation 145
6.1.1 The Experimental Design Space 145
6.1.2 Specification And Construction of the Variable Length Cell . . 147
6.2 Modelling HHG in a Variable-Length Gas Cell 151
6.2.1 The Simulation Process 151
6.2.2 Simulating Phase-Matching in the Overdriven Regime 157
6.2.3 A Short-cut to Estimating High Harmonic Flux 162

7 The Interaction of Liquid Jets and Intense Laser Fields 183
7.1 Liquid-phase HHG: Experimental Background 185
7.2 The Interaction of Few-Cycle IR pulses with Thin Liquid Jets 190
7.3 Liquid Phase HHG and the Scattering of Harmonic Generating Electrons 199
7.3.1 Scope for Future Development 207

8 Discussion and Conclusions **212**

8.1 Summary of Results 212

8.2 Future Work 214

8.2.1 The Resonant Dispersive Wave System 214

8.2.2 The Variable Length Gas Cell 215

8.2.3 Laser-Liquid Jet interactions and HHG 216

8.3 Wider Implications 218

9 Appendix **220**

9.1 Elemental Edges 220

9.2 Figure Permissions 240

List of Figures

1.3.1 Reaction Coordinate Example 21

1.3.2 Solvent and Solute Absorption of X-rays 22

2.1.1 The effect of CEP 31

2.2.1 Spectral rearrangement by Self-Phase Modulation 40

2.3.1 Fundamental Bessel Modes 46

2.3.2 Soliton order and the periodicity of pulse compression 54

2.3.3 The effect of non-integer soliton orders 55

2.3.4 RDW emission wavelengths for a variety of HCF parameters 58

2.3.5 Pulse self-compression and RDW formation during propagation along a gas-filled HCF 60

3.0.1 Multi-photon vs tunnelling ionisation 63

3.0.2 The Validity of Ionisation Rate Models as a Function of Peak Field Intensity 65

3.1.1 The Three Step Model 67

3.1.2 Motion of HHG Electrons 69

3.1.3 An Example HHG Spectrum 71

3.1.4 Coherence and Absorption Length in HHG Phase-matching 83

4.1.1 A block diagram for the modified KM Labs Red Dragon laser 86
4.2.1 HE-TOPAS Schematic Drawing 88
4.3.1 Pre-existing Fibre Compressor 92
4.3.2 Pre-existing UV Pump Arm 93
4.4.1 A generalised FROG interaction Region 95
4.4.2 SHG and SD FROG Design 97
4.4.3 A diagram of the APE SPIDER 101
4.5.1 Current Layout of the SXR-TAS Beamline 103
4.5.2 A needled drilled for use in HHG within a differential pumping jacket 104
4.5.3 X-ray transmission through metallic filters 104
5.1.1 An Example of Beam Coupling Efficiency 111
5.1.2 Design for a Home-built Fibre Stretching and Mounting system . . . 113
5.1.3 Design for a Home-built Fibre Stretching and Mounting system . . . 115
5.1.4 The Travers Group at Heriot-Watt's Fibre Tensioning Apparatus . . 116
5.1.5 Mapping the HCF Parameter Space 118
5.1.6 Broadening of the OPA Signal 120
5.1.7 Full Signal Broadening HCF Layout 122
5.1.8 Real and Ideal Beam Modes 124
5.1.9 The used Deformable Mirror 125
5.2.1 RDW Generation Layout at Heriot-Watt 130
5.2.2 RDWs in a 150 µm ID HCF 131
5.2.3 RDWs in a 150 µm ID HCF 132
5.2.4 RDWs in a 150 µm ID HCF 133
5.2.5 RDWs in a 150 µm ID HCF 134
5.2.6 Optical Layour for RDWs at Imperial College 135
5.2.7 Contamination of RDWs by Perturbative Harmonics 137
5.2.8 IR Filtering Scheme using Pinholes 138
5.2.9 Static-fill HCFs generating RDWs 140
5.2.10 Gas Density Profile in an HCF 141
5.2.11 RDWs Generated in a Gradient-fill HCF 142

5.2.12 RDW Transport Design from Fibre to the HHG Beamline 143
6.1.1 Types of Gas Cells for HHG 146
6.1.2 Design of a Variable Length Gas Cell for HHG 150
6.2.1 HHG Code Functional Breakdown 152
6.2.2 An Example of Gas Target Density Profiles 156
6.2.3 Phase Matching Plots at 350 eV 158
6.2.4 Plasma Defocusing and Phase Matching 161
6.2.5 Drop in Harmonic Flux through Reabsorption in HHG 165
6.2.6 Factors Contributing to the Figure of Merit 168
6.2.7 The FOM in Context of Recent Works 172
6.2.8 Full HHG simulations as a comparison to the FOM 174
6.2.9 SFA and FOM lineout comparison 176
6.2.10 FOM Plots Clipped by the edge of the Resampling Region 178
6.2.11 FOM Values calculated when removing the spatial clipping condition 180
6.2.12 A More Rapidly Varying Gas Density Profile 181
6.2.13 FOM calculations using the Rapidly Decaying Gas Target 182
7.1.1 Liquid Jet HHG Experimental Design 186
7.1.2 Key Harmonic Emission Results From Liquid HHG 187
7.1.3 Positional dependence of HHG on the liquid jet's surface 188
7.1.4 VUV Transmission through 20 nm of Isopropanol 189
7.1.5 Images of the emission of the plasma plume for the liquid jet 191
7.2.1 Simulated and Experimental Transmission of the IR Beam Through the Liquid Jet 198
7.3.1 Electron Excursion Distances Compared to Mean Molecular Spacing in Liquid HHG 200
7.3.2 No-Scattering Probability vs. Photon Energy in Liquid HHG 202
7.3.3 Experimental vs Computed Liquid HHG Spectra 204
7.3.4 Pulse intensity envelopes for liquid-phase HHG 207
7.3.5 A First Estimate of a Potential Landscape for Electrons Undergoing HHG 209

List of Tables

3.1 Table of Scaling Laws 84

5.1 Normalised Laser Transmissions through evacuated HCFs 119

6.1 Parameter Limits for Variable HHG Cell Design 149

1 Introduction

The ability to study changes in matter with ever-greater precision drives humanity's increasing understanding of the mechanisms that underpin our universe. As we extend the range of physical and chemical systems that we investigate, the timescale for such examination continues to shrink. Indeed the associated timescales of atomic and electronic motion are femtoseconds (10^{-15} s) and hundreds of attoseconds (10^{-18} s) respectively [1]. To maintain temporal clarity in any measurement, the measuring probe (whether a camera or laser pulse) must have a duration shorter than the time scale of the dynamics we intend to study. The advent of ultrafast physics — in this case, the study of dynamics shorter than a picosecond (10^{-12} s) — and the development of femtosecond laser sources has allowed our continued push to shorter timescales and more complete understandings of physical and chemical dynamics in matter.

The instrumentation and methods developed in this thesis are for the purpose of measuring time-resolved absorption spectra, where light-matter interactions will create changes in the spectral absorption bands of a material [2]. Static absorption spectroscopy, where a single pulse is incident on a sample, provides us with a starting point for understanding a chemical system. An absorption at a particular wavelength tells us that some state in the system has been excited, and some change has been induced in the sample.

To give us time resolution, we use a scheme known as *transient absorption spectroscopy* (TAS), where an initial "pump" pulse is used to instigate some dynamics and a second "probe" pulse is used to observe the state of the system after some delay, with the delay varied to map out the dynamics over their lifetime. Decreases in absorption of the probe pulse spectrum tell us that the pump has "bleached" an area, meaning that state is now less populated and will no longer absorb as much radiation. Increases in absorption of the probe, however, indicate that new states have been populated after excitation by the pump pulse. In this way, we can see how chemical and physical

systems evolve over time. As discussed above, as long as the duration of these pulses is less than the time scale of the dynamics we hope to measure, we can map the transfer of states through the system in time.

In this thesis we will focus on laser absorption spectroscopies. It is worth noting, however, that other types of measurement are also available such as electron- or ion-spectroscopies, where charged particles are measured after atomic or molecular ionisation, and can provide differing but complimentary information [3, 4]. These techniques provide different types of information to laser spectroscopies, particularly regarding atomic and molecular binding energies. They allow a wide range of experiments, such as mass spectrometry [5], Auger spectroscopy [6], or angle-resolved photoelectron spectroscopy [7].

TAS experiments are far more general than the methods using ultraviolet and X-ray pulses that will be discussed in this thesis, and the choice of pump and probe wavelengths is entirely dependant on the types of mechanics one seeks to observe [8–10]. The pump pulse is usually used to simulate some external phenomena: in the terrahertz and *infrared* (IR) this includes molecular vibration and heating; in the visible and *ultraviolet* (UV) this includes photo-physical and ionisation dynamics. The probe wavelengths then examine a particular kind of expected result: bond vibrations and molecular structure changes in the IR; electronic motion and molecular conformation changes in the visible and UV; and atomic structure changes in the *extreme UV* (XUV) and X-ray [9–12].

To generate X-rays for X-ray TAS *high harmonic generation* (HHG) is often employed, and to understand this we will employ a semi-classical picture known as the 3-step model [13–15]. In this technique, an intense laser field (on the order of hundreds of TW/cm^2) reshapes the potential well of a parent atom. This then allows an electron to tunnel into the continuum. The electron can then be accelerated away from, and then back toward, the parent atom by that same laser field. Upon return, the

electron may recombine with its parent, and a photon is emitted. The energy of this photon depends on the characteristics of the laser field, including its peak intensity and wavelength, and the parent atom. HHG has yielded photon energies up to 600 eV that have been used in TAS experiments [16].

Ultrafast X-ray transient absorption spectroscopy experiments in particular are often broken down as being either *x-ray absorption near edge structure* (XANES) and *extended x-ray absorption fine structure* (EXAFS) [17]. In XANES, as the name suggests, the X-ray is exciting a core electron with a photon close to the energy needed to make a specific transition between a core state and another state, often a valence state. Through quantum mechanics, we know that the energy needed for this transition is well defined, and we call these transition energies "edges". A number of these edges, corresponding to photon energies achievable with HHG, can be seen in Section 9.1. Observing the dynamics at these edges gives us specific information regarding the electronic structure in a chemical system. One can also observe the excitation of an electron from core states to Rydberg states, which are higher-lying energetic states which become close in spacing as they approach the ionisation threshold, or quasi-bound states, immediately above the ionisation threshold. With the knowledge that a fixed amount of energy will liberate an electron from the core state of the atom, and that any additional energy will be carried by the electron as kinetic energy, EXAFS gives us information about the atomic structure in the neighbourhood of an atom from scattering events on the liberated electron.

Facility-based X-ray sources have improved rapidly over the last 15 years, with LCLS-II and European-XFEL providing a multi-kHz X-ray source from 0.3 – 11.2 keV [18], and developments in self-amplified spontaneous emission providing coherence for *free electron laser* (FEL) pulses [19]. Where the benefit of facility experiments lies in high brightness X-ray sources at MHz repetition rates, tabletop sources still show advantages in multi-colour coherent pulse experiments, and at longer wavelength UV (i.e. < 5 eV) tabletop sources remain more practical. Also, while the timing

jitter in laser tabletop X-ray TAS can be on the sub-femtosecond scale, the jitter at FEL sources is on the scale of 50 fs [19, 20]. These stem from a fluctuations in a combination of environmental factors (e.g. humidity, temperature and pressure) and experimental factors (e.g. control of the steering magnets on the beam path) which, while individually small, become significant over the few-hundred metre beam path of the electron beam [21].

Furthermore these HHG setups provide easier experimental access once constructed, not requiring scientific panel applications for access, and can more readily be used for benchmarking, prototyping or proof-of-principle experiments. Tabletop sources are also comparatively portable, particularly with recent developments in high-repetition rate ytterbium laser sources and pulse compression methods providing low-maintenance routes to few-femtosecond pulses [22–24], meaning these sources could be brought for on-site industrial applications.

1.1 Tunable Ultrafast UV Sources

Experiments in tabletop ultrafast spectroscopy have developed rapidly through the emergence of sources in the IR, UV and X-Ray (in particular in the water window, spanning 283 – 532 eV, the corresponding to a window that covers the Carbon, Nitrogen and Oxygen K-edges — elements critical to biologically relevant systems) [23, 25, 26]. Biochemically relevant targets such as retinol (vitamin A1, which is key in mechanisms for low-light vision [27]) and cysteine (found in human hair and skin and interesting for examining the mechanisms of UV damage [28]) demand UV pump pulses in the 100 – 400 nm range, and X-ray probe pulses in the hundreds of eVs for examination of core to valence hole transitions. While sources for these pump wavelengths have long since been available in the form of perturbative harmonics from 800 nm Ti:Sapphire lasers and optical parametric amplifiers (OPAs) operating in the short-wave infrared (SWIR, 1.4 - 3 μm), they require variation of driving wavelengths in order to tune the generated UV wavelength. This requires tweaking alignment and crystal angles downstream, and makes these impractical sources for spectroscopy

on an ever-expanding collection of biochemical samples. Four-wave mixing (FWM) has been a longstanding candidate for tunable sources [29], but at efficiencies around 10^{-3} and pulse durations in the tens of femtoseconds these pulses cannot support TAS experiments requiring few-cycle UV pulses alongside high harmonic-generated X-rays.

Recent advances in *resonant dispersive wave* (RDW) emission show promising and reproducible UV sources by utilising cross-phase modulation and a resonance condition set by the gas fill pressure, driving wavelength and capillary diameter. While results thus far limit RDW emission to few microjoule levels similar to the limits of FWM, these have provided sources both brighter and more tunable than these perturbative harmonic and FWM sources in the UV, being achieved with as little as 10 times less pump energy, and by the nature of the emission method and the pulses are emitted with few-fs durations[23].

This stems from the fact that in the process of generating these pulses in capillaries the normal and anomalous dispersions of the system balance to form an optical soliton — a shape-preserving pulse which propagates either unchanged or with well defined periodic changes (further details can be found in section 2.3) [30]. This soliton undergoes a process known as soliton self-compression, where a laser pulse becomes temporally shorter as it propagates. This continues until it reaches optimal compression and undergoes a process known as soliton fission, where the pulse is then temporally dispersed. A more complete description of this process can be found in Section 2.3. When the soliton reaches its greatest temporal compression point (generally on the order of few femtoseconds long) the energy in the fundamental field is most efficiently transferred to the UV through a phase matched process. The soliton then temporally disperses and the energy transfer is terminated, while the short UV pulse continues to propagate to the end of the capillary.

The limiting factors for RDW systems are the laser coupling efficiency and temporal and energy stability of the input pulse. With a beam input determined by the compressed output of a *hollow core fibre* (HCF) compressor and characterised using *frequency resolved optical gating* FROG [31], however, these systems can be tuned for experiments on a day-by-day basis, and have UV emission energy fluctuations well characterised and monitored.

1.2 Optimising High Harmonic Generation for TAS Experiments

Recent developments in ultrafast laser science have seen a wide range of sources reach the 280 eV photon energy harmonics required for experiments probing the carbon K-edge and sulphur L-edges, including systems driven by 100 kHz repetition rate off-the-shelf ytterbium-based laser systems [32], Cr:ZnSe systems providing few-mJ driving pulses at 2.5 μm [25], and a variety of *optical parametric amplifier* (OPA) sources in the 1–2 μm range driven by titanium-sapphire lasers [33–35]. Increasing the level of experimental availability and reproducibility to the ≥400 eV energies needed to reach the nitrogen and oxygen K-edges for probing bio-molecular samples and metal-ligand complexes however remains a challenge.

Works improving the efficiency of X-ray generation from HHG are yielding greater flux and higher cutoffs [36, 37], with some works claiming an order of magnitude higher photon fluxes achieved by careful selection of their HHG source [38], but there is a diversity in the characteristics of HHG sources across the many active research groups. This can make the relative efficiency of each method hard to compare. This has generally come about either due to the specificity of the wavelengths targets for a group's experiments, or because the techniques used to generate the harmonics are technically difficult to reproduce due to the means by which they are engineered.

A good example of the latter comes from diffuse gas jets flowing into vacuum pumped chambers [39, 40], or sub-mm targets which are drilled in-situ by the laser which drives harmonics to create short, high density gas cells, leading to a cell which, while relatively efficient, must be changed if there is significant realignment of the laser or any changes in the vacuum chamber in which it is housed [41]. Furthermore, in the laboratory our group wish to conduct an array of experiments in both the liquid and gas phase, with varying targets and probe wavelengths in the X-ray region. As different harmonic energies require differing backing pressure and focal spot sizes, an HHG source that can reproducibly provide harmonic spectra across the *soft X-ray* (SXR, 150 eV – 3 keV) range is essential for maintaining experimental efficiency.

1.3 Developing Pump-Probe Spectroscopies to allow for Control

As RDW generation can require only tens to few-hundreds of microjoules of energy in a narrow (≈100 μm) capillary fibre, they can be driven by a small amount of energy split from the beam used to drive HHG. Alternatively, as they do not share the *carrier envelope phase* (CEP) dependence of HHG, as will be discussed in section 2, they can be used by the non-CEP stabilised output of the same OPA that drives HHG for a TAS experiment. Both of these cases mean that the pump pulses for the intended TAS experiment can be synchronous with the probe pulses, with timing jitters below 0.3 fs reported from RDW systems [20]. This becomes increasingly important as experiments move from pump-probe spectroscopy to so-called "quantum control", where a control pulse is placed between the pump and probe to manipulate the molecular dynamics instigated by the pump pulse [42, 43].

A simple coordinate-space model of such a system with this pulse configuration can be seen in Figure 1.3.1. The systems of particular interest here involve conical intersections, where the potential surfaces of two states intersect, with a point at which they become degenerate. Manipulation of the wavepackets near the conical intersection,

or a dressing of the intersecting potential energy surfaces (where a light-matter interaction causes modifications to electronic states), therefore provides new mechanisms by which the final state of the system can be manipulated.

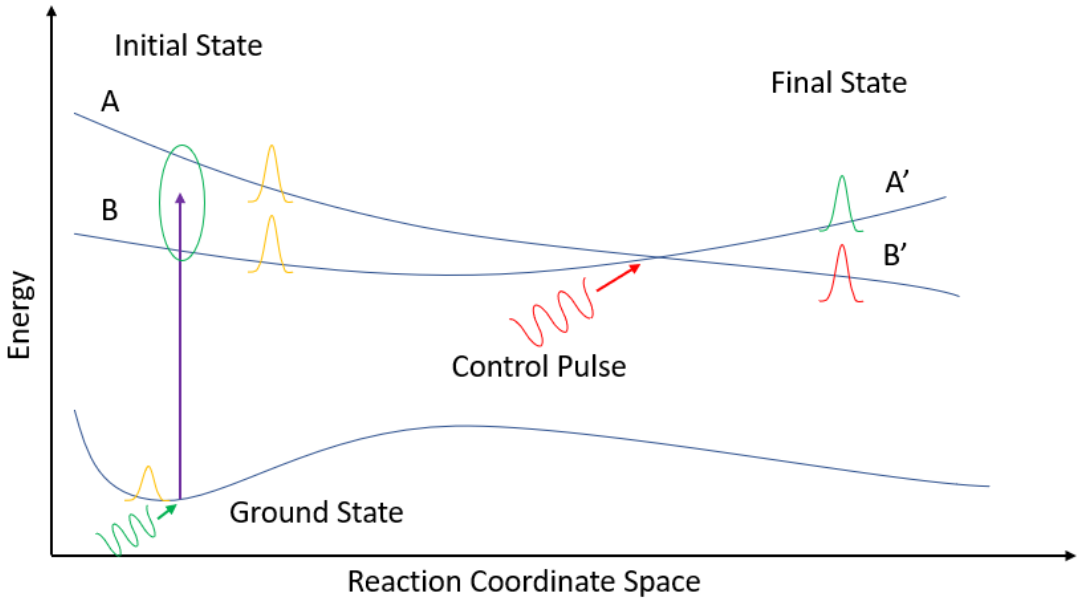


Figure 1.3.1: The basic design concept for a quantum control experiment. An electron wavepacket is excited into a superposition of states A and B by a broadband pulse, which propagates along the coordinate space. While the final state of the system without the control pulse will be most likely to end in the state A', the addition of a control pulse while the electron wavepacket passes through a conical intersection allows experimentally steering the wavepacket into the B' final state.

For liquid phase transient absorption experiments in particular the signal-to-noise is generally limited by background X-ray absorption in the solvent and the solubility of the solute. For example photons at the sulphur $L_{2,3}$ edge (165 eV) are needed for probing sulphur bridges, while chlorine or calcium $L_{2,3}$ edges (200 and 350 eV respectively) are needed to probe bio-molecular samples soluble in alcohols and water. With a continuously flowing thin liquid jet to inject the sample these systems can be used for absorption spectroscopy at high repetition rates. This would overcome the limitations set by sample heating and other forms of damage such as photobleaching

by having the sample refresh rate limited only by the flow of the jet (the liquid in the jet in this thesis flows at 14 ms^{-1}), and a recirculating system could support such an experiment for long periods of time.

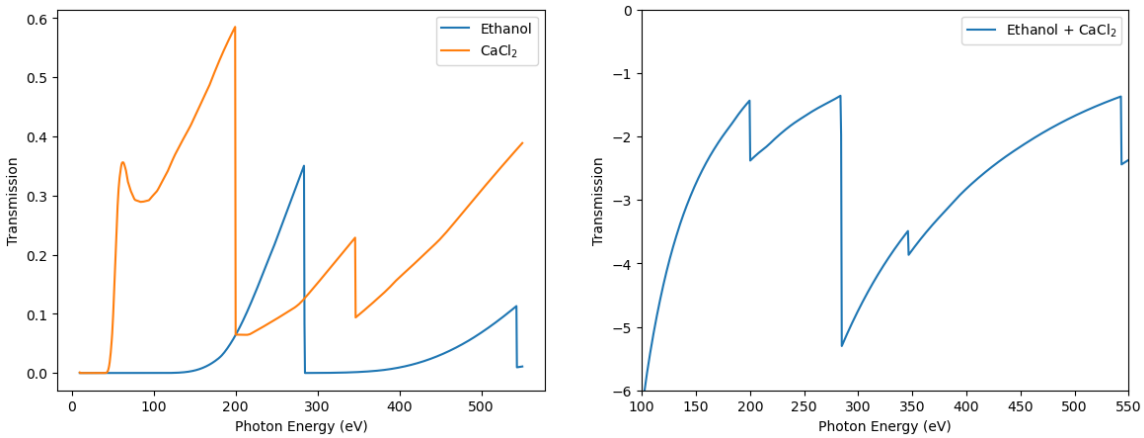


Figure 1.3.2: Left: Transmission through a 1.6 µm sample of ethanol and a 0.4 µm sample of $CaCl_2$ (Data from [44]). Right: A $\log_{10}$ transmission curve of the transmission through a combination of the the two media. Combined, these curves allow us to estimate observable signals in a 25 g/100 g solution of $CaCl_2$ in ethanol, which represents maximum solubility.

Given a 2 µm thick jet such as the one presented by our lab in previous publications [45, 46], the graphs in Figure 1.3.2 give an example of absorption peaks for calcium chloride ($CaCl_2$) in ethanol, as was planned to benchmark the transient absorption setup in the laboratory after a set of updates to the beamline (although those works will not be covered in this thesis). Here a solubility of 25.8 g/100 g is achievable, and at the calcium and chlorine $L_{2,3}$ edges (350 and 200 eV respectively) one would expect a 90% or 99% signal loss respectively from static absorption in the solvent.

The absorption rate is dependent on the absorption cross-section of the samples. For $CaCl_2$ the absorption cross-sections are on the order of 2.7×10^{24} cm^{-2} and 3.7×10^{24} cm^{-2} at the calcium and chlorine $L_2, 3$ edges, respectively[44]. Given that resolving X-ray absorption peaks in complex molecules can provide a challenge in the solid phase, where solvent dynamics are not an issue, these low signal levels limit our ability to

resolve the absorbance changes, meaning increasing harmonic flux to enable study of a wider range of systems at lower noise levels is essential.

1.4 Overview of Works in This Thesis

This thesis discusses a project to further develop UV-pump, X-ray probe systems that can be well characterised, so that both can be wavelength tuned and optimised to best suit any experiment they are used for. Section 2 discusses the theory of non-linear optics, both in general concepts and those pertaining to the construction of HCFs and and the generation of RDWs. Section 3 continues the theoretical background focussing on the interaction of intense laser pulses with matter, in particular concerning ionisation, and the generation of plasma and high harmonics, using the strong field approximation. Section 4 gives an introduction to the experimental apparatus used in this thesis, including the tools that these works are developed to enhance and instruments for the characterisation of few-fs laser pulses.

Section 5 covers the design and implementation of a hollow core fibre compressor for 1300 nm IR pulses for use in RDW generation and HHG, including in-house designs, construction and laser coupling optimisation considerations and pulse characterisation. The consequent generation of tuneable femtosecond UV pulses is demonstrated, both through external collaboration and in-house, and schemes for filtering and connecting these systems to a HHG beamline are outlined.

Section 6 discusses modelling the interaction of high intensity laser pulses with liquid jets, and the generation of HHG in the liquid phase, with direct comparison to experimentally achieved results. The few-cycle generation of a plasma mirror, scattering of electrons during HHG, and analysis of the recombination-picture of harmonic generation in the liquid phase is presented. The discussion of liquid phase models for HHG, their current limitations and next steps for development are outlined. Furthermore, a scalable gas cell for HHG is constructed to enable reproducible production of SXR HHG for TAS, operating in regimes of few-bar pressures, of lengths from

few-hundreds of micron to centimetres, driven with energies up to few-hundreds of microjoules.

An approach to modelling parametric characterisation of HHG systems is detailed, in particular for systems beyond the usual parametric scaling laws which require low-plasma density. The model reduces the computation time of large simulations by an order of magnitude by instead producing a numerical figure of merit that represents harmonic flux. This can allow rapid optimisation of experimental design, and a brief presentation of steps towards parametric characterisation of these figures of merit is outlined. While the accuracy of the model still needs to be established through experimental comparison, the computation time is reduced by at least two orders of magnitude.

1.5 Contributions

These works were performed collaboratively with the contributions of both colleagues and external collaborators. The development of in-house fibre cells was performed by the author, Clement Ferchaud, Esben Witting-Larsen and Daniel Walke. The designs for external cells and code for modelling laser propagation through HCFs were provided through collaboration with the John Travers group at Heriot-Watt university. The system construction and RDW data taken at Heriot-Watt was performed by the author and Christian Brahms. The construction of the RDW system at Imperial College was performed by the author, in particular the selection laser and gas parameters for both the OPA signal compressor and the RDW system, construction of the signal compressor, temporal measurement and characterisation of the pulses, construction of the chirped mirror compressor breadboard, and building up the RDW fibre system. Assistance for this work was provided by Clement Ferchaud, Douglas Garratt, Jacob Lee and Katarzyna Kowalczyk. The construction of the modified cells was and Brewster angle window mounts performed by Andy Gregory and Conor O'Donovan to the authors specification.

The experimental data from the liquid jet system was primarily acquired by Sebastian Jarosch, Oliver Alexander and Jonathan Barnard, with assistance from the author. The code for modelling laser propagation and HHG was written by Dane Austin. The adaptions, on the order of few-hundreds of lines, to the code for liquid phase HHG were performed by the author. The laser-jet interaction data interpretation was performed by the author and Clement Ferchaud. The modelling of electron scattering and recombination was devised by the author, Oliver Alexander and Jonathan Barnard, with advice provided by Misha Ivanov. The calculation and integration of the scattering probabilities of propagated electrons during HHG into the simulated HHG was performed by the author. This involved calculating the emission at each point in space, applying the recombination probabilities, and propagating the resultant harmonic emission to the end of the target region. The interpretation of these results in relation to the experimental data and developing understanding of the data was performed by the author, Oliver Alexander, Jonathan Barnard, Sebastian Jarosch, Esben Witting-Larsen, Mary Matthews, and Prof. Jon Marangos.

Design of the variable length HHG system was performed by the author and Clement Ferchaud, and its production was performed by Conor O'Donovan to the authors specification, with technical assistance from Susan Parker. Commissioning of the system was performed by the author and Jacob Lee. Modifications to the simulation code for phase-matching plots, and interpretation of the data, was performed by the author and Allan Johnson. Adaption of the data code for figure-of-merit calculations and the code's adaption for high throughput computing was performed by the author. This involved using the non-linear propagation code, and combining the phase-matching calculations with other calculated factors to create a figure of merit. Data analysis of all HHG simulations was performed by the author.

1.6 Publications arising from works in this thesis

References

[1] Lee, J. P., **Avni, T.**, Oliver Alexander, O., Maimaris, M., Ning, H., Bakulin, A. A., G. Burden, P. G., Moutoulas, E., Georgiadou, D. G., Brahms C., Travers, J. C., Marangos, J. P., and Ferchaud, C., *Few-femtosecond soft X-ray transient absorption spectroscopy with tuneable DUV-Vis pump pulses.* Optica 11, 1320-1323 (2024)

[2] Alexander, O., Barnard, J. C. T., Larsen, E. W., **Avni, T.**, Jarosch, S., Ferchaud, C., Gregory, A., Parker, S., Galinis, G., Tofful, A., Garratt, D., Matthews, M. R., Marangos, J. P. . *Observation of recollision-based high-harmonic generation in liquid isopropanol and the role of electron scattering.* Phys. Rev. Research 5, 043030 (2023) https://doi.org/10.1103/PhysRevResearch.5.043030

[3] Ferchaud, C., Jarosch, S., **Avni, T**., Alexander, O., Barnard, J. C. T., Larsen, E. W., Matthews, M. R., Marangos, J. P. *Interaction of an intense few-cycle infrared laser pulse with an ultrathin transparent liquid sheet.* Optics Express, 30(19), 34684 (2022).. https://doi.org/10.1364/oe.457470

[4] Johnson, A. S., **Avni, T.**, Larsen, E. W., Austin, D. R., Marangos, J. P., *Attosecond soft X-ray high harmonic generation.* Philosophical Transactions of the Royal Society A: Mathematical, Physical and Engineering Sciences, (2019.) https://doi.org/10.1098/rsta.2017.0468

[5] Murari, K., Zhou, F., Yin, Y., Wu, Y., Weaver, B., **Avni, T.**, Larsen, E., Chang, Z. . *Ho:YLF amplifier with Ti:Sapphire frontend for pumping mid-infrared optical parametric amplifier.* Applied Physics Letters, 117(14), 141102 (2020). https://doi.org/10.1063/5.0021438

2 Theory of Non-linear Optics

Non-linear optics is largely the process of controlling a combination of higher order refractive indices and phase matching conditions to enable a given phenomena. While complex processes in their own right, *high harmonic generation* (HHG) and *resonant dispersive wave* (RDW) emission can be reduced to a delicate balance of competing refractive indices, and hence dispersions, in a spectral region in which a phase-matching condition is met.

In this chapter the basic mathematical tools for ultrafast optics will be introduced, and the formal descriptions of their interaction with matter at low and high intensities will be presented, with elements drawn from a range of standard texts [47–49]. The mechanisms for ultrafast dynamics in *hollow capillary fibres* (HCFs) and an introduction to HHG are also given. Finally, an introduction will be given to some of the experimental methods and tools common to both Section 5 and Section 6.

2.1 Fundamentals of Ultrashort Pulses

The propagation of a real-valued, linearly polarised field, $\mathcal{E}$, in a vacuum or a dielectric medium is effected by the polarisation response, $\mathcal{P}$, of the medium. We restrict ourselves to these dielectric media as there are no free charges. $\mathcal{P}$ is defined by Maxwell's wave equation:

$$\nabla^2\mathcal{E} - \frac{1}{c^2}\frac{\partial^2\mathcal{E}}{\partial^2 t} = \frac{1}{\varepsilon_0 c^2}\frac{\partial^2\mathcal{P}}{\partial^2 t}, \tag{2.1.1}$$

where ε_0 is the permittivity of free space, and $\mathcal{P}$ is an expansion of polarisability coefficients, χ, given by

$$\mathcal{P} = \varepsilon_0 \sum_{n->\infty} \chi^{(n)} \mathcal{E}^n. \tag{2.1.2}$$

Each successive term of χ represents a greater order of nonlinear response in a medium.

In the general case χ is a tensor, and this dimensionality allows for dynamics driven by anisotropy in materials the field encounters [49]. Second harmonic generation, as will be mentioned later, requires that the material be non-centrosymmetric (that is, the crystal exhibits different structure along at least one of its symmetry axes that the others), and this anisotropy also gives rise to birefringence in the material, where there refractive index varies with the angle of the crystal.

In general however, for the phenomena explored in this thesis we will be examining the interaction of lasers with gasses and liquids. In these cases, the tensorial nature of the susceptibility can be suppressed, as there is no coupling between the the propagating field with any kind of structural axes in the medium. As such, for now we shall continue to write χ as a scalar.

While there is no requirement for the polarisation of electric fields in general to be linear, all of the beams we will consider in the following sections and chapters will be linearly polarised. For HHG in gasses, harmonics are generated using linear polarisation, and while circularly polarised harmonics have been generated [50] these schemes will not be considered in this thesis, and they are generated by the superposition of two linearly polarised fields. In the gas phase any ellipticity drastically reduces the intensity of generated harmonics [51], and while harmonics have been generated with

circularly polarised driving lasers in other media, such as solids [52], these will not be considered here.

For pulses propagating in HCFs, there is no requirement that the propagating pulse be linearly polarised to propagate in a capillary — indeed, recent studies have shown compressed solitons and resonant dispersive wave emission in the UV using circularly polarised laser fields [53]. A capillary can support a wide range of polarisations, but for the experiments in this thesis, only linear polarisations were used, as the experiments for which the ultrashort pulses are being supplied need only linear polarisation.

For the time being we will return to the case of a linearly polarised pulse propagating through a vacuum, our wave equation from Equation 2.1.1 reduces to the wave equation

$$\nabla^2\mathcal{E} - \frac{1}{c^2}\frac{\partial^2\mathcal{E}}{\partial^2 t} = 0, \tag{2.1.3}$$

whose solutions include the linear superposition of plane waves. Rather than using the real valued $\mathcal{E}$ field, we choose here to use the complex analytical field, E, for the rest of this thesis, as we lose no accuracy in doing so and it is more convenient to manipulate. In general space-time co-ordinates, $(\mathbf{x}, t)$, we define E by

$$\mathcal{E} = \frac{1}{2}(E(\mathbf{x},t) + E^*(\mathbf{x},t)) = \Re E(\mathbf{x},t). \tag{2.1.4}$$

By choosing z as our propagation axis, and defining a point $z = 0$ for the initial centre of the pulse we can describe the propagation of the pulse by

$$E(x,y,z,t) = E(z=0,t)\exp(ik_z z), \tag{2.1.5}$$

where k_z is the z component of the plane wave wave vector defined by

$$k^2 = k_x^2 + k_y^2 + k_z^2. \tag{2.1.6}$$

We can express time or frequency domain variations in these fields as Fourier transforms of one another, written as

$$\begin{aligned} E(t) &= \frac{1}{\sqrt{2\pi}} \int_{-\infty}^{\infty} \tilde{E}(\omega) \exp(-i\omega t)\, d\omega, \\ \tilde{E}(\omega) &= \frac{1}{\sqrt{2\pi}} \int_{-\infty}^{\infty} E(t) \exp(i\omega t)\, dt. \end{aligned} \tag{2.1.7}$$

We also use Equation 2.1.7 to define the temporal or spectral intensity of the field, I. This is the quantity we can physically measure in the laboratory and is given by

$$I(t) = \frac{n\varepsilon_0 c}{2}|E(t)|^2 \quad \text{and} \quad \tilde{I}(\omega) = \frac{n\varepsilon_0 c}{2}|\tilde{E}(\omega)|^2 \tag{2.1.8}$$

Temporal Phase

For ultrashort pulses is often more convenient to condense this expression down to the slowly varying Gaussian envelope E_0(t) with a peak value E_{pk}, and a carrier wave, expressed as

$$E(t) = E_0(t) \exp(-i(\omega_0 t + \Phi(t))) = E_{pk} \exp\left(-\left(\frac{t}{2\tau_g}\right)^2\right) \exp(-i(\omega_0 t + \Phi(t))), \tag{2.1.9}$$

where τ_g is the Gaussian temporal width of the pulse and $\Phi(t)$ is the temporal phase of the pulse. Rather than using the Gaussian pulse width, we often use the *full-width at half-maximum* (FWHM) duration τ, which is given by $\tau = 2\sqrt{2ln(2)}\tau_g$.

While phases in the spectral domain will be discussed in detail later, we will focus on two main aspects of temporal phase here. First is the existence of the phase difference

between the carrier wave, of frequency ω_0, and the envelope, ϕ_0 . This is referred to as the carrier-envelope phase (CEP) and can become crucial in the pulses as they approach the few-cycle limit. This is because the phase will determine where in the pulse envelope the peaks of the carrier field will fall, as seen in Figure 2.1.1. When observing peak intensity-dependent phenomena such as HHG, fixing the CEP can be critical. Methods for doing this in practise are outlined in section 4.2.

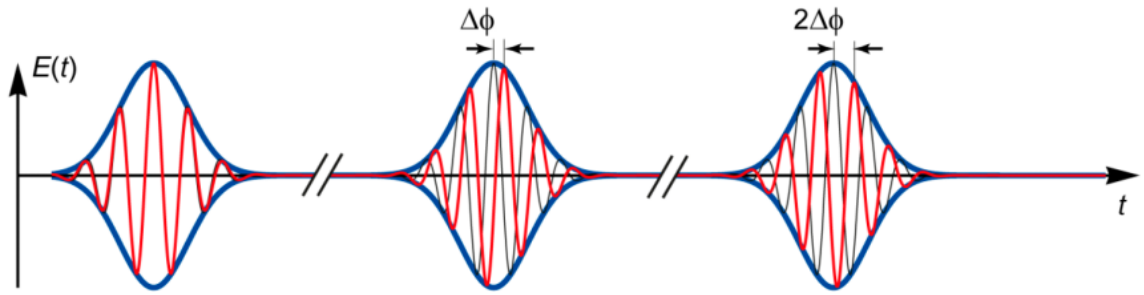


Figure 2.1.1: A depiction of the effect of CEP of an few-cycle laser field. Here $\Delta\phi$ denotes an arbitrary shift away from the maximal carrier wave peak intensity. The grey waveform indicates the original pulse, and the red waveform is the phase-shifted pulse. Adapted with permission from [54] under CC BY-NC 4.0.

The second is the identity that the time derivative of the phase defines the instantaneous frequency of the field, i.e.

$$\omega = -\frac{d\Phi}{dt}. \tag{2.1.10}$$

In cases where there is a time-varying phase, as will become relevant in later sections, these effects will then create frequency shift in the pulse.

2.2 Non-linear Optics and Refractive Indices

The refractive index, $n(\lambda)$, defines the speed of light in a medium, and is generally wavelength dependent. This is an approximation however, and is limited to interaction with weak electric fields where Equation 2.1.2 reduces to $P = \varepsilon_0\chi^{(1)}\varepsilon$, as

$\chi^{(1)} >> \chi^{(n>1)}$. This regime is referred to as linear optics, and is where the refractive index can be expressed as as $n = \sqrt{1 + \chi^{(1)}}$.

As we increase the intensity of the however field this approximation breaks down, as the contributions of the $n > 1$ orders of the polarisation as expressed in Equation 2.1.2 become more significant. With each order of the susceptibility we consider the interactions become substantially weaker: barium borate, for example, which exhibits both second and third order nonlinearity has the following susceptibilities [49]:

$$\begin{aligned} \chi^{(2)} &= 1.94 \times 10^{-12}\,\mathrm{mV^{-1}} \\ \chi^{(3)} &= 3.78 \times 10^{-24}\,\mathrm{m^2V^{-2}} \end{aligned} \tag{2.2.1}$$

For the purposes of this treatment, we will limit the expansion of the interaction to third order, following common convention. The first step now is to fully expand the polarisation response of a system from eq. (2.1.9) to third order, which gives us:

$$\begin{aligned} P(t) &= \sum^{n\leq 3} \epsilon_0 \chi^{(n)} \left(\frac{(E_0(t)\exp(-i\omega t)) + E_0^*(t)\exp(-i\omega t))}{2} \right)^n \\ &= \frac{\epsilon_0\chi^{(1)}}{2}[E_0\exp(-i\omega t) + E_0^*\exp(i\omega t)] \\ &+ \frac{\epsilon_0\chi^{(2)}}{4}[2|E_0|^2 + (E_0^2\exp(-i2\omega t) + \text{c.c.})] \\ &+ \frac{\epsilon_0\chi^{(3)}}{8}[2E_0^3\exp(-i3\omega t) + 6E_0\exp(-i\omega t)|E_0|^2 + \text{c.c.}] \end{aligned} \tag{2.2.2}$$

We first remove the term of the form $|E(t)|^2$, which represents a process known as optical rectification. This process is used to generate terahertz pulses [55], but is not pertinent to the dynamics we will consider in this thesis.

We will next remove the terms that correspond to perturbative harmonic generation, which do not represent changes to the response experienced by the field but rather

the generation of a new field. For the q^{th} harmonic, these terms take the form:

$$P_{\text{harm}} = \frac{\varepsilon}{2^{q-1}}\chi^{(q)}E^q(t) = \frac{\varepsilon}{2^{(q-1)}}\chi^{(q)}E_0^q \exp(-iq\omega_0 t). \tag{2.2.3}$$

In this form it is clear that these terms are harmonics of the original field, as the power that the field is raised to simply multiplies the frequency of the carrier field in the exponent of the oscillatory component of the field.

As mentioned earlier, in any medium with centrosymmetry $\chi_2 = 0$, and so without exploiting phenomena which explicitly break this symmetry (for example interactions at a material surface) one will not observe second order nonlinear effects, or indeed any higher even term [49]. Centrosymmetric materials include most crystaline and amorphous glasses, liquids and noble gasses, and as such second order non-linearities will not be discussed much in this thesis, and so we drop this term in Equation 2.2.4. Formally, this mean that we will exclude even-order non-linearities from our discussions, and leave out any terms in even-order χ in our expansions of P.

The only exceptions here are the non-linear crystals used in the optical parametric amplifier for generating IR beams and in the construction of a diagnostic, both of which are described in Section 4. These are due to the noncentrosymmetric nature of the crystals used, which in the case of the diagnostic is barium borate (BBO). BBO is a commonly used crystal for SHG as it has broad-band phase matching from 405–3500 nm, with the matched wavelength selected by rotating the crystal (beyond which range its absorption coefficient sharply increases).

This is due to the birefringence of the material, where the refractive index along the ordinary and extraordinary axes of the crystal differ due to crystallographic structure. Rather than rotating a crystal to match the angle needed for the system, crystals are often purchased cut at angles relative to the optical axis, such that a beam at normal incidence sees the angle needed to phase-match second harmonic generation in the crystal.

With the above terms removed, and recalling from eq. (2.1.8) that $I(t) = \frac{c\varepsilon_0}{2}|E(t)|^2$ we are left with the following expression:

$$\begin{aligned} P &\approx \varepsilon_0(\chi^{(1)}E(t) + \frac{3}{4}(3E(t)|E(t)|^2\chi^{(3)})) \\ &= \varepsilon_0(\chi^{(1)}E(t) + \frac{3}{4}\frac{2}{c\varepsilon_0}\chi^{(3)}E(t)I(t) + O(5)) \end{aligned} \tag{2.2.4}$$

This drives both self-focusing and self-phase modulation (SPM), and gives us an effective refractive index, n_{eff}, of

$$n_{\text{eff}} = \sqrt{n_0^2 + \frac{3}{4c\varepsilon_0 n_0^2}\chi^{(3)}I} \approx n_0 + n_2 I, \tag{2.2.5}$$

where we define the term $\frac{3}{4c\varepsilon_0 n_0^2}\chi^{(3)}$ as the intensity dependent refractive index, or n_2, and the approximation here is justified by the fact that $n_2 \ll n_0$. Nonlinear refractive indices in gasses and solids at STP (standard temperature and pressure) are on the order of 10^{-7} and 10^{-5} respectively, making the value of the nonlinear component of the refractive index significantly smaller than the linear component. The overall effect here, whereby the refractive index is altered by the local intensity of the field, is known as the optical Kerr effect[49].

Higher Order Phases

Careful consideration of linear and non-linear refractive indices becomes vital in a number of scenarios. The first is where any phase-matching condition must be met, as these processes rely on conservation of momentum, meaning that a varying refractive index will cause variation in the phase matching angles. These will be discussed later for optical parametric amplification (OPA), but are also true for second or third harmonic generation, for example.

The second is when considering ultrashort pulses, as the refractive index describes a difference in the local speed of light in a medium. For pulses on the timescale

of femtoseconds, these difference in local speed can amount to significant delays for differing wavelengths, and can act to change the duration of the pulse. To understand how this can impact an experiment, we must first introduce the bandwidth theorem which (in terms of wavelength) states simply that for a pulse of central wavelength, λ_0,

$$\Delta t \Delta \lambda \geq \frac{\lambda_0^2}{c}, \tag{2.2.6}$$

where Δt and $\Delta \lambda$ correspond to the temporal duration and spectral bandwidth of the pulse respectively, both given as a full-width at half maximum (FWHM), c is the speed of light, and λ_0 is the central wavelength of the laser field. To give a numerical example, this means that for a pulse with a central wavelength of 800 nm and a FWHM duration of 30 fs a minimum spectral bandwidth of 22.4 nm is required. This becomes pivotal to the way we choose materials for experiments with few-cycle pulses as the refractive index n is typically wavelength dependent, and the wider the spectral bandwidth the greater the phase added to the pulse as it passes through the medium.

This can be made explicit by Fourier transforming Equation 2.1.9 to express spectral phrase of the pulse $\Phi(\omega)$ and Taylor expand it to give

$$\Phi(\omega) = \sum_{n=0}^{\infty} \frac{1}{n!} \phi_n(\omega)(\omega - \omega_0)^n. \tag{2.2.7}$$

The zeroth term, ϕ_0, is the CEP we defined in Equation 2.1.9. We label the higher order terms with increasing n as the group delay (GD), group delay dispersion (GDD), and third order dispersion (TOD). There is an $n!$ in the denominator of Equation 2.2.7, and so the phase terms become rapidly smaller in magnitude with increasing order. Typically we truncate the Taylor series to exclude terms beyond the third order, both because terms have exponentially lower effects as the order increases, and as the accuracy with which we can interpolate and correct these orders decreases correspondingly with order.

The first order term, the GD, is constant in time, and therefore indicates a flat temporal delay of the pulse. While this indicates a shift between arrival times across multiple pulses, it is not impactful for a single pulse. The TOD imparted by all materials in the regions we examine in this thesis is positive, and cannot be corrected by transmission through a bulk medium. In other wavelength ranges (for example in the 800 nm range provided by the driving laser from the Red Dragon system mentioned later) one may have the options of using schemes such as a pair of prisms for fine control of the dispersion. Instead we must use a specialist instruments, for example an acousto-optic modulator, 4-f pulse shapers, or with reflections from dispersive optics such as diffraction gratings or chirped mirrors, which will be discussed further shortly. TOD both stretches the pulse in time and creates temporal satellites around the pulse, which one always seeks to avoid as a pre-pulse can pre-ionise a sample prior to the arrival of the peak intensity of the laser pulse. For processes such as HHG this is particularly disruptive, as this both reduces the number of available emitters and can induce plasma defocusing, leading to a reduced peak intensity.

The second order phase is also known as "chirp", and describes the linear discrepancy in arrival time of frequencies in the pulse. A positive chirp describes a pulse whose shorter frequencies arrive earlier than its longer frequencies. There are two main methods of compensating chirp for few-fs pulses. The first is known as bulk compression, where a pulse is propagated through a medium with known dispersion, to a set length to compensate chirp. In transmission the measure for imparted GDD is the delay per unit length, or group velocity dispersion (GVD). Alternatively, chirped mirrors can be used, which are multi-layer optics where each layer is transmissive, with the phase accumulation between each each layer defining accumulated phase shifts between them which imparts GDD [56].

It is possible to analytically quantify the temporal phase accumulated while propagating through a dispersive medium, which will become important when considering

HCFs. To do this, we consider a field defined as in eq. (2.1.7) propagating with a central frequency ω_0

$$\tilde{E}(\omega) = \sqrt{2\pi} E_0 \tau \exp\left(-\frac{1}{2}\tau^2(\omega-\omega_0)^2\right). \tag{2.2.8}$$

We propagate this through a material with dispersion β_2 over a distance L, giving us

$$\begin{aligned}\tilde{E}(\omega, L) &= \sqrt{2\pi} E_0 \tau \exp\left(-\frac{1}{2}\tau^2(\omega-\omega_0)^2\right) \exp\left(i\frac{1}{2}\beta_2 L(\omega-\omega_0)^2\right) \\ &= \sqrt{2\pi} E_0 \tau \exp\left(-\frac{1}{2}\frac{(\omega-\omega_0)^2}{(\tau^2 - i\beta_2 L)^{-1}}\right)\end{aligned} \tag{2.2.9}$$

By Fourier transforming back this to the time domain, we find that we have an explicit expression for the accumulated phase:

$$\begin{aligned}E(t, L) &= E_0 \exp\left(\frac{1}{2}\frac{t^2}{(\tau^2 - i\beta_2 L)}\right) \exp(-i\omega t) \\ &= E_0 \exp\left(\frac{1}{2}\frac{(\tau^2 + i\beta_2 L)}{(\tau^4 + \beta_2^2 L^2)} t^2\right) \exp(-i\omega t) \\ &= E_0 \exp\left(-i\left(\omega t + \frac{\beta t^2 L}{\tau^4 + \beta^2 L^2}\right) + \frac{\tau^2 t^2}{\tau^4 + \beta^2 L^2}\right) \\ \implies \phi_{\mathrm{GVD}}(t) &= \frac{\beta_2 t^2 L}{\tau^4 + \beta_2^2 L^2}\end{aligned} \tag{2.2.10}$$

Self-Phase Modulation

Since we know that the effective refractive index is dependent on the intensity of the pulse, we now have a time-dependent refractive index. This will impart a phase onto the pulse and is known as self phase modulation (SPM). We define the instantaneous

frequency, $\omega(t)$ of a pulse as the time derivative of the phase of the pulse, Φ. For a pulse travelling through a medium with linear and nonlinear refractive indices n and n_2 over a distance L, the accumulated nonklinear phase Φ_{NL} can be expressed as [49]

$$\begin{aligned} E(z,t) &= A(z,t)\exp(i(k_0 z - \omega_0 t))\exp(-i\Phi_{NL}) \\ &= A(z,t)\exp(i(k_0 z - \omega_0 t))\exp(-i(-k_0 n_2 I(t) L)). \end{aligned} \tag{2.2.11}$$

Using the expression from eq. (2.1.9) for the time dependent field, we then find that the instantaneous frequency can be written as

$$\omega(t) = \omega_0 + \frac{\partial \Phi_{NL}}{\partial t} = \omega_0 - \left(k L n_2 \frac{\partial I(t)}{\partial t} \right), \tag{2.2.12}$$

and removing the expressions for the initial frequency and phase of the pulse, ω_0, and ϕ respectively, we can define the instantaneous nonlinear frequency shift $\delta\omega$, as

$$\delta\omega(t)_{SPM} = -\left(k L n_2 \frac{\partial I(t)}{\partial t} \right), \tag{2.2.13}$$

and we assume a Gaussian temporal intensity for the pulse, with a temporal FWHM of τ.

As the effect of the nonlinear refractive index is strongly dependent on the instantaneous intensity, we will make the approximation that we are considering only times close to the peak of pulse, meaning that the time derivative of $I(t)$ can, using a Taylor

expansion to first order, be expressed as

$$\begin{aligned}\frac{\partial I(t)}{\partial t} &= \frac{\partial}{\partial t} I_0 \exp\left(-\left[\frac{t}{\tau}\right]^2\right) \\ &\approx I_0 \frac{\partial}{\partial t}\left[1-\left(\frac{t}{\tau}\right)^2\right] \\ &\approx -2I_0 \frac{t}{\tau^2}\end{aligned} \tag{2.2.14}$$

where I_0 is the initial peak intensity of the pulse. We can then rewrite eq. (2.2.13) as

$$\delta\omega(t)_{\mathrm{SPM}} = 2kLn_2 I_0 \left(\frac{t}{\tau^2}\right). \tag{2.2.15}$$

As this is linear in time, it acts to shift the spectral intensity of the pulse away from the peaks. This leads to spectral broadening of the pulse and, using Equation 2.2.6, means that the pulse can potentially be further compressed.

While the broadening described by eq. (2.2.13) is symmetric there is another process that acts when in this regime known as self-steepening which introduces clear asymmetry in the temporal domain, as seen in fig. 2.2.1. While a derivation for the mathematical terms that introduce self-steepening will not be provided here, we can understand it by first by observing that, for materials with $n_2 > 0$ (as is the case for the materials considered in this thesis), the refractive index will increase with intensity.

We therefore see an intensity asymmetry appear in the pulse in the time domain as peak of the pulse is delayed, shifting it toward its trailing edge. Given that the effect of SPM is dependent on the temporal gradient of the field, and the trailing ($t > 0$) edge of the pulse has a sharper gradient. The spectral broadening through SPM therefore acts to spread the spectral intensity profile more to higher frequencies than to lower ones as self-steepening also effects the spectral-temporal structure of the pulse.

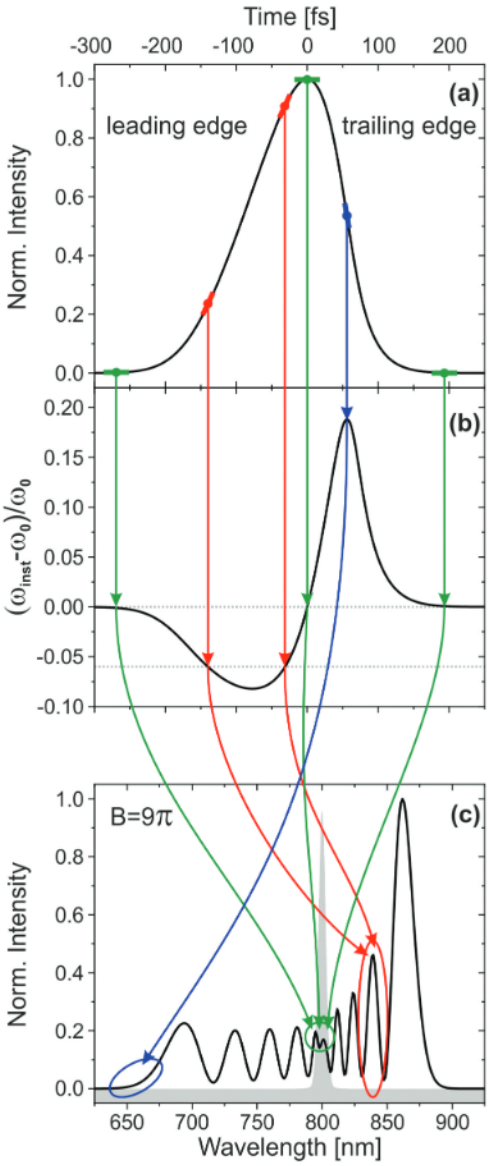


Figure 2.2.1: An illustration of self-phase modulation for an 800 nm laser pulse. Each colour arrow indicates a matching region in temporal gradient that will be shifted together. The green arrows show all the low-gradient points that see the lowest shifting. The blue and red show the most negative and positive gradients in intensity gradient, giving them the most negative and positive frequency shifts respectively. (a) shows the original temporal profile of the original pulse, (b) the corresponding shift in the intensity profile from SPM, and (c) the resultant spectral profile of the system. Figure adapted with permission from [57] under CC BY-NC 4.0.

The last feature of this spectrally broadened pulse that we will discuss are the oscillations in the spectral domain. These can be easily understood by considering that a given spectral element of the pulse will be delayed by different amounts, depending on time-dependent refractive index of the system, and so will constructively and destructively interfere, leading to oscillations in the spectrum.

The B-integral

It is worth introducing here the concept of the B-integral, which is the total nonlinear phase accumulated in an ultrashort pulse while passing through a medium, and is defined by

$$B = \frac{2\pi}{\lambda} \int n_2 I(z) dz, \tag{2.2.16}$$

where n_2 is the second-order refractive index, λ is the wavelength and I is the intensity of the beam. By providing a single value for the accumulated nonlinear phase, the B-integral, while simplistic, provides a useful tool for estimating the total phase accumulated in a system of transmissive optic.

B-integral values above 2 are generally considered problematic as they indicate the onset of self-focusing, which when attempting to couple into an HCF could lead to poor matching between the beam radius and capillary diameter, and hence coupling losses. It is wise when considering a small beam passing through transmissive optics to ensure that the B-integral is low and that the non-linear refractive index is relatively smooth, as otherwise one may also induce coupling losses into a HCF due to self-focusing, or introduce temporal aberrations such as spatial chirp or satellite pulses.

2.2.1 Frequency Mixing and Phase Matching

So far we have considered the interaction of individual frequency components with a medium. Let us now consider a field in a medium formed by multiple superimposed pulses, as is often used for the generation of new frequencies of light. A simple example of this might be the generation of perturbative harmonics as described earlier. If one were to divide a single field into two identical copies and then recombine them colinearly in a medium, the form of the superposition would be identical to the original field. This would take the form

$$E(t) = \frac{1}{2}([E_1(t) + E_1^*(t)] + [E_2(t) + E_2^*(t)]) = \frac{1}{2}((A_1(t)\exp(-i\omega_1 t) + A_2(t)\exp(-i\omega_2 t)) + (A_1^*(t)\exp(i\omega_1 t) + A_2^*(t)\exp(i\omega_2 t))) \tag{2.2.17}$$

where A_1,A_2 are the envelopes of the two overlapped pulses, and $E(t)$ is the resultant field. The factor $\frac{1}{2}$ is to normalise the magnitude of the field, and means that this expression simplifies to simply become the fundamental field in the case of two identical fields. Indeed, in the case that $E_1(t) = E_2(t)$, all the polarisation expansions discussed in the following section reduce to the expressions described earlier in this chapter.

We may more commonly need to overlap these identical fields in a non-collinear geometry, as this allows us to generate the harmonic we desire without having to then remove the fundamental frequencies from the resultant field. To do this we must ensure that the wave vectors of the pulse obey conservation of momentum — that is

$$\mathbf{k}_3 = \mathbf{k}_2 + \mathbf{k}_1, \tag{2.2.18}$$

where $\mathbf{k}_3$ is the k-vector of the newly generated pulse, and $\mathbf{k}_1$, $\mathbf{k}_2$ are those of the two driving pulses.

Second harmonic generation, as laid out in eq. (2.2.3), is a relatively simple process to demonstrate this set of dynamics, but contains some important underlying features. If we label the harmonic and fundamental frequencies as ω_h and ω_f respectively, we see that $\omega_h = 2\omega_f$ which in turn means that $k_h = 2k_f$, where k_h, k_f are the wavenumbers of the harmonic and fundamental frequencies respectively. When attempting the match the k vectors for eq. (2.2.18), this reduces to $n(\omega_h) = n(\omega_f)$.

While this condition cannot be met for most materials we can use birefringent materials, where the orientation of the medium determines the refractive index along each axis. The overall requirement described here for the newly generated frequencies of light and their corresponding k-vectors to satisfy conservation of momentum is known as phase-matching, and is a critical underlying feature of many nonlinear processes.

Effects to Second Order

To further explore the implications of eq. (2.2.17) we will now consider two fields of differing frequency, and examine the resultant polarisation. Expanding this to second order P_2 using eq. (2.1.2), we get [49]

$$P_2(t) = \varepsilon_0\chi^{(2)}[|A_1|^2+|A_2|^2+(A_1\exp(-i2\omega_1 t) + A_2\exp(-i2\omega_2 t) + 2A_1A_2^*\exp(-i(\omega_1-\omega_2)t) + 2A_1A_2\exp(-i(\omega_1+\omega_2)t) + \text{c.c.})]. \tag{2.2.19}$$

The first four terms here are familiar, and represent the optical rectification and second harmonic generation from each fundamental field. The latter two terms however represent difference frequency generation (DFG) and sum frequency generation (SFG) which, as the names suggest, are the generation of new frequencies of light at lower or higher frequencies.

Observation of these frequencies is dependent on the phase-matching described above, and the crystals used for them are selected according to the intended driving and output frequencies. To see how this phase matching affects the generated field, we may consider the variation of the polarisation for SFG over a distance in a medium. We must now reintroduce the spatial dependence of the propagating field, and this takes the form

$$\begin{aligned} P_{\mathrm{SFG}}(t) &= \frac{\varepsilon_0 \chi^{(2)}}{2} A_1 A_2 \exp(-i((\mathbf{k}_1 + \mathbf{k}_2)z + (\omega_1 + \omega_2)t)) + \text{c.c.} \\ &= A_3 \exp(-i(\mathbf{k}_3 z + \omega_3 t)) + \text{c.c.}, \end{aligned} \tag{2.2.20}$$

where we have now given the pulse generated through SFG a slowly varying envelope A_3 and wave vector and frequency $\mathbf{k}_3$ and ω_3. The magnitude of the emitted field will depend on $\partial_z A_3$, and so the oscillating term can be moved to join those of the driving fields, giving us

$$\begin{aligned} \frac{\partial A_3}{\partial z} &= \frac{\partial}{\partial z} \left[A_1 A_2 \exp(-i((\mathbf{k}_1 + \mathbf{k}_2)z + (\omega_1 + \omega_2)t)) \exp(i(\mathbf{k}_3 z + \omega_3 t)) + \text{c.c.} \right] \\ &= \frac{i\chi^{(2)}}{2} (A_1 A_2 \exp(i\Delta\mathbf{k} z) + \text{c.c.}) \end{aligned} \tag{2.2.21}$$

where $\Delta\mathbf{k} = \mathbf{k}_3 - (\mathbf{k}_1 + \mathbf{k}_2)$ is the wave vector mismatch, and $\Delta k = 0$ is the case of ideal phase-matching, i.e. $\mathbf{k}_3 = \mathbf{k}_1 + \mathbf{k}_2$.

The above processes come with a number of observations. The first is that, when the pulses are in a collinear geometry, the notation can return to describing wave numbers rather than wave vectors, i.e. $\Delta\mathbf{k}$ becomes Δk. Next, the above form of the wave vector mismatch is valid for SFG, but the specific form will vary depending on the nonlinear process in question- for DFG for example, it takes the form $\Delta k = k_3 - k_2 - k_1$. The inverse of the wave vector mismatch gives us a quantity known as the coherence

length, L_{coh}, which is used to describe the distance over which a nonlinear process can maintain phase-matching to generate these new frequencies.

2.3 Wave Guiding and Hollow Core Fibres

In this thesis we will consider hollow core capillaries, where a circular glass boundary encloses a volume that has been either evacuated or filled with gasses to pressure of a few bar. While other fibres, such as step-index fibres, guide propagating fields using total internal reflection, this is not possible in our scenario as the refractive index of the boundary will always exceed that of the interior volume.

For these capillaries, therefore, we use the principal of glancing angle reflection — that the reflection from a surface at very shallow angles will be large, provided the refractive index difference is large [58]. The propagation of a beam in such a cylindrical waveguide, with radial and azimuthal angular coordinates r and θ, can be described by a combination of n modes defined by [59]

$$\sum_n E_n(r,\theta,z,\omega) = a_n(\omega)e_n(r,\theta)\exp(i\beta_n(\omega)z), \tag{2.3.1}$$

where a_n is the spectral laser field amplitude in the mode, e_n is the transverse spatial mode of the pulse, and $\beta_n(\omega)$ is the propagation constant, whose dependence on ω defines the modal dispersion of the fibre system.

The spatial modes that satisfy propagation in a circular capillary are limited by the symmetry conditions of the system. For this thesis, we will focus on the propagation of a linearly polarised, spatially Gaussian laser pulse in a cylindrically symmetric capillary of radius a. The class of modes that can propagate through the HCF given these restrictions are hybrid modes meaning that, unlike free space propagation of the laser field, it is not possible for both the electric and magnetic fields to be per-

pendicular to the propagation direction. This means that there must be components of the wave vector both in the longitudinal and transverse directions. The transverse field profile is defined by

$$e_m(r, \theta) = J_0(k_{m\perp} a). \tag{2.3.2}$$

J_0 is the zeroth order Bessel function and $k_{m\perp}$ is the n^{th} order transverse wave vector. The Marcatili model for propagation analytically describes the propagation of a pulse in these modes in a rectangular boundary, which remains valid due to cylindrical symmetry, and sets the boundary condition that the field vanishes at the capillary walls [60]. The shapes of the lowest order, centro-symmetric modes of this type can be seen in Figure 2.3.1.

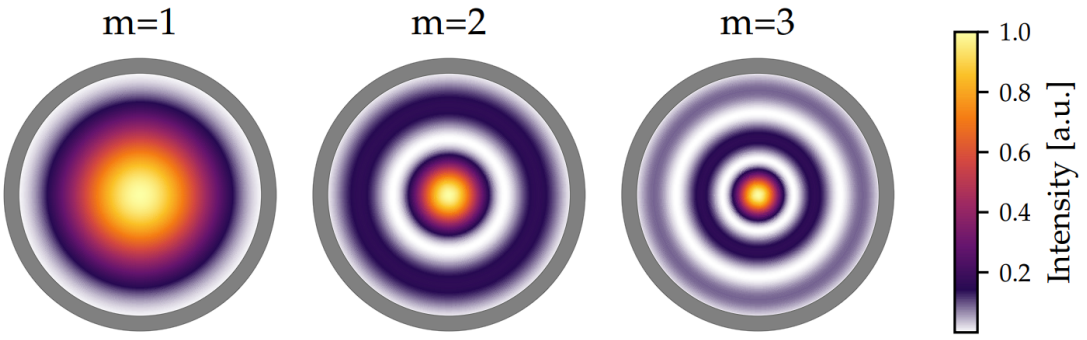


Figure 2.3.1: The first three Bessel modes, with the boundary of the HCF represented by the grey circle. Reproduced with permission from [61] under CC BY-NC 4.0.

These boundary conditions give us

$$e_m(r = a, \theta) = J_0(k_{m\perp} a) = 0 \implies k_{m\perp} = \frac{u_m}{a}, \tag{2.3.3}$$

where u_m is the m_{th} root of the truncated Bessel function $J_0(x)$ (truncated as the boundary of the field cannot be placed at infinity). For systems using these Bessel modes, the propagation constant, $\beta_n(\omega)$, is given by

$$\beta_m(\lambda) = k^2 - k_{m\perp}^2 = \frac{\omega}{c}\sqrt{\left(n(\omega)^2 - \left(\frac{cu_m}{\omega a}\right)^2\right)}. \tag{2.3.4}$$

The discussion thusfar of laser field propagation in an HCF hold true for a rigid, lossless and otherwise flawless fibre. There is, however, an intrinsic loss α_0 in the fibre, caused by the interaction of the field with the dielectric medium of the waveguide. We must also consider that, due to the nature of gravitational action on the fibre, no fibre will every be truly straight, and that bending losses α_r are inevitable [57, 60].

For a capillary with bend radius R, these can be quantified by

$$\alpha = \alpha_0 + \alpha_R. \tag{2.3.5}$$

α_0 is the attenuation in the fibre regardless of curvature, given by [60]

$$\alpha_0 = \left(\frac{cu_m}{a\omega}\right)^2 \frac{1}{a}\frac{\nu^2+1}{\nu^2-1} \propto \frac{\lambda^2}{a^3} \tag{2.3.6}$$

where ν is the ratio of the refractive index of the cladding and core of the fibre. The losses due to curvature of the fibre α_R are given by

$$\alpha_R = \frac{a^3}{\lambda^2 R^2} V(\nu), \tag{2.3.7}$$

where $V(\nu)$ is an attenuation function whose value depends on ν and the spatial mode in which the light is propagating. While the exact forms of these losses are less important, the proportionality relations are key to understanding the scaling of losses in fibres as we design systems in the lab to match the optimal core radius and gas fill pressure for a system.

The vertical sag due to gravity δy_g of a string of mass per unit length μ and length L tensioned by a force T_0 is described by the catenary equation, given by

$$\delta y_g = \frac{T_0}{\mu g} \cosh\left(\frac{L\mu g}{2T_0}\right) \approx \left(\frac{L}{2}\right)^2 \frac{\mu g}{T_0} \tag{2.3.8}$$

where we have used the small angle approximation. The force required to tension a fibre to be nearly flat (i.e. to reduce the cosh function to the small angle approximation) is on the order of Newtons, meaning that the radius of curvature depends linearly on μ. If we make the reasonable assumption that the $\mu \propto a^2$, we find a proportionality relation for the bending losses of

$$\alpha_R \propto \frac{a^5 L^2}{\lambda^2}, \tag{2.3.9}$$

which shows that the bend losses increase dramatically with the length and wall thickness, and therefore that, when scaling up the core of a fibre of the same length held at the same tension, the losses will increase.

A gas pressure limitation exists as we must take care not to exceed the critical ionisation limits in the fibre. This is the usual expression for critical power, given by

$$P_c = \frac{\alpha\lambda^2}{4\pi n_2 n_0}, \tag{2.3.10}$$

where α here is a constant that depends on the spatial beam profile. For a Gaussian beam, $\alpha \approx 1.896$ [62]. As the refractive index of the filling gas scales linearly with the medium pressure ρ, we see that $P_c \propto 1/\rho$.

In hollow core fibres, the effect of the plasma is further amplified by the fact that the beam is confined to propagate through the fibre using grazing-angle reflection, unlike filamentation where the beam can defocus around a plasma hot-spot. Instead the generated plasma becomes a medium for loss, and neither the gas pressure nor driving pulse energy can be increased arbitrarily without negative consequence. While some recent publications have claimed that these effects can be utilised to generate few-fs ultra-broadband visible sources [63], these methods are largely unexplored so far and will not be considered in the scope of this work.

In the following sections, we will not be focusing on the particular dynamics that emerge in different modes, and so will not use the m subscript to denote spatial modes in the fibre. Instead we will use β_m for the m^{th} frequency derivative of wavevector of the propagating pulse — that is

$$\beta_m = \frac{\partial^m \beta}{\partial \omega^m}. \tag{2.3.11}$$

2.3.1 Optical Capillary Dynamics and Solitons

A soliton is a general mathematical description of a self-reinforcing wavepacket which does not disperse as it propagates. While a spatio-temporal Gaussian pulse in free space can theoretically propagate without dispersion, this is not achievable in nature, as material responses to radiation inevitable have a frequency dependence. Solitons, on the other hand, use their self-reinforcing nature to propagate stably over long distances.

To describe the propagation of laser fields in a fibre accounting for this spectral dispersions, we start by using the nonlinear Schrödinger equation (NLSE), written as [64]

$$i\frac{\partial}{\partial z}A - \frac{\beta_2}{2}\frac{\partial^2}{\partial t^2}A + \gamma|A|^2A = 0 \tag{2.3.12}$$

where $A = A(z,t)$ is once again the complex amplitude of the electric field as it varies in space and time, β_2 is the group velocity dispersion (GVD) in the system, and γ is the coefficient of nonlinearity. It has been shown that a soliton solutions exist for such a system, and can be written as [64]

$$\begin{aligned} A(z,t) = \sqrt{P_0}\,\mathrm{sech}\left(\frac{(t-t_\mathrm{s}) - \Omega\beta_2\,(z-z_\mathrm{s})}{T_0}\right) \\ \times \exp\left[i\frac{\gamma P_0}{2}\,(z-z_\mathrm{s}) - i\Omega\left((t-t_\mathrm{s}) - \frac{1}{2}\Omega\beta_2\,(z-z_\mathrm{s})\right) + i\varphi_\mathrm{s}\right]. \end{aligned} \tag{2.3.13}$$

Here, P_0 is the peak power of the pulse, T_0 is the initial pulse duration, and t and z are the time and space propagation coordinates of the propagating pulse. t_s, z_s and ϕ_s are the central time coordinate, starting position and phase offset respectively. For simplicity, we may set $z_s = 0$. Ω is the shift of the central frequency of the pulse.

By requiring that the pulse we consider is a soliton which propagates unchanged through the medium, we place the restrictions that the phase and central time and frequency shifts must remain zero throughout propagation. These simplify eq. (2.3.13) to

$$A(z,t) = \sqrt{P_0}\,\mathrm{sech}\left(\frac{t}{T_0}\right)\exp\left(\frac{i\gamma P_0 z}{2}\right). \tag{2.3.14}$$

We may often wish to generalise our discussion of solitons to propagating waves in different media, and to do this we would need to normalise the instantaneous intensity of the propagating pulse. To achieve this, we create a normalised time co-ordinate $\tilde{t} = t/T_0$ using the pulse's initial duration, and define the pulse's field strength by the square root of its peak power P_0. We can then express the wave equation from eq. (2.3.12) using the normalised form of the field, which we will call $U(z,t)$:

$$i\frac{\partial}{\partial z}U - \frac{\beta_2}{2T_0^2}\frac{\partial^2}{\partial \tilde{t}^2}U + P_0\gamma|U|^2U = 0 \tag{2.3.15}$$

From this we extract two characteristic lengths: a linear dispersion length L_D whose magnitude depends on the GVD β_2, and the nonlinearity length L_N whose magnitude stems from the Kerr effect (expressed here as $|U|^2$). We define each of these as

$$L_\mathrm{D} = \frac{T_0^2}{|\beta_2|} \qquad \text{and} \qquad \mathrm{L_{NL}} = \frac{1}{\mathrm{P_0 fl}} \tag{2.3.16}$$

We can understand the physical meaningfulness of these lengths by considering the accumulated phases imparted by the linear and nonlinear mechanisms. We first consider for the linear dispersion, whose source is GVD as discussed in section 2.2. Noble gasses used in HCF compression are normally dispersive, where the refractive index

n decreases with wavelength. The guiding capillary on the other hand has anomalous dispersion, where the refractive index, n, increases with wavelength. This can be rephrased as normal and anomalous dispersion introducing positive and negative chirp respectively.

The nonlinear processes are self-phase modulation and self-steepening, as described in eq. (2.2.12). We discussed previously that the action of SPM and self-steepening introduce positive chirp that will need to be compensated by the system, as well as broadening the spectrum of the pulse. We recall that eq. (2.2.10) and eq. (2.2.14) gave us the following expressions for the the phase induced by GVD and SPM in the fibre:

$$\phi_{\mathrm{GVD}} = \frac{\beta_2 t^2 L}{\tau^4 + L^2\beta_2^2} \qquad , \qquad \phi_{\mathrm{SPM}} = L n_2 I_0 \left(1 - \left(\frac{t}{\tau}\right)^2\right) \tag{2.3.17}$$

for a pulse with a temporal Gaussian FWHM given by τ. By requiring that these phases act in opposition and therefore have the opposite sign, we can then consider what happens in the cases that these are unbalanced. In the case where the GVD is much less than SPM, the SPM will act to spread the frequencies of the pulse and this spectral broadening will lead to a broad-band but uncompressed pulse. In the case of insufficient SPM, the pulse will simply stretch in time without spectrally broadening.

When the two processes compete however we first observe that the self-phase modulation and self-steepening act to shorten the pulse temporally. As the pulse shortens however, while the GVD itself is constant, the phase it imparts is proportional to $1/\tau^4$ meaning that its effect increases greater than the rate of the SPM-induced phase's $1/\tau^2$. Provided these two mechanisms are of a comparable magnitude, this allows the formation of the self-compressed soliton.

With the above in mind, the linear dispersion length is therefore the distance over which the temporal shape of the pulse would change appreciably though linear mechanisms while the nonlinearity length N_{NL} is the distance over which self-phase modulation does the same.

Until now, we have only considered what is known as the fundamental soliton. It is easy to see, however, that the nonlinear dynamics we are considering may lead to a pulse which sees linear and nonlinear processes of a similar magnitude, but not of identical value while the pulse propagates. In this case, the time dependence of the refractive index will cause a cyclical temporal compression and lengthening of the pulse as it propagates. Using the dispersion lengths described above we define characteristic periodicity in the evolution of the pulse as the soliton order, N, where

$$N^2 = \frac{L_{\mathrm{D}}}{L_{\mathrm{NL}}} = \frac{\gamma P_0 T_0^2}{|\beta_2|} \tag{2.3.18}$$

A soliton of order N contains N spatial peaks over a distance z_0 that we shall label the soliton period, given by

$$z_0 = \frac{\pi L_D}{2}, \tag{2.3.19}$$

as seen in fig. 2.3.3. The soliton of order $N = 1$ is known as the fundamental soliton, $A^{(1)}$, where the field does not vary with propagation length, as seen in fig. 2.3.3.

By examining eq. (2.3.14) we see that the only way that this solution may propagate is in the case where the nonlinearity $\gamma = 0$, as any other value will create an oscillatory

behaviour in the field intensity that varies with distance travelled. This in turn gives us

$$A_{sol}^{(1)}(z,t) = N\sqrt{P_0}\,\mathrm{sech}\left(\frac{t}{T_0}\right). \tag{2.3.20}$$

A visualisation of the first three soliton orders and how they propagate over a distance z_0 can be seen in fig. 2.3.2. It is important to highlight that, while numerically we can simply set the soliton order, this does have implication for z_0, T_0 and P_0. To achieve a higher order soliton in the same fibre, one would either have to reduce the pulse duration or increase the pulse energy, and these would in turn effect on the soliton period and relative intensity.

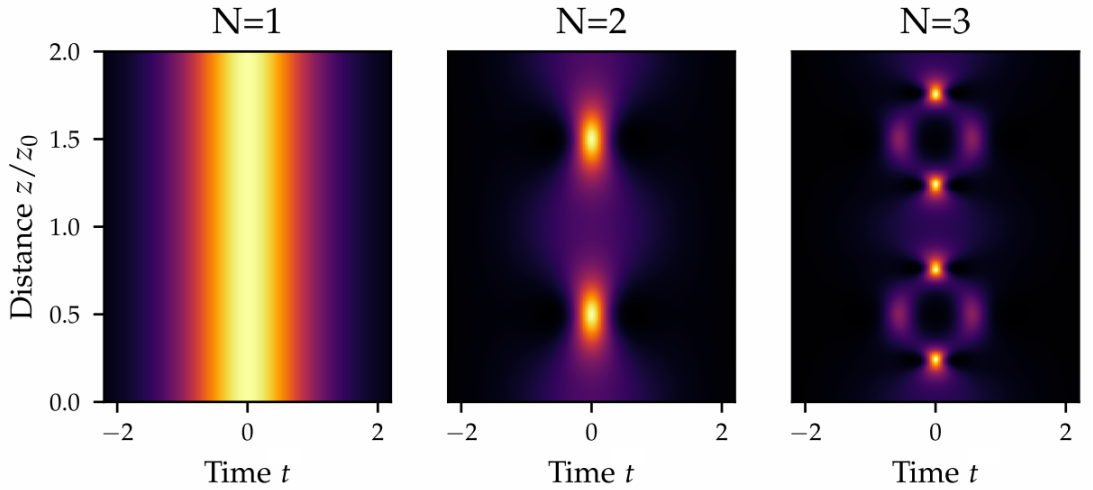


Figure 2.3.2: A plot of the first three soliton order propagating over the distance z_0, with normalised intensities and temporal coordinates (i.e. $P_0 = 1, T_0 = 1$). Adapted with permission from [61] under CC BY-NC 4.0.

The above model of solitons is idealised and ignores many real world factors when considering experimental implementation. Foremost is that N is necessarily defined as an integer, where in a real system not all of the energy in the propagating wave will match exactly the value for integer N. In this case the remaining energy remains as non-solitonic radiation, known as a dispersive wave, which propagates alongside

the soliton but is slowly dispersed over the propagation of the field. This can be seen in fig. 2.3.3.

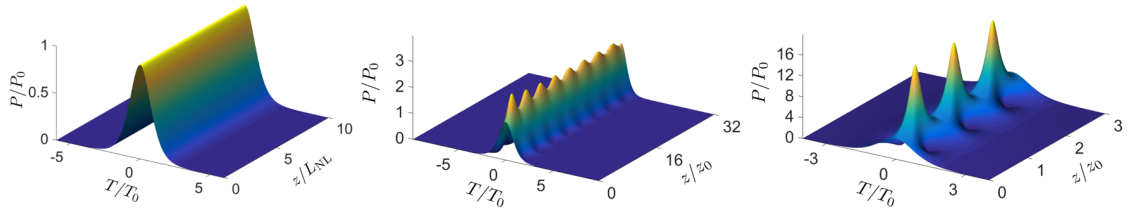


Figure 2.3.3: The propagation of a solitons of order 1 (left), 1.2 (middle) and 2 (right). While the fundamental ($N = 1$) soliton has no oscillation, the $N = 2$ soliton oscillates with 2 peak over the course of z_0. In the case of a non-integer soliton order, we see an element of the propagating field that does not oscillate in intensity with the solitons and remains as radiation that prevent clear distinction of the peaks that we see at $N = 2$. The propagation axes differ in each of these to illustrate fundamental differences in the behaviour of each case. Reproduced with permission from [64] under CC BY 4.0

Next, our pulses are not perfect sech functions, meaning that our pulse will never be able to take the shape of a "perfect" fundamental soliton. Instead, when considering realistic systems, we will be propagating a number of superimposed solitons of different order. The simplest case of this would be considering the launch of a superposition of two of the fundamental solitons, $A^{(1)}$,

$$2A^{(1)}_{sol}(z = 0, t) = 2\sqrt{P_0}\,\mathrm{sech}\left(\frac{t}{T_0}\right) = A^{(2)}_{sol}(z = 0, t), \tag{2.3.21}$$

showing that the superposition of a pair of fundamental solitons gives us a 2^{nd} order soliton. As the two superimposed fundamental solitons propagate, the beating between the two waves gives us the characteristic emergence of a sharp peak in the propagating field, as seen in fig. 2.3.3.

2.3.2 Dispersive Wave Emission

As discussed regarding section 2.2.1, the introduction of third order wave mixing into the system allows two key mechanisms to enter our discussion: four wave mixing (FWM) and cross-phase modulation (XPM). XPM is important as it allows us to

understand the phase modulation imparted on the pulse across the frequency spectrum, but more important for our understanding of resonant dispersive waves is the inclusion of FWM. To do this for eq. (2.3.13) we extend our wave equation to third order, giving us

$$i\frac{\partial}{\partial z}A - \frac{\beta_2}{2}\frac{\partial^2}{\partial t^2}A - i\frac{\beta_3}{6}\frac{\partial^3}{\partial t^3}A + \gamma|A|^2A = 0. \tag{2.3.22}$$

If one were to ignore the final, nonlinear interaction term for the field here, a plane wave solution to this wave equation would provide [65]

$$A_l = \exp(-i(\beta_l z - \Omega t)) \qquad \Longrightarrow \qquad \beta_l(\Omega) = \frac{\beta_2\Omega^2}{2} + \frac{\beta_3\Omega^3}{6} \tag{2.3.23}$$

where β_l is the linear wave's propagation constant, and $\Omega = \omega_s - \omega_l$ is the frequency shift between the soliton frequency ω_s and the linear wave ω_l. The next step is to find a phase matching condition that would allow energy to be transferred into this wave. To do this we must write the phase accumulated by the driving soliton ϕ_s and that of the dispersive wave ϕ over a distance x [59, 66, 67].

This wave would not be a part of the soliton and so, as mentioned above, would be included in the "dispersive wave" of the propagating field. The time elapsed for each part of the field to travel this distance will be different, and so we normalise the temporal coordinate to $t = x/v_g$, where v_g is the group velocity, and express the accumulated phases as

$$\begin{aligned} \phi_s &= \beta(\omega_s)x - \frac{x\omega_s}{v_g} + \frac{\gamma P_s x}{2} \\ \phi_l &= \beta(\omega_l)x - \frac{x\omega_l}{v_g}. \end{aligned} \tag{2.3.24}$$

Rather than P_0, the power of the pulse launched into the fibre, we consider P_s, the peak power achieved in the soliton (this is achieved during soliton fission, as will be discussed shortly). The exclusion of the final, non-linear term in the expression for ϕ_l stems from the fact that we are treating this wave as linear. We recall from

eq. (2.3.16) that the nonlinear dispersion length $L_{\mathrm{NL}} = (\gamma P_0)^{-1}$, and so we use $L_{\mathrm{NL}} \to \infty \implies (\gamma P_0)^{-1} \to 0$ to justify omitting this term.

By setting the phase mismatch to zero, and recalling that β_1 is simply the inverse of the group velocity of the field (i.e. $\beta_1 = \frac{\partial \beta}{\partial \omega} = (\frac{\partial \omega}{\partial \beta})^{-1} = (v_g)^{-1}$) we get the expression

$$\beta(\omega_l) = \beta(\omega_s) + \beta_1(\omega - \omega_s) + \frac{\gamma P_s}{2} \tag{2.3.25}$$

By equating the linear wave vector in eq. (2.3.23) and eq. (2.3.25), we get an expression for the propagating wave:

$$\beta_1(\omega - \omega_s) + \frac{\gamma P_s}{2} = \frac{\beta_2 \Omega^2}{2} + \frac{\beta_3 \Omega^3}{6} \tag{2.3.26}$$

Because the process includes third order nonlinearities we know a number of things regarding its behaviour. Firstly its cubic dependence means that it will dominate far from the central frequency of the driving soliton ω_0. Second there will be a region in which its value will be opposite to that of β_2.

From the roots of eq. (2.3.26) we now have an expression for the shifted frequency Ω at which the linear wave will be phase matched [65, 68, 69]

$$\Omega = \frac{\gamma P_0 \beta_3}{3\beta_2} - \frac{3\beta_2}{\beta_3} \tag{2.3.27}$$

Because β_2 is negative for the materials in this thesis, the phase matched frequencies will be higher than that of the driving soliton. A graph of the RDW wave frequencies calculated using these difference frequencies for a range of gas pressures, driven by pulses at 1350 nm is shown in fig. 2.3.4.

Now that we have an expression for the phase matched frequency, we focus on how the energy transfer occurs. Initially the propagating field in the HCF is limited to

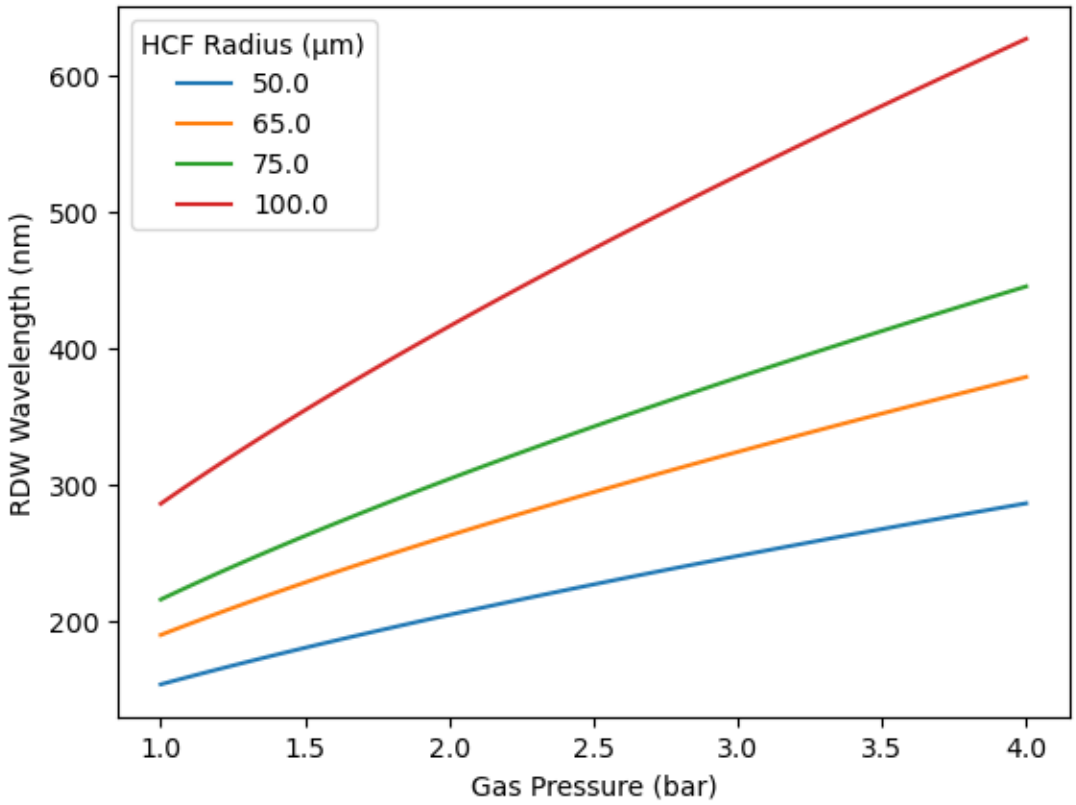


Figure 2.3.4: The phase-matched wavelength for dispersive waves in the UV region at a range of argon gas pressures and a range of capillary core radii. These were computed assuming a 20 fs FWHM spatio-temporally Gaussian 1350 nm central wavelength laser pulse, using eq. (2.3.27).

the frequencies of the launched pulse, as it forms a soliton at its central frequency. As it propagates, however, sidebands are formed in the pulse from SPM in the fundamental field which we can now explicitly describe as a combination of SPM and XPM combined with four-wave mixing spectrally spreading the pulse as it propagates [61, 69, 70]. The spectral intensities at these side frequencies are very low, but eventually they may spread to reach β_L. At this point, the energy in the phase-matched spectral region described by eq. (2.3.23) effectively seeds a directly phase-matched FWM process for energy transfer from the fundamental field to the dispersive wave frequency [68, 71].

It is important to reiterate here that the generation of these new frequencies is dependent on nonlinearities of at least third order. This means that, as the driving pulse temporally dissipates, the rate of energy transfer to this dispersive wave will decrease.

In fig. 2.3.3 we saw that the propagating soliton will periodically separate and reform as it propagates. However in cases where the peak field creates substantial nonlinearities the propagating soliton can be sufficiently temporally and spectrally dispersed that a soliton will not reform in this manner [67]. This process is known as soliton fission, and is given a characteristic length L_{fiss} of

$$L_{\text{fiss}} = \frac{L_{\text{D}}}{N} = \sqrt{L_{\text{D}} L_{\text{NL}}} = \sqrt{\frac{T_0^2}{\gamma \beta_2 P_0}} \tag{2.3.28}$$

where T_0 is the is the duration of the driving pulse and N is the soliton order. Recalling that the soliton order defines the number of peaks formed over the soliton period z_0, we see that the higher the soliton order of the driving field, the shorter the distance needed for the RDW to be formed.

Scaling laws for solitons have been proposed in recent years, to add intuitive understanding to the variation of nonlinear optical phenomena to changes in gas pressure, pulse energy, and capillary length and diameter. While these are discussed further in section 3.2, for a given soliton the fission length can be scaled as

$$L_{fiss} \propto \frac{\tau a^2}{\sqrt{I_0}}. \tag{2.3.29}$$

We now have a relatively complete picture of the concept of soliton self-compression and dispersive wave emission, as can be seen in fig. 2.3.5. A pulse is coupled into

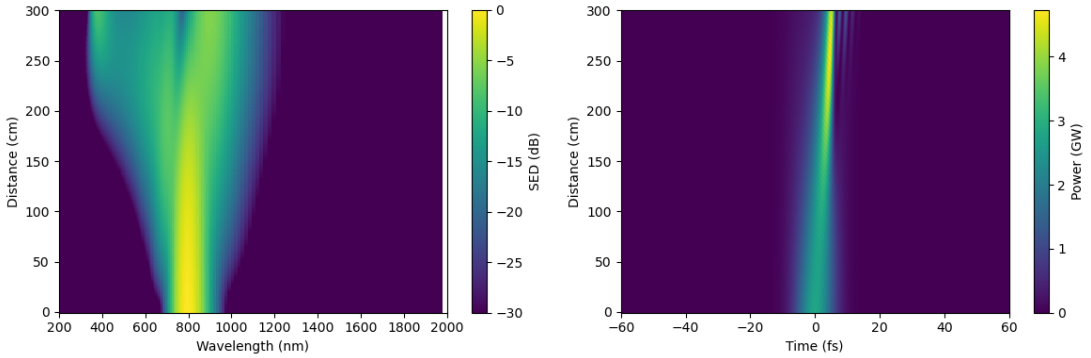


Figure 2.3.5: Simulated propagation of a 20 fs, 800 nm laser pulse in a 3 m, 65 μm ID HCF in the spectral (left) and temporal (right) domains. In the spectral domain (left image), we see a broadening of the pulse through SPM until the phase-matched RDW wavelength is reached at 350 nm. Substantial energy in the pulse then moves down to the dispersive wave. We see that, in the temporal domain (right image), this corresponds to the optimal compression point of the pulse, and shortly after the pulse is beginning to break up, with clear post-pulses emerging by the end of the pulse's propagation. This propagation was performed using the LUNA package presented in [72].

a capillary, propagates for some distance, and the soliton begins to compress. As this occurs, the spectral bandwidth increases until the sideband frequencies reach the phase-matched frequency for RDW emission. Energy is then transferred to the RDW frequency from the driving pulse through FWM. This occurs when the pulse is both optimally temporally compressed and spectrally broadest, meaning that the effects of XPM and SPM are strongest here. These lead to soliton fission, which then terminates the compression of the pulse and energy transfer to the RDW.

Effects to Third Order

The expansion of two fields interacting to third order, in the same vein as eq. (2.2.19) would yield an expression of 12 terms, expressed as the third order polarisation P_3 as

$$P_3 = \frac{\varepsilon_0 \chi^{(3)}}{32}[A_1^3 \exp(i3\omega_1 t) + A_2^3 \exp(i3\omega_2 t) + 3A_1|A_1|^2 \exp(i\omega_1 t) + 3A_2|A_2|^2 \exp(i\omega_2 t) + \frac{3}{2}P_{\text{FWM}} + 6A_2|A_1|^2 \exp(i\omega_2 t) + 6A_1|A_2|^2 \exp(i\omega_1 t) + \text{c.c.}]. \tag{2.3.30}$$

P_{FWM} here represents a set of 4 terms that represent the process of four-wave mixing (FWM), so called because they consist of waves at three incoming frequencies and one outgoing frequency. Returning the oscillating parts of the fields to our notation, these interactions take the form

$$P_{\text{FWM}} = A_n^2 A_m \exp(-i(2\omega_n - \omega_m)t), \tag{2.3.31}$$

for $n, m \in [1, 2], n \neq m$ and generate fields with frequencies through shifts of the form $2\omega_n \pm \omega_m$. The first line of interactions therefore describes the familiar terms for third harmonic FWM, and the second describes the Kerr effect and FWM.

The third line in eq. (2.3.30) describes a phenomena known as *cross-phase modulation* (XPM) and is represented by terms that take the form

$$P_{\text{XPWM}} = \frac{6}{4} A_n |A_m|^2 \exp(-i\omega_n t). \tag{2.3.32}$$

These terms are of the same form as SPM seen in eq. (2.2.4), but have a coefficient twice those of SPM in eq. (2.3.30). This means that the nonlinear refractive index changes due to XPM is twice that of SPM.

These processes are critical to the dynamics that will be discussed in HCFs. As mentioned earlier, laser pulses can be considered a superposition of a continuum of fields at differing frequencies. This means that as a pulse spectrally broadens and the spectral intensity decreases, we may explicitly justify the most intense parts of the pulse imparting phase shifts onto the spectral wings of the pulse through XPM. Four wave mixing also explicitly describes a mechanism by which spectral broadening occurs, and is key for resonant dispersive wave emission.

3 Interaction of High Intensity Laser Fields with Matter

As the peak intensity of an electric field in a medium begins to reach the scale of gigawatts and terawatts per square centimetre (or, in terms of field strength, around 1V/Å) we begin to see substantial effects from the resultant ionisation on the laser field itself. To discuss this, we must introduce the concept of ionisation under intense fields, namely *multiphoton ionisation* (MPI) and tunnelling ionisation.

The distinction between MPI and tunnelling ionisation lies in the strength of the field propagating through the medium. In MPI, the ionisation is initiated by the absorption of multiple photons, sufficient to exceed the ionisation potential of the parent atom. This does not require the electric field to be particularly "strong", and can be considered on the scale of multiple cycles of the laser field. To separate these two regimes we use the Keldysh parameter, γ_K, given by

$$\gamma_K = \omega_0 \frac{\sqrt{2I_p}}{E} = \sqrt{\frac{I_p}{2U_p}}. \tag{3.0.1}$$

Here E is the electric field strength, and U_p is the ponderomotive energy, describing the cycle-averaged energy of a free electron in an oscillating electromagnetic field. This quantity is proportional to the peak intensity, I, of the driving pulse, and given by

$$U_p = \frac{e^2 I}{2c\varepsilon_0 m_e \omega_0^2} \propto \lambda_0^2 I. \tag{3.0.2}$$

e and m_e are the electron charge and rest mass respectively, c is the speed of light in vacuum, ε_0 is the permittivity of free space and ω_0 is the central frequency of the driving laser. Given these, we can therefore see the regimes separated by the Keldysh parameter. For $\gamma_K > 1$ however, the instantaneous intensity is lower, and hence multi-photon ionisation dominates as the ionisation occurs on the multi-cycle timescale. For $\gamma_K < 1$, the instantaneous intensity of the field is very high, meaning that tunnelling ionisation dominates, and so we focus on ionisation at the few-cycle

timescale. Tunnelling ionisation occurs in the presence of a strong field and results from the distortion of the local potential well of a parent atom or molecule as seen in Figure 3.0.1. As these tunnelling ionisation rates describe sub-cycle dynamics, they are critical for calculating both high harmonic generation and the interaction of a propagating field with the plasma generated by leading sub-cycles of that field.

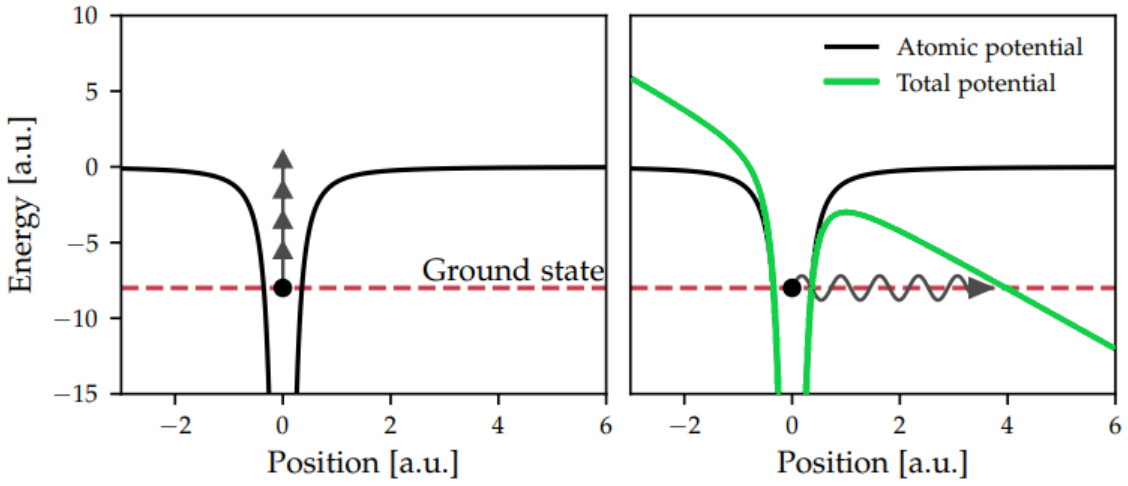


Figure 3.0.1: An illustration of the difference between MPI (left) and tunnelling (right) ionisation. In MPI, a number of photons exceeding the ionisation potential of the parent must be absorbed to allow ionisation. In tunnelling ionisation, a field strong enough to distort the Coulomb potential must be present, at which point the electron may tunnel into the continuum. Figure adapted with permission from [61] under CC BY-NC 4.0.

To calculate ionisation rates in this thesis we will use either the *Perelomov-Popov-Terentev* (PPT) or *Ammosov-Delone-Krainov* (ADK) ionisation rate [73–75]. The PPT ionisation rate, W_{PPT}, is given by

$$W_{\mathrm{PPT}} = C_{n^*} f_m I_p \left(\frac{2E_p}{E(t)}\right)^{2n^*-|m|-1} \exp\left(\frac{-2g(\gamma_k)E_p}{3E(t)}\right) A(\omega,\gamma_K)(1+\gamma_K^2)^{|m/2|+3/4}, \tag{3.0.3}$$

where C_{n^*} is a function of the effective principal quantum number, $n^* = Z/\sqrt{2E_i}$, and effective angular quantum number l^*. f_m is a function of the actual angular quantum number l and magnetic quantum number m. $E_p = (2I_p)^{\frac{3}{2}}$ where I_p is the ionisation potential of the medium and $E(t)$ is the and time-dependent electric field. $g(\gamma_K)$ is known as the Keldysh function and determines the frequency dependence of

the ionisation probability, and $A(\omega, \gamma_K)$ is a coefficient that represents the changes in ionisation mechanisms in the multiphoton ionisation regime [76].

The ADK ionisation rate W_{ADK} is the limit of the PPT rate as the Keldysh parameter shown in Equation 3.0.1 tends to zero. When we combine it with the assumption that $\omega_0 << I_p$ this is also known as the quasi-static limit as it represents the case where a strong field induces ionisation but the oscillations of the laser field are much slower than the ionisation dynamics, meaning that the ionisation rate can be calculated using a static ionisation rate. This second assumption is easily justified, as I_p for noble gasses and the liquids considered in this thesis are $> 10\,\text{eV}$, and the photon energy of an 800 nm laser field is 1.5 eV. In this limit, $A(\omega, \gamma_K), g(\gamma_K) \to 1$, and so W_{ADK} is given by

$$W_{\text{ADK}} = C_{n^*} f_m I_p \left(\frac{2E_p}{E(t)} \right)^{2n^* - |m| - 1} \exp\left(\frac{-2E_p}{3E(t)} \right). \tag{3.0.4}$$

This approximation is valid as we reach high peak field intensities. While the PPT method is a more computationally expensive calculation, Figure 3.0.2 shows that at lower peak intensities one must use the PPT method.

For the effects of strong field ionisation we must also consider the ionisation of a propagation medium and the effects of plasma formation on the propagating laser field. When an electron is ionised there is a change in the local polarisation response of the medium proportional to the displacement of the electron [77, 78]. Using our time-dependent expression for the electric field from Equation 2.1.7, this displacement, x_e, can be defined by

$$x_e(t) = -\frac{e}{m_e \omega^2} E(t). \tag{3.0.5}$$

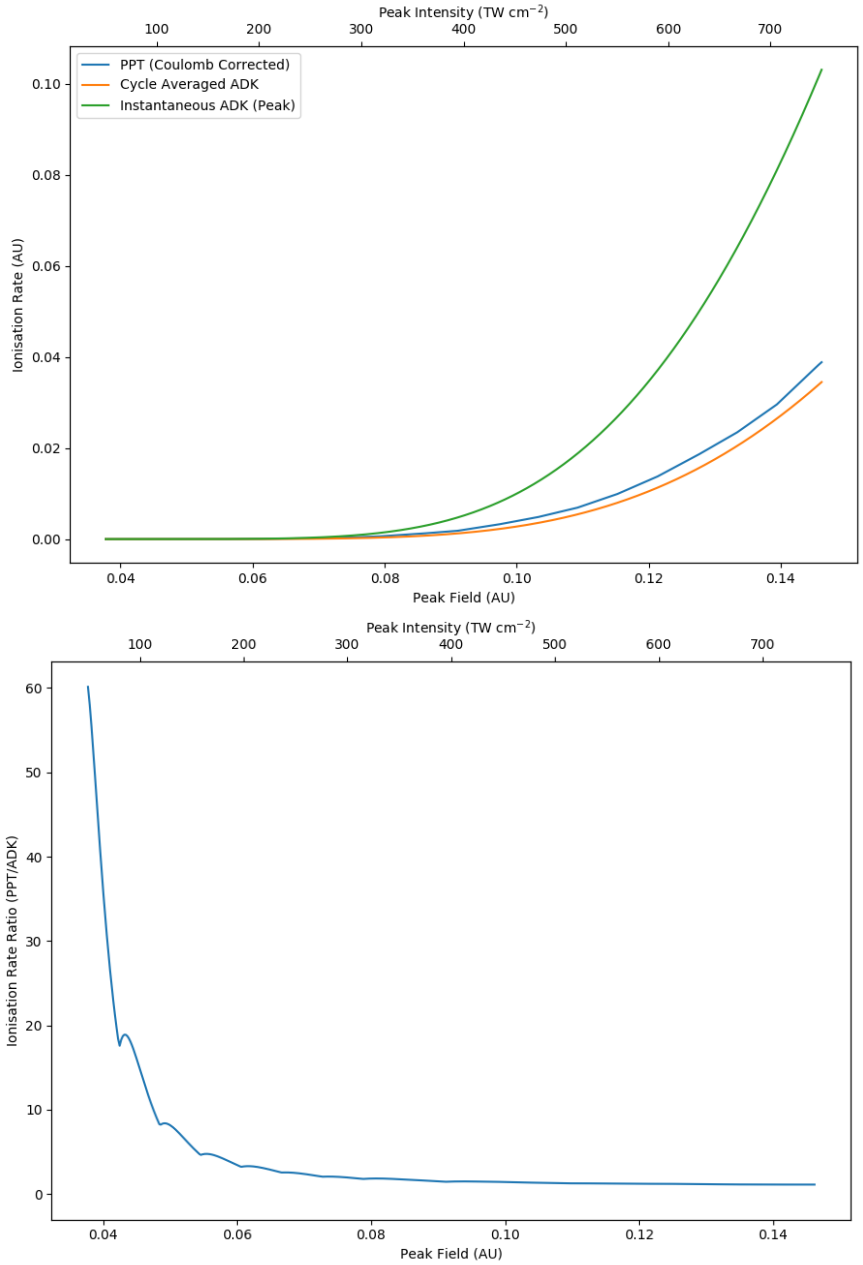


Figure 3.0.2: Upper: The ionisation rate in argon for an 800 nm driving field as a function of peak field intensity calculated using the PPT and ADK models. As we are performing simulations where both the time averaged ionisation and instantaneous ionisation rates in the system are considered, a plot is also included here to show the discrepancy between the average and peak ionisation values using the ADK model. Lower: The ration between the PPT and ADK models.

The polarisation response induced by the free electrons in the plasma, P_e, is then defined by

$$P_e(t) = -\varepsilon \frac{\omega_p^2}{\omega^2} E(t), \tag{3.0.6}$$

where ω_p is the plasma frequency, given by

$$\omega_p = \sqrt{\frac{n_e e^2}{m_e \varepsilon_0}}. \tag{3.0.7}$$

This polarisation response is proportional to the field, so we see that it acts similarly to the nonlinear refractive index listed in Equation 2.2.4, and adds Equation 2.2.5 to give:

$$n_{\text{eff}} = n_0 + n_2 I - \sqrt{\frac{\omega_p^2}{\omega^2}} \tag{3.0.8}$$

This effect is known as plasma defocusing, because the sign of the incurred refractive index change is negative. Furthermore, because the refractive index scales only with the plasma frequency relative to the driving laser, the effect of the plasma is always to blue-shift the pulse, or to add positive chirp. This means that, while both plasma defocusing and χ^3 are intensity dependent, they act in opposite directions.

3.1 High Harmonic Generation

3.1.1 The 3-Step Model

When an intense laser field is incident on an atom, it can cause an electron to tunnel into the continuum and then be accelerated by that laser field. When the electron recombines with its parent atom a burst of light, with a photon energy equal to the sum of the electron's kinetic energy and the ionisation potential of the parent. This process is known as *high harmonic generation* (HHG), and has been used to generate

extreme-UV (XUV, 10 – 150 eV) and soft X-ray (SXR, 150 eV – 3 keV) pulses with attosecond durations. To provide approximate numbers, a peak intensity of around 50 TWcm^{-2} from a short wave IR (SWIR, 1.4 - 3 µm) laser in argon is sufficient to distort a potential well sufficiently to allow an electron to tunnel out and begin generating harmonics — though the value for peak intensities required will differ from medium to medium. As will be discussed shortly, we are not limited to the use of SWIR lasers or atomic gasses for HHG, but these form the best picture to introduce the basic concepts of the method [13–15, 79].

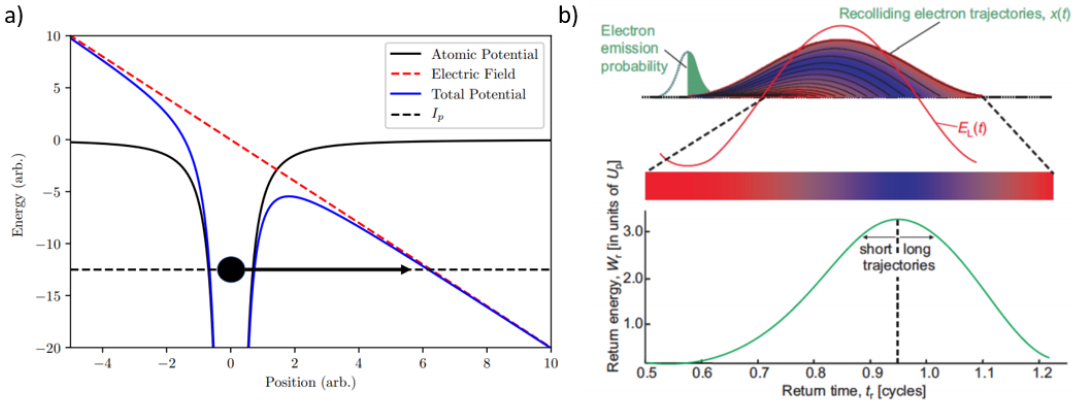


Figure 3.1.1: The 3-step model. a) An intense laser field modifies the potential well for an atom, allowing the electron to tunnel into the vacuum. b) The electron is driven away from, and then back towards, the parent atom, and radiatively recombines. Longer and shorter trajectories are defined by recombination after the peak recombination energy. Figures reproduced with permission from [80] under under CC BY-NC 4.0. and [81].

The fundamentals of HHG are encapsulated by the so called 3-step model, as depicted in Figure 3.1.1, and can be expressed as follows:

1. Tunnel Ionisation

   For the electron to be ionised to facilitate HHG, it must undergo tunnel ionisation — that is, the laser field must distort the local potential well enough that the electron tunnels into the continuum, as seen in Figure 3.1.1(a).

Formally, we set electron position $x(t = t_b) = 0$, where t_b is the known as the birth time. This will later also be justified by the strong field approximation (SFA), which states that once the electron has tunnelled beyond the parent, the strength of the laser field is very much larger than the potential well of the parent. We also set the velocity of the electron $x'(t = 0) = 0$ as it has not yet gained kinetic energy by laser acceleration, having only just tunnelled through the Coulomb barrier of the parent.

2. Propagation of the Electron in the Continuum

Once the electron has tunnelled out, it propagates under the force of the laser field. Given a driving laser frequency ω_0, and using our previous assumptions to set $x = 0$ at t_0, and we now use the following classical equations of motion:

$$\ddot{x} = -E_0 cos(\omega_0 t), \tag{3.1.1}$$

$$\dot{x} = -\frac{E_0}{\omega_0}(sin(\omega_0 t) - sin(\omega_0 t_0), \tag{3.1.2}$$

$$x = \frac{E_0}{\omega_0^2}[(cos(\omega_0 t) - cos(\omega_0 t_0)] - \frac{E_0}{\omega_0} sin(\omega_0 t_0)[t - t_0] \tag{3.1.3}$$

Under these equations of motion, we see the electron will be accelerated until the field changes polarity, then be decelerated and accelerated back towards its parent. This is illustrated in Figure 3.1.2.

3. Radiative Recombination

When the electron returns back to the parent, it can radiatively recombine with the parent atom, releasing a photon which is the n^{th} harmonic of the driving laser field, and equal to the sum of the kinetic energy of the electron and ionisation potential, I_p, of the parent atom. This is illustrated in Figure 3.1.1(b).

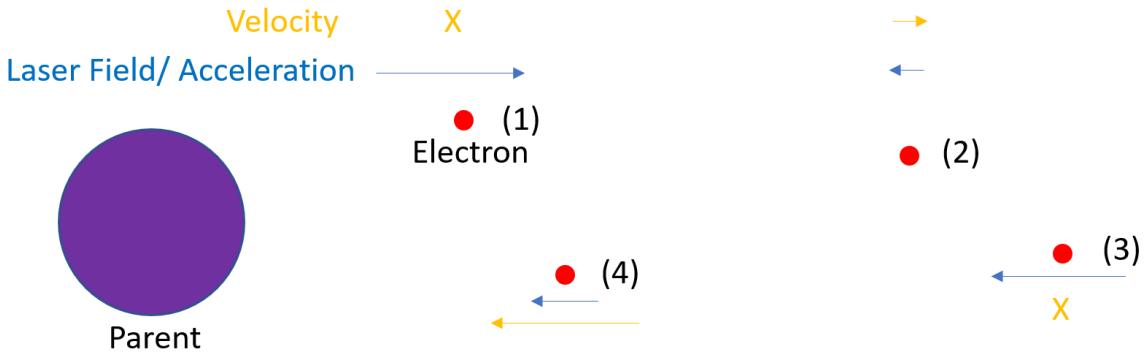


Figure 3.1.2: An illustration of the motion of an electron in the laser field. The laser field vector is proportional to the acceleration of the electron, and is indicated but the blue (inner) arrows. The velocity is indicated by the yellow (outer) arrows. (1) The electron has been liberated and is accelerated away from the parent atom until the field direction reverses (2) and the electron is accelerated back towards the parent (3). The electron approaches its maximum kinetic energy shortly before it recombines (4) which corresponds to the photon energy of the released harmonic.

To find the energy of the emitted photon, we define the "birth" time of an electron as the point in the laser half-cycle that the electron is ionised, and the "return" time as the point at which it recombines with the parent atom. From Equation 3.1.2 we see differing points in the laser field will emit different energy harmonics, as the recombination energy is dependent on the field strength at time of ionisation, and each photon will have an energy of $\frac{(m_e\dot{x})^2}{2} + I_p$, as seen in Figure 3.1.1. Using Equation 3.0.4 and Equation 3.1.2 we can start to construct a simple model for emitted harmonic spectra.

The highest energy photon emitted, also known as the cutoff energy E_c, is given by the sum of the highest kinetic energy the electron can reach in this motion, proportional to the ponderomotive energy defined in eq. (3.0.2), and the ionisation potential of the atom. This gives us the expression [13, 82]

$$E_c = 3.17U_p + I_p. \tag{3.1.4}$$

As U_p is proportional to the frequency of the laser field, the wavelength scaling of the cutoff harmonic with wavelength mentioned earlier is made explicit. The value of 3.17 that defines the cutoff energy stems from the maximum kinetic energy, arising from the velocity distribution of the electron ionised from the parent.

The resultant emission is co-linear and co-propagating with the driving laser field, which can be understood by considering a simple phase matching for the generated field. Because there is no second field involved in HHG, and momentum must be conserved, the direction of the k-vector of the generated photons must match that of the driving laser field.

The emitted burst is a coherent pulse with huge bandwidth as different points in the laser cycle will produce different harmonics, as shown in Figure 3.1.1, and for harmonics driven by a single half-cycle of a laser field one would observe a continuum of frequencies. We seldom have a harmonics driven by a single half-cycle however, and the typical shape of gas phase HHG spectra driven by a multi-cycle laser pulse can be seen in Figure 3.1.3.

The harmonic spikes here correspond only to odd-numbered harmonics. This stems from the fact that each half cycle will generate harmonics, and the polarity will alternate with each half cycle. As a result harmonics of even number will destructively interfere, and only odd harmonics will be observed. This is in contrast to a similar

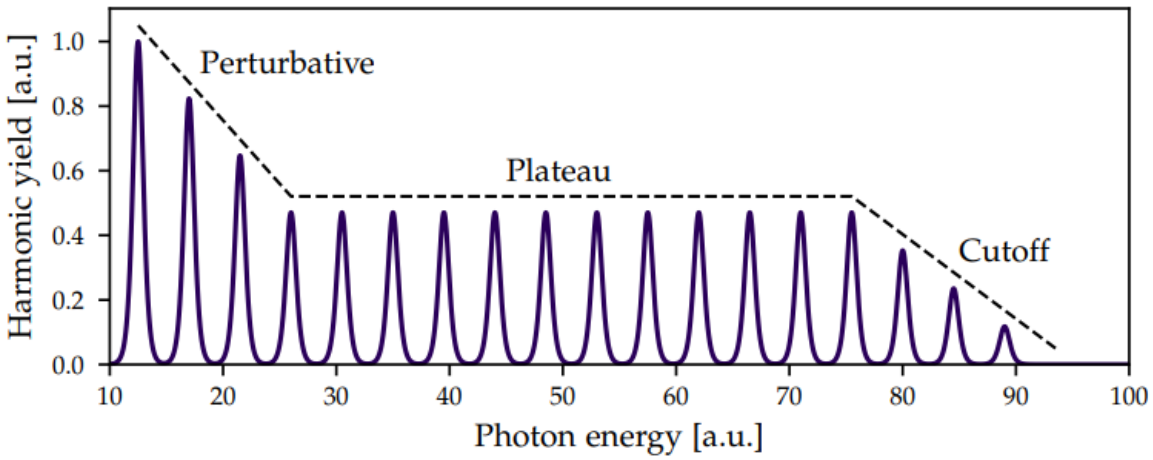


Figure 3.1.3: An example HHG specrum. The perturbative section here matches the harmonics described in Equation 2.2.3, with a generation efficiency decreasing rapidly with harmonic order. Once the non-perturbative regime is reached, we see the high harmonic plateau, where the yield is approximately flat until we reach the cutoff, and the yield drops rapidly. Reproduced with permission from [61] under CC BY-NC 4.0.

phenomena when observing perturbative harmonics, where even harmonics are forbidden for only centrosymmetric materials due to parity constraints, as discussed in section 2.2.

This generation method, with the electron driven away from, and returning to, the parent atom, requires a few important observations. First is that the generation of a q^{th} harmonic photon depends strongly on the local instantaneous intensity. This means that the generation of a given harmonic is never guaranteed simply by having a beam whose theoretical peak intensity exceeds the desired photon energy — one must consider factors such as beam quality, spectral and temporal phases, and plasma defocusing to make sure the peak intensity allows the cutoff to exceed the desired photon energy. Because harmonics in the cutoff region rapidly decrease in flux, as seen in fig. 3.1.3, we typically seek to extend the photon energies generated as far into the cutoff region and towards the plateau as possible.

Second is that longer driving wavelengths will give higher peak return energies. This can be understood through the particle-photon interpretation, as longer wavelengths mean longer cycle times for the laser. The electron therefore spends more time being accelerated by the field before recombination. We see this explicitly from eq. (3.0.2), where we saw that the pondermotive energy $U_p \propto \lambda_0^2 I$.

The third follows from the second, and requires a wave-like picture. As the electron is driven away from the parent atom, its wavepacket will begin to spread. The longer the electron remains in the continuum the greater the spread, and therefore the greater the probability that the electron will not return to the parent. The most generous studies place this efficiency loss, δI, at $\delta I \propto \lambda^{-3}$.

This stems from the wavepacket's spread with time, which scales as a function of $\tau^{3/2} \propto \lambda^{3/2}$, which leads to an equivalent decrease in the emitted field on recombination. We then square this to get the harmonic intensity, which is our measurable observable [82]. This estimate, however, concerns itself only with the simplest picture of the single-atom response to the laser field, and not the wider system of a gas target used for HHG. More realistic estimates range from a scaling on the order of λ^{-5} – λ^{-9}.

The more optimistic of these expresses the scaling of harmonic flux at the cutoff I_{harm} as [83]

$$I_{\text{harm}} \propto \frac{\omega^5}{\Gamma}, \tag{3.1.5}$$

where Γ is the ionisation rate of the laser and ω is its frequency. The expression originates from an inclusion of the effects of laser frequency on the ionisation rate of the generating media, and the fact that shorter wavelength driving fields allow the generation of higher frequency harmonics at lower orders (thereby decreasing the peak intensity requirement). It also includes the fact that there is a coherence length over which generated harmonics are phase matched, after which the plasma generated through ionisation will impart substantial phase. It is interesting to note that the

terms discussed here for efficiency focus less on the electronic wavepacket as above, and more on the kind of phase matching considerations discussed in section 2.2.1. Numerical studies focusing on quantum path interference [84] and experimental works [85] have also found results on the scale of λ^{-5} – $\lambda^{-6.5}$

The more pessimistic of the scaling expressions estimates the scaling at $I_{\text{harm}} \propto \lambda^{-x}$, for $x \in [7, 9]$ tending towards 9 as the photon energy of the target harmonics increases[86]. To understand the source of this scaling however we must find have a full quantum mechanical treatment of HHG, which will be discussed shortly. The key factors leading to the lower efficiency however stem from a more rigorous treatment of the time spent in the continuum for electrons as the wavelength and relative intensity scale.

It is important that we acknowledge now that, while in the classical picture we consider the trajectory of the whole electron as a particle, in the quantum mechanical picture we are rather considering the propagation of a fraction of the wavefunction of the electron. When the propagating portion of the electron wavefunction returns, its recombination with the ground state causes high frequency oscillations in the electronic wavefunction, leading to the emission of the harmonics. Between this and the fact that not every atom in a target region will be an emitter, among other inefficiencies, the HHG process has a relatively low efficiency — typically around 10^{-7} [87].

3.1.2 The Strong Field Approximation

When seeking to calculate the quantum mechanical behaviour of the electron wavepacket through HHG and calculating the resultant harmonics, we begin by defining the time

dependent electronic wavefunction, $\psi(t)$, as a coherent superposition of the ground state $|0\rangle$ and continuum states $|\mathbf{p}\rangle$ [82]:

$$|\psi(t)\rangle = \exp(iI_p t)(a(t)\,|0\rangle + \int d^3\mathbf{p}\, b(\mathbf{p},t)\,|\mathbf{p}\rangle\,, \tag{3.1.6}$$

where $a(t)$ is the amplitude of the ground state, and I_p is the usual expressions for the ionisation potential. We note that, for this equation and the rest of this section, we are using atomic units (i.e. $\hbar = e = m_e = 1$). $b(t)$ is the transition amplitude to the continuum states, which necessarily depends on both the momentum of the electron and the laser field. This expression carries a number of key observations and assumptions.

First, we note that only the ground state of the parent system is considered, and that the only other dynamics to be considered are the continuum states. The second links to the first, and is that the continuum states can also be described without the potential well of the parent, that is

$$\hat{H}_0\,|\mathbf{p}\rangle = \left(\frac{1}{2}\mathbf{p}^2 + \mathbf{V}\right)|\mathbf{p}\rangle = \frac{1}{2}\mathbf{p}^2\,|\mathbf{p}\rangle\,, \tag{3.1.7}$$

where $\hat{H}_0$ is the Hamiltonian of the system in the absence of the laser field. This is a key part of the strong field approximation (SFA), and dictates that the behaviour of the liberated electron is dominated by the laser field, and so we can ignore the potential of the parent. Third is that the amplitude of $a(t)$ must be known. While we will not discuss ways of calculating this function here, there are a number of methods including numerically costly solutions to the time-dependent Schrödinger equation (TDSE) or "cheaper" methods using truncated Wigner approximations [88]. For the sake of qualitative discussions however, we can consider two simple cases. In the

case the pulse is very short, there is very little depletion of the ground state, and $a(t) \approx 1$. In the case that the pulse is slightly longer (i.e. few-cycle) and still very intense, one can use the ADK rate outlined in eq. (3.0.4) to calculate the ground state depletion.

The dipole moment of an electron's propagation through the continuum and recombination with its parent can be expressed as the time dependent dipole moment

$$\mathbf{D}(\mathbf{t}) = \langle \psi(t) | \, \hat{\mathbf{r}} \, | \psi(t) \rangle \tag{3.1.8}$$

where $\mathbf{D}(\mathbf{t})$ is the time-dependent electric field dipole, $\hat{\mathbf{r}}$ is the spatial coordinate, which can be used to define a bound-free transition dipole matrix element$\mathbf{d} = \langle \mathbf{p} | \, \hat{\mathbf{r}} \, | 0 \rangle$ is. The Fourier transform of $\mathbf{D}(\mathbf{t})$ yields the spectrum from the resultant HHG.

We now seek a way to calculate the dipole moment, and for this the TDSE is often used [89]. The TDSE is computationally expensive however, and we must apply restrictions in order to perform useful calculations with it. One of these is the *single active electron limit* (SAE), which states that we only need account for a single electron with the lowest ionisation potential when considering tunnel ionisation.

We also limit the effect of the electron propagation to the time domain — that is we assume that there will be no interactions in space as the electron propagates, either from the parent or any other atom or electron. This justifies our earlier statement regarding the initial position and velocity of the electron as it propagates. This also means that we have assumed that strength of the electric field will be spatially uniform as the electron propagates, and so the variation of the laser field will only be in time. This is known as the dipole approximation, and is justified by the fact that distance travelled by an electron while in the continuum during HHG is substantially less than the laser wavelength (typically on the order of an angstrom)[89].

Given these approximations, the Schrödinger equation for our system now reads

$$-i\frac{\partial}{\partial t}\left|\psi(t)\right\rangle = \left(\frac{\mathbf{p}^2}{2} + \mathbf{d}\cdot\mathbf{E}(t)\right)\left|\psi(t)\right\rangle. \tag{3.1.9}$$

To find solutions to this, we calculate its overlap integrals with the ground and a secondary continuum state $|\mathbf{p}_2\rangle$ and find the coupled differential equations

$$\dot{a}(t) = i\int d^3\mathbf{p}\,\mathbf{E}(t)\cdot\mathbf{d}^*\,b(\mathbf{p},t), \tag{3.1.10}$$

$$\dot{b}(\mathbf{p},t) = -i\left(\frac{\mathbf{p}^2}{2} + I_p\right)b(\mathbf{p},t) + i\mathbf{E}(t)\cdot\mathbf{d}\,a(t) - (\langle\mathbf{p_2}|\,\mathbf{E}(t)\cdot\hat{\mathbf{r}}\,|\mathbf{p}\rangle\,b(\mathbf{p},t)). \tag{3.1.11}$$

We make one further assumption here to limit the trajectories to only ones with a probability for the electron to recombine with the parent. This means that there will be no scattering for the propagating electron between continuum states, or more formally that

$$\langle\mathbf{p_2}|\,\mathbf{r}\,|\mathbf{p}\rangle = -i\delta(\mathbf{p_2}-\mathbf{p})\nabla_p + G(\mathbf{p},\mathbf{p_2}) \approx -i\delta(\mathbf{p_2}-\mathbf{p})\nabla_p, \tag{3.1.12}$$

where $G(\mathbf{p},\mathbf{p_2})$ is the scattering matrix, and ∇_p is the gradient in momentum space. A solution for the above differential equations can be found with an expression for the continuum state population of

$$b(\mathbf{p},t) = -i\int_{-\infty}^{t} dt_b\,a(t_b)\mathbf{E}(t_b)\mathbf{d}(\mathbf{p}-\mathbf{A}(\mathbf{t_b}))\exp(-iS(\mathbf{p},t,t_b)) \tag{3.1.13}$$

where t_b is the space of "birth" times over which an electron can be liberated from the parent,

$$S(\mathbf{p}, t, t_b) = \int_{t_b}^{t} dt' \left(\frac{[\mathbf{p} - \mathbf{A}(\mathbf{t}')]^2}{2} + I_p \right). \tag{3.1.14}$$

is the quasi-classical action and $\mathbf{A}(\mathbf{t})$ is the vector potential of the electric field. t' is a dummy variable constructed to allow integration over the time domain.

The final step is to calculate the dipole moment, whose expression has now simplified to [82]

$$\mathbf{D}(\mathbf{t}) = i \int_{-\infty}^{t} dt_b \int d^3\mathbf{p}\, a(t)\mathbf{d}(\mathbf{p} + \mathbf{A}(\mathbf{_b t})) \cdot a^*(t)\mathbf{d}^*(\mathbf{p} + \mathbf{A}(\mathbf{t})) \cdot \exp(-iS(\mathbf{p}, t, t_b)) \,. \tag{3.1.15}$$

Lewenstein *et al.* provide a good qualitative description for the physical meaningfulness for the three terms in this expression. The first term in this integral, $\mathbf{d}(\mathbf{p}-\mathbf{A}(\mathbf{t_b}))$, represents the probability amplitude for the ionisation of the electron through tunnelling ionisation. The latter two expressions then represent the recombination of the electron, $\mathbf{d}^*(\mathbf{p}-\mathbf{A}(\mathbf{t}))$, and the phase gained by the electron, $\exp(-iS(\mathbf{p}, t, t_b))$. This can be understood as a Feynman path integral over all the possible electron trajectories, and using saddle point analysis we reduce this to the points at which the gradient of the action $\nabla S(\mathbf{p}, t, t_b) = 0$ — that is, the points of "stationary action".

To further simplify this integral for computation, we also will use the stationary phase approximation, which is the final part of the SFA. Here, we use the principle that we have outlined above that we seek to use the points of stationary action, and that the dependence of the momentum integral in eq. (3.1.15) can be broken into two

components: the slower varying dipole moment and the faster varying exponential term. Using the concept of stationary phases in this integral, we can say that the "faster" elements will average out, and so a stationary momentum, $\mathbf{p}_{st}$, can be defined to reduce the momentum space considered in the integral. This is given by

$$\mathbf{p}_{st} = \frac{-1}{t - t_b} \int_{t_b}^{t} dt' \mathbf{A}(t'), \tag{3.1.16}$$

where t' is again a dummy time variable for the calculation of the momentum. This substitution then simplifies eq. (3.1.15) to

$$\mathbf{D}(\mathbf{t}) = i \int_{-\infty}^{t} dt_b \left(\frac{2\pi}{t - t_b} \right)^{3/2} a(t) \mathbf{d}(\mathbf{p} + \mathbf{A}(\mathbf{_b t})) \cdot a^*(t) \mathbf{d}^*(\mathbf{p} + \mathbf{A}(\mathbf{t})) \cdot \exp(-iS(\mathbf{p}, t, t_b)) \,. \tag{3.1.17}$$

This equation, now that it has been reduced to a single integral over the birth times, is rather more tractable than eq. (3.1.15). There are further benefits to the stationary phase approximation, however, that provide key insight into HHG. To find these, we first set the time coordinate $t = t_r$ as the return time for propagating electron, as we will be considering the case of a recombining electron's harmonic emission. To calculate this emission we then Fourier transform eq. (3.1.17), which provides an extra factor of $\exp(i\omega t_r)$, which is then rolled into the expression for the action. We therefore find the following series of equations:

$$S_\omega(\mathbf{p}, t_r, t_b) = \int_{t_b}^{t_r} dt' \left(\frac{[\mathbf{p} - \mathbf{A}(\mathbf{t}')]^2}{2} + I_p \right) - \omega t_r \tag{3.1.18}$$

$$\nabla_{\mathbf{p}} S_\omega = \mathbf{r}(t_r) - \mathbf{r}(t_b) = 0 \tag{3.1.19}$$

$$\frac{\partial}{\partial t_r} S_\omega = \frac{\mathbf{p}(t_r)^2}{2} + I_p - \omega = 0 \tag{3.1.20}$$

$$\frac{\partial}{\partial t_b} S_\omega = \frac{\mathbf{p}(t_b)^2}{2} + I_p = 0 \tag{3.1.21}$$

Each of these saddle point equations carries explicit meaning for our understanding of HHG. eq. (3.1.19) is known as the return equation, and shows that we have harmonic emission when the electron returns to the position at which it was born. Equation 3.1.20 is known as the recollision equation, and tells us explicitly what we had gleaned intuitively from the semiclassical model: that the energy of the emitted harmonic will be equal to the sum of the ionisation potential and the electron's kinetic energy.

Equation 3.1.21 is known as the tunnelling equation, and says that the kinetic energy of the electron upon tunnelling away from the parent must be negative, which in turn necessitates the velocity to be complex, and therefore complex values for the birth time. This is consistent with the expressions for tunnelling presented by Ammosov *et al.*, and the imaginary part of the complex time co-ordinate represents the tunnelling time [73].

By setting $\omega = 2N + 1$ for integer N it is also possible to further derive the familiar expression for the cutoff energy,

$$\omega_{2\mathrm{N}+1} = 3.17U_p + F(I_p/U_p)I_p, \tag{3.1.22}$$

where $F(I_p/U_p) \in [1.0, 1.32]$ is a multiplying factor ionisation potential that tends to 1.32 in the limit $U_p \gg I_p$ and arises from the derivation of the cutoff energy, though we will not derive or discuss this further here.

3.1.3 HHG Beyond Monatomic Gasses

As mentioned before, we are not bound to the use of SWIR lasers or noble gasses for HHG. HHG has been driven by laser sources from the UV [90] to the mid-IR [35], and in noble gasses [91], molecular gasses [66], plasma [92], solids [52], and most recently liquids [93, 94]. The model outlined above does not apply to all of the sources of HHG.

While the recombination picture has proved a good match for gas and plasma HHG, for solid phase targets a semiconductor-Bloch (SBE) model is sometimes thought to be a more appropriate description of the system, as they describe the interaction of optical fields with semiconductors [95]. Here electrons move from conduction to valence bands and propagate along the band surface rather than propagating through free space.

In a plasma, depending on the specifics of the experimental design, either a recombination model or a second model known as coherent wave emission (CWE) are used. In CWE, the driving laser no longer propagates through the generation medium — harmonics are generated by electron bunches being "swept" along the surface of a plasma on a surface, typically glasses[92, 96] or liquid jets [97]. To achieve this the electrons are accelerated to relativistic speeds, requiring peak intensities on the order of $10^{18}\,\mathrm{Wcm^{-2}}$. This, however, is a very different mechanism to the HHG mechanisms discussed in this thesis, and so will not be discussed any further in this thesis.

Finally, in liquids, the mechanisms are not yet fully established- this motivates the study in this thesis. It remains unclear to what extent one must use SBE models, as the liquid phase exhibits only short, not long, range order. This short range order is exhibited over distances of few-nm, shorter than the electron excursion distances for propagating electrons, which can exceed this at $10^{16}\,\mathrm{Wcm^{-2}}$. This in turn also exceeds the inter-molecular spacing in liquids which is often on the sub-nm scale. It is also

unclear to what extent we are free to use recombination based models, as one would expect electrons to propagate freely, but the molecular spacing of a liquid suggests electrons would be scattered as they propagate. These discrepancies will be discussed in Section 7.

In a simple recombination picture however we may return to the concept of the returning electron and an accumulation of coherent emission co-linear with the driving field. As such, we may pivot the discussion to the phase-matching of this process over the propagation volume to maximise the flux of harmonic generation.

3.1.4 High Harmonics and Phase-matching

It is important to remember that the emission we detect from HHG in an laboratory setting is not from a single point source, but from an extended series of emitters that produce coherent and co-linear emission. For this to be the case, we must define a phase-matching equation for the system. The temporal phase matching of harmonics requires both that the harmonics emitted during each half cycle and in consecutive bursts of harmonics can form a coherent pulse train.

The latter effect is responsible for the shift from a continuum of harmonics seen when generating isolated attosecond pulses from single cycle driving laser fields, to the characteristic harmonic fringes commonly seen in experiments using HHG for probe pulses [98–100]. The former of these, however, requires us to understand what elements of the HHG process can lead to phase discrepancy in the emitted harmonics.

Given that HHG is a strong field process, and therefore we will have significant ionisation, we know that both the optical phase imparted by the neutral gas and the plasma must be incorporated into any phase-matching. Further, the Gouy phase, Φ_{Gouy}, defines the beam's transition from focusing to defocusing as it passes through the focus, and so we define $\nabla\Phi_{Gouy}$ as the variance of the phase as the beam propa-

gates through the focus. We therefore say that the phase matching of the process is described by:

$$\Delta\mathbf{k} = q(\Delta\mathbf{k}_{\omega_0} + \nabla\Phi_{Gouy} + \Delta\mathbf{k}_{\omega_0,plasma}) - \Delta\mathbf{k}_{\omega} + \Delta\mathbf{K}_{Dip}. \tag{3.1.23}$$

where $\mathbf{k}_{\omega_0}$ and $\mathbf{k}_{\omega_0,plasma}$ are the wave vector of the driving laser in the medium and plasma respectively, $\mathbf{k}_{\omega}$ is the wave vector of the harmonic. $\mathbf{K}_{Dip}$ is the intensity dependent dipole phase, stemming from the phase in the dipole calculated in Equation 3.1.17, and can be given by [101, 102]

$$\mathbf{K}_{Dip} = \nabla\Phi_{\omega,\omega 0}(r, I) \propto \frac{U_p}{\lambda^3}, \tag{3.1.24}$$

Using eq. (3.0.8) we find the phase mismatch due to the plasma as

$$\Delta\mathbf{k}_{\omega_0,plasma} = \frac{q\omega_0}{c}(n_p(\omega_0) - n_p(\omega_1)) = 2\pi c N_a \eta r_e \frac{\omega - \omega_0^2}{\omega_0^2 - \omega} \tag{3.1.25}$$

With these factors combined, we can linearise the phase mismatches to optimise harmonic emission from a target. One of these is the ponderomotive energy, but in a more experiment-specific manner the ionisation fraction of the generating medium, which depends on the gas used and system backing pressure. These combine to form an equation for optimal backing pressure for a given gas and target harmonic energy, given by [33]

$$P_{pm}(\omega) = \frac{-q\nabla\Phi_{Gouy} - \mathbf{K}_{Dip}}{(1-\eta)\frac{\omega}{c}(n(\omega) - n(\omega_0)) - 2\pi c N_a \eta r_e \frac{\omega-\omega_0^2}{\omega_0^2-\omega}}. \tag{3.1.26}$$

We must further consider the effect of the medium on the emitted harmonics. The atoms that generate harmonics may also strongly absorb them, and so propagating long distances through the medium after the generation of harmonics is usually detrimental. This is not necessarily the case in the soft X-ray region, where noble gasses become increasingly transparent with photon energy. For the *extreme ultraviolet* (XUV), however, [103], suggests the general rules of

$$L > 3\,L_{\mathrm{abs}} \quad \text{and} \quad \mathrm{L_{coh}} > 5\,\mathrm{L_{abs}}, \tag{3.1.27}$$

where L, L_{abs} and L_{coh} are the interaction, absorption and coherence lengths respectively and the yield varies, as seen in Figure 3.1.4.

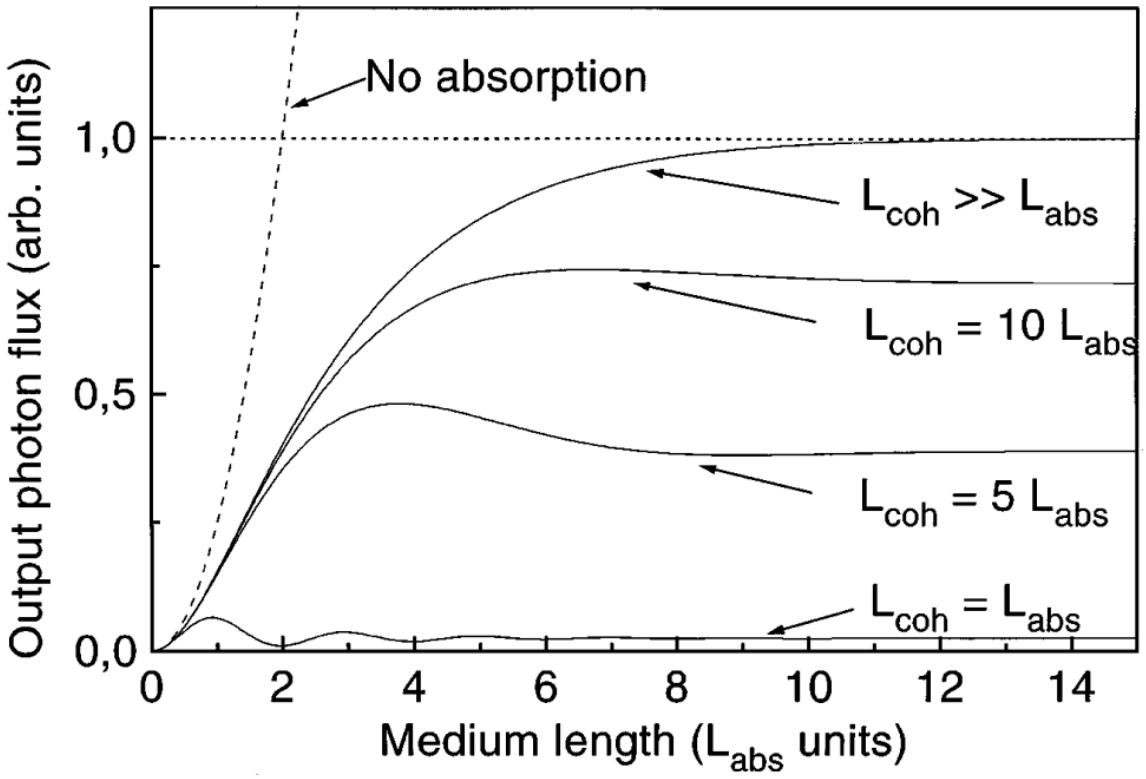


Figure 3.1.4: The variation of HHG efficiency with interaction length. Reproduced with permission from [103].

3.2 Scaling Laws for Non-linear Optics

Having seen the basics of phase-matching for both *resonant dispersive waves* (RDWs) and HHG, we can observe that both are dependent on similar factors— interaction volumes, which are tied to an interaction region radius, r, and length, l; pulse energy, ϵ; and gas pressures, ρ. This is not a coincidence, and it is generally observed that gas-phase non-linear optical processes scale with the same parameters, as they tend to require the same balance of physical factors, up to the limit that contributions from the plasma begin to dominate [23, 104]. These are tabulated in Table 3.1, and are generally described as a scaling factor η that is applied to each input parameter to the system in order maintain the characteristics of considered outgoing pulses (whether these are X-rays from HHG or solitons in a *hollow core fibre* (HCF)). For example, if one wished to maintain the same level of broadening in an HCF but with twice the input energy, we would use $\eta = \sqrt{2}$ and alter the other parameters of the system accordingly.

Parameter	Symbol	Scaled Parameter
Focal spot radius	r	$r\eta$
Length of interaction medium	z	$z\eta^2$
Target density	ρ	ρ/η^2
Pulse energy	ϵ	$\epsilon\eta^2$

Table 3.1: A table of the generalised scaling laws for non-linear optical processes in gasses. η is the scaling parameter used to maintain a particular outgoing state of laser pulses. r, z, ρ and ϵ are the initial laser focal spot, system interaction length, gas density and incoming pulse energy respectively.

It is worth noting however that, while these scaling factors will apply well when we come to discuss the construction of HCF-based systems, where maintaining a low plasma density is critical for propagation, they will quickly deteriorate in discussions of lasers and liquid jets, and in studying the overdriven regime of HHG. In [104], Heyl *et al.* explicitly state that at gas pressures over 70 bar these scaling laws will

almost certainly be invalid - a threshold easily reached in the liquid phase where the equivalent gas pressure to the liquid density is on the order of hundreds of bar.

The limit placed on these scaling laws by Heyl *et al.* is loose, and they propose that at the point that the non-linear interaction being studied "critically depend[s] on plasma dynamics" it is "not fully scalable according to [their] formalism", providing avalanche ionisation (where high-energy liberated electrons collide with atoms in a medium, liberating further electron on a picosecond timescale) as an example. It seems pertinent to state here that the process of transient phase-matching, as will be discussed in Section 6, requires the plasma to generate harmonics at higher wavelengths and with greater efficiency than would otherwise be possible. This said, systems that involve filamentation — where a propagating beam balances self-focusing and plasma defocusing to maintain a narrow propagating radius to induce SPM without confinement in an HCF — generally require plasma, and is a part of their discussion of scaling laws. It is unclear whether HHG in our regimes falls into the former or latter category, and this will be investigated further.

4 Experimental Apparatus and Methods

The laser system presented in this chapter and its diagnostics drive the processes and works in the following chapters, though new elements were added through this project.

4.1 Titanium:Sapphire Chirped Pulse Amplifier

The laser used here is a heavily modified commercial KM Labs Red Dragon and produces pulses at 8 - 9 mJ at 1 kHz after compression[105]. In it, a Kerr-lens modelocked, *titanium-doped sapphire* (Ti:Saph) oscillator, operating at 80 MHz and with a central wavelength of 800 nm, is amplified in two cryogenically cooled amplifiers, a 13-pass ring amplifier and 5-pass bow-tie amplifier. A block diagram of this can be seen in fig. 4.1.1 The cryogenic cooling reduces thermal lensing in the crystal, as well

as reducing temperature-dependent fluctuations in the refractive index of the crystal and increasing its thermal conductivity [106, 107].

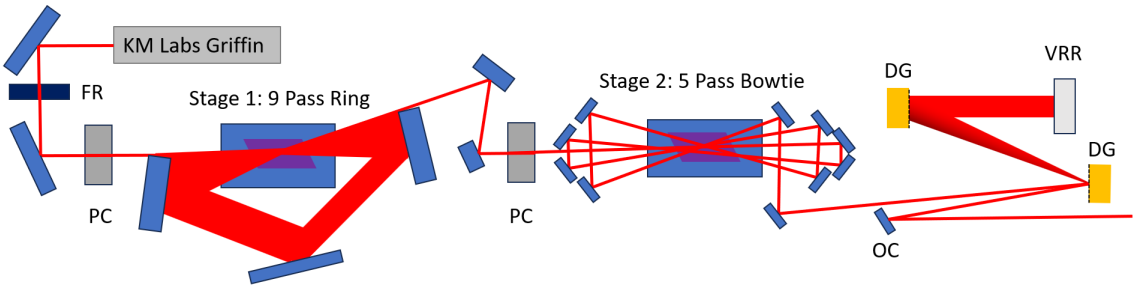


Figure 4.1.1: A block diagram for the modified KM Labs Red Dragon used for the experiments in this thesis. FR is a Faraday Rotator, PC are Pockels cells, DG are diffraction gratings, VRR is a vertically oriented retro-reflector, and OC is the output coupling mirror, which is vertically spaced from the beam incoming to the grating compressor. The first amplifier stage is a 9-pass ring amplifier, and the second is a 5-pass bow-tie amplifier. The crystals in both amplifier chambers are cryogenically cooled.

A pair of Pockels cells with few-ns rise times are present, one before and one after the first amplifier. Pockels cells work under the principle that, under the application of a high voltage, polarisation of a pulse travelling through the cell will be rotated by $\pi/2$, creating a half wave plate that can be switched on the nanosecond scale [47].

The first Pockels cell reduces the repetition rate in the pulse train from 80 MHz to 1 kHz, and the second filters *amplified spontaneous emission* (ASE) from the first amplifier. The pulse duration is stretched from 30 fs FWHM before the first amplifier to hundreds of picoseconds to allow amplification, and is recompressed by a diffraction grating pair to around 30 fs. The amplified pulses are characterised using a commercial pulse diagnostic (APE SPIDER, see Section 4.4.4).

Motorised pointing stabilisation into both the first and second amplifier stages are present, as well as pointing stabilisation and power tuning using a beam-splitter to optimise coupling out of the amplifiers and into a commercial *optical parametric amplifier* (OPA) (Light Conversion TOPAS-PRIME-HE) [108].

4.2 Optical Parametric Amplifier

Optical parametric amplification is a second order process, and therefore requires a non-centrosymmetric material as discussed in section 2.2.1. In optical parametric amplification, a "pump" photon is divided into two photons whose energies sum to that of the pump. This process here is *difference frequency generation* (DFG), and as mentioned in section 2.2.1 must be phase matched by setting the crystal angle appropriately such that the k-vectors for the desired, amplified wavelengths are matched by driving field.

DFG can be seeded, meaning that the generation of a desired wavelength can be stimulated by the introduction of that same wavelength, rather than relying on that wavelength being spontaneously generated as in SFG or in the generation of perturbative harmonics [49]. Because we seed this process with signal wavelength, and the DFG process is stimulated to produce photon with a seed with higher flux than in the spontaneous case, this process can be viewed as an amplification of the signal.

The nonlinear polarisation in DFG takes the form

$$P = 2\varepsilon_0 \chi^{(2)} E_1 E_2^* \tag{4.2.1}$$

which, when arranged to give the frequencies of the generated field as we did in section 2.2.1 for SFG, gives the equation

$$\omega_3 = \omega_1 - \omega_2, \tag{4.2.2}$$

where ω_1 is the pump wavelength, and ω_3 and ω_2 are labelled the signal and idler respectively.

In the experiments described in this thesis, the amplified 800 nm pulses from the Ti:Saph laser are converted into a signal and idler at 1.4 µm and 1.8 µm respectively. The signal and idler carry around 2 and 1.5 mJ respectively, and are both measured at around 60 fs FWHM using the home-built second harmonic FROG (see Section 4.4.2).

The pump arm is divided into four upon entering the HE-TOPAS, and part of the first arm is passed through a telescope to reduce its FWHM diameter to 15 mm. This portion undergoes *self-phase modulation* (SPM) in a sapphire plate (≈2 mm thickness) to dramatically spectrally broaden the pulse such that it covers the spectral region we seek to seed (i.e. up to around 1.6 µm). It is then propagated through a few-mm thick block of dispersive glass to temporally stretch the white light to a duration of hundreds of femtoseconds. This forms the seed for the OPA, and allows the interaction in the first non-linear *barium-borate* (BBO) crystal to amplify a selected wavelength by varying the time delay of the pump beam such that it overlaps in time with the desired wavelengths. The pump and seed in the first stage are non-collinear to provide broad-band phase-matching, while the second and third are collinear to maximise gain. The crystal mount in each amplification stage has controls for the delay and crystal angle to be optimised. The pump pulse is dumped after each BBO to allow each amplification stage to be individually optimised.

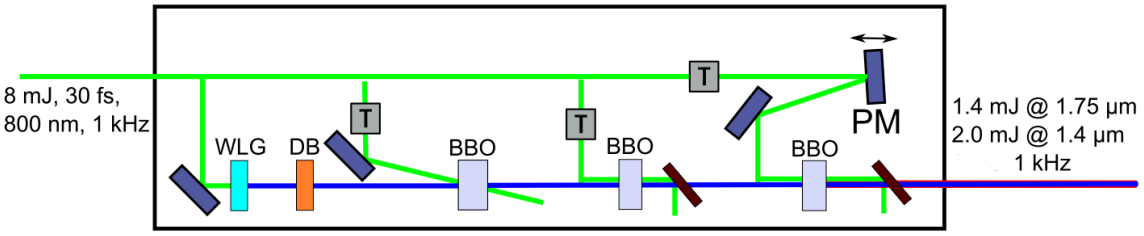


Figure 4.2.1: A schematic representation of the layout of the HE-TOPAS used for the works in this thesis. WLG is a white light generation plate made of sapphire, DB is a dispersive block of glass, T are the delay stages for the pump arm into each BBO cystal, and PM is the piezoelectric mount for the final mirror to allow CEP stabilisation. Reproduced with permission from [33] under CC BY-NC 4.0.

The final delay arm is mounted on a piezo stage, allowing it to be translated on the sub-micron scale and therefore providing sub-cycle control of the amplification using a PID control loop. This can be used to set the *carrier-envelope phase* (CEP) of the idler. To explain this we must revisit CEP as discussed in eq. (2.1.9). In self-seeded OPA such as the TOPAS used here, the spectral phases of the pulses of the pump, signal and idler ,ϕ_p, ϕ_s and ϕ_i respectively, are given by [109]

$$\phi_p = \phi_s + \phi_i + \pi/2. \tag{4.2.3}$$

The idler pulses have "automatic" CEP stabilisation, while the signal inherits the CEP fluctuation of the pump pulses. To measure the CEP, ϕ_0, the pulses must be broadened sufficiently that two harmonics of the laser field are spectrally overlapped. To achieve this, we first broaden the pulses using SPM as was discussed in section 2.3. While the first stage is non-collinear to allow fine control of the amplified frequency in the seed amplification stages, the following two stages are collinear.

Following this, the 2^{nd} harmonics of the beam is generated in a BBO crystal and interfered with the 3^{rd} harmonic that is generated during propagation in the fibre to generate a beat frequency interferometer. To use this CEP diagnostic, the requirement is that the fundamental pulse of central frequency ω_0 must have a spectrum that spans $\Delta\omega_0 = h_{\text{low}}/h_{\text{high}}\omega_0$ where $h_{\text{low}}, h_{\text{high}}$ are the numerical orders of the higher and lower harmonics of the fundamental field being used to diagnose the CEP [110].

To understand how we retrieve and stabilise the CEP of a laser we must first understand the source of CEP drift. In the oscillator a phase $\delta\phi$ is accumulated between each mode in the cavity, as the frequency of the modes does not in general correspond to an integer number of round-trips of the cavity [111]. The phase difference

accumulated per round-trip for a laser at frequency ω_0 can defined simply using the cavity length L, group velocity v_g, and group velocity v_p as

$$\delta\phi = L\omega_0 \left(\frac{1}{v_g} - \frac{1}{v_p} \right). \tag{4.2.4}$$

If we briefly consider the longitudinal modes of the oscillator in the frequency domain rather than the time domain, the spectrum is a frequency comb with frequencies f_n. The separation of the comb peaks is set by the repetition rate of the laser, f_{rep}, and an offset decided by the CEP. As such we find that

$$f_n = f_{\text{rep}} \left(n + \frac{\delta\phi}{2\pi} \right). \tag{4.2.5}$$

where the numerator under the phase slip is needed to account for the difference between linear and angular frequency between the two expressions above. If we now consider the interference between the broadened second and third harmonics described earlier, the interferogram of these two pulses $S(\omega)$ will have an oscillating component given by

$$S(\omega) = E_{2f} \cdot E_{3f} = \sqrt{(I_{2f} I_{3f})} \exp(\omega_{3f} - \omega_{2f}) \tag{4.2.6}$$

The beat frequency ω_b in the exponent can then be written as

$$\omega_b = \omega_{3f} - \omega_{2f} = (\omega_{ov} + 3\frac{\delta\phi}{2\pi}) + (\omega_{ov} 2\frac{\delta\phi}{2\pi}) = \frac{\delta\phi}{2\pi}. \tag{4.2.7}$$

Here we have labelled ω_{ov} as the overlapping laser frequency, which cancels leaving us with a simple expression that shows that the beat frequency will be set by the CEP [110]. Because the CEP can also be understood as a delay caused by instabilities such as air flow and thermal variation, we can also understand that small drifts will be introduced over time to even the CEP-stable idler.

Equation 4.2.4 can be rewritten to use the refractive indices experienced by the envelope and carrier, n_g and n_p respectively, as

$$\delta\phi = \frac{2\pi L}{\lambda}(n_g - n_p). \tag{4.2.8}$$

For the 1.8 µm OPA idler propagating through fused silica, $n_g = 1.4648$ and $n_p = 1.4409$ [112]. Using this, one can calculate that 77 µm of fused silica would correspond to $\delta\phi = 2\pi$. Given that this corresponds to a very small GDD accumulation ($\approx -5\,\mathrm{fs}^2$), these wedges can in practise be used both for bulk compression of the laser pulses and managing the CEP of the laser field. As such, while the piezo mount mentioned in Figure 4.2.1 allows one to set a desired CEP, in practise a pair of fused silica wedges (Laser Quantum) with a maximum combined glass insertion of 5 mm was used.

4.3 Spectral Broadening in Hollow Core Fibres

While prior to the start of this project the signal was unused, a diagram of the coupling of the idler into a fibre can be seen in Figure 4.3.1. This HCF is a rod fibre, of few-mm outer diameter (OD) and 430 µm inner diameter (ID). The front and back were evacuated down to around few-10^{-1} mbar before argon gas was added to the rear cell. The gas was drawn through the fibre by the pressure gradient and evacuated in the front cell, which maintained pressures at a few mbar while in operation. The back cell was filled with around 1.2 bar Argon to broaden the pulses to a spectral bandwidth supporting a minimum pulse duration of around 12 fs FWHM while avoiding unstable white-light generation, identified by visible sharp fluctuations in the stability in the

spectral profile. The broadened beam was then temporally compressed using bulk compression in a pair of anti-reflection (AR) coated thin fused silica wedges (Laser Quantum, as above) to sub-20 fs. At this point, around 500-600 µJ remain in the idler pulse.

The diagnostics on the beam path from the OPA comprise of a pair of cameras for two-point pointing stabilisation for the input to the fibre, a camera to image the output of the HCF and a second to monitor the pointing of the beam into the HHG chamber for experimental alignment, and a pickoff sent to the 2f-3f interferometer for CEP characterisation.

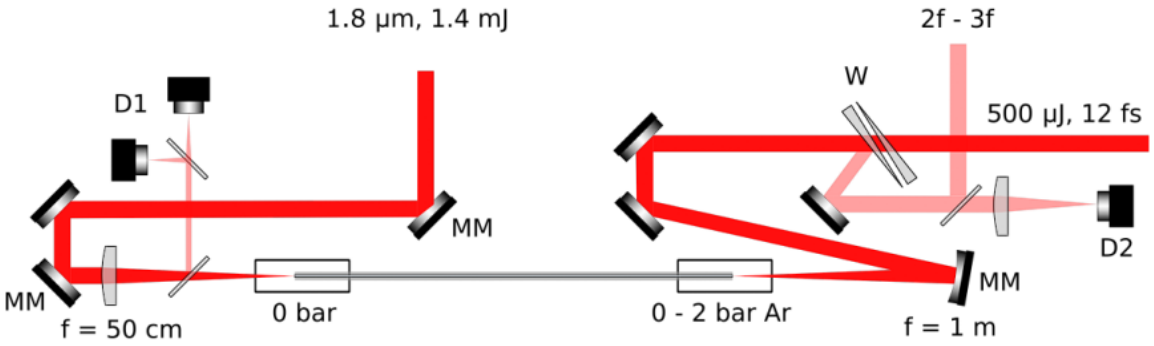


Figure 4.3.1: The layout of the coupling into the rigid HCF for the idler beam. MM are motorised mirrors, D1 and D2 are cameras for fibre input alignment, and the 2f-3f path is used for CEP characterisation. Reproduced with permission from [80] under CC BY-NC 4.0.

At this point the beam is divided by a holey mirror — a mirror with a machined hole at 90 or 45 degrees to the mirror surface to split off an incident beam at normal or 45 degree incidence respectively. One portion of the beam was used to generate perturbative harmonics for UV pump pulses, and the rest drove HHG in a differentially pumped gas-filled needle target. The proportion of energy sent to each arm were experiment-dependent and not fixed. The design of the HHG line will be covered in detail in Section 6. A schematic of the arm that generated the UV pump beams can be seen in Figure 4.3.2.

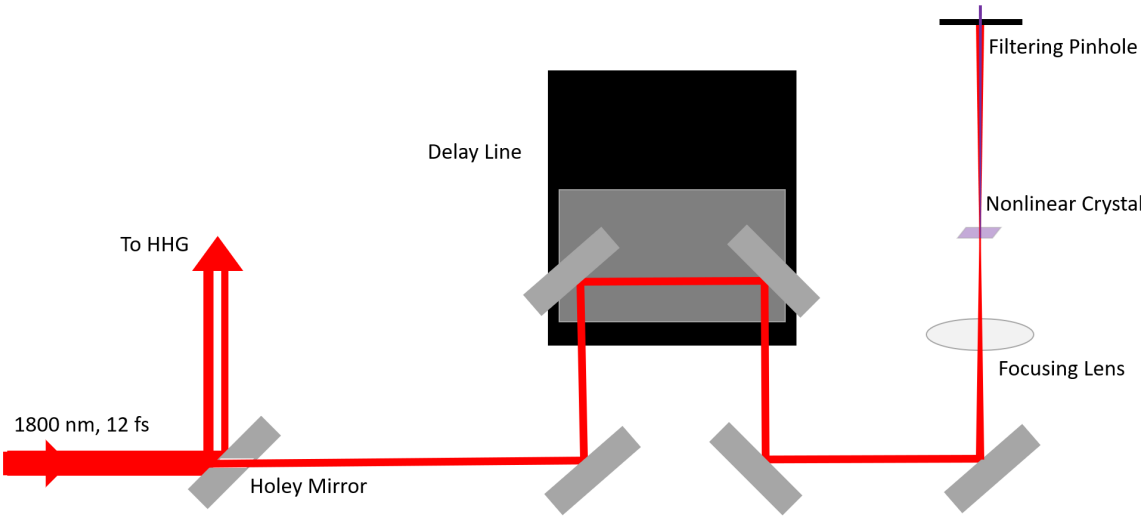


Figure 4.3.2: The layout of the previous experimental arm in the beamline for generating UV through perturbative harmonics. A holey mirror is used to extract a small portion of the beam, which is put through a delay line on an electronic delay stage and focused into a nonlinear crystal using a broad-band lens. The beam is then immediately spatially filtered using a pinhole.

4.4 Characterisation of Femtosecond Pulses

While a wider variety of methods are available [113], the measurement of femtosecond pulses is generally performed with one of 3 methods: frequency resolved optical gating (FROG) [31]; spectral phase interferometry (SPIDER)[114, 115]; and dispersion scanning (D-Scan) [116]. Both FROG and SPIDER systems are used to characterise the pulses which drive pump-probe experiments in this laboratory.

In this project, 2 home-built FROG systems are used — a *second harmonic generation FROG* (SHG FROG) and a *self-diffraction FROG* (SD FROG) — along with a commercial SPIDER supplied by APE. The SPIDER is used to characterise the beam driving the OPA which generates the signal and idler which are necessary for the experiments herein, so will be described briefly, but as it is not critical to the function of the experiments, will not be examined in particular detail.

4.4.1 FROG

FROG, broadly speaking, is a family of techniques in which two or more pulses are interfered - with at least one acting as a "gate" pulse - to create a new pulse by some nonlinear mechanism which is spectrally dispersed so as to be spectrally resolved on a sensor array[31].

The basis of this technique stems from the concept of intensity autocorrelation, a specific case of cross-correlation. In cross-correlation two pulses are spatio-temporally overlapped in a non-linear medium and produce a signal depending on both their delay and overlap region in an interaction medium with a known nonlinearity. If the two pulses are the same, this then becomes an autocorrelation. In the simplest case second harmonic generation can be used for this purpose. Using a non-linear crystal, we can generate an autocorrelation signal, A, from two identical pulses with intensity profiles, I_n, defined by

$$A = \int I_1(t) I_2(t - \tau) dt, \tag{4.4.1}$$

and we detect the resultant harmonic on a photodiode or other "slow" detector. Here we arbitrarily choose the second pulse to be delayed by some variable delay τ. While autocorrelation is a good starting point for retrieving pulse duration, it forces certain conditions onto the retrieved pulse shape, as the autocorrelation will always be symmetric around $t = t_0$, and we do not have spectral resolution meaning we cannot intuit spectral phase. For many applications in ultrafast non-linear optics this would be too limiting, and so we need a method that will give us these added details about to provide us values of the higher order phases that need to be compensated to achieve optimally compressed pulses.

To shed these limitations we replace the "bucket" detection using a single element detector with a spectrometer. In doing so we both add spectral resolution, and can resolve the spectral phase across the bandwidth of the pulse so that we can account for some degree of asymmetry. Many FROG apparatus' generate a signal that could be contaminated by the presence of the fundamental field, and for these we place the beams in a non-colinear geometry. We want to overlap individual time points in the pulses at any given delay to accurately map the temporal shape of the pulse, as seen in Figure 4.4.1, and therefore split the beam we wish to characterise into at least two arms, and scan one pulse to "gate" the non-linear interaction.

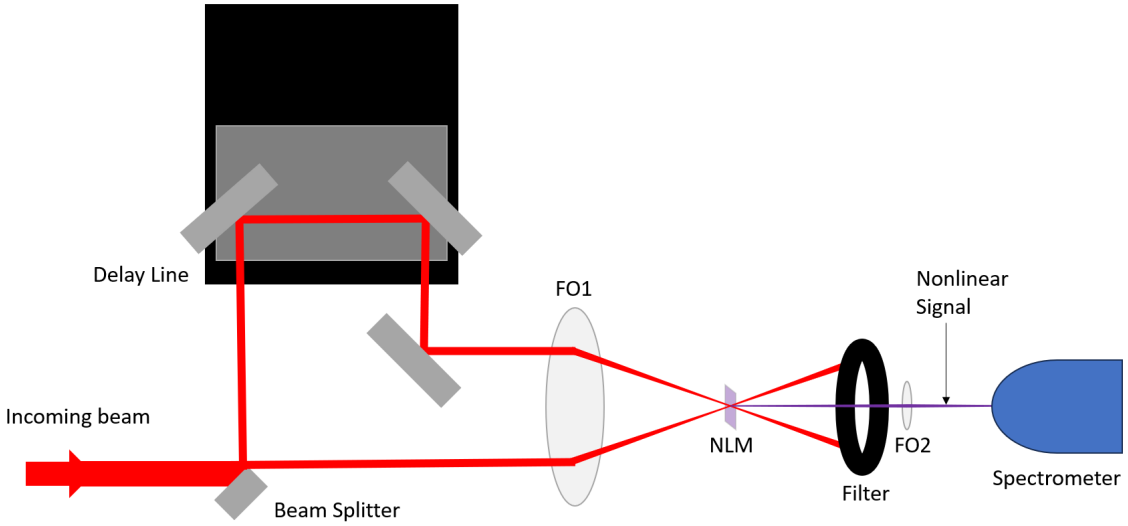


Figure 4.4.1: An example of a simple FROG, with two beams generated by splitting an incoming pulse, with one arm delayed using a simple delay line. These are focused using an optic FO1 onto a nonlinear medium NLM, and the fundamental fields are removed by a filter, often spatial, while the signal generated by the nonlinear interaction in NLM is focused into a spectrometer.

We can do this either by placing one of the arms of the interferometer on a translation stage, or by using a non-symmetric beam configuration or non-circular focal spots and mapping the temporal structure of the pulse onto a spatial axis. The latter of these designs are called single-shot FROGs, and while effective, are challenging to design and require careful attention to avoid propagating spatial aberrations (e.g. astigma-

tisms) into the reconstructions. The interference is then resolved by a spectrometer or imaging spectrometer for the scanning or single-shot methods respectively.

4.4.2 Second Harmonic FROG

By taking Equation 2.1.5, we can write an expression for two overlapped pulses, E_1 and E_2, propagating in parallel in one plane and converging in another as

$$E_t = E_1(t)\exp(i\mathbf{k}_{x,1}\mathbf{X} - \omega t_1) \cdot \times E_2(t)\exp(i\mathbf{k}_{x,2}\mathbf{X} - \omega t_2), \tag{4.4.2}$$

where $\mathbf{X}$ is the position, E_n are the magnitudes of the two pulses and we define the beams as parallel in the y-plane, and converging in the x as this best represents the experimental implementation.

By experimentally obtaining these two pulses by splitting a single beam and ensuring that they follow the same effective path, do not pass through any dispersive optics and are incident on as many common optical elements as possible, we can ensure that these two pulses are as close to identical as possible, and in doing so reduce Equation 4.4.2 to

$$E_t = |E(\Delta t)|^2\exp(2i(k_y\mathbf{X} - \omega\Delta t)), \tag{4.4.3}$$

where Δt is simply the delay between the two pulses. For future reference to these generated pulses, as we assume that the spatial component will not factor into the traces, as we are not using any single-shot FROGs, we will omit the k-vector term.

By directing the fields in this configuration onto a non-centrosymmetric crystal which permits SHG at our wavelength, such as BBO, we can phase-match the second har-

monic of this combined field. One can interpret this harmonic signal as the auto-correlation of the original pulse, as we are overlapping it with a copy of itself to generate a field which well describes its source.

We then focus the resultant second harmonic onto a compact UV-Vis Spectrometer, and scan the delay stage seen in Figure 4.4.2 to generate a time-varying map of the spectrally resolved auto-correlation in 2D which is then fitted using projection algorithms to find the phase and true pulse duration of the original pulse.

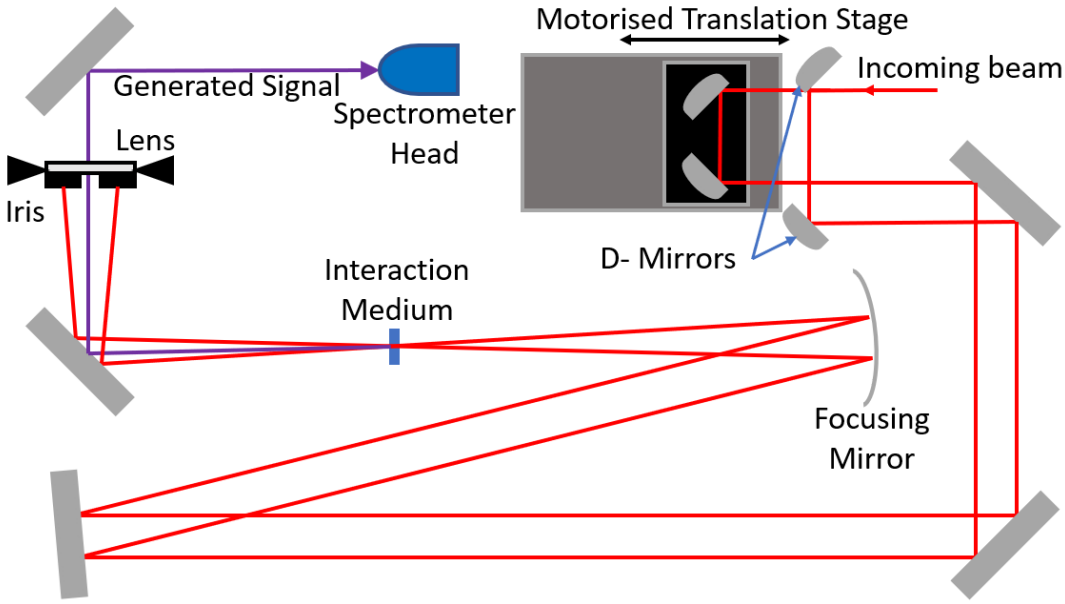


Figure 4.4.2: A general layout that suits both types of FROG described in this thesis. The beams here are separated spatially using D-mirrors to avoid introducing any spectral phase from a transmissive beamsplitter. The split beams are focused onto a nonlinear medium as described above with the delay in one arm scanned to generate the FROG traces. For SHG-FROGs the interaction medium is a BBO crystal (0.2 mm), and for SD-FROG a thin piece of glass (0.5 mm) would be used. A high precision motorised stage is used to allow resolutions of sub-10 fs pulses in both cases.

SHG FROG has a major benefit over most other FROG configurations in that it requires second-order non-linearity, where most others require third. This means it can operate at far lower pulse energies, and can often be easier to construct as initial

alignments need not be as precise while still able to produce a trace whose fitting can then be optimised. The major drawback however is that, as we are using a second order linearity, and therefore only two beams, the traces received are symmetric, meaning they are less visually intuitive and also do not inherently provide the direction of retrieved phases. To resolve this a material with well understood dispersion, often a piece of glass, is placed in the beam and a second FROG trace taken to establish the direction of the chirp. The second limitation is lies in the fact that the phase-matching process is angularly dependent, and so broadband pulses can often be limited in the wavelength ranges that can be phase matched in any given configuration.

For the experiments presented here, a few-fs 1800 nm or 1400 nm pulse is spatially divided by a pair of d-mirrors, with one on a motorised translation stage acting as the delay line, and a second as the gate pulse, as seen in Figure 4.4.2. The two beams are spatio-temporally overlapped when refocused into a 200 μm thick BBO, and the resultant SHG is measured by an Ocean Optics 2000+ spectrometer [117]. The crystal is mounted on a rotational stage to allow change between P and S-polarisations in the FROG, meaning the TOPAS Signal and Idler can both be measured with this system.

4.4.3 Self-Diffraction FROG

Schematically, the design of an SD-FROG matches that of an SHG-FROG almost exactly, with the exception that rather than a crystal, a piece of glass will be our interaction medium, but again the overlap of the two pulses generates a combined field in the medium at the point of interaction. Unlike SHG however, for self-diffraction a transient grating is formed, so named as it is generated by the temporal interference of the beams interacting with a medium via the Kerr effect [118]. As such there is no parametric or phase-matched process generating new wavelengths. In this case, the grating causes the diffraction of the transient field, the 0^{th} order of which lies along the axis at which the k-vectors of the two beams cancel. As a result, we are now

looking at the interaction of three fields, as the grating is only formed by the overlap of the incoming beams, and so our trace is generated by the equation

$$E_t = |E(t)|^2 E^*(t - \Delta t) exp(-i\omega\Delta t). \tag{4.4.4}$$

The true benefits of an SD-FROG lie in that it requires no reference pulse or polarisers. Provided the the medium the grating is generated in is suitably thin, a signal of almost any wavelength can be generated as third-order responses are always present— typically a thin (sub-mm) piece of fused silica is used, as these are readily commercially available. Unlike in SHG-FROG, the trace itself is also intuitive as the direction of the phase can be distinguished visually, though the measurement sensitivity is around three to five orders of magnitude lower, depending on if the system is single- or multi-shot, due to the relative strength of second and third order non-linear responses.

It is worth briefly discussing the transient grating (TG) frog here, which also uses a transient grating in the sample, but requires three beams, and so must often be operated in a "box-cars" geometry, which adds operational complexity. Box-cars is an experimental design geometry where four beams, forming the corners of a square, are focused to a single point at their centre. In this case, three of the beams are focused onto a medium (two to form the transient grating, and the third to be scattered from that grating). The fourth beam is then generated in the interaction medium, but propagates with a k-vector that matches the path of a beam from the fourth corner due to conservation of momentum (and hence phase matching) rules. While a TG-FROG operates under the a similar principle to the SD-FROG its sensitivity for pulse measurement and reconstruction are higher as it is a phase-matched process rather than simply the scattering from one of the fundamental beams from the transient grating. This also means that a thicker sample maybe use to yield greater signal as, unlike and its operational complexity is greater [31].

The pulse energies required to run an SD-FROG with multi-shot averaging are on the order of a microjoule, which is readily available with the laser pulses seen in this work. If the experimental design for the RDW emission discussed here were of lower pulse energies, using the TG-FROG would become favourable, though some design challenge would be present in attempting to split the beams into more than simply half without introducing any spectral phase from transmissive optics or significant risk of spatial chirp considerations.

In the following works, UV Pulses are generated using RDW emission down to 200 nm. A pair of d-mirrors will be used to spatially divide the pulse, creating multiple beams which are then refocused by a 30 cm focusing lens onto a 200˙µm piece of fused silica, in approximately the schematic seen in Figure 4.4.2, with the resultant self-diffraction effects measured using a UV-Vis spectrometer. While the design for this system was finalised, as will be shown in section 6, it could not be implemented within the timeline of this project.

4.4.4 SPIDER

Rather than overlap the pulses and interfere them by temporal overlap as in FROG, the SPIDER works by the process of shearing interferometry [114]. For this, three copies of the original pulse are taken.

The first is separated and significantly temporally and spectrally dispersed. In the SPIDER used here, this is achieved with a pair of diffraction gratings, though in principle this can be performed using bulk glass or any other temporally dispersive apparatus. This is then sent onto a non-linear crystal with the second and third pulse, which are temporally separated, and therefore overlap with differing spectral elements of the stretched pulse. The non-linear crystal is used for sum frequency generation, meaning that the two pulses are now at differing frequencies and, once sent into a spectrometer, will provide spectral fringes which allow temporal characterisation of

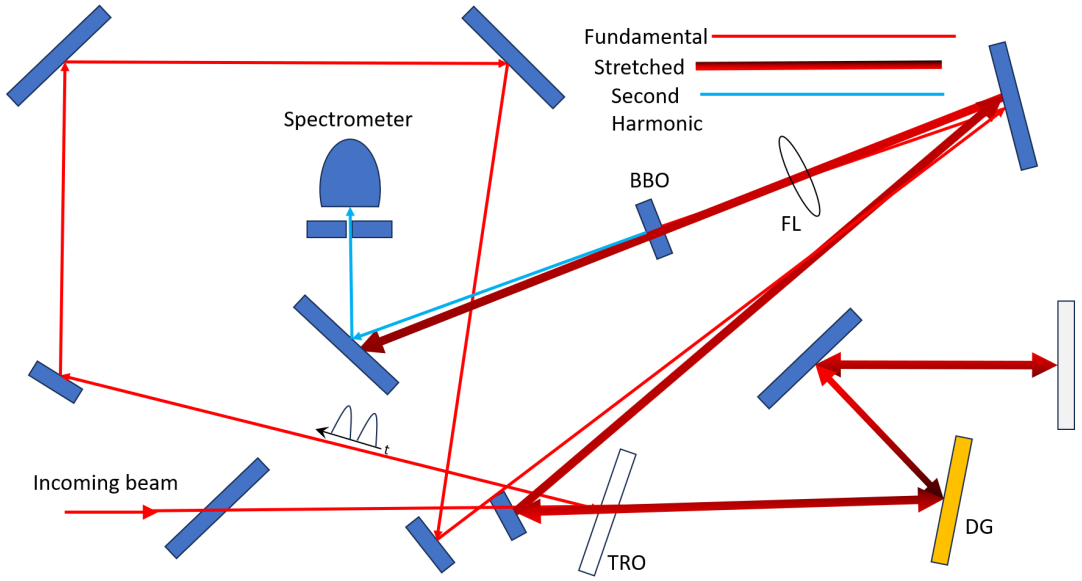


Figure 4.4.3: A diagram of the APE SPIDER used in our laboratory. TRO is a transmissive optic that provides a front and back reflection to provide two temporally offset copies of the pulse to be diagnosed. DG is a diffraction grating used to temporally stretch the pulse. The stretched pulse along with the temporally delayed pulses are overlapped in the BBO crystal after being focused in by a focusing lens FL. The second harmonic generated in the BBO is resolved using an in-built spectrometer. The traces from this system are analysed using manufacturer-supplied software.

the beam through a direct (i.e. non-iterative) process. A layout of this system can be seen in fig. 4.4.3.

4.5 HHG Apparatus

The experimental beamline for TAS experiments can be seen in Figure 4.5.1. A 15 fs, $\geq$ 500 µJ, 1750 nm pulse enters the source chamber and is split by a holey mirror to provide the pump and probe pulses. The hole has a diameter of $\approx$1 mm and transmits around 5% of the beam. The pump pulse generates perturbative harmonics (typically third of fifth order harmonics) in a crystal (100 µm thick BBO in this case), with a pair of coarse and fine translation stages to scan its experimental delay (Physik Instrumente M- 403.4VP and P-622.1UD respectively). The coarse stage has a scan

range of 200 mm (corresponding to around 667 ps) to find the temporal overlap of the pump and probe pulses, the fine stage has a repeatability of 1 nm and is used for delay scans over its travel range of 250 μm (around 1.65 ps).

The remaining 95% of the pulse forms the probe beam which is focused into a differentially pumped gas cell to generate high harmonics. The existing cell is constructed of sub-mm hypodermic needles drilled in-situ by the focusing of the pump beam. This gas needle target is housed in two differential pumping jackets as seen in Figure 4.5.2.

The IR component is removed by a 0.2 μm thick metallic filters selected to match the harmonic photon energy edges needed for the experiment. Examples include tin, titanium or zirconium, with typical transmission curves as seen in Figure 4.5.3.

A 1 m focal length toroidal mirror, with a gold coating and at a 5° incidence angle, is used to focus generated harmonics onto an experimental target, and the transmitted spectrum is resolved by the 1^{st} order reflection in a flat-field X-ray spectrometer. The spectrometer is comprised of a grazing-incidence reflection from a gold-coated, variable line spacing diffraction grating (Hitachi 001-0660) and X-ray CCD camera (Andor Newton 940). The 0^{th} order reflection from the grating is blocked ≈15 cm upstream from the camera in order to reduce detector saturation from its scatter. The diffraction grating is mounted on translation and rotation stages (Smaract SLC and SR respectively) for alignment. The camera can be cooled to -100 °C thermoelectrically to reduce dark counts due to thermal noise, and to prevent this cooling leading to dust or humidity buildup on the sensor a liquid nitrogen-cooled cold finger is used. The camera is also mounted on a movable flange to allow selection of the spectral window for experiments.

There are a combination of vacuum isolation valves, pinholes and differential pumping sections between each chamber in Figure 4.5.1 with few-mm apertures to allow beam

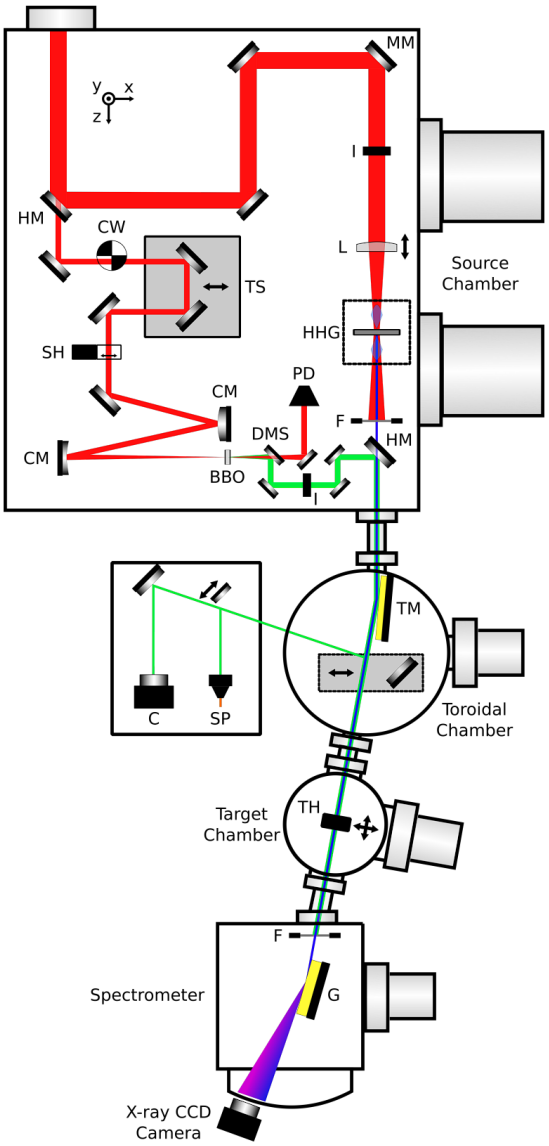


Figure 4.5.1: The current design of the beamline for TAS experiments. In the experimental pump arm, HM are holey mirrors, CW is a chopper wheel, TS is a translation stage, CM are curved mirrors, SH is a shutter, DMS is a dichroic mirror seperator, PD is a photodiode and I is an iris. In the experimental probe arm MM is a motorised mirror, L is a lens and F is a filter. The pulses are refocused into the target housing, TH, using a toroidal mirror, TM, and the spectrum is imaged on an X-ray CCD camera using a grating, G. A camera and spectrometer, C and SP, are outside of the harmonic chambers as diagnostics, with a pick-off mirror on a motorised stage in the toroidal chamber for this purpose. Figure reproduced with permission from [80] under CC BY-NC 4.0.

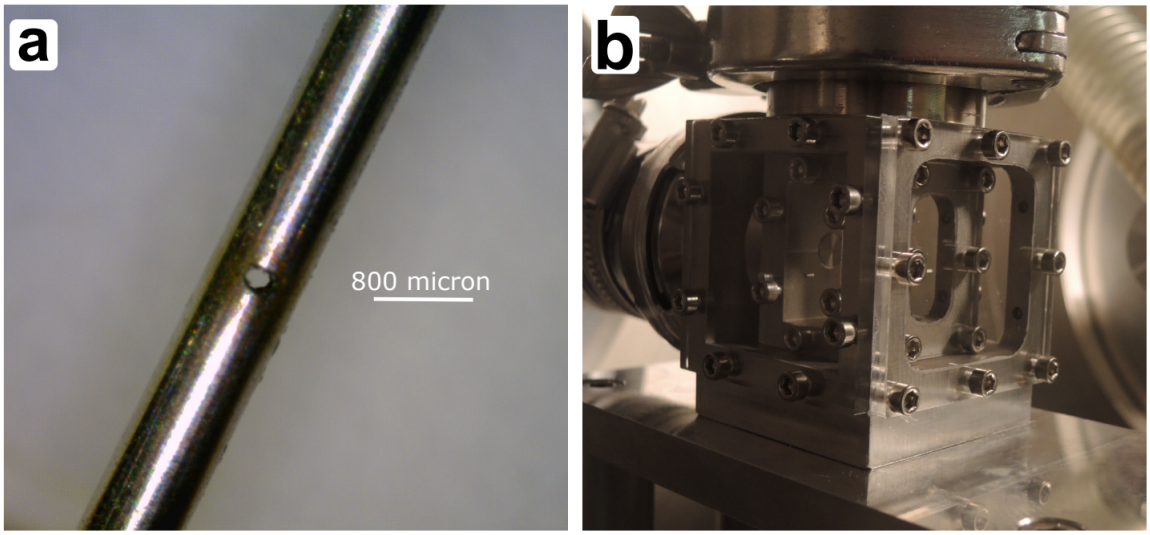


Figure 4.5.2: The laser drilled needle used for HHG (a) and the differential pumping jackets in which it is housed (b). Reproduced with permission from [41].

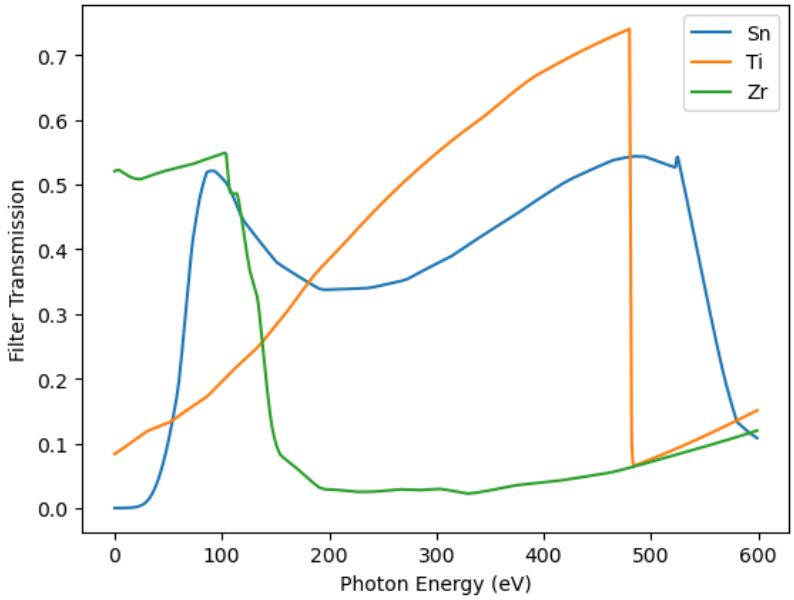


Figure 4.5.3: Calculated transmission of X-rays through 0.2 µm thick metallic filters of a variety of elements used in the HHG beamline shown in Figure 4.5.1, using data from [44].

propagation without compromising the vacuum of any chamber. As mentioned above, the future experiments in our lab will use a liquid jet to allow solution phase samples in the target chamber, and as such the differential pumping to ensure that no vapour or spray from the liquid samples contaminates any of the other chambers. It is the access to these liquid phase targets that most urgently drives the requirement for well optimised gas-phase HHG in our laboratory. A $1360\,\mathrm{Ls^{-1}}$ turbomolecular pump (Pfeiffer ATH1603M) is mounted on the target chamber, alongside a liquid nitrogen cooled cold trap adjacent to the sample delivery region, to minimise the pressure in this chamber during experiments.

5 Implementations of Flexible Hollow Core Fibres for Ultrafast Beamlines

Hollow-core fibre (HCF) broadening is a widely used technique employing self-phase modulation with ultrashort pulses to spectrally broaden and temporally compress an intense pulse, as discussed in Section 2. HCFs are versatile in their uses, allowing for spectral broadening, pulse compression and dispersive wave generation, as well as providing passive spatial mode correction and pointing stabilisation for the emitted pulses. The spatial mode correction comes inherently from the restriction of modes that can propagate through the fibre — any energy not coupled into one of the Bessel modes discussed in section 2.3 will be dissipated at the fibre entrance, and only the energy in those modes will propagate to the end of the fibre. Given that the position of the fibre is fixed, we can infer similar facts about the outgoing pulse: the beam will necessarily be in shape allowed by its propagation through the HCF at the fibre's exit, and the propagation from there will be simply the far-field diffraction of that profile.

As detailed by Travers et al., [23] and detailed in Table 3.1, there are scaling laws which allow us to tailor the *zero dispersion wavelength* (ZDW) of a fibre to allow HCF broadening and *resonant dispersive wave* (RDW) emission wavelength to match experimental requirements. For the pulses required for *high harmonic generation* (HHG), we must seek to maximise bandwidth of the driving *infrared* (IR) pulses to allow for a few-cycle pulse. At 1.35 and 1.8 µm, a single cycle corresponds to around 4.7 fs and 6 fs respectively, or FWHM bandwidths of 615 nm and 800 nm respectively. The primary concern of the works described in this chapter is to develop well tuned and optimised systems for the production of few-cycle IR pulses and UV pulses by replication of recently developed techniques for construction of tensioned HCFs [23, 119], as well as investigating methods to further improve beam coupling or construction methods where possible.

The implementation of an HCF in our laboratory predates the beginning of this project, and the broadened pulses emitted from that system were used to perform the experiments described in [16, 80, 93]. Using the broadened idler of the TOPAS (as outlined in Section 4), photon energies up to 600 eV were recorded from HHG. Reproducing these photon energies, which reach the limit of what HHG systems are capable of at the current state of the art, is both challenging and hard to optimise. This is because they require both the use of transient phase matching and large ionisation fractions. To maximise the flux in these systems, additional energy headroom is always desirable both to increase harmonic cutoff energies and allow the use of larger focal spots, thereby increasing the harmonic generating volume. Optimising the transmission of these HCF systems — as well as optimising the pulse broadening and system stability to avoid unstable white-light generation — is key, and for flexibility of design a tensioned flexible HCF is ideal for this, for reasons that will be discussed shortly.

As mentioned in Section 2.1, optimal compression of a femtosecond pulse can be obtained by creating a soliton in a hollow core fibre [23, 120]. Once a pulse passes beyond the point at which the soliton is formed however, the distance over which the soliton remains stable is on the order of centimetres for a fibres around a meter long. This is a delicate balance, and it is instead more reliable to end pulse compression just before soliton formation, as soliton fission would cause spectral and temporal break up of the pulse that would be detrimental to experimental use.

Additionally, producing solitons would require the pulses to be delivered directly to the experiment with minimal additional dispersion — a difficult feat at the large bandwidths required for such short pulses, and given the complexity of the experimental beamline in question. While it may have been possible with substantial system redesign, the table space and driving laser stability requirements to operate such a system would likely have been beyond what are readily available in our laboratory. Furthermore, while a second fibre compression stage could be used to achieve

optimally compressed pulses, this would require further losses in the process of re-coupling the beam into the fibre; table space to be consumed by this second stage which was simply not available; and design consideration for removal of gas from beamline chambers, which must be kept at low vacuum ($<10^{-5}$ mbar) for generating harmonics.

In short, while these options do exist, they would have required beamline redesign that would have been beyond the remit of this project, and the existing pulse duration optimisation method (bulk compression in fused silica) can already bring pulses down to around a 2-cycle limit while minimising power loss and introducing little additional complication, provided the pulse is sufficiently broadened in the primary fibre stage.

In Section 5.1 work on the broadening and compression of a 1.35 µm, 1.5 mJ laser pulse will be presented, first using home-built tensioning apparatuses, then with elements provided by an external collaborator, culminating in a sub-20 fs compressed pulse in Section 5.1.2. Work in attempts to optimise coupling into HCFs with a deformable mirror will be presented in Section 5.1.3. Results on RDW emission are then presented, first with an external collaborators laser system at Heriot-Watt university in Section 5.2.1, and then in the lab at Imperial College in Section 5.2.2 using the previously compressed 1.35 µm laser pulses.

5.1 Flexible Fibres for IR Compression

Prior to the start of this project, the group's laboratory setups used rigid fibres for pulse broadening [16]. While these do not inherently have worse specification for pulse compression or propagation, they may be improved on by replacement with stretched fibres on the following accounts:

- Any manufactured capillary is prone to defect in production. While these defects are unavoidable, the cost per length of fibre of flexible fibres runs at least an order of magnitude cheaper (£10 per metre compared to £100 per metre)

- Length is a variable in system design. While large scale reorganisation of lab setups is not frequent, changes to the system upstream of the fibre system, for example gains in pulse energy or changes to pulse duration, mean changes to the optimal design parameters for the fibre system. While these can be tuned to some extent using the gas fill pressure, having the option of also altering the fibre length with ease makes flexible fibres preferable. While rigid fibres can be shortened by cleaving, this is a unidirectional process and places a life span on a fibre that, as mentioned above, is not necessarily easy to replace. Precision and cleanness of finish when cleaving rigid fibres are also far less consistent, creating additional sources of loss in the system.

- Adding length as a variable for system design, as well as the ability to freely purchase fibres of various core diameters, allows gas pressure to be used not just to broaden the laser pulse, but also to mitigate ionisation losses and instabilities from white light generation. In doing so, total beam transmission can be increased, improving the energy budget for experiments.

- Swift setup for new designs. Where procurement time for rigid fibres can be weeks, the production time for flexible fibres is on the order of days, and ordering in reels at multiple core diameters means that new fibre systems can be implemented as and when necessary to match changing laser powers and broadening requirements.

All of these factors are useful, as an optimal transmission and broadening in the fibre is necessary for more complex experimental design downstream. Prior to the start of the works listed here, with around 1.5 mJ input energy to the HCF, the emitted

broadband pulse was limited to around 550 µJ. Simulations for the propagation of the beam through hollow capillaries using [72] and performed by the author. We estimate a theoretical transmission of 93% through the fibre using Equation 2.3.6, with a further 5% loss from windows and other beam pick-offs.

To calculate the coupling efficiency η_0 of the beam into the fundamental mode of the fibre we compute the overlap integral between the fundamental Bessel mode and the beam focal spot, given by [59]

$$\eta_0 = \frac{\int_0^\infty \int_0^2 \pi E(r,\theta) e_m^*(r,\theta) r \, dr \, d\theta}{(\int_0^\infty \int_0^2 \pi |e^m(r,\theta)|^2 r \, dr \, d\theta)(\int_0^\infty \int_0^2 \pi |E(r,\theta)|^2 r \, dr \, d\theta)}. \tag{5.1.1}$$

$e_0(r,\theta)$ is the 0^{th} order Bessel function, and $E(r,\theta)$ is the laser field at focus, both of which are a function of angle radial θ and the radial axis r. While for a perfect Gaussian a $1/e^2$ beam diameter of 0.64 times the beam radius gives optimal coupling, the focal spots of beams in use in the lab are never a perfect Gaussians. An example of this can be seen in Figure 5.1.1, where we see a focal spot of a beam from the laboratory.

The fibre this beam was previously coupled in to had an inner core diameter of 450 µm, and for a Gaussian spot this would give us a, ideal focal spot diameter of 288 µm. The ellipticity of the beam, however, means that while the mean diameter of the pulse is close to that value, the coupling would be improved if the spot were 1.45 times larger.

If we take these efficiency values as representative, one would expect a transmission of up to 70%, or around 1 mJ, meaning there is roughly 500 µJ of "lost" power to potentially be recovered. As mentioned in Section 1, current experimental designs aim to use the same pulse for RDW generation as to drive the HHG. Given the high pulse

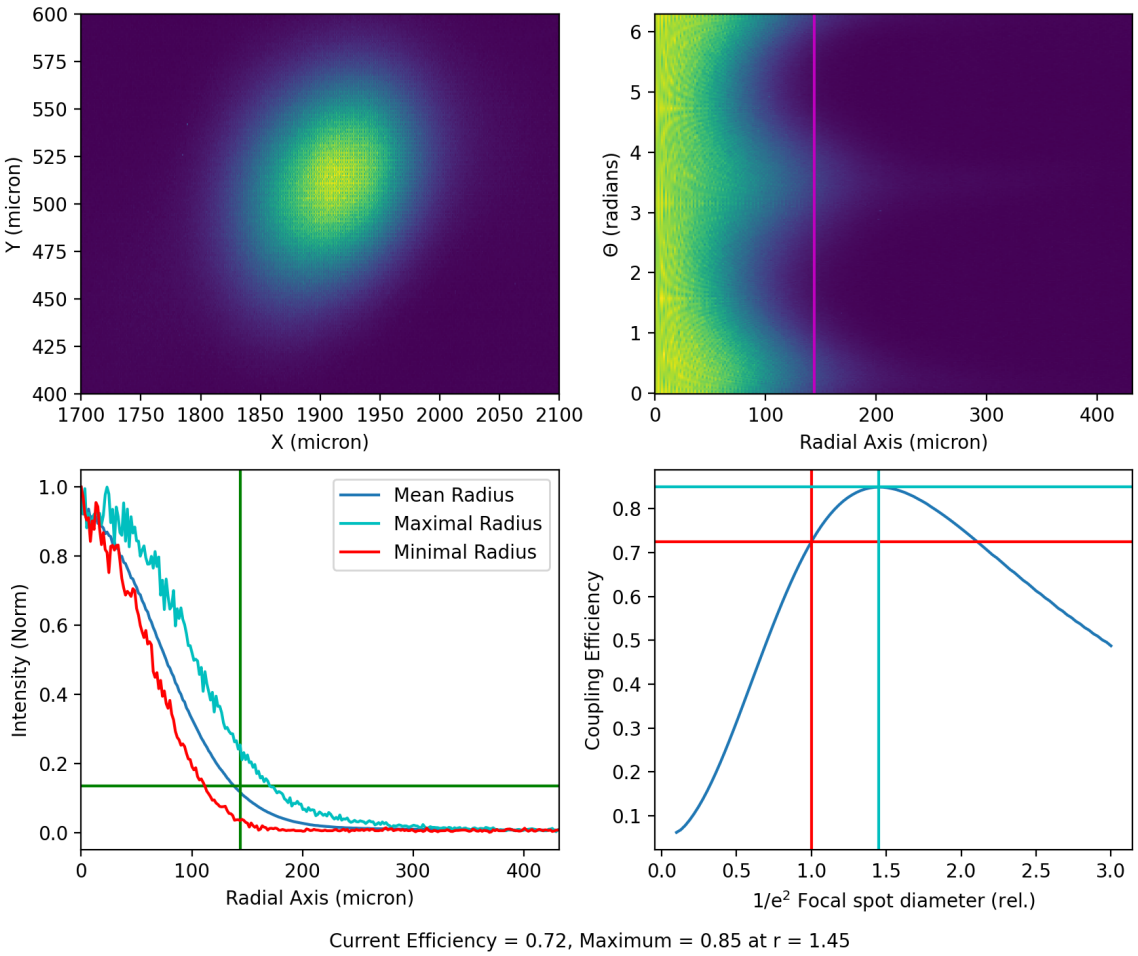


Figure 5.1.1: An example beam spot (top left) that would be coupled into a HCF in our laboratory setting, and that same spot transformed to polar coordinates (top right). The vertical line here indicates the ideal $1/e^2$ radius of the focal spot. This spot is for coupling into a 450 µm inner diameter fibre. The mean, maximal and minimal radii can be seen (bottom left) compared to the ideal for a perfect Gaussian (blue crossing lines). The coupling efficiency can be computed using Equation 5.1.1, and a coupling efficiency of this spot into this HCF can be calculated as 0.72. By simply increasing the size of the spot, one can find the maximal efficiency one could achieve for this focal spot (bottom right), and this can be calculated as 0.85, if the spot were 1.45 times larger.

energy requirements for generating soft-X ray harmonics, extending the experimental energy budget by improving this fibre transmission efficiency is essential.

5.1.1 Implementation of Flexible Fibre Stretching

The construction of systems using flexible fibres requires careful consideration of the capillary's waveguiding effect on the laser. Bending losses for the lowest order fibre modes scale proportionally to the bend radius and the square root of the core diameter, as mentioned in Section 2.3.

Initially, a home-built design was used for mounting the capillary, as seen in Figure 5.1.2. Two aluminium blocks were machined with fittings to allow 5 mm screws for securing KF seals around the end of the fibre. The fibre could then be passed through the opening, sealed from behind by an o-ring on a narrow support, and glued into place on a 20 mm ferrule using a simple two-part epoxy (Araldite Rapide). The ferrule was supported from behind by a simple backstop. The aim of such a simple design was to make the system as easy to produce and reproduce as possible, also minimising cost in the process. By achieving this, one could set up numerous fibre compression systems throughout a lab at low cost (on the order of a few hundred pounds, including machining costs provided the parts remained sufficiently simple) and allow broadening and RDW systems to be established easily.

To achieve sufficient fibre tension, the blocks were mounted on 5-axis translation stages. Hypothetically, this would allow the fibre end to be manipulated to maximise straightness, as well as establishing the requisite tension to minimise bending loss, and would further allow the system to be aligned onto the beam path to optimise the transmission.

The last of these points was drawn from systems using rigid HCFs: while the installation of a fibre can yield high transmission with the beam pointing matched parallel to the fibre at the coupling aperture, this can be a difficult process, and some groups implementing these systems add translation stages below the entrance and exit to allow the fibre to be matched onto the beam. As the final optic prior to a

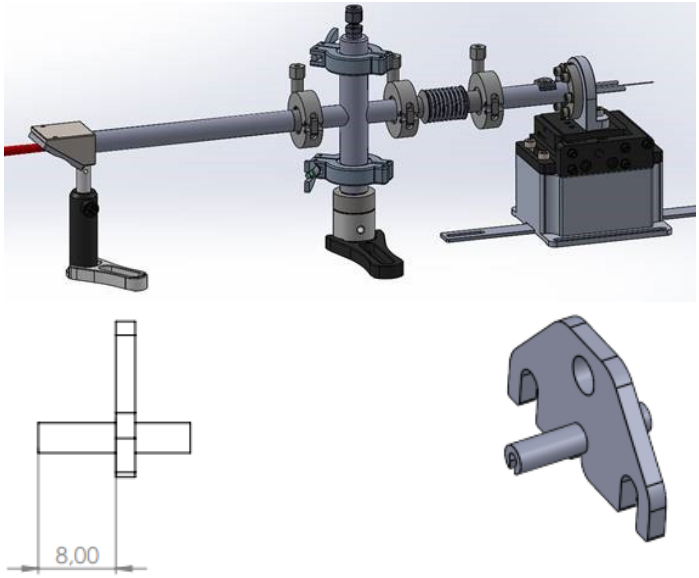


Figure 5.1.2: The designs for a home-built fibre stretching and mounting system. Left : the original design for both sides of the fibre. In these images, the beams are 165 mm from the optical table, and the tubing is 16 mm diameter. The ferrule maintainers used to hold the 2 mm ferrules in place. Images courtesy of Clement Ferchaud.

capillary entrance can often be >50 cm from the entrance, the sensitivity needed for control of the focal spot to match the same level of translational control of a stage with micron-scale adjustment precision at the fibre exit is not possible. Mitigating this discrepancy would accelerate coupling optimisation and could help yield higher transmission. To test the transmission of the fibres using these techniques 450 µm *inner diameter* (ID) fibres were used, and a Thorlabs Green Helium-Neon (HeNe) alignment laser (Thorlabs HGR020) was used with a central wavelength of 543 nm, and measured using a photodiode power sensor (Thorlabs S120VC). Using eq. (2.3.6) we estimate the transmission for these test systems over a 1 m fibre at 99%.

Unfortunately, the implementation of these stages provided the first hurdle to construction in this system. While theoretically one could straighten any kink in the fibre with their use, given the level of precision needed to match exactly the fibre path, simple alignment methods (i.e. visual inspection and adjusting stage positions)

proved ineffective in optimising throughput. Furthermore, in tensioning the fibre, the stress would overcome one of the translation axes of the stages and create backlash in the system, making tensioning the system unreproducible and unreliable, disrupting alignment procedures, and creating a kink in the fibre where the ferrule touched the mounting support.

To eliminate these issues, the stages were exchanged for static stands. This highlighted a new problem- the interface between the ferrule and the rear support. As the ferrule was glued into the end, and bends in the system were no longer being corrected by the translation stage, both sides of the ferrule could no longer be sealed to ensure a good binding to the fibre. Further, the use of epoxy around the entrance of the fibre was creating an issue. The strain induced by the curing of the epoxy as it shrunk and set onto the circular face of the ferrule would create small kinks in the fibre. To overcome this a small modification was made to the ferrules, opening a small square window at the centre on one side, as seen in Figure 5.1.3. This would allow the fibre to be glued directly into the machined channel without risking the capillary shifting while the glue cured.

This method, unfortunately, also proved insufficient for achieving sufficient fibre straightness. Keeping a single translation stage for the second mount maintained the issue of finding a stage position that optimised transmission. Replacing both translation stages provided no way to correct for the fine difference in the placement of the fibre blocks on the table, causing an inherent bend, as well as creating the need to manually tension the fibre by pushing the mounting stands apart. In both of the above cases the transmission was below 20% and the mode quality was very poor, with the beam clearly not matching a Gaussian profile on transmission visually.

Rather than continue exploring the design space for the system, through a collaboration with the Travers group at Heriot-Watt University, a new cell design and fibre implementation was acquired. Here, two large aluminium cells are manufactured to

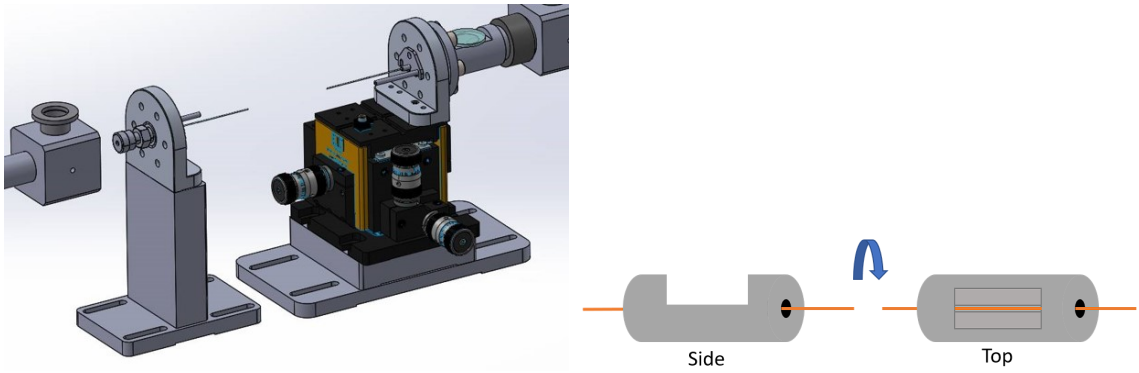


Figure 5.1.3: The modified designs for a home-built fibre stretching and mounting system. Left: After initial attempts to stretch and couple beams into a system with two 5-axis translation stages, one cell was swapped for a static mount, and the second exchanged for a 3-axis translation stage, to reduce system complexity while maintaining options to stretch the fibre in-situ. Image courtesy of Clement Ferchaud. Right: The modified designs for the machined ferrules, with a rectangular opening over the centre to allow stable mounting of the fibre and reduce bending from the glue.

allow a perspex lid to be screwed on, and a mounting chuck to be placed into the system, as seen in Figure 5.1.4. To mount the fibre in these cells, the fibre is first glued using UV-curing glue (Norland Optical Adhesive 81, NOA81) onto two stands exterior to the length of fibre that will be implemented, which is then tensioned, glued onto the chucks in the cells, and the fibre is then cleaved. This particular glue was selected for its strong adhesion to glass and metallic surface, and a UV LED was used for curing the adhesive (Thorlabs CS2010, 365 nm). The UV-cured glue has a shrinkage of $\leq$1.5 % (values of $\leq$0.2% have been suggested for this particular glue, however data for this was not available), compared to standard shrinkage values for two-part epoxies of up to 8 % [121, 122]. To cure the glue in any instance the lamp was set to full power and suspended above the fibre chuck at a distance of approximately 5 cm while the glue was left to cure for approximately 10 minutes.

Because the fibre is first tensioned at points outside of the chucks, it can be guaranteed that the capillary will be completely straight. Rather than using translation stages to tension the fibre, tension was applied by hand, with the limit of tension clear to

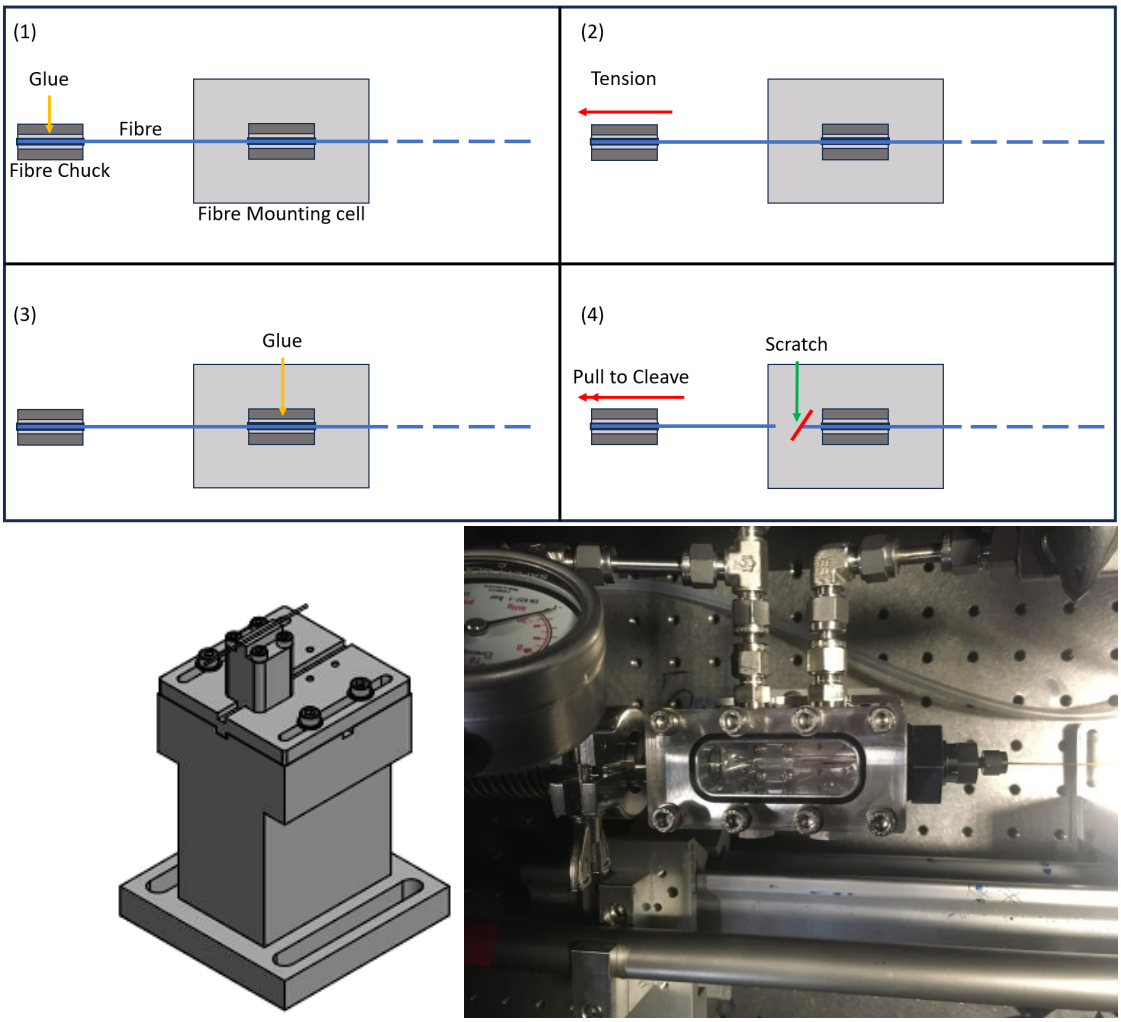


Figure 5.1.4: Top: The schema for mounting the fibres in the cells provided by the Travers group. We see that the fibres are first fixed at points exterior to the length of fibre needed for experiments and tensioned by hand, and the fibre is fixed onto the central chucks. The red arrows direction of motion for the external chucks, and the orange line indicates where a ruby scribe is used to gently score, but not cut, the fibre to cleave. Bottom Left: One of the stands used for mounting exterior to the fibre cells. A base plate is included under the cell to ensure all four chucks in the system are held at the same height. Image courtesy of Christian Brahms. Bottom Right: A fibre mounted in one of these cells.

a user when the fibre was taut. To verify this, this pieces of material, such as a lens tissue or a thin strip of paper could be moved across the middle fibre, which should not bend or move on contact when suitably taut.

This method was used for all the fibres systems listed in this thesis, and also highlights the issues with the previously discussed design. In giving the fibres an external point of contact and tensioning the fibres prior to fixing it into the experimental system, it could be guaranteed that no kinks were introduced to the stretched fibre. While the exterior gluing system was then attempted with the home-built system, it appears that the main issue lies in the contact of the ferrule to the rear support. While these can both be machined as carefully as possible, a bend can easily be introduced when screwing the support into the rear face of the mounting block, or as a result of the tension of the fibre pulling on the ferrule after tension is released from the exterior gluing points.

5.1.2 Broadening Near-IR Pulses using HCFs

Currently, to simulate the propagation of these pulses in order to estimate maximum transmission and compression, a Marcatili Mode propagation model, provided by collaborators is used [72]. The code solves the used generalised nonlinear Schrödinger equation described in section 2.3, with the wave propagated using split-step propagation [123]. These simulations have previously been experimentally benchmarked and used for calculating and reproducing soliton fission lengths in IR and RDW pulses [23].

To understand the range of output pulses from the fibre system, simulations were first run for an idealised, temporally Gaussian pulse at 1350 nm, 1.5 mJ, 65 fs with no higher order phases (chirp or third order dispersion, TOD). The free variables in this system are the fibre core radius, fibre length and gas pressure. Figure 5.1.5 shows the temporal bandwidth of pulses generated by this fibre while scanning over gas pressure and fibre length with a uniform gas load, and the spectral broadening achieved in a fibre with a 0.8 bar Ar gas load on the rear cell, and a scroll and turbo pump reducing the pressure to 1 mbar in the front cell. The Fourier transform limit (FTL) of these pulses can be calculated by Fourier transforming the pulse and calculating the full-width at half-maximum (FWHM) of the temporal profile in the time domain.

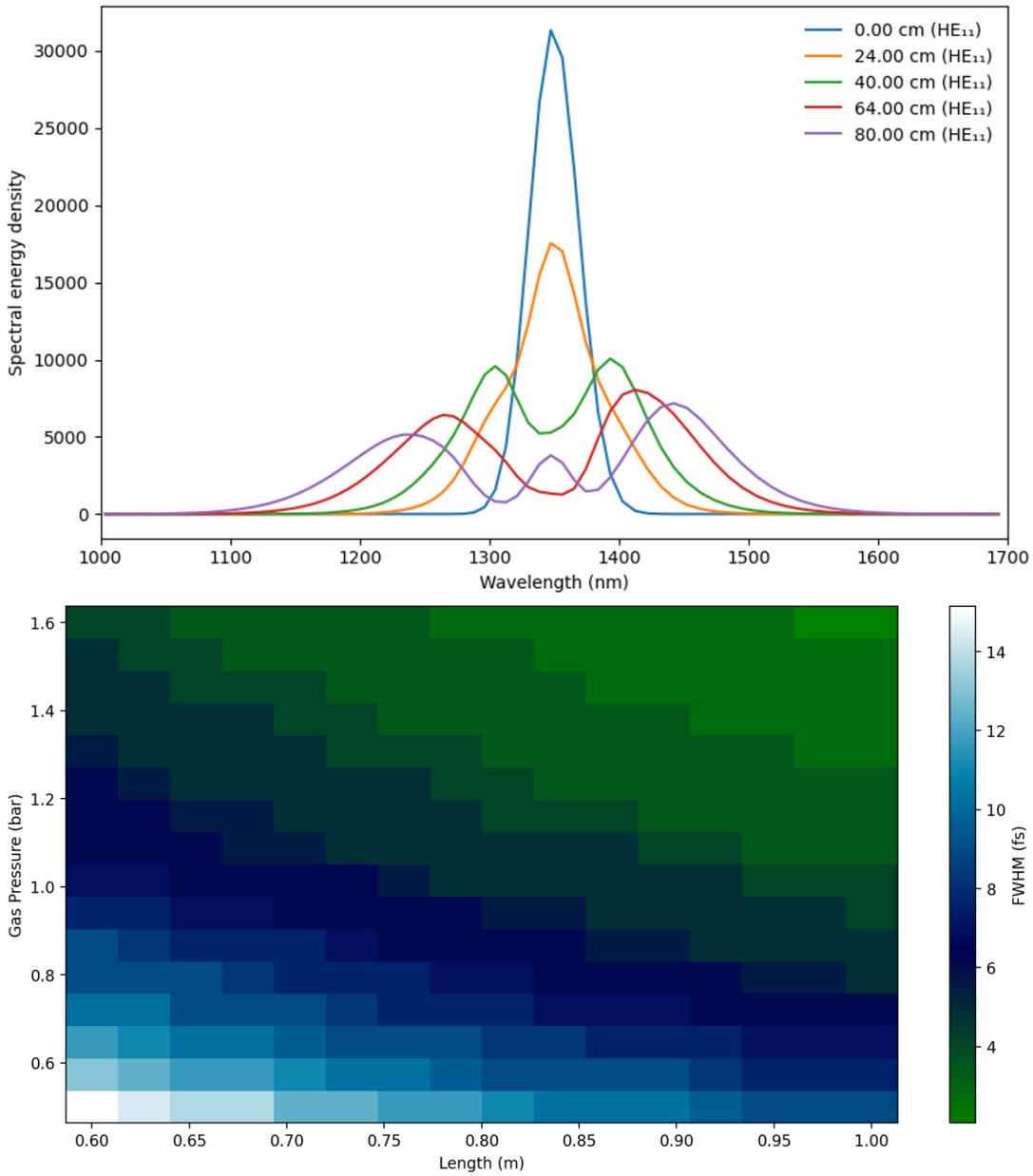


Figure 5.1.5: Above: The spectrum of a 65 fs, 1.5 mJ, 1.35 µm central wavelength laser pulse propagating in a gradient-filled gas fibre with the front and back ends held at 1 mbar and 0.8 bar respectively. The 300 nm spectral bandwidth here corresponds to a 9 fs FTL. The non-Gaussian spectral profile is normal for beams undergoing SPM and XPM, and stems from the fact that the spectral broadening is driven by the gradients of the spectral intensity profile, as described in Section 2.3. Below: Simulations of the fibre parameters for highest bandwidth, scanning through pressure and length.

As the optimal transmission from the fibre can be found at vacuum, we see in Table 5.1 that reducing the diameter beyond 450 µm results in substantial losses. Also, in increasing the core diameter we must increase the gas load to achieve equivalent laser broadening. According to Section 3.2, we see that an increase to the next available core inner diameter, 700 µm, would require a pressure increase of 72%, for which the window thickness would need to be increased to avoid breakage.

ID (µm)	Transmission @ 1.8 µm (Norm.)	Transmission @ 1.4 µm (Norm.)
320	0.71	0.81
450	0.88	0.93
530	0.93	0.96

Table 5.1: A table of normalised pulse transmissions though an evacuated fibre with standard inner diameters as listed in the Molex Polymicro standard capillary tubing stock, the supplier used for the fibres in this thesis.

For a pressurised window of length L and width W, a minimum thickness T_{min} for a given gas pressure difference across the window, P, can be defined by defined by [124]

$$T_{min} = L\sqrt{\frac{K_s K_u F(1+R^2)}{2P}}, \tag{5.1.2}$$

where K_s is a safety factor and K_u is an empirical constant set at 0.75 or 1.125 for clamped and unclamped windows (i.e. windows with flexure at their edge mounting, such as with o-rings) respectively. F is the rupture modulus of the window material, and $R = L/W$. In this case a pressure difference of 2 bar is necessary and the industry standard safety factor of 4 is applied. This safety factor is a measure of the multiple by which the pressure on the window could be exceeded before it would be expected to rupture, and is a measure used in safety factor calculations in science and industry [124]. The maximal beam diameter, considering a minimal diameter of 6 mm on the

window from empirically obtained damage limits and a Brewster angle of $\sim 55°$, is 11 mm. A minimum thickness of 0.6 mm is calculated, and so the standard thickness of 1 mm is used for the fibres at 530 and 450 µm.

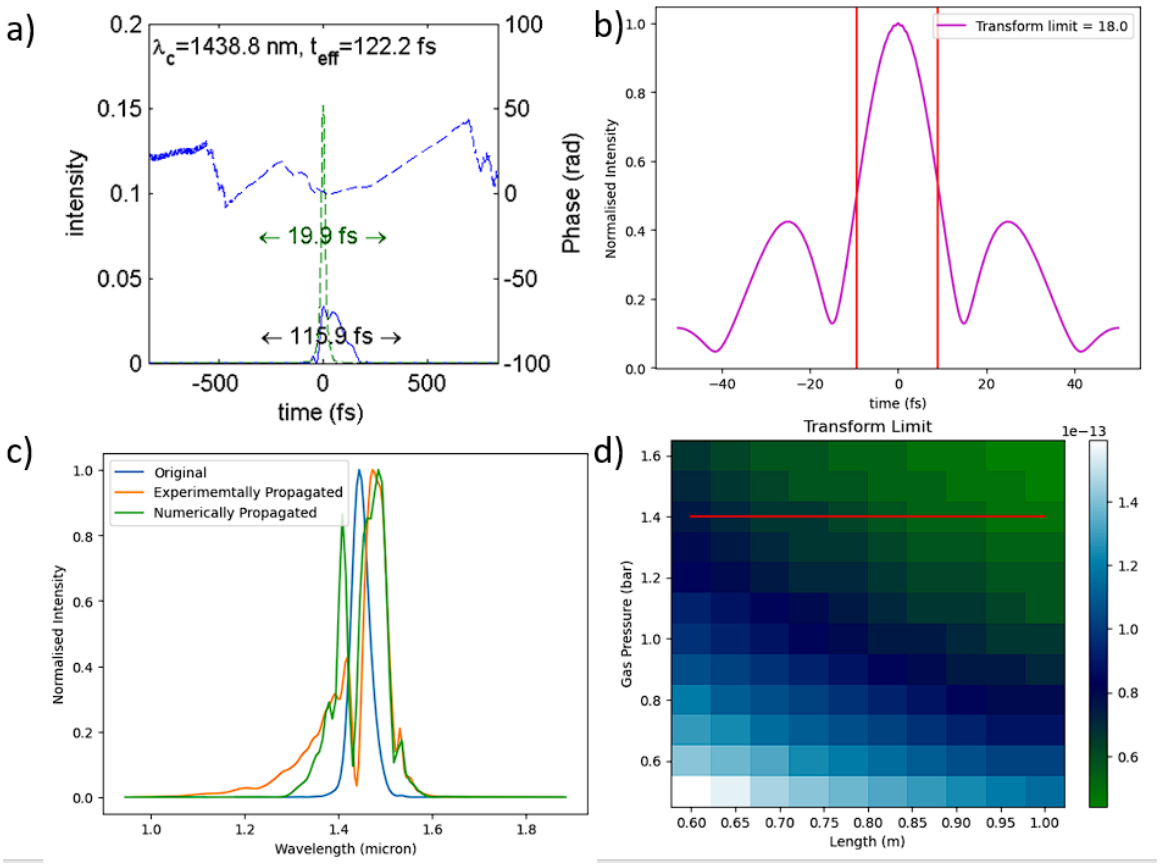


Figure 5.1.6: Simulations of the emitted pulses from the fibre. a) The measured transform limit of the pulse through the 0.85 m fibre.This length is chosen by limit of table space, and parameters are chosen to optimise spectral broadening while avoiding unstable white-light generation. b) The Fourier transform of the spectrum of this simulated pulse with initial conditions for the pulse set by experimental retrieved from the SHG-FROG shown in Figure 4.4.2. The FWHM of this trace gives us the bandwidth-limited duration of the pulse. c) A comparison of the simulated and experimentally obtained spectra with a 1.0 bar rear fill, with the front cell pumped down to 40 mbar d) A parametric scan of the length and gas fill pressure in the fibre, showing the pressure limit of the fibre system before the critical power for self-focusing, as given by Equation 2.3.10, would be exceeded.

Considering the table space limitation of the laboratory, a larger core diameter is impractical. Not only would the gas pressure need to increase by 72%, but as a longer focal length lens would be needed, leading to a longer tubing for the window mounts to prevent burning (a longer focal length leads to a smaller beam diameter at equivalent distances from the focal spot). As such a wider open aperture on the window would be needed. Given a roughly linear scaling of the beam power with the focal length, a 30% increase in window size would be needed to accommodate this, and combined with the pressure increase this leads to a minimum window thickness of 1.2 mm, corresponding to a commercially available window of 2 mm.

While increasing the tubing length listed here is impractical as it would push the system beyond the reasonable limit of the available table space for practically being able to align the laser and operate the system, not increasing it and increasing only the window thickness to allow wider beam diameters on the windows in turn imparts greater phase and B-integral effects. Without increasing the tubing length, not only does the damage risk to the window increase substantially, but the B-integral increases from around 0.3 to around 1.9, putting the beam in danger of self-focusing with the natural fluctuations of the laser. To avoid this, an upper limit of 530 μm is maintained when considering the construction of these systems. The trade off for this, however, is that in the alignment of the bean into the fibre, the window diameter and tubing diameter limit may also cause clipping of the beam, a small amount of which was present in this system but was not consistent as it fluctuated with the beam diameter and pointing of the idler when leaving the TOPAS.

The fibres for spectral broadening here were designed with a "gradient fill" of gas where the front cell was pumped down to few-millibar pressures while the back cell was filled to a target pressure. This is to mitigate ionisation as the beam is focused into the fibre, as otherwise this ionisation can lead to coupling instabilities (as opposed to a "static fill", where the front and back cells are held at the same pressure, which is more commonly used at lower pulse energies).

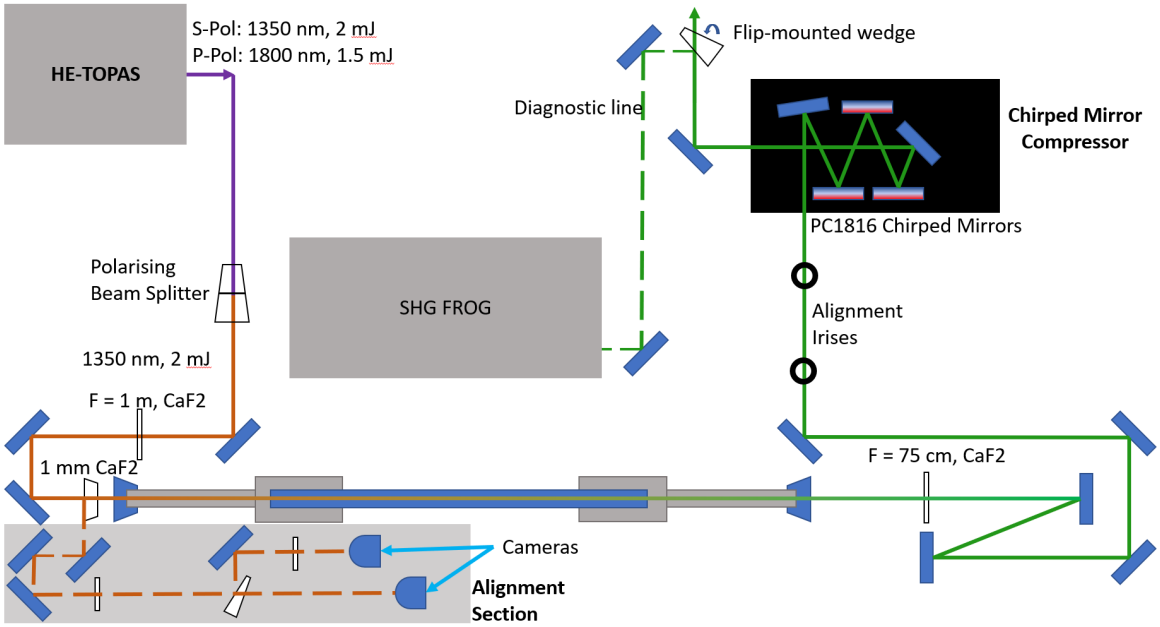


Figure 5.1.7: Compressor design at 1350 nm, including chirped mirror compressor and diagnostic line to the SHG-FROG. The number of mirrors in the chirped mirror compressor was varied according to the third-order phase of the pulses from the fibre. The alignment section was vertically below the fibre area, as the polarisation of the signal beam required that the windows and pick-offs be tilted to send reflections in the vertical place.

A full compressor was then constructed for the 1350 nm TOPAS signal beam using these coarse simulations to identify an approximate region for best gas fill pressure and fibre length. A finer scan was then run using the FROG traces of the driving laser field in the simulation, as seen in fig. 5.1.6. This procedure was only carried out for the signal pulse as this was to be constructed within the duration of the project. Using the results from the above simulation, the fibre was constructed as seen in fig. 5.1.7. An optimum transmission was observed at 1.0 bar, with a throughput of 700 to 750 µJ (50% transmission) through a 530 µm ID fibre, which was then compressed down to transform limit using a chirped mirror assembly and characterised using the SHG FROG. The chirped mirror assembly consisted of 4 – 6 reflecrtions from chirped mirrors imparting -100 fs^2 GDD per reflection (Ultrafast Innovations complimentary pair PC1708_RC2_L and PC1708_RC2_R), with an output coupling mirror on a rail

to allow a variable number of bounces depending on the chirp of the broadened pulses.

In conclusion, a transmission of 50% was achieved through a 530 µm ID fibre for 1.5 µJ, 1350 nm, 60 fs laser pulses, which were then compressed to sub-20 fs using a chirped mirror assembly. While this does not reach the 70% theoretical transmission limit through the fibre, a number of factors have been identified that contribute to this, including focal spot quality and clipping on the entrance aperture of the Brewster window assembly, but cannot be rectified as their source is due to fundamental elements of the beamline (the focal spot quality after the OPA, source laser stability, and available table space). A number of in-house methods were tested for tensioning hollow capillaries for ultrashort pulse broadening, and it was found that post-gluing tension was ineffective at creating a transmissive fibre system. Instead, cells from the Travers group at Heriot-Watt were used for this setup, and as such were used, either directly or as a template for in-house cells, that appear in the following sections.

5.1.3 Optimisation of Fibre Coupling

As discussed in section 5, the coupling of a beam into an HCF is highly dependant on the mode of the the beam, and optimal coupling comes from a $J_{1,1}$ Bessel mode focal spot. A $J_{1,1}$ beam could be described as a "clean" Bessel mode. Unfortunately, the beam profiles of many OPA's are distinctly "messy", as seen in fig. 5.1.8. One option for "cleaning" these beams is the implementation of a spatial filter, commonly in the form of focusing the beam into a pinhole or coupling into a short stretch of optical fibre. These methods however, as implied by the name, function by filtering out unwanted spatial components of the beam, and thus lead to energy loss.

As capillary fibres are used for pulse broadening and compression, and the transmitted pulses are used for HHG and RDW generation, minimising loss is essential. Furthermore once a beam has coupled into a fibre, any non-linear optical effects are highly energy-dependant. Minimising the instability of a beam coupled into a HCF

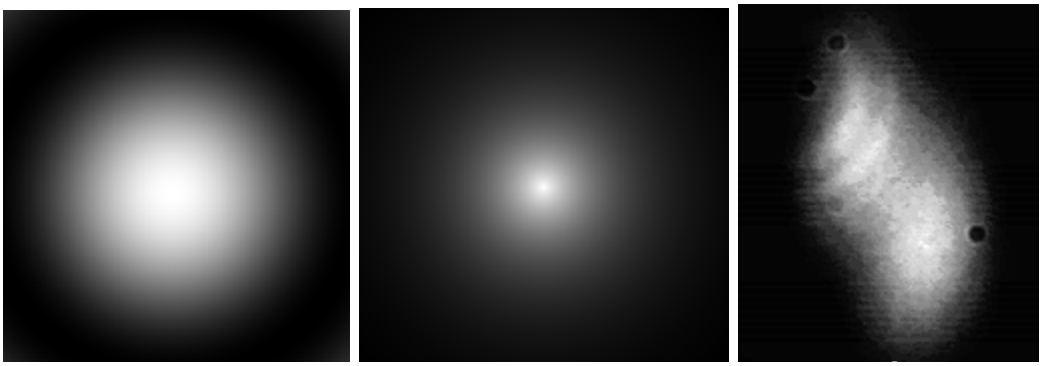


Figure 5.1.8: The ideal (Bessel) beam mode for coupling into a fibre (left), an ideal Gaussian mode that one could hope to achieve from a laser system (middle) and an example focal spot of the OPA output beams found in the laboratory (right).

is therefore essential, as one always seeks a spectrally reproducible and stable source for laser spectroscopies.

An alternative method of mode cleaning is the use of an adaptive optic to alter the spatial profile of the beam such that at focus it is a $J_{1,1}$ beam. In order to do this, we use a 40 segment deformable mirror, as seen in Figure 5.1.9.

Prior to considering use of these mirrors, one must be aware that, as the surface of these optics are not flat, they can create space-time coupling in the pulse, as the distances travelled by separate sections of the beam vary. For the Thorlabs DMP40/M-P01 mirror used here, the maximum stroke distance of a given actuator is 8 µm. This is equivalent to ≈53 fs. There are two key aspects, however, in which this temporal stretching is mitigated: first is that, once the beam is coupled into the fibre, these spatial inhomogeneities are essentially "smoothed" by the symmetry conditions of the propagation of the pulse in the fibre, and the output pulse will be a cylindrically symmetric combination of Bessel modes according to the coupling into the fibre. Secondly, the range of the actuators can be limited, and the maximum temporal stretch can be easily estimated using the linear relationship between applied voltage and deformation. These limitations will necessary in any case as excessive beam

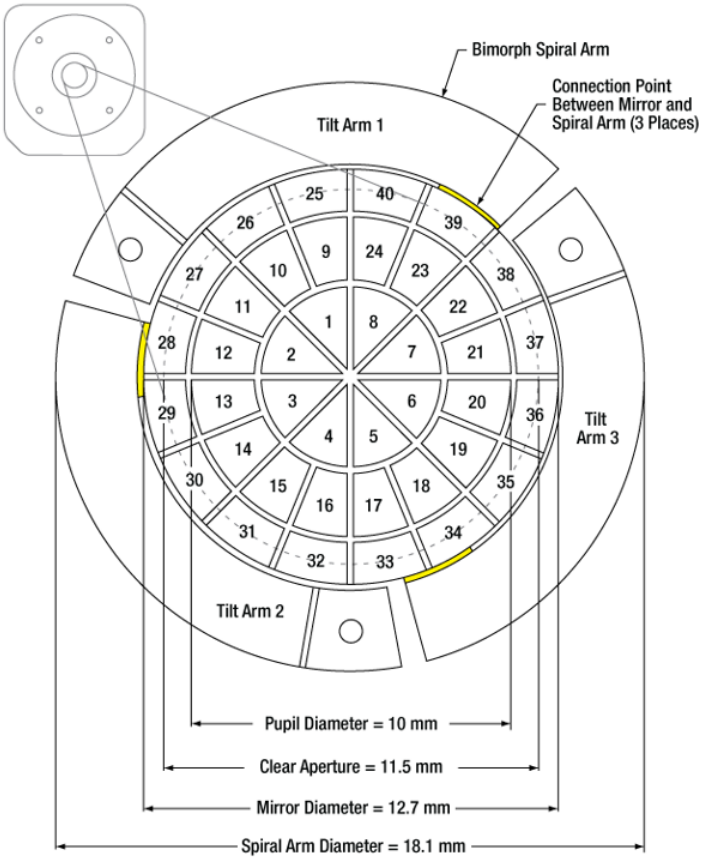


Figure 5.1.9: A schematic diagram of the deformable mirror used for this proof-of-principle study (Thorlabs DMP40/M-P01). Reproduced from [125].

steering will prevent the beam from coupling into the fibre. A maximum of $\pm 1.6\,\mu$m actuator motion is used for this purpose, limiting the temporal stretch to 10.7 fs, less than the 65 fs duration of the pre-compressed pulse. While the temporal phase that could be added by this mirror could be detrimental to the overall compression of the beam, this would be a factor to diagnose and consider once the coupling optimisation had been carried out.

With a 40 segment mirror the spatial profile can be significantly reshaped, but to individually tweak each segment would be very time consuming. While often adaptive systems use Zernike polynomials to adjust the beam, an accurate characterisation of the Zernike decomposition of the pulse requires a shack-Hartman sensor (>£3000).

If these costs can become avoidable then the control of these systems can be greatly advanced. Furthermore, as the spot shape complexity increases, Zernike polynomial methods increase in adjustment time, and can need to be recalibrated if the beam incident on the mirror drifts, as is often the case in high average power lasers where thermal energy accumulated in mirrors can cause beam drift.

Additionally, rather than simply optimising beam transmission, the coupling of the beam into the fibre can be used to manipulate nonlinear phemonema, such as those induced by the coupling the parts of the beam into higher order Bessel modes by over- or under- focusing the beam, for example [63]. While these goals cannot be simply fed into commercial wavefront-correction software, an algorithm with suitably defined success criteria can be used to optimise the transmitted beam according to customised fitness conditions.

To this end an evolutionary algorithm was written to adapt and test a random walk of possible mirror configurations through limited ranges of the deformable mirror actuators. While machine learning algorithms are often used for iteratively learning to solve problems in large parameter spaces, the day-to-day variation in focal spot shapes from OPAs can be large. To have a learning algorithm trained to optimise each of these would require a large training set and would require retraining any time sufficiently new spots had to be adapted.

We know that optimised coupling into an HCF depends on achieving both an ideal focal spot size and beam shape at the point of the fibre entrance, and will result in an optimised transmission. A success metric must be designed to combine all of these into a single value. While they could be separated, optimisation of each metric in series would be needlessly time consuming as the algorithm can be given any arbitrary function to optimise. We may also add in a stability and broadening metric for the spectral bandwidth as these are critical to the downstream function of the beamline.

The optimisation of the power and spectrum of the beam are continuous and unbounded beyond the theoretically maximal transmission of the beam. While the algorithm will seek to escape local minima, unless a target value for transmission and spectral stability or bandwidth are provided the optimisation routine could run indefinitely. With all of the above in mind, an optimisation protocol with the following properties were chosen:

1. The maximum deformation of elements of the deformable mirror are limited after manually examining the variation of the focal spot with mirror voltages.

2. After running a brief optimisation of the beam's focal spot size without the beam coupled into the fibre, a full optimisation can be run to achieve ideal coupling into the fibre, with the first generation of parents centred around the result of the initial optimisation.

3. A single metric for the focal spot size and shape must be constructed for feedback to the algorithm.

4. A target power and spectral bandwidth are be provided for the pulse.

5. There is no memory of previous generations beyond the survival of the top 25% of parents from the previous generation.

A proof of principle test was run for an algorithm with these properties. Unfortunately, while the response time and adjustment rate could be maintained a few the 100-Hz level, the mirror system system, not being based on zernike polynomial methods for adjustment, reached its limit due to fundamental instrument limitations. When slowly varying mirror actuator values to minimise polynomials, the step size between measurements is small, and strain across the surface remains low. As the step size increase however, the large jumps in actuator positions appear to create tension

gradients across the mirror surface, which took longer to dissipate, as the actuators had to make larger corrective motions to compensate for a larger step size. In the case of the mirror used for this study, a settling time on the order of a second could be seen for jumps changing the configuration of multiple actuators approximately 1/4 of the dynamic range of the mirror.

These limitations could possibly be overcome using least-distance sorting algorithms for the mirror configurations to minimise relaxation time. To implement this, however, a comprehensive study would need to be performed on the relation between actuator motion, relaxation time and response rate of the system, which was beyond the limits of the study for this thesis.

The work on this beam optimisation system was stopped for two main reasons. Firstly, efforts needed to be focused on building the signal compressor system, as this had consumed considerable time and was the main focus of lab development at the time, as it would enable the HHG and RDW developments to be independently progressed. Secondly, it was clear that instrument limitations were the bottleneck to development, and to continue this work a number of iterative studies would need to be performed characterising the instrument.

In particular, the settling time for any given step size would need to be calibrated, and factored into the waiting time and permutation order for the deformable mirror. Unfortunately, given the time constraints of the project, implementing these adaptions was not possible. While attempts were made to couple the a clipped alignment diode and a highly attenuated copy of the Ti:Saph laser output into an HCF, the results were highly inconsistent, and the mirror deformations would would often decrease the coupling after the relaxation times had occurred, as the reshaping of the beam in this settling period was unpredictable.

As a result, the deformable mirror was not used to couple the high-power beam into HCFs. If this were to be implemented, one would also need to account for the shift in the beam during these pointing during the deformation process, as this could easily damage the entrance aperture of the fibre. To rectify this a shutter with a repetition rate dictated by signals from the algorithm as to when the beam has settled would be necessary, as the stabilisation control of the input pointing to the fibre can be utilised here to compensate for shifts in the focal spot position while the beam shape settles.

5.2 Resonant Dispersive Waves: A Tunable UV Source for Pump-Probe Experiments

As seen in Section 2.3, the generation of UV pulses using RDW is highly tunable. For transient absorption experiments in liquids, targets with strong absorption and UV-induced femtosecond dynamics in the range of 250 - 370 nm have been considered ($CaCl_2$ at 287 nm to 2-adrithiol at 367 nm), though RDW emission has previously been observed down to 200 nm and as high as 450 nm [23].

RDW systems typically have a few-percent conversion efficiency, and, as will be discussed further, in the current configuration of the experimental beamline losses of up to 50% are anticipated between UV generation and the experimental target, meaning that to achieve 1 μJ pulse energies on-target requires 2 μJ after any spectral filtering. Using the 1350 nm laser source constructed in Section 5.1, a 600 μJ, few-cycle pulse is available, meaning that even at 1% generation, headroom would be available to provide necessary energy for experiments.

5.2.1 Data Collected with Heriot-Watt's Laser System

As a proof-of-principle experiment, a static-fill RDW system was constructed at Heriot-Watt university as part of a collaboration with the Travers group, who have previously demonstrated the implementation of these sources [23]. To drive these

pulses, a 12 fs, 1800 nm IR pulse was generated using the idler of a TOPAS, propagated through a 3 m, 450 um diameter, Argon filled HCF, attenuated using a Brewster angle reflection from a silicon window and passed through a polariser, as seen in Figure 5.2.1.

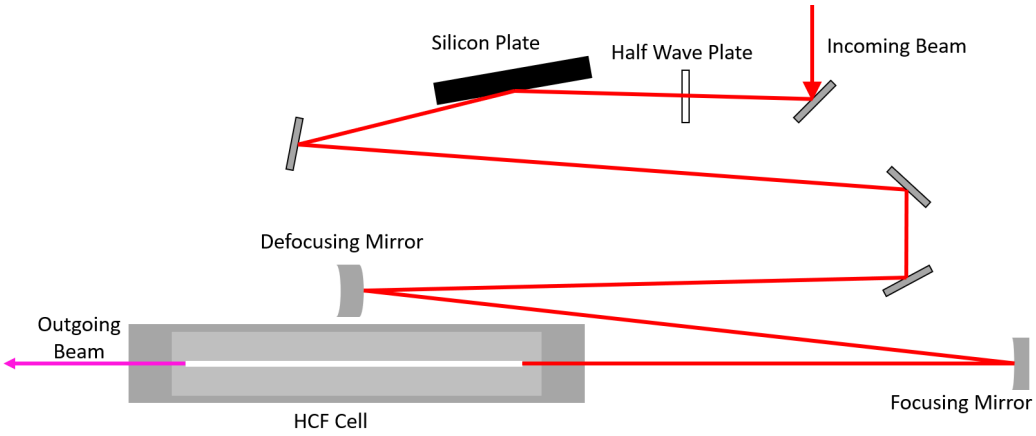


Figure 5.2.1: A layout of the RDW generation setup used for proof-of-princple experiments at Heriot-Watt university. As a range of focusing optics, HCF core sizes and lengths were used, these numbers are omitted here. The combined effective focal lengths achieved by the two-optic focusing assembly were on the order of around 28 and 42 cm for 100 and 150 nm fibre core diameters respectively.

The pulses were characterised with a *polarisation-gated FROG* (PG-FROG) and measured using a pair of IR and UV-Visible (Avantes Avaspec) spectrometers combined using an integrating-sphere with a calibrated energy response to verify spectral intensity data with a power meter. This system was used to generate pulses from 230 – 400 nm, as seen in Figure 5.2.2 and Figure 5.2.4, with fibres at 150 and 100 μm core ID.

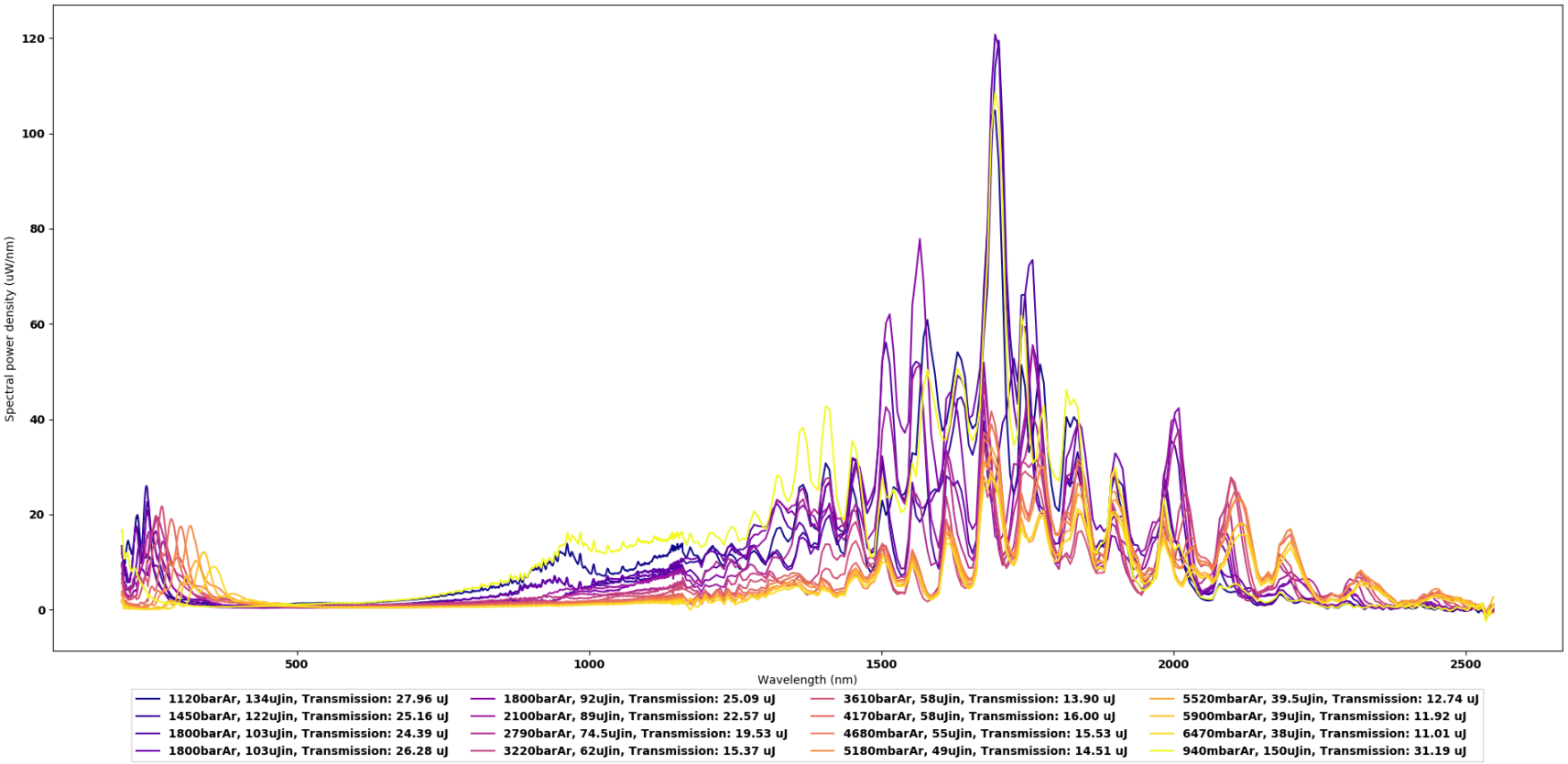


Figure 5.2.2: The full pulse transmitted through a 150 µm core ID HCF. The IR pulse, centred at 1800nm has been significantly broadened, and the UV can be seen, with its magnitude relative to the IR driving pulse clear.

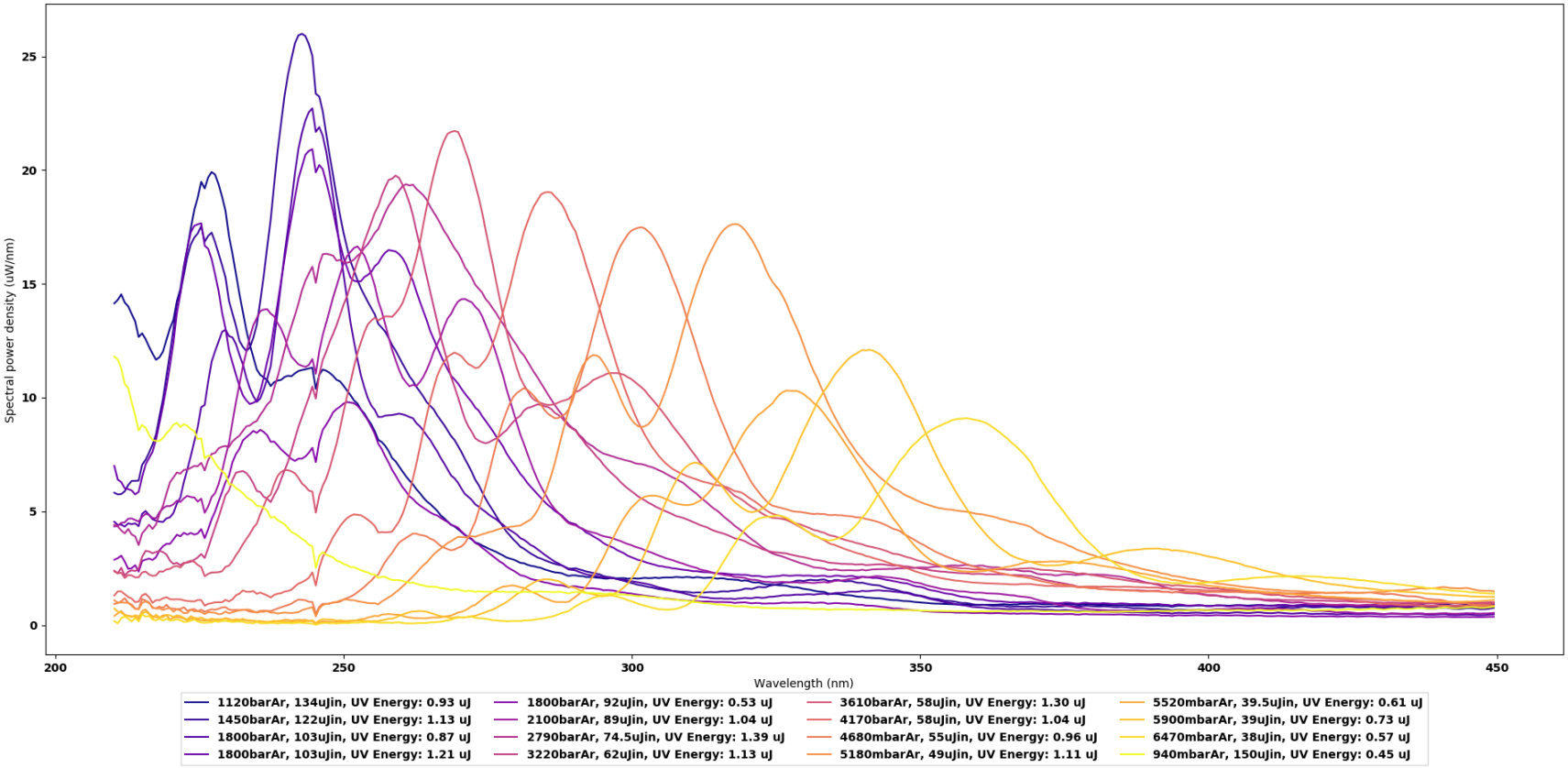


Figure 5.2.3: A cropped view of the UV pulses emitted from the HCF shown in fig. 5.2.2, with values for the integrated transmitted UV spectrum provided.

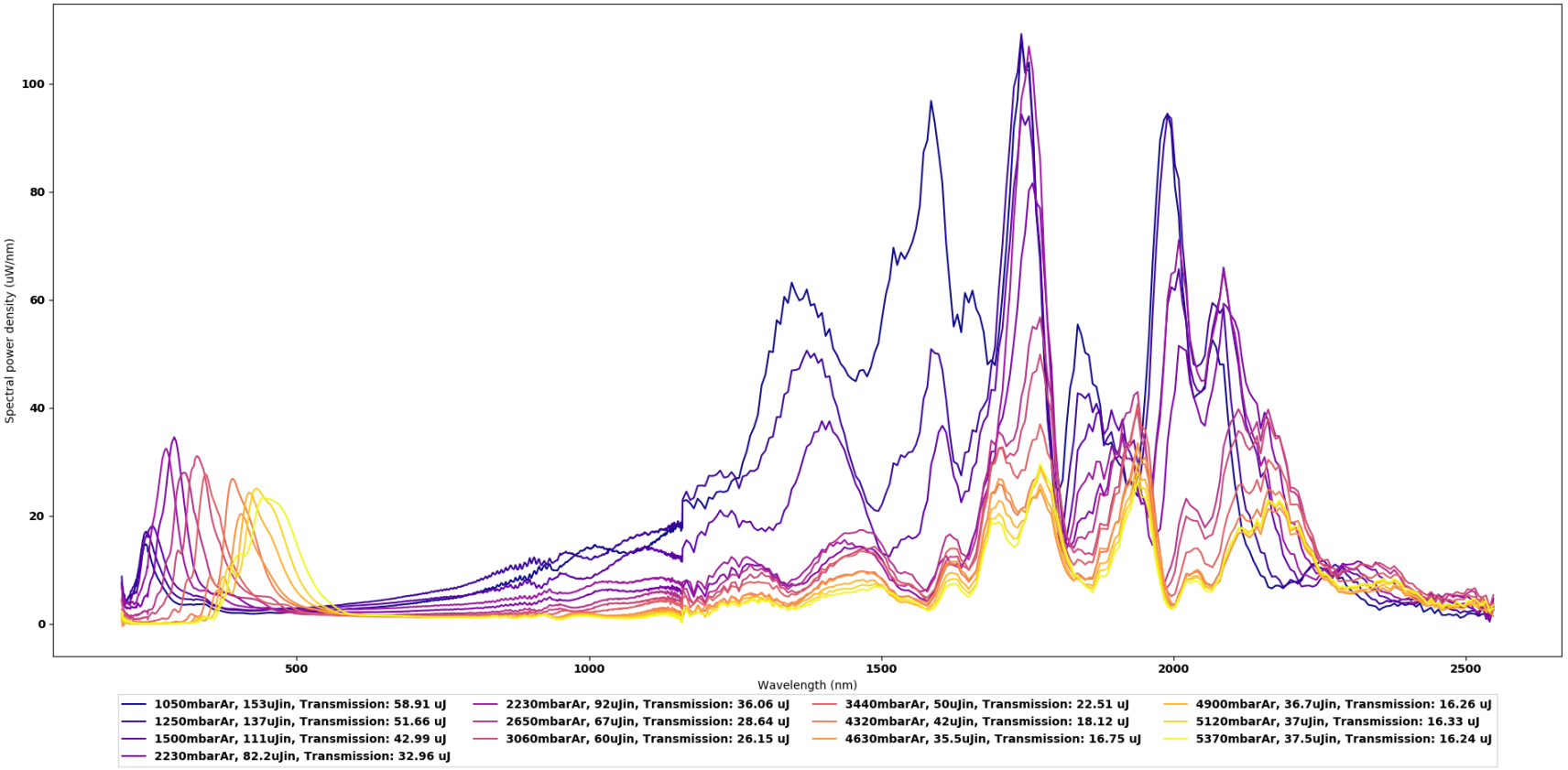


Figure 5.2.4: The full pulse transmitted through a 100 µm core ID HCF. The IR pulse, centred at 1800nm has been significantly broadened, and the UV can be seen, with its magnitude relative to the IR driving pulse clear.

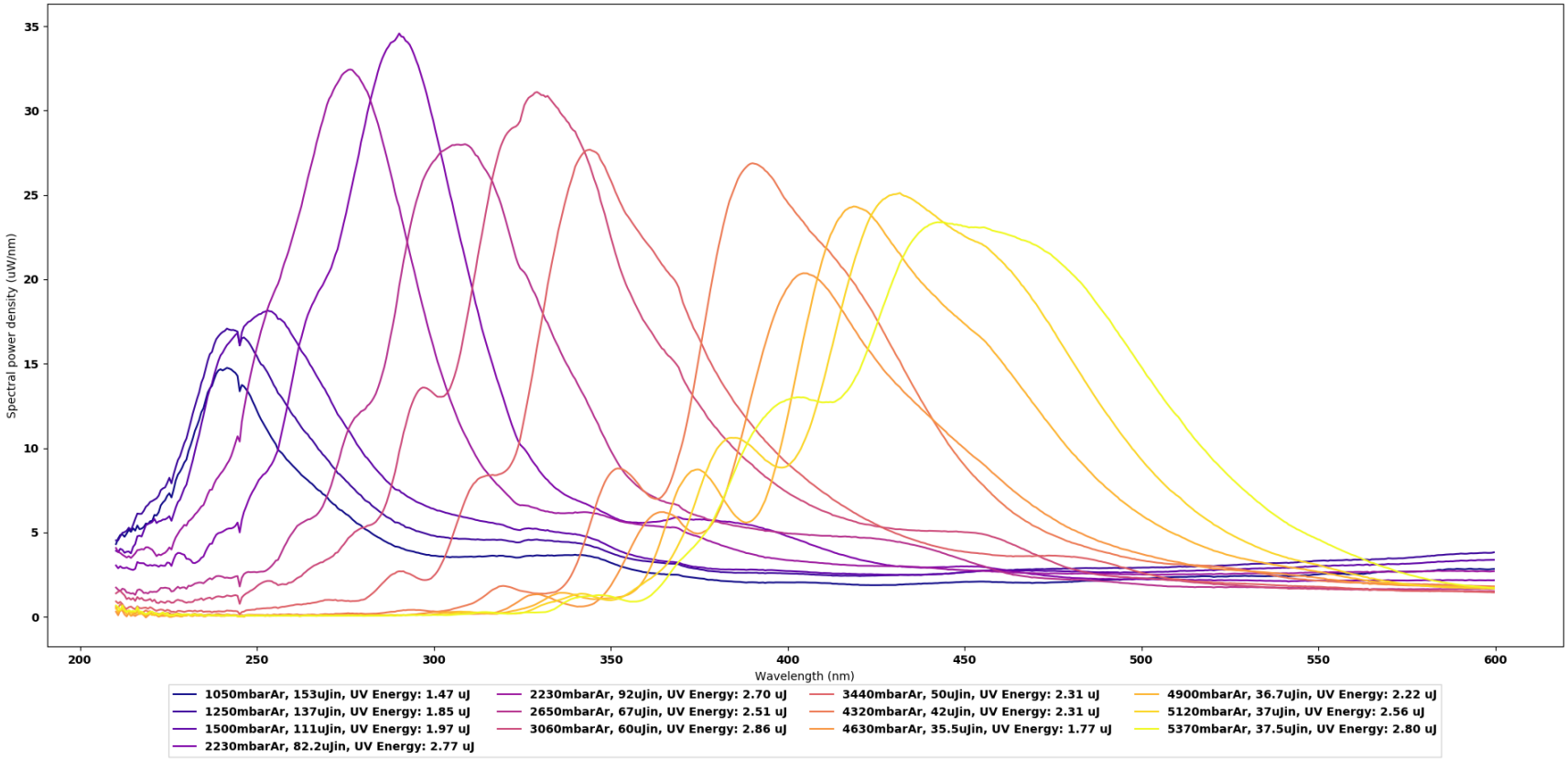


Figure 5.2.5: A cropped view of the UV pulses emitted from the HCF shown in fig. 5.2.4, with values for the integrated transmitted UV spectrum provided.

5.2.2 Construction of a Vacuum-Coupled RDW Source

For the experiments at Imperial College, a new fibre system, with the ends housed in individual cells was constructed as seen in Figure 5.2.6. This design allows a high pressure gas fill (up to 8 bar) at the entrance with the exit held at 10^{-3} mbar allowing the cell to be connected to the beamline chamber shown in Figure 4.5.1 without compromising the vacuum level necessary for HHG.

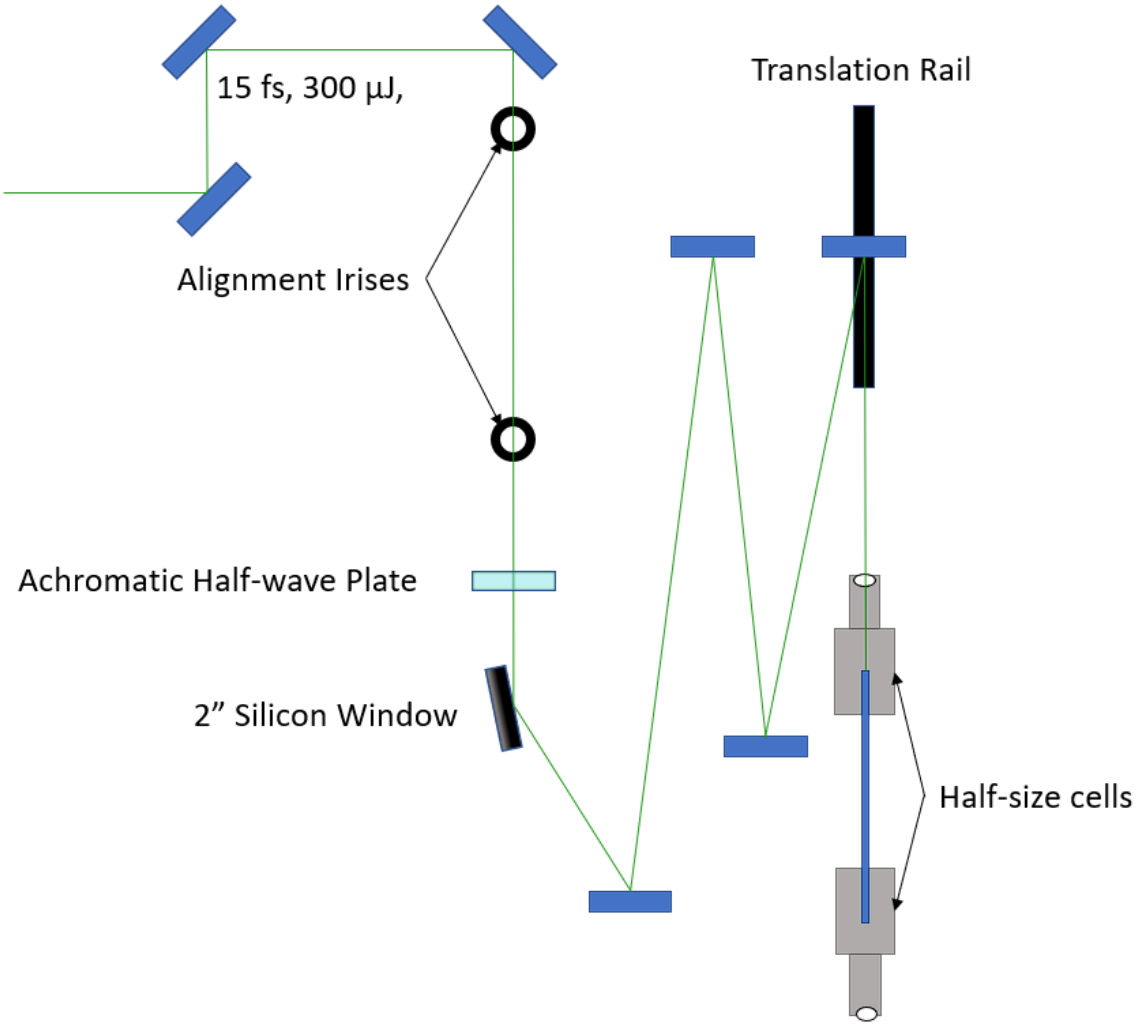


Figure 5.2.6: The layout of the RDW system at Imperial College. The cells have 10 mm x 1 mm MgF_2 windows mounted to minimise imparted phase, and allowing them to be rated up to 8 bar with a safety factor of 4. As this system was constructed for testing RDW generation, the back cell is also sealed by a window, rather than being attached to the beamline chambers, and the cell is pumped down to a few-10^{-1} mbar.

As the length of fibre needed for RDW here was on the order of 15 cm and the cells shown previously were on the order of 10 cm long, new cells were designed with the same elements but at half the length. A pair of Brewster angle window mounts were also designed for this system to accommodate 1 mm thick, 15 mm diameter MgF_2 windows (Crystran). Brewsters angle for MgF_2 at 1350 nm is 55°.

The foremost task in implementing the above source into the beamline shown in Figure 4.5.1 was to reproduce the results shown in Figure 5.2.2 at Imperial College. Firstly, work was performed to recreate the static-fill generation method implemented above. Due to an increased pulse duration, this generation both required more energy, and was more restrictive in achievable wavelengths.

Spectra of the RDW pulses were taken using a spectrometer (Ocean Optics 2000+) connected to an integrating sphere ((Thorlabs 2P4/M)). As can be seen by comparing Figure 5.2.7 to Figure 5.2.2, the tuning range of the RDW was significantly limited in these first tests. While the pulse had an FTL of 17 fs, the configuration of the chirped mirror compressor and spectral phase accumulated between the two fibres was not well matched, leading to pulse durations around 25 fs.

While this mismatch was corrected by adjusting the number of bounces on the mirrors and the reflection angles, these data sets are a clear demonstration of the aforementioned limitations of using longer pulses to attempt to generate UV through RDW emission. In Figure 5.2.7, we see that the shorter wavelength RDWs become inaccessible with longer pulses as greater pulse energy was used to compensate for the longer pulse duration.

A 3-aperture filtering method was designed to spatially filter the IR driving laser from the emitted UV for use in transient absorption experiments, as shown in Figure 5.2.8. This filtering system works on the principle that the divergence of a beam is directly proportional to the wavelength, and so wide pinholes of 1 mm diameter at a distance

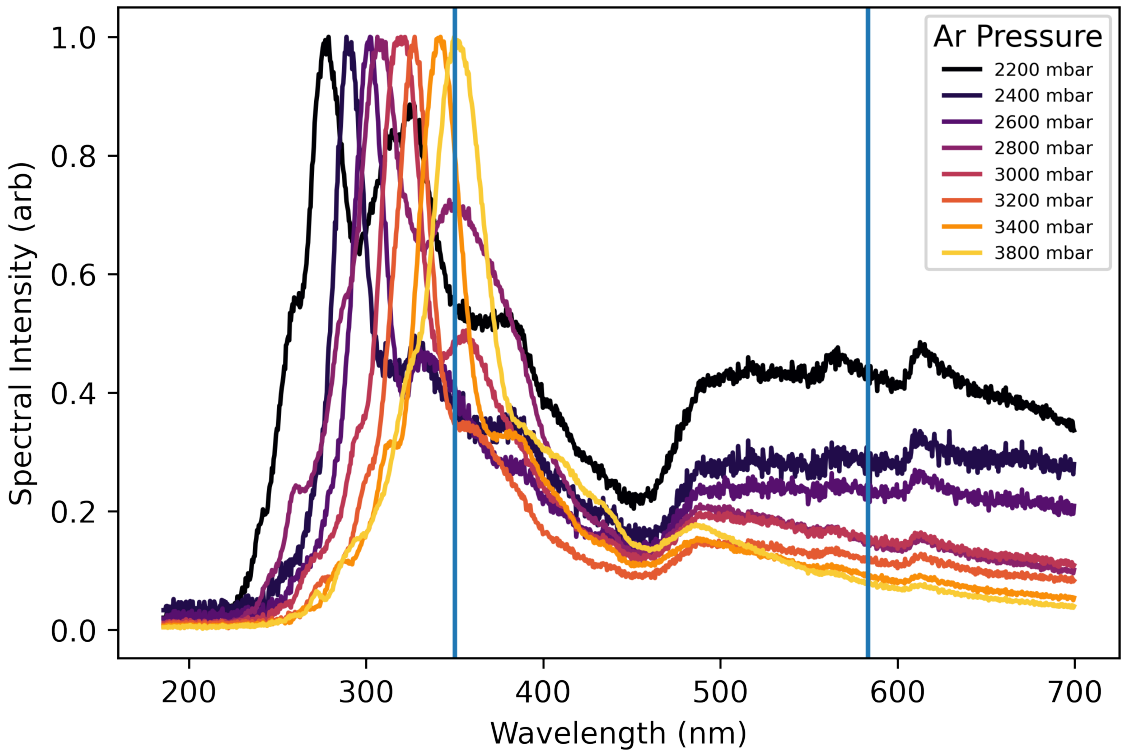


Figure 5.2.7: UV pulses generated in a 100 µm fibre with a 30 fs, 1800 nm driving field, with each line self-normalised. Vertical lines are placed at the 3rd and 5th harmonics for reference. As these pulses were generated with a longer driving pulse (>25 fs), the harmonic contamination is substantial.

of 25 cm after both the fibre and a 200 µm diameter pinhole at the focus of a 20 cm lens provides the transmission curve Figure 5.2.8, with an extinction ratio of 457 compared to the transmission at 1.4 µm to 300 nm.

Applying this extinction ratio to the pulses produced in Figure 5.2.2, where the IR peak is roughly four times the peak of the UV, we see a peak energy ratio of around 115, providing substantial energy spectral contrast in the transmitted pulse, and with a minimum transmission of 91% at 300 nm, transmitted UV pulse of around 2 µJ.

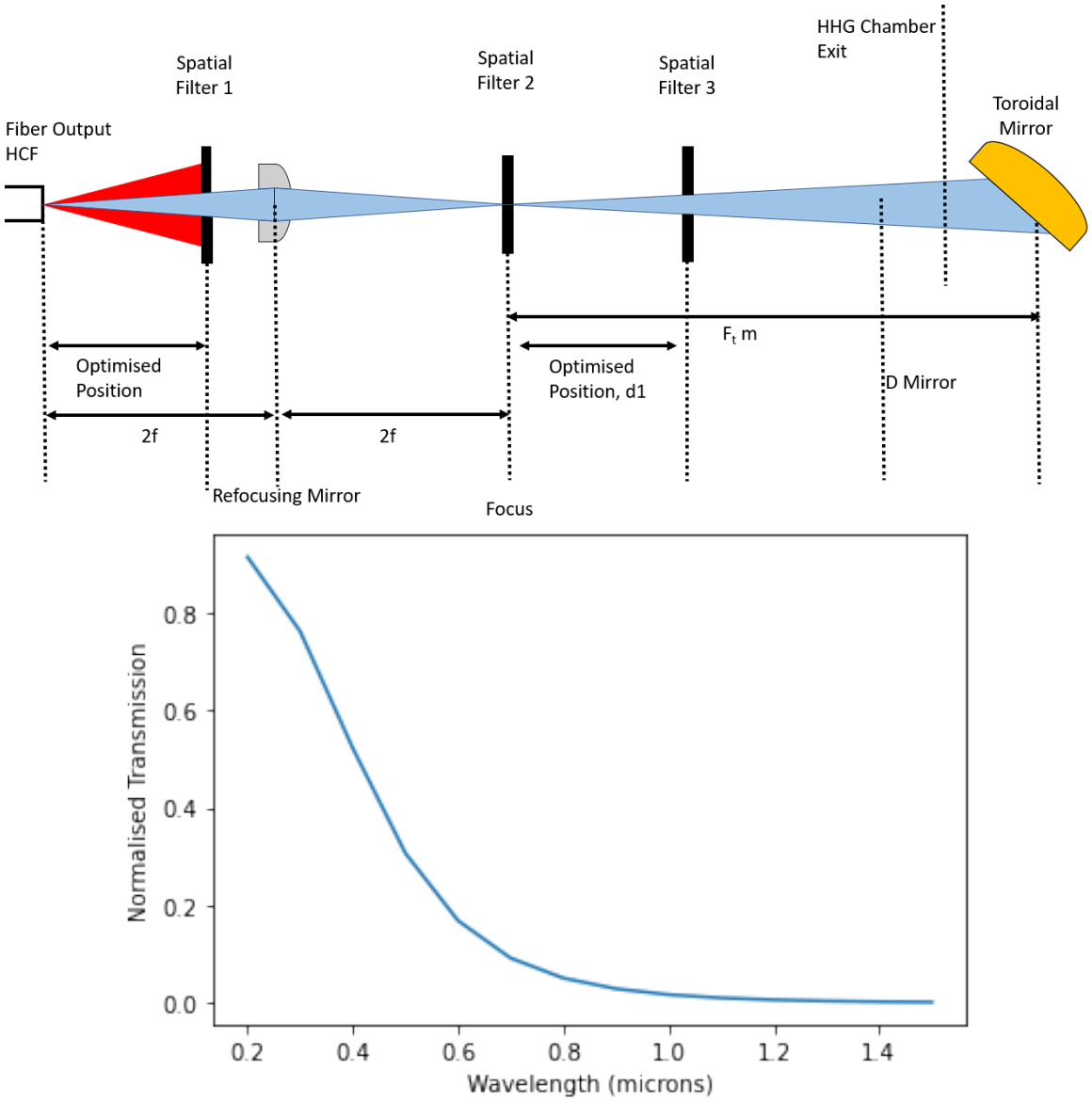


Figure 5.2.8: Above: The pinhole-based spectral filtering system designed for the RDW pulses. Spatial filter 2 here is a 200 µm pinhole, whereas spatial filter 1 and 3 are adjustable irises. Below: A numerically calculated wavelength-dependant transmission graph for pulses filtered through the system using LightPipes [126].

While a wavelength limitation for the RDW emission is set by the pulse energy and duration itself, as described in Section 2.3, a further limitation in wavelength arises from the increasing third and fifth harmonic signals (THG and FHG respectively). This originates from the higher energies needed to generate shorter wavelengths in

RDW emission. As the filtering system seen in Figure 5.2.8 works using the divergences of the IR and UV beams, the THG and FHG extinction is significantly less effective. At 1800 nm, these signals are at 580 nm and 350 nm respectively, meaning that for THG the filtering is significantly less efficient, and for FHG it is not possible. While these perturbative harmonics are emitted at a similar wavelengths to the dispersive waves, they are generated throughout the propagation of the driving field through the fibre. As described in Section 2.3, the soliton that drives RDW emission necessarily dissipates temporally through the UV generation process, and therefore these perturbative harmonics are of durations close to the fundamental field rather than the few-fs duration of a RDW. As these harmonics cannot be effectively filtered, this contamination therefore limits the temporal resolution of any experiment that wishes to use pulses generated in this way.

To ensure that the pulse was optimally compressed to permit RDW emission as deep into the UV as possible, the FROG shown in Section 4.4.2 was used immediately next to the entrance of this fibre, keeping the air paths to the BBO crystal and fibre entrance approximately equivalent (to within a few cm). Following the FROG trace being taken, a pre-compensation for the MgF_2 windows and beam paths through air was calculated and implemented by optimising the thickness of wedges and number of chirped mirrors in the beam path. Through this process, optimum pulse durations on the order of 15 fs were achieved for the 1350 nm driving laser, with typical pulse characteristics as seen in Figure 5.2.9.

As the RDW system is designed for operation at gradient fill, its production of RDWs using a constant gas fill is poorly optimised, as the pulse will see both formation and temporal dispersion of the RDW along the length of the fibre. This is because the dispersive wave was formed far earlier in the propagation of the pulse than the point of exit from the HCF, as seen in Figure 5.2.9.

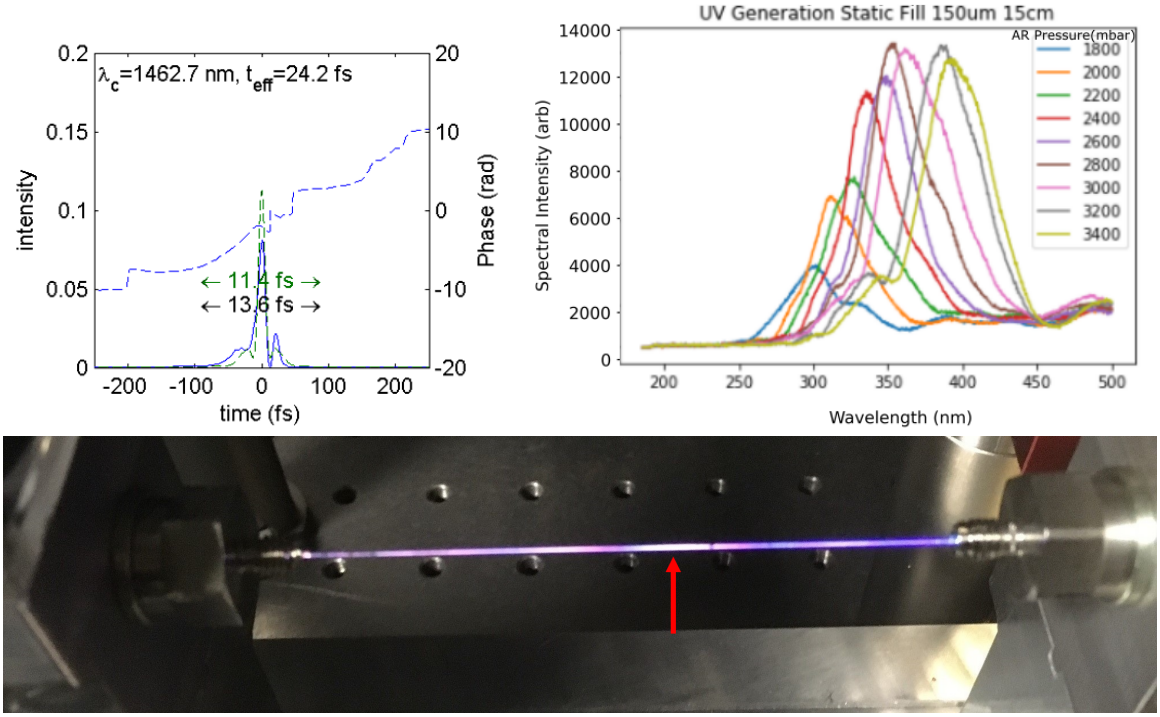


Figure 5.2.9: RDWs generated by the layout shown in Figure 5.2.6. Above: The characterised pulse used for generating RDWs in the system (left), and RDWs generated in the statically filled system (right), as a stepping-stone to implementing a gradient fill. In the characterisation plot, the green dashed line is the transform limited pulse, the solid blue line is the retrieved pulse, and the dashed blue line is the phase. Below: an image of the HCF at static fill generating RDWs. A bright spot (indicated by the arrow) can be seen at the point that the dispersive wave is formed and the driving pulse is maximally compressed, significantly before the end of the fibre.

Unlike in the gradient fill case however, the pulses here will accumulate chirp from the gas and window as they exit the fibre assembly. Unless a method for compensating this phase is available, experiments with high spectral phase sensitivity using these pulses may not be feasible. For experiments which require high-bandwidth vis-UV pulses without the same few-cycle limitation, however, static fill RDW form HCFs presents a simple and compact solution. These include 2D Electronic Spectroscopy and impulsive Raman spectroscopy experiments [11], where the precise temporal structure of the pulse is not critical on the timescales of few-cycle pulses, as experiments use

pulses on the order of 30 - 40 fs, and only the delays of particular spectral components are critical to the dynamics. As such the chirp imparted by windows or gas at the exit of the pulse are not limiting to the system design - these will be discussed further in Section 8.

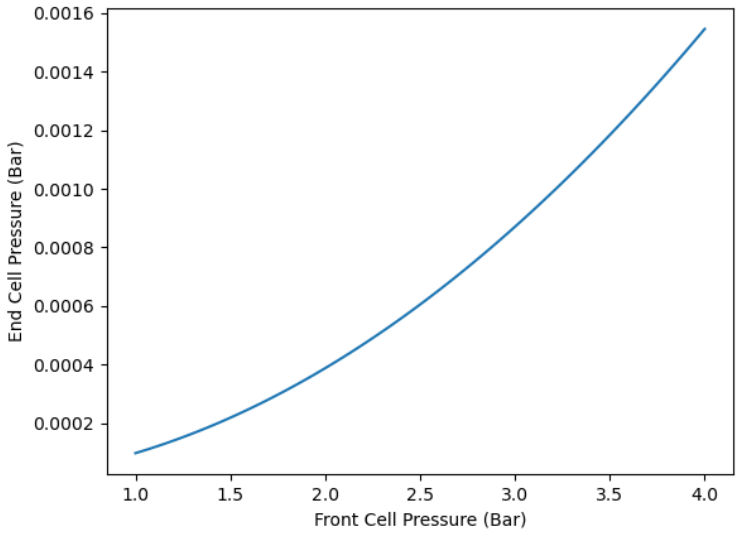


Figure 5.2.10: A calculation of the end cell pressure of the gas, for an Argon-filled 150 µm-ID HCF using a range of up to 4 bar backing pressure on the front cell, based on a scroll pump with a pumping speed of 7 m^3h^{-1}.

A simulation using the CoolProp Python package [127] was run to confirm the scalability of this design, as the entrance cell pressure was scaled from 1-4 bar pressure. We see in Figure 5.2.10 that the gas pressure in the rear cell, even above the gas load used in these experiments, does not exceed 1.5 mbar, which can be handled by the turbo pump on the measurement chamber.

The gas needle cell currently used for high harmonic generation results in a pressure of approximately 0.1 mbar in the beamline chamber, which is maintained by turbo pumps on the HHG chamber and a differential pumping jacket around the needle. The final cell used here will be connected to a diagnostic chamber used for characterisation that will also be pumped by a turbo pump and therefore act as a differential pumping

section between the cell and the HHG chamber. As such we can be confident that we are not introducing additional gas load on the system, or risking reducing the vacuum level of the HHG generating chamber. Following this, the rear of the setup was evacuated and held at 5×10^{-2} mbar by a scroll pump, and the data seen in Figure 5.2.11 was taken. The system was also connected to the HHG chamber, as seen in Figure 5.2.12.

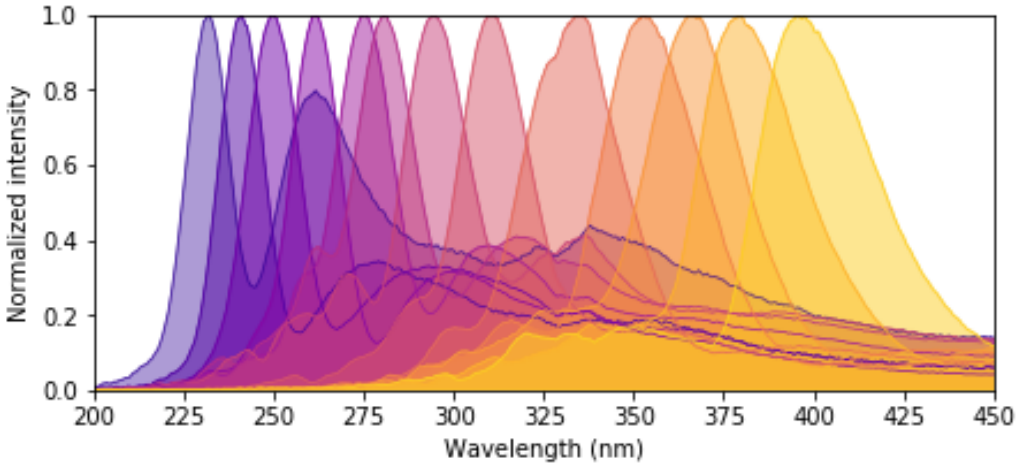


Figure 5.2.11: RDW pulses generated in a gradient fill configuration. The 150µm fibre is driven with 46 - 104 µJ (purple to yellow), 15 fs pulses at 1350 nm, and the front cell is filled with 0.8 - 3 bar (yellow - purple) of Argon. Here we see full coverage of the 225-425 nm range. Figure courtesy of Jacob Lee and Clement Ferchaud.

In conclusion, a tunable source of few-fs UV pulses in the between 250 – 450 nm is demonstrated with front cell pressures of 3 – 0.8 bar of Argon respectively, and the back cell held at a roughly sub-mbar pressure by vacuum pumps. The latter of these means that this versatile pump-pulse source for TAS experiments is compatible with our existing HHG beamline without a need for additional differential pumping stages. This UV pulse generation is driven by the compressed OPA signal pulses generated in section 5.1.2 with few-percent conversion efficiencies, and a scheme for spatially filtering the IR pulses that drive the RDW emission is outlined alongside a self-diffraction FROG to verify the few-femtosecond nature of the RDW emission from the hollow capillary.

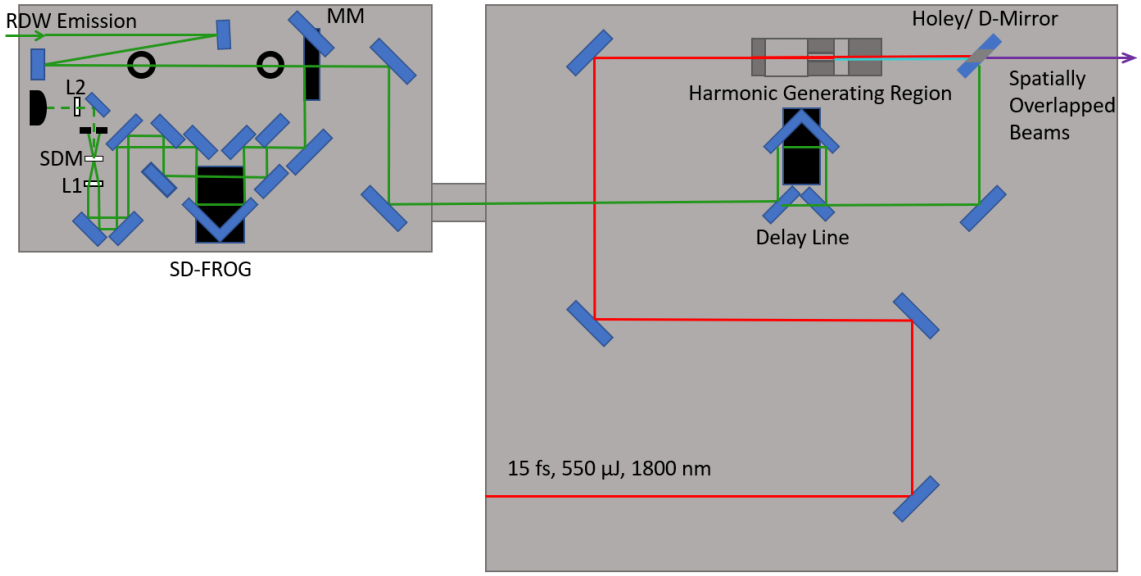


Figure 5.2.12: The Beam path from the exit of the RDW generation cells to combination with the HHG beam. The beam immediately enters the diagnostic chamber containing the SD-FROG, where an motorised translation stage (MM) is used to pick off the beam. Two Irises are placed after the entrance to maintain consistent alignment both for the FROG and beamline chamber. As the diagnostic chamber is pumped independently of the main beamline chambers, this means an alignment of the beam can be adjusted without having to break the vacuum of the main chambers. In the SD-FROG, the beams are spatially separated and recombined using a lens (L1) onto a 0.5 mm glass window, then reimaged by a second lens (L2) onto a spectrometer. This matches the design outlined in section 4. At the end of the beamline, the RDW pulses are spatially overlapped with the beam from the harmonic generating region.

6 Development and Modelling of Optimised High Harmonic Generation in the Gas Phase

As previously discussed, *high harmonic generation* (HHG) is a tabletop method for generating photons from the *vacuum ultraviolet* (VUV, 10 – 210 nm) to *soft X-Ray* (SXR) light in laboratory environments, driven by a wide range of laser systems. As shown in Section 3.1 the characteristics of the driving laser field places limits on the harmonic flux at a given photon energy, through a combination of the driving wavelength, pulse energy and pulse duration of the field, as these define the ponderomotive energy, as well as its interaction with plasma generated during the HHG process.

Given the sensitivity and non-linear nature of HHG, numerical simulation of experiments can be vital in optimising the flux of high photon energy harmonics (e.g. in the water window, 280 – 550 eV). For this purpose, prior to the works in this thesis, a code to evaluate HHG emission in 3 spatial dimensions and time ((3+1)D) was written to recreate HHG in idealised laboratory conditions [16, 33]. This code was used and modified to model the experimental regimes examined in this thesis by the author, with the contributions of collaborators, as seen for example in [128] which forms the basis of the phase matching plot results discussed in section 6.2.3.

In this chapter, first designs for a variable length gas target will be outlined for the purpose of creating an optimised HHG cell in Section 6.1. In Section 6.2.1 overall simulation method used to calculate HHG in this thesis with then be described. Finally a number of simulations will be described performed with the intent of optimising HHG in the gas phase for laboratory experiments. A figure of merit value is presented in Section 6.2.3 to provide a short-cut to a quantitative value for the HHG yield at a given photon energy in a system, and is compared to other recent works in the field.

6.1 Development of a Variable-Length Target for High Harmonic Generation

6.1.1 The Experimental Design Space

The universal scaling laws for nonlinear optics outlined in Table 3.1 hold only below the critical power where plasma-induced effects do not disrupt the propagation of the beam [129]. Recent studies have also suggested that harmonic cutoffs can be extended using transient phase-matching in the overdriven regime [16]. While a wide range of studies on harmonic generation have been conducted scanning over pulse energies, gas pressures and focusing geometries, many fix at least one parameter [35, 38, 130]. As such, a study which characterises HHG while varying focal spot parameters, gas cell geometry, gas pressure and pulse energy could be used both to aid in new source development and deepen our understanding of the HHG process. Parametric scans in this regime exploring the effects of key experimental design parameters (i.e. gas pressure, generating medium length and focal spot size) are therefore crucial to optimising the design of SXR-TA experiments.

Previous experiments in our group have seen benefits from short cells (<1 mm interaction length) for high flux SXR generation [131], while other works have claimed diminishing or negligible benefits from similar geometries [38]. Gas sources for HHG range from millimetres to tens of centimetres in length, as seen in Figure 6.1.1, providing 3 orders of magnitude of experimental range to explore.

Cells on the tens of centimetres are often labelled "semi-infinite", so called because the beam propagates through the cell for longer than the Rayleigh length of the beam. In this geometry the beam is focused at the rear aperture of the cell to prevent reabsorption of harmonics by the neutral gas, as shown in Figure 6.1.1. These cells maximise harmonic flux by scaling the number of available emitters, and the pulse propagation through the elongated medium allows further spectral broadening and

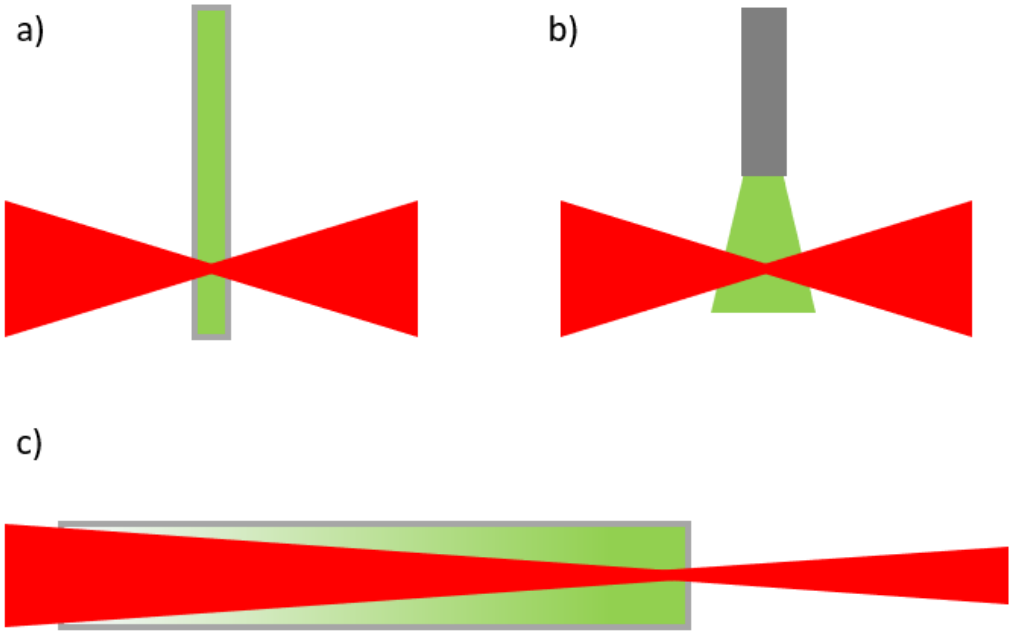


Figure 6.1.1: The typical geometries used for HHG. The shaded green cells here represent gas filled regions, and the red bow-ties represent the propagating laser field. a) gas cells, which confine gas to maintain local high pressure targets. b) diffuse jets and valves, with the gas pumped at lower pressures directly into the vacuum. c) semi-infinite cells, where gas fills a cell, highest in pressure at the exit end, with the beam travelling a long path through the target medium.

self-phase modulation through the focus. While this means the system can compensate for chirp accumulated from optics such as lenses, it also means lower gas pressures are used to avoid distortion of the propagating laser. These distortions would largely arise from ionisation of the medium near the focus, and become more pronounced as the peak intensities near the critical power. While this does make prediction of the peak intensities and harmonic flux in the generating volume simpler, it also reduces the number of emitters available to perform HHG, and therefore lowers the flux per unit volume of the target.

Shorter cell geometries rely on an "overdriven" regime, maximising harmonic flux with high peak intensities tightly focused into a few-bar gas medium. In a longer focusing geometry this ionisation would rapidly become prohibitive, however the short cell length means that the harmonics are generated before ionisation dynamics cause the beam to be spatially dispersed. Distortion from plasma is thereby mitigated over the propagation distance and transient phase-matching is relied on to produce HHG. The higher pressure also means a larger numbers of available emitters to produce harmonics. The harmonic cutoffs and yields are harder to estimate in this regime as plasma accumulated on the sub-cycle timescale will substantially change the phase-matching in the later half-cycles of the pulse. To optimise HHG from these systems, the plasma term in the phase mismatch must be accounted for when targeting particular harmonics using Equation 3.1.26.

6.1.2 Specification And Construction of the Variable Length Cell

To study this reliably a cell was designed with a reproducibly adjustable interaction volume, moving from the overdriven to semi-infinite cell geometries to allow for parametric optimisation and characterisation of the system. Previous interaction length studies have required scanning of a diffusive gas jet [132] (sacrificing a well-defined gas region) or individual cells at varying diameters, sacrificing reproducibility through the need to realign cells onto the driving laser and fixing coarser target sizes [38].

The more general requirements for the construction of this cell are to provide a vacuum-compatible volume whose mechanical adjustment would provide reproducible scanning of the length of a beam path through a noble gas. This problem is not unique and has been previously addressed by the filamentation and laser acceleration communities, where an ability to vary the length and pressure of gas the beam propagates through provides control of the spectral broadening [133]. The difference between the requirements of the filamentation and HHG communities come down to vacuum and pulse compression limitations.

Firstly, after exiting the system the beam must not pass through any transmissive optics as this would lead to absorption of the X-rays. The minimum length of the system must also be thin enough to allow overdriven HHG (on the order of few mm). This means that the walls of the cell must have both a small aperture and thin wall. As seen in [134] and examined in the supplementary material of [131] the thin wall limitation is needed to prevent extension the interaction length, as otherwise a supersonic gas jet would propagate through the aperture and beyond the limits of the system. The walls must also be thick enough to prevent drilling by the focused laser, as is the method used to prepare needle cells used in overdriven HHG regimes.

Secondly, as a compressed femtosecond pulse will be sent into this system using a short focal length focusing optic ($\leq$50 cm) a window cannot be placed on the entrance side, as it would both accumulate substantial B-integral and be prone to damage. If a window was used to contain the gas, it would need to be placed at a distance from the focus that would prevent this phase accumulation, extending the gas cell length. These first two requirements make it clear that this entire system must be held in a differential pumping jacket, as a cell with high gas load (up to 8 bar) and no entrance or exit windows will otherwise quickly compromise the vacuum of the surrounding chamber.

Thirdly, the cell extension system must be operable under external vacuum, to allow in-situ variation and adjustment. This requires a seal tight enough to contain the gas without preventing the cells extension. In conjunction with this, we do not want to place any material into the system that could contaminate the generating region or spread through the wider system, for example vacuum greases.

One specific task for this cell is also to be able to reproduce HHG data seen in literature. As such we define the list of experimental parameter ranges seen in Table 6.1. Scanning this entire parameter space poses a number of challenges, in particular scanning the cell diameter and beam waist. It must be noted that the energy scale listed

here includes pulse energies beyond what is currently available in the laboratory, but are available in the literature at a laboratory with an ongoing collaboration with the group of Zenghu Chang at the University of Central Florida [135]. At the time these specifications were collected, the laboratory was also developing an amplifier stage for the 800 nm Ti:Saph pulses to reach 70 mJ pulses at a 100 Hz repetition rate for experiments including high pulse energy HHG and filamentation, as well as the construction of other new secondary sources. As such this table includes those parameters.

Parameter (unit)	Minimum	Maximum
Gas Pressure (bar)	0.05	8
Cell Length (mm)	0.5	750
Beam Waist (μm, $\frac{1}{e^2}$)	30	780
Pulse Energy (μJ)	400	7×10^4

Table 6.1: List of minimum and maximum parameter limits for gas pressure [16, 136], cell length [16, 136], beam waist [135, 136], and pulse energy [135, 137], as found in the literature. These limits cover both semi-infinite and overdriven regimes, as well as experiments with lower repetition rate, higher pulse energy systems.

The solution devised to match these requirements can be seen in Figure 6.1.2, with a cell diameter that can be varied from few-mm to tens of centimetres smoothly in vacuum without realignment. The cell is mounted on a stage that can provide a maximum force of 44 N (Thorlabs MTS50-Z8). Using $p = F/A$ for a pressure p, force F and area A, the force exerted on the 7.5 mm diameter plunger can support a maximum pressure of 9 bar. An o-ring is connected around the head of the plunger, and copper tape is placed on the entrance and exit pinholes to create sharp interfaces between the cell interior and exterior.

The construction of the stage was tested up to a load of 4 bar by connecting a compressed air gas line to the stage and translating the system while under gas load and monitoring for slippage in the stage motor. To test the cell up to the full 8 bar requirement it will be placed into the vacuum chamber such that it can be safely tested

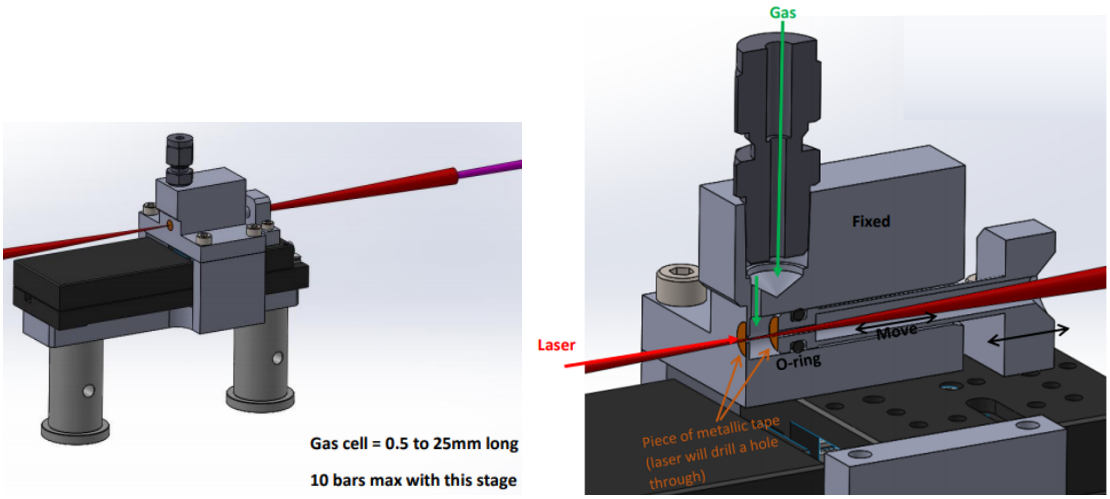


Figure 6.1.2: The designs for the variable length cell for HHG. Left: an external view of the cell, demonstrating its intended position affixed to a translation stage supported by 1" diameter posts, as well as its positioning relative to the laser. The beam height here is 8.5 mm. The laser enters on the flat side of the cell, with the plunger extended along the path of the beam. Right: A cross sectional image of the cell. The green arrows indicate the flow direction of the gas. The gas lines are perpendicular to the cell to the translation axis and staggered to reduce load. The laser propagates from left to right. The orange arrows indicate where tape may be added to create thin-wall limits for overdriven HHG. The plunger is surrounded by a nitrile o-ring. The black arrows indicate the translation axis of the plunger. Images courtesy of Clement Ferchaud.

with leaked gas pumped away. This cell will be placed into an aluminium differential pumping jacket, with power and gas line ports separated from the pumping ports used to maintain vacuum, and this differential pumping must also be tested to minimise vacuum contamination of beamline chambers.

By drilling the tape rather than a full target for scaling to an over-driven system the cell may reduce down to only the distance between the two pieces of tape (i.e. the front of the face of the cell and the plunger at full insertion). The step change in radius between the drilled hole and plunger radii will cause rapid diffusion, effectively ending the interaction region as the gas is extracted by the differential pumping jacket [134].

Specifically, a standard copper tape (RS PRO 176-7498) has a thickness of 0.06 mm compared to the thinnest-walled needles at 0.15 mm (Birmingham gauge 21).

With the construction of the cell complete, what remains now is to integrate it into the experimental beamline. This was not possible during this project. As previously stated however the aim of this cell is not simply produce harmonics, but specifically to so both reproducibly and in a way that can be used to compare differing cell geometries to the results presented by other laboratories. As such, other than taking experimental results, there are three next steps: establishing a platform for simulations to represent scans across the parameter space of this cell; testing that model against literature to show efficacy; and modelling the experiments to act as a predictive tool for experimental HHG.

6.2 Modelling HHG in a Variable-Length Gas Cell

6.2.1 The Simulation Process

A breakdown of the simulation process can be see in Figure 6.2.1. This code was originally developed by Dane Austin, with work published on its implementation and efficacy in reproduction of experimental HHG spectra [16]. The driving laser is propagated with adaptive step-sizing using split step propagation and the *forward Maxwell equation* (FME) in three dimensions with cylindrical symmetry. Dispersion, paraxial diffraction, the third-order nonlinearity, plasma dephasing, and multiphoton absorption are included here [123].

The FME is obtained by first separating the propagation of the electric field into its forward and backward spatial components, and identifying that the backward component (e.g. back reflections from material surfaces) is negligible for a laser field propagating through free space [67, 138]. The use of this method requires that the system stays within the paraxial approximation — that is, that the angles between rays of the beam stay significantly less than 1 radian, typically a few degrees, or a

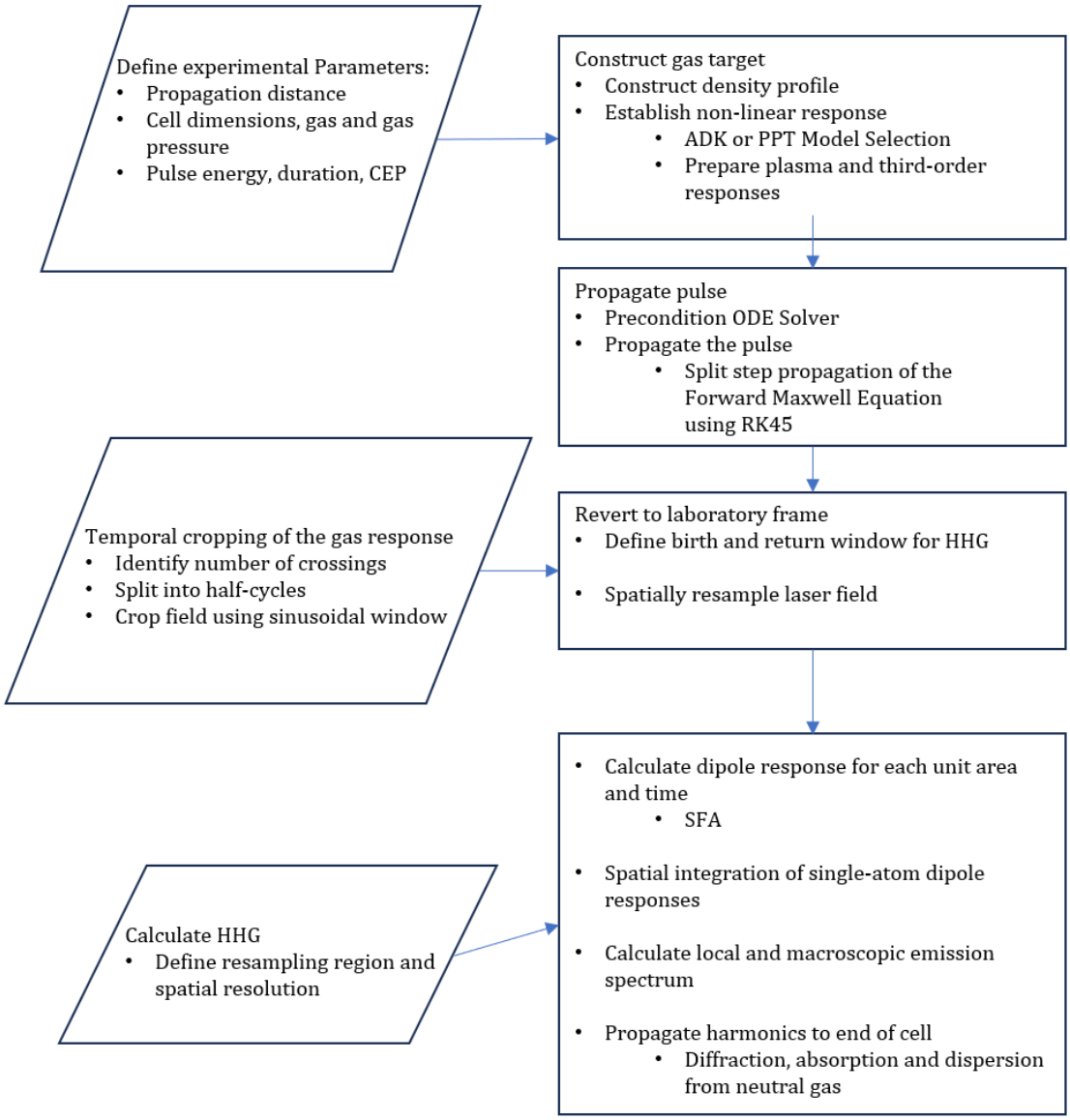


Figure 6.2.1: A breakdown of the simulation process for HHG used in this thesis, with further details provided in the main body of text.

numerical aperture of around 0.1 for focusing beams [123]. Firstly this means that diffraction and focusing due to frequency differences can be handled more simply in the space-time rather than spectral domain. Secondly, and perhaps more importantly for this project, it means that the nonlinear polarisation can calculated more naturally in the space-time domain, where for non-paraxial propagation equations this

response would need to be three-dimensionally Fourier transformed to the spectral domain.

The second assumption made is the slowly evolving wave approximation, which hinges on the fact that we can propagate the pulse in its local frame, rather than the laboratory frame. This requires that the interactions that we wish to study act on the same timescale as the propagation of the pulse; that the total travel length of the pulse is "long" compared to the physical space representation of the pulse itself; and that the interactions involving any back-reflections of the pulse are negligible. The first of these is certainly true, as a femtosecond pulse is being propagated and we examine dynamics on the femtosecond scale. The second is always true, as we always propagate the pulse over the order of millimetres to allow it to focus into the medium accounting for any ambient gas or vapour, and a 20 fs pulse is around 60 μm in axial extent. The last point will become a point of interest during high-intensity liquid phase interactions, but this will be discussed later.

Given our need to resolve the sub-cycle dynamics of the propagating field, we seek what is known as a carrier-resolved propagation equation, so called because they resolve the carrier field oscillation of the propagating pulse rather than simply the envelope. We hence define the general propagation equation for an electric field, E, propagating within its own local pulse frame along a co-ordinate ζ as

$$\frac{\partial E}{\partial \zeta} = i(K_z(\omega, \boldsymbol{k}_\perp) - \frac{\omega}{v_g})\tilde{E} + \frac{i}{2\varepsilon} Q(\omega, \boldsymbol{k}_\perp)\tilde{P}. \tag{6.2.1}$$

Here v_g is the group velocity of the pulse, $\tilde{E}$ and $\tilde{P}$ are the electric field and nonlinear polarisation of the pulse respectively. ω denotes the carrier frequency of the field, and $\boldsymbol{k}_\perp$ its k-vectors perpendicular to the propagation direction. This expression stems from the equation seen in Equation 2.1.9, but with the linear and non-linear responses separated. When implementing a propagation method, it is K_z - the k-vector along

the axis of pulse's propagation - and Q - the non-linear dispersion operator - that describe the evolution of our pulse. For the FME, we define these as

$$K_z(\omega, \boldsymbol{k}_\perp) = k(\omega) - \frac{k_\perp}{2k(\omega)} \qquad \text{and} \qquad Q(\omega, \boldsymbol{k}_\perp) = \frac{\omega}{n(\omega)c}, \tag{6.2.2}$$

where $n(\omega)$ is the frequency dependent refractive index and c is the speed of light in vacuum.

Within these bounds, the FME is used to model the propagation of the electric field over finite time steps by solving the ODE for propagating the laser field using the Runge-Kutta 4/5, also known as RK45 or Dormand-Prince method [139]. The RK45 method in particular uses 4^{th} order Runge-Kutta formulae with a truncated 5^{th} order term used to estimate errors [139]. Dispersion and diffraction are applied in the frequency domain while nonlinear effects are applied in the real-space domain [140]. The linear optical terms are added into the preconditioning of the ODE solver (a method by which a matrix calculation is simplified by making assumptions which limit the number of computed matrix elements), as this has previously be shown to provide computational speed-up by an order of magnitude [140]. Ionisation rates are calculated using the ADK or PPT methods as described in Section 3.1.1.

Electron trajectories are then calculated using local field strength, where the simulated region is returned to the laboratory frame and re-sampled to create finer resolution for harmonic calculations. Temporal windowing is used to filter long or short trajectories to restrict the number of calculations performed for each half cycle. This is done by applying a cosinusoidal window (over the period $[\frac{-\pi}{2}, \frac{\pi}{2}]$, mapped to the times one wishes to perform calculations for) over a central electron return phase after the ionisation time, such that the selected photon energy is calculated entirely and that the applied window does not have "sharp" edges that would create artifacts once Fourier transformed into the spectral domain. One can understand this as limiting

the number of spectral points used in the calculation of the time dependent dipole to reduce memory usage. Considering the ponderomotive energy of an electron and its relationship to the cutoff harmonic, it can be shown that the energy of a liberated electron as a function of birth time is dictated by $\omega_q(t) \propto v^2 \propto E(t)^2$, where v and E are the electron velocity and the local electric field strength respectively [82]. This means that the number of points one would need to calculate trajectories for, and hence the memory consumption, increase quadratically as the temporal window increases.

In the case of HHG at the cut-off, we filter symmetrically around the temporal peak of the pulse as the trajectories are no longer meaningful, photon energy distribution becomes a Gaussian distribution of the electron momenta at the cut-off energy. These filters also mean that we remove the multiple-returns electrons, which "miss" recombination after the first half-cycle. While these are always present, they are generally neglected in literature, as their contribution is considered negligible over propagated volumes. This can be understood due to their substantially increased time spent before recombination leading to increased wavepacket spreading which decreases recombination probability, as discussed for wavelength scaling of HHG in section 3.1.

This means that short trajectory, cutoff, or long trajectory harmonics can be selected to allow analysis of their relative efficiency in given experimental design geometries. The single-atom dipole responses are then spatially integrated over the resampled volume to generate the macroscopic harmonic field. This field is then propagated to the end of the cell, accounting for diffraction, the local medium density, and absorption and dispersion by the neutral gas.

For this thesis, this code has been used to study four separate experimental designs: thin gas cell ($\approx 1\,\mathrm{mm}$) HHG; extended gas cell ($<10\,\mathrm{cm}$) HHG; "reduced" calculations

for phase-matching; and laser propagation and HHG in a thin ($\approx 2\,\mu m$), optically flat liquid jet.

For gas targets, the density profiles used in simulations have previously been verified by comparison to published work on gas flow through short tubes into vacuum [33, 134]. These describe the flow of a gas from a thin needle target through few-hundred micron drilled holes into a differential pumping jacket, as described in Section 4.5. An example of these gas profiles can be seen in Figure 6.2.2.

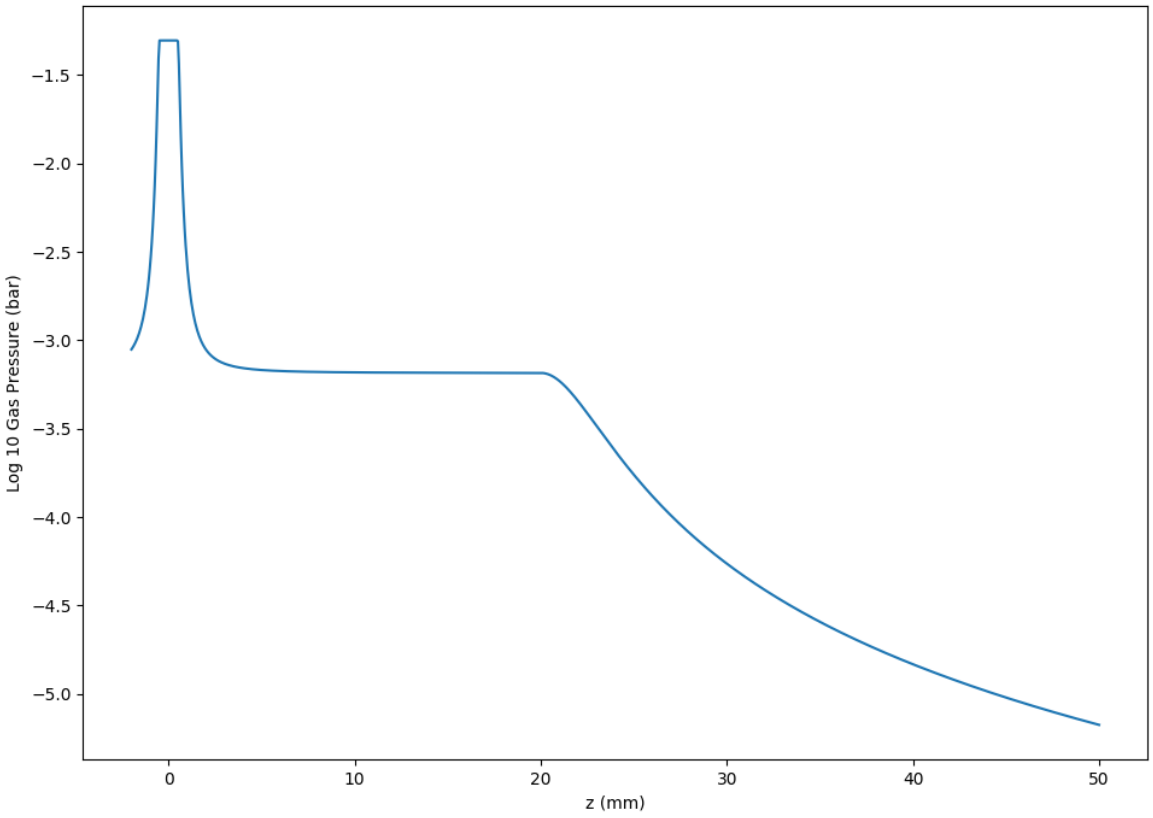


Figure 6.2.2: An example density profile used in gas phase simulations. The peak pressure in the needle is 0.5 bar, and the medium pressure region due to the rapid expansion of the gas has a decay length of 105 µm to a few-mbar pressures, before decay to lower pressure due to the differential pumping jacket.

The profile can be understood in three parts: a central, high density (0.1-8 bar, depending on the simulation) region representing the needle backed directly by gas inlets; a secondary, medium density region where the gas has expanded rapidly through

the holes in the target (few-mbar pressures); and a low pressure region pumped effectively the differential pumping jacket (towards 10^{-6} bar). For a given backing pressure P_B, the characterisation performed in previous works shows that the peak pressure in the target is $0.875P_B$, before decaying to the medium pressure given by $(1.4\times10^{-3}\times P_B)+0.58\times10^{-3}$ with a decay length of 105 µm. This then decays with a decay length of 3 mm towards the lowest pressure of 10^{-6} bar far from the target.

6.2.2 Simulating Phase-Matching in the Overdriven Regime

The development of a model for rapid, quantitative understanding of optimised parameters for HHG in the water window is underpinned by a theory of non-adiabatic, transient phase-matching [141], where the ionisation dynamics in the target create a complex system for which there is no obvious method to fully quantify *a priori*. An ideal phase matching pressure can be defined for a particular gas and target harmonic energy, as shown in Equation 3.1.26. For a predictive tool in an overdriven HHG experiment however one would need to characterise the sub-cycle ionisation driven by the laser field using one of the sub-cycle ionisation methods described in section 3.1.1 during the propagation methods and calculating the spatially resolved HHG emission in the target region.

Running full simulations would be inefficient, as a parametric scan is necessary to characterise each combination of parameters, and this can quickly sum up to hundreds of simulations each of which would take several hours on a high performance computing (HPC) cluster node. For example, the scans shown later in this thesis will consist of 32 pressure values, 32 length values and were run for 4 differing pulse energies, giving 4096 total simulations.

The upper row of plots in Figure 6.2.3 shows the propagating field for a 12 fs, 1.8 µm laser across the first three half-cycles (-6, -3 and 0 fs corresponding to half-cycles 1, 2 and 3 respectively, as the laser cycle duration is 6 fs at 1.8 µm). While the intensity profile of the first half cycle appears Gaussian about its focal point, the ionisation

generated the second half-cycle defocuses the beam, to be refocused by laser self-focusing. The third half cycle however is defocused by the cumulative plasma from the previous two half cycles and so the most intense half-cycle of the field does not converge at its intended focal point. The colour map of the lower row of plots show the phase mismatch (the inverse of the coherence length, i.e. $1/L_{coh}$) for 350 eV harmonics at each point along the propagation coordinate space using the phase-matching equations outlined in section 3.1.

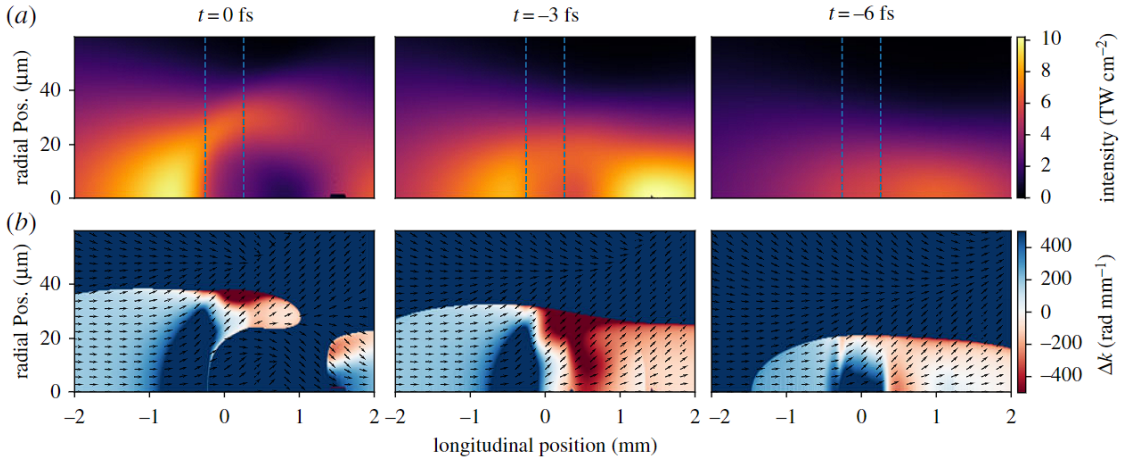


Figure 6.2.3: Peak intensity (a) and phase-matching (b) plots for the short trajectory harmonics at 350 eV harmonics generated in helium. The beam is focused 1.4 mm behind the centre of the gas target. The dashed vertical lines show the boundaries of the cell itself, representing the edges of the high pressure zone in Figure 6.2.2. The cycle times are relative to the centre of the pulse, i.e. negative terms arrive earlier. In (b) the colour map shows the total phase mismatch, while the arrows show the (exaggerated) angle of the emitted harmonics. The colour maps are limited to show colour variation only where the instantaneous field intensity exceeds that required to provide cutoff energies of the intended harmonic. Reproduced with permission from [128].

In particular, after spatially resampling the propagated laser we calculate instantaneous field strength at the peak-crossing time for each half cycle (i.e. the time at which the cosine laser field has its peak value). This, and every other step to follow, is calculated at every spatial point in the resampled grid, using numpy's broadcasting functionality, which computes all calculations across a given array space. The relative

time at which a photon with the desired harmonic energy would have to have been born and return are calculated, t_b and t_r respectively, given the local driving field. This also gives the birth and return phases, ϕ_b and ϕ_r. These values provide us a trajectory time, $\tau = t_r - t_b$.

First the vector potential seen by the electron during its trajectory $\mathbf{A_{br}}$ is calculated from the local field strength E as

$$A_{br} = \frac{E}{\omega_0} \int_{tb}^{tr} \cos\phi(t)\, dt \tag{6.2.3}$$

and this is then used to calculate the canonical momentum of the electron

$$\mathbf{p} = \frac{-A_{br}}{\tau}. \tag{6.2.4}$$

The equation for the action S outlined in Equation 3.1.15 can be used,

$$S_\omega(\mathbf{p}, t_r, t_b) = \int_{t_b}^{t_r} dt' \left(\frac{[\mathbf{p} - \mathbf{A}(\mathbf{t}')]^2}{2} + I_p \right) - \omega t_r. \tag{6.2.5}$$

which provides the phase term in the dipole moment $\mathbf{D}$, known as the Volkov phase, given by

$$\mathbf{D}(\mathbf{t}) = i \int_{-\infty}^{t} dt_b \left(\frac{2\pi}{t - t_b} \right)^{3/2} a(t)\mathbf{d}(\mathbf{p} + \mathbf{A}(_\mathbf{b}\mathbf{t}))\cdot \\ a^*(t)\mathbf{d}^*(\mathbf{p} + \mathbf{A}(\mathbf{t})) \cdot \exp(-iS(\mathbf{p}, t, t_b))\,. \tag{6.2.6}$$

This is then combined with the Guoy phase ϕ_G — the fundamental phase caused by the focussing and defocussing of the beam as it passes through a focus — given by

$$\phi_G = \arctan(z/z_R) \tag{6.2.7}$$

where z and z_R are the propagation coordinate and Rayleigh length respectively.

The Gouy, plasma and neutral gas phase accumulation terms between the fundamental field and harmonics are combined to create an array of vectors representing the phase mismatch in the propagation and radial directions.

Phase mismatches closer to zero (and therefore closer to white on these colour scales) indicate better harmonic emission. While the earliest half-cycle shows good phase matching at the focus, where the intensity and therefore fraction of atoms ionised is highest, the number of potential emitters is low here. Conversely where the second half-cycle shows good phase matching within the gas target, i.e. where the number of potential emitters is highest, the peak intensity is decreased here due to plasma defocusing and so the ionisation rate is lower. The short region over which phase-matching is maintained, and the observation that the earlier half-cycles will better phase-match higher photon energy harmonics as predicted by the model are in agreement with previous works from our group [16].

Overall, these plots demonstrate that simulations of these high intensity systems cannot be simply reduced to on-axis or 2D simulations, as the off axis contributions are significant and full spatio-temporal resolution is required to capture the full extent of the contributions from each half-cycle. The $t = 0$ fs peak half-cycle seen in Figure 6.2.3 would show no harmonics in an on-axis simulation, and the $t = -3$ fs half-cycle would underestimate the harmonic flux without the ability to resolve the off-axis emitters. As these plots only calculate the phase-matching however they cannot provide a numerical value for this discrepancy.

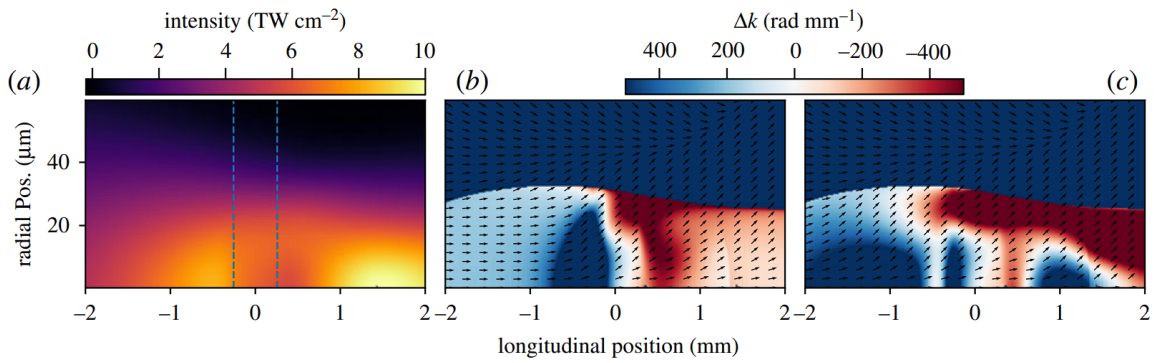


Figure 6.2.4: A comparison of the propagation of a laser field (left) to the harmonic phase-matching of a single half-cycle for both the long (middle) and short (right) trajectories at the -3 fs cycle time, under the same conditions as Figure 6.2.3. The arrows again represent the exaggerated phase-matched emission angle for the emitted 350 eV harmonic. Reproduced with permission from [128].

Using these plots, we can compare the phase-matching angle and phase mismatch for these systems. As the long and short trajectories are individually calculated, we can retrieve some information regarding the harmonic generating efficiencies. Figure 6.2.4 shows that the long and short trajectories also phase-match in differing regions of space in the interaction region. While this is not in itself surprising it highlights an interesting point that by claiming either trajectory to be negligible, or to focus on optimising one for harmonic generation, one may lose harmonic flux. It should be mentioned that this system is not in the near-cutoff regime of harmonic generation where long and short trajectories become indistinguishable, as the available peak intensity here significantly exceeds the necessary limit.

One would assume that strong laser-plasma interactions may disrupt the generation of long-trajectory harmonics, as longer propagation in charged space would allow more opportunity for scattering or dephasing effects to occur. These results appear to suggest that the strong gradients in the local electric field provide in themselves pathways for phase-matching from which the harmonics to be emitted. It is worth noting, however, that with these simple models it is not currently possible to tell

whether the measured harmonics at the end of a beamline would be enhanced or reduced by the existence of the plasma.

6.2.3 A Short-cut to Estimating High Harmonic Flux

To improve on this model we ideally seek a diagnostic that is meaningful in estimating harmonic yield, and by reducing the problem to a combination of key quantities we can attempt to create a simple yet comprehensive model for experimental optimisation. To do this, a simulated laser pulse is propagated as mentioned in Section 6.2.1. Once the laser has been propagated over the interaction volume the field is spatially resampled with few-micron resolution (0.5 x 0.1 micron in the z and radial axis respectively) to compute harmonic yield from regions on the order of millimetres in the gas phase.

When performing the complete HHG simulations, large computational complexities are introduced when calculating the full integrated harmonic spectrum across the interaction region. To minimise this computational load, it is simpler to select a particular harmonic and calculate the generation efficiency for that photon energy from the relevant instantaneous parameters [89]. We must now consider what quantities are needed to construct a model that could be experimentally meaningful, with the caveat that every level of computational complexity may significantly increase calculation time. As discussed in Section 3.1, the following factors are necessary to calculate phase-matching and harmonic flux for HHG:

- The number of emitters, N_e, as this fundamentally limits the total flux per half-cycle

- The wavelength and instantaneous peak intensity, I_M, as these define both the harmonic cut-off from the driving field and ionisation probability

- The total phase mismatch of the beam, Δk

- The angular divergence, $\Delta\Theta_{pm}$, of the beam from the on-axis direction of the beam, calculated using an exaggerated physical angle of emission to limit spatial divergence from the fundamental beam. This means that, even if a harmonic were to be phase matched, if its emission angle would exceed that which would be collected by the spectrometer in the laboratory, it can be ignored.

The geometry and detector size in use in the experimental beamline limit the divergence of the harmonic source to 10 mrad. Beyond this solid angle any photons will clip on the edge of the detector.

Large numbers of these phase-matching plots can be generated, but seeking the ones that indicate best harmonic yield is non-trivial without a metric to numerically estimate the anticipated harmonic flux. To do this we must decide on what terms we wish to represent in a *figure of merit* (FOM) utilising the above factors.

The first term we need must describe the number of emitters we anticipate, given by the target medium density multiplied by the ionisation rate [73, 142]. For this work we use either the PPT or ADK methods depending on if the Keldysh parameter γ_K, is close to or much less than 1 respectively. The general rule of thumb suggests that it is reasonable to select the ADK method for $\gamma_K \leq 0.5$ [143].

The next key terms must represent the reabsorption and decoherence of the emitted harmonics. We derive these from a work by Constant *et al.* who provided an expression for the anticipated flux of HHG emitted within a particular target volume [103] with a simplified solution provided for a target with a constant gas density distribution. This work stated clearly its limitations, including making the assumptions that the local atomic response would be independent of z (i.e. the laser has a "loose" focus), that the gas density ρ would be constant, and that the coherence length for the generated harmonics can be taken as a single value.

Instead we calculate harmonic transmission function for that point in the grid using the expressions given in [103]. This can be seen clearly in Figure 6.2.5, where the comparison of harmonic flux from a system with a constant density profile compared to a Gaussian profile with an equivalent density-length profile. To calculate this, the equation for harmonic flux F is taken from [103]:

$$F = \frac{\omega_q}{4c\varepsilon_0\hbar}\left|\int_{L_{med}} dz\,\rho A_q(z)\exp\left\{-\frac{L_{med}-z}{2L_{abs}}\right\}\exp\{i\phi_q(z)\}\right|^2. \tag{6.2.8}$$

Here ω_q and ϕ_q are the frequency of the target harmonic photon energy and the phase it has accumulated propagating through a medium of length L_{med}. L_{abs} is the absorption length for the harmonic photons. A_q is the atomic response at the harmonic frequency, and Constant et al. suggest that $A_q \propto d_q$ where d_q is the intensity dependant dipole. That work however makes a number of assumptions to limit the complexity of the calculations presented, including assuming a constant density, that the atomic response is constant (i.e. that the laser is in a loose-focusing regime) and that the harmonic emission will end at the end of the target region.

To remove these limitations, the density is written explicitly as a function of the propagation distance, and the integral expanded beyond the boundary of the target. For the atomic response, we will use the suggested proportionality and extract the dipole phase shown in Equation 6.2.6. This will mean that while the original work by Constant et al. used only the phase accumulated by the propagating harmonics, this model will now also include the dipole phase. What will be missing however are the full birth and recombination dipole matrix elements, which are also intensity dependant. While there have been works to study the intensity scaling of the [144], the conclusion here was that no simple power law exists to describing the scaling, though. Typically one may use the approximation provided by Lewenstein *et al.* in [82] as

$$\mathbf{d}(\mathbf{p}) = i\frac{1}{(\pi\alpha)^(3/4}\frac{\mathbf{p}}{\alpha}\exp\left\{-\frac{\mathbf{p^2}}{2\alpha}\right\}, \tag{6.2.9}$$

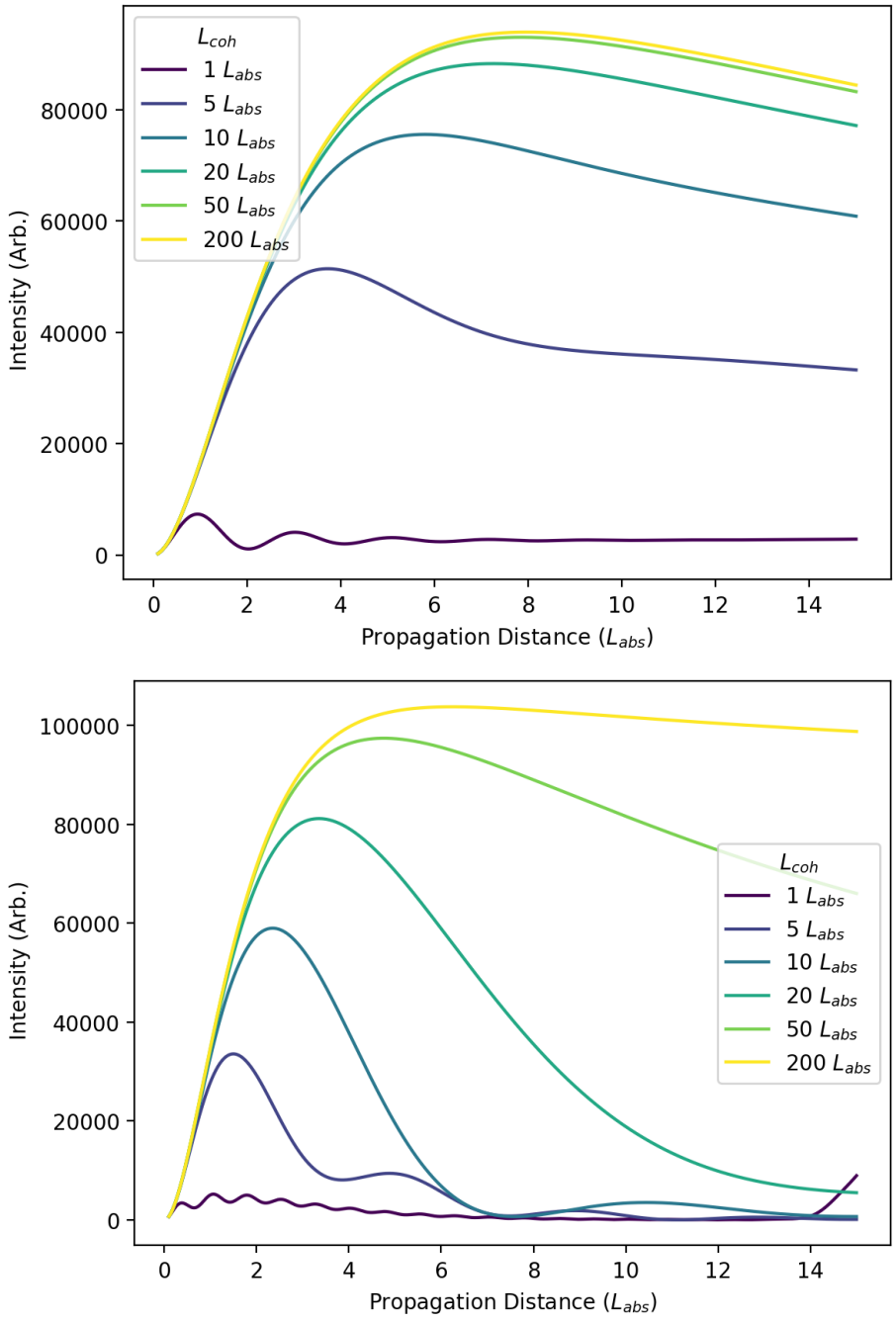


Figure 6.2.5: A comparison of HHG from media where harmonics from a flat-top (above) and Gaussian (below) gas profile along the propagation axis with equivalent density-length products. Each line represents the flux generated when harmonics in the medium all have a fixed coherence lengths L_{coh}, expressed as multiples of the absorption length L_{abs}.

where $\alpha = 2I_p$ and p is the usual expression for the complex momentum vector. As we are not explicitly calculating the electron momenta, and are instead only calculating the canonical momentum for the purpose of calculating birth and return times to give the Volkov phase, this is not an option for these calculations, and we calculate the phase using eq. (6.2.5).

Finally we can use a super-Gaussian envelope to limit the accepted angular spread of generated harmonics. This is used to limit the FOM to represent the harmonics one would realistically detect in an experiment.

A figure of merit value, F, is proposed here, combining these terms and integrating them over a 2D slice of the radial axis r, and propagation axis z, to calculate a value proportional to harmonic yield, given by

$$\mathrm{F} = \left| \int dr \int dz\, \rho \cdot W_{\mathrm{ion}}(I_m, n^*, m) \cdot \exp\left(- \left(\frac{|\Delta\Theta_{\mathrm{pm}}|}{\theta_{\mathrm{acc}}} \right)^{10} \right) \right. \\ \left. \cdot \exp\left(-\frac{L_{\mathrm{prop}}(z)}{2L_{\mathrm{abs}}(\rho)} \right) \cdot \exp\left(\frac{i\pi z}{L_{\mathrm{coh}}(\rho)} \right) \right|^2 . \tag{6.2.10}$$

$W_{\mathrm{ion}}(I_m, n^*, m)$ is the ionisation rate, recalling that that I_M is the instantaneous peak intensity and n^* and m are the angular momentum and magnetic numbers. $\Delta\Theta_{pm}$ is the phase matched angle of the harmonic energy in question relative to that of the propagation of the laser. $L_{\mathrm{coh}} = 2\pi/\Delta k$ is the coherence length, and $L_{\mathrm{abs}}(\rho)$ is the absorption length of the medium for the photon energy of interest as a function of $\rho(z)$, the target medium density profile. δz is the length of the grid element in the propagation direction. θ_{acc} is the acceptance angle for detector from the target, which for our system we stated was 10 mrad. $L_{\mathrm{prop}}(z)$ is the distance from the point of emission of a harmonic to the end of the simulated region.

As with the plots shown previously, the FOM is calculated for each half-cycle of the laser field, and the data is then collated and summed over the half-cycles.Figure 6.2.6 shows an example of some factors involved to calculate a FOM value for a given half-cycle. The dipole phase is included in these plots as it is the least intuitive source of phase shift and therefore is included in every set of plots as a diagnostic, to help identify outliers - the other macroscopic phase-matching terms (gas and plasma density, and Guoy phase) can be more easily inferred from the other plots.

The plots in Figure 6.2.6 show steps in the simulation of a much lower target photon energy harmonic than previously discussed: the 23^{rd} harmonic of an 810 nm laser field generated in argon. Compared to the 350 eV harmonics in helium where the attenuation length is 3.45 mm, the attenuation length at 34 eV in argon is 20.6 µm. This means that, where one might have expected optimal harmonic emission in the central region of the gas target, this plot indicates that the reabsorption in the gas beyond the boundary of the gas target would prevent this from reaching the detector, and the observed harmonics would instead be generated in this lower density medium.

These simulations were performed on the high performance computing clusters hosted by Imperial College. The simulated space was resampled to 1200 by 200 points ($z \times r$). 10 simulations could be run on a single core on a compute node within 8 hours, using around 68 GB of memory. The largest use of memory in these simulation is dictated by the resampling used for the FOM calculation: 1000 points in the propagation direction required around 54 GB per job, and 1200 points required around 68 GB, showing a linear dependence. As such the number of simulations performed on each job was dictated only by the time allowance on the computation queue the jobs were submitted to.

For a representative number, the datasets presented here were calculated using sets of 4096 simulations (32 peak pressure values, 32 target length values, and 4 pulse energy values). The "short jobs" queue was used, as this allows for a large batch of

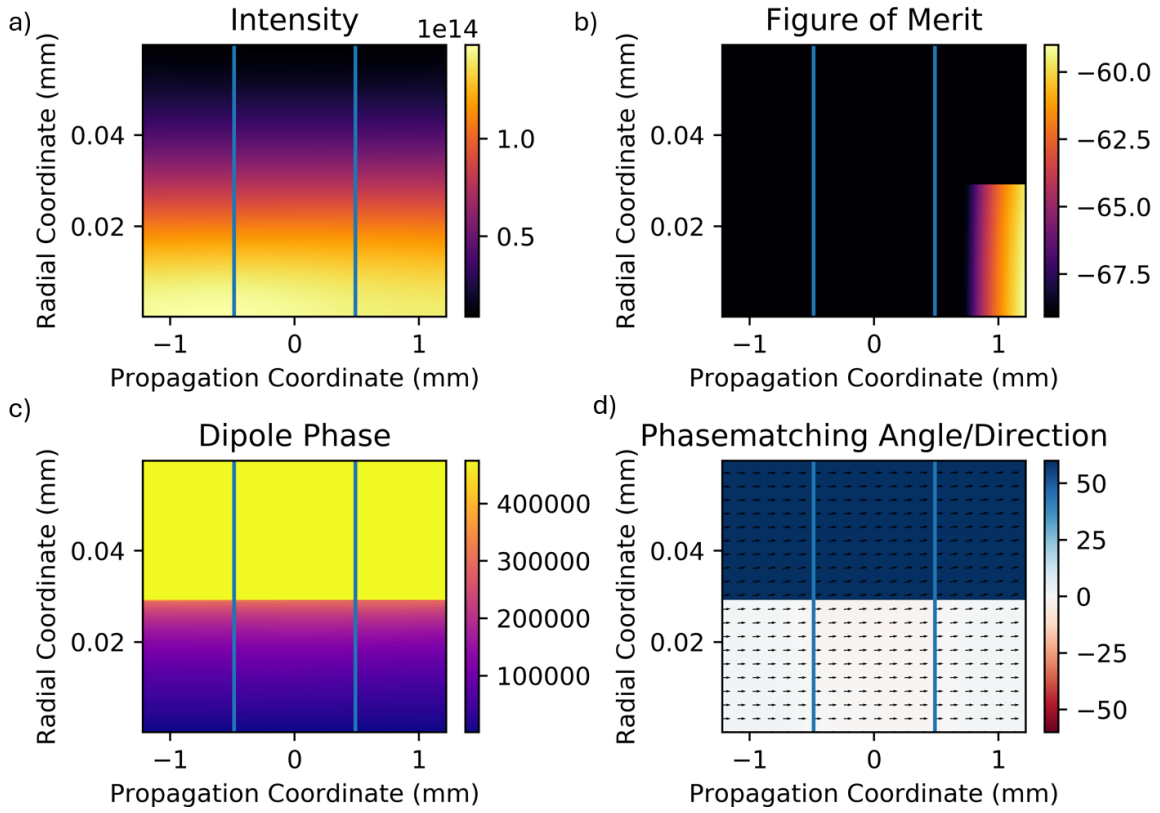


Figure 6.2.6: A visualisation of some of the steps in calculating a FOM value. These plots are for a 12 fs, 810 nm, 75 µJ pulse focused to a 50 µm focal spot diameter. a) The intensity profile of the propagating laser through a gas target and (b) The natural log of the FOM calculated for each point in the propagated field. c) and d) show the dipole phase and phase matching plot as described in Figure 6.2.3 and Figure 6.2.4. A hard cut in the radial extents in the phase matching and FOM plots as the local peak intensity drops in the radial profile of the laser field for the cut-off to reach the target photon energy.

jobs to be submitted, and 384 of these jobs each using a single CPU on a node (i.e. unparallelised) and the full batch of jobs was completed within 9 hours, including the waiting time required in the jobs queue. Given a maximum memory allowance of 920 GB and CPU count of 256, with careful parallelisation one could maintain this same level of precision and time per computation and perform 76 parallel FOM computations on a single node, reducing the batch size of jobs for this same number of computations lusted here to only 5. Using this method a finer resolution may be measured to create an interpolable grid as a lookup table for anticipated harmonic

flux, or the bounds of the simulations can be increased to provide a wider sample region to study the scaling laws of HHG. With the scripts as currently available, the pulse energy and duration, focal spot size and position, gas used, peak pressure and profile shape and laser wavelength can all be freely scanned without further modification to the code.

Returning to the calculated FOM data, we seek to find a comparison to other works in the field, such as a recent work which has similarly sought to parameterise and analytically optimise the HHG process by matching experimental results to numerical models using the SFA [37]. The publication prefaces this work with the statement that they "limit [the study] to intensities in the medium well below 10^{15} Wcm^{-2}, where conventional phase-matching dominates". They also note that there may be regions beyond critical ionisation thresholds in the medium that may make phase-matching possible. Finally, the harmonics shown here are limited to the XUV, and the authors do not explore the few-hundred eV photon energies we seek to reach in this work. Nonetheless this publication provides a good framework with which to consider the data in this work.

A density-length product relation between the minimum phase-matching medium pressure, p_0, and Rayleigh length, z_R, for harmonic phase-matching proposed in [37], defined by

$$p_0 z_r = \frac{2\varepsilon_0 c k_B T f_i}{\omega \Delta\alpha_q}. \tag{6.2.11}$$

where ε_0 is the vacuum permittivity, c is the speed of light in vacuum, k_B is the Boltzman constant, and ω is the central frequency of the driving laser. $\Delta\alpha$ is the

difference in polarisability of the medium for the target harmonic, q, and driving laser ($q = 1$) given by

$$\Delta\alpha_q = \frac{2\varepsilon_0(n_q - n_1 - 2)}{\rho}, \tag{6.2.12}$$

where n_q is the refractive index for the q^{th} harmonic. f_i is a spatial phase-matching parameter derived from the laser focal position relative to the centre of the cell defined by

$$f_i = \frac{z_R^2}{z_R^2 - z^2}\left(1 - \frac{2z\beta(z)}{qz_R}\right), \tag{6.2.13}$$

where

$$\beta(z) = \alpha_i I(z) - \frac{g_i c m_e}{\alpha\lambda I(z)}(q\omega - (I_p/\hbar))^2. \tag{6.2.14}$$

Here g_i is a constant related to whether the short or long trajectories are being considered, and are 0.22 and -0.19 respectively. m_e is the electron rest mass, and $\hbar$ is the reduced Plank constant. α_i is 0 for short trajectories, and $-0.16\alpha\lambda^3/(m_e c^3)$ for long trajectories, where α is the fine structure constant.

Using these expressions we can calculate an expected p_0 for a given system. For the nitrogen K-edge, we find a value of 6.3 bar, consistent with previous findings in the group that high backing pressures are needed to optimise phase-matching in the SXR region.

The issue here, however, is that to be able to use p_0 for phase-matching it is required that we operate in the "low ionisation degree" regime. We know explicitly that in order to reach 400 eV harmonics with a 1.8 μm wavelength driving field in helium we must have peak intensities of at least 500 TWcm^{-2}. While this is not a challenge to achieve experimentally, corresponding to only 150 μJ with an 77 μm beam waist and 12 fs pulse duration, there will undoubtedly be strong ionisation at these peak intensities.

As such we must move to the scaling regime the authors of that work outlined, which describes pressure-length scaling of the HHG flux. For this a hyperbolic relation was provided for the efficiency at a given pressure, p,

$$(p - p_0)L = \frac{\zeta k_b T f_i}{\sigma_{abs}}. \tag{6.2.15}$$

L here is the medium length, σ_{abs} the absorption length for the calculated harmonic, and ζ, an empirical factor of 3 corresponding to an optimum harmonic flux for a cell of length 3 L_abs (where L_abs the absorption length of the system), provided as 3 by Weissenbilder et al. in their work. That work states that this second regime is shown on the vertical branch of the hyperbola in Figure 6.2.7, and corresponds to a short cell at pressures larger than the p_0, such that the phase mismatch added by the plasma cancels the intrinsic phase mismatch of the neutral gas, as described both by Equation 3.1.26 and the wider literature [141, 145].

If we are correct that harmonic flux is linearly proportional to the calculated FOM, we would expect the FOM to follow these same scaling relations, at least within a non-overdriven regime. To begin understanding this, we attempt to plot the FOM data in a similar form as is presented in [37]. To draw a direct comparison between the FOM and that work we compare the emission of harmonics under the same conditions: a central laser wavelength of 810 nm and with peak intensities of 150 and 450 TWcm^{-2}. More specifically, we use a focal spot diameter of 50 μm, pulse energy of 75 μJ and pulse duration of 12 fs.

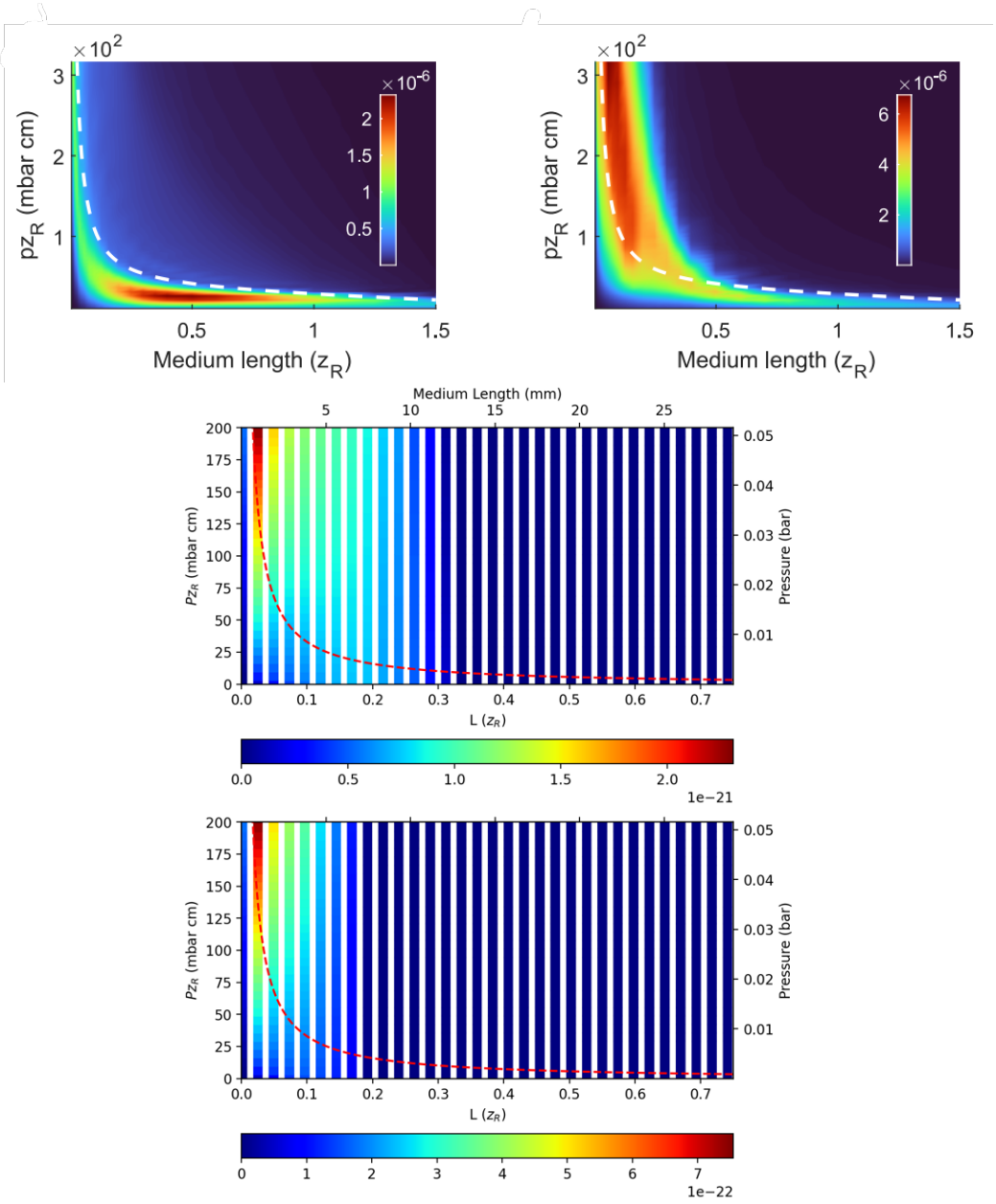


Figure 6.2.7: A comparison of HHG flux in low (top left) and high (top right) intensity regimes (reproduced with permission from [37]) compared to the calculated FOM values for the high (middle) and low (below) intensity regime (below). The high and low intensity correspond to 450 and 150 $\mathrm{TWcm^{-2}}$ respectively. The HHG is is the $q = 23$ harmonic of an 810 nm, 12 fs pulse in argon, matching the work by Weissenbilder et al. As the FOM plots are scatter plots, the white areas indicate spacing between data points.

The hyperbola presented by Weissenbilder et al. ¿ matches the position corresponding to greatest peak harmonic fluence at higher peak intensities in the resulting FOM calculations. In Figure 6.2.7 we see a comparison of the data from a FOM scan with data presented in that work, simulated with the same peak intensities and and the same photon energies as in [37]. We see a good qualitative agreement in the shape of the data. The red dashed line in those figures represent the pressure-density curve defined by eq. (6.2.15).

The peak harmonic intensity values from the figure of merit broadly match the position of the anticipated optimum flux using the density-length product hyperbola presented by Weissenbilder et al. at higher peak intensities. We do not however see the expected shift through the elbow of the hyperbola at lower intensities towards an optimal flux in longer cells.

To examine whether the results of this FOM model are comparable to the full SFA calculations, fig. 6.2.8 shows the harmonic flux for the same set of parameters at only the lower peak intensity ($150\,\mathrm{TW}^{-2}$), using the full SFA HHG code. The harmonic flux is calculated by integrating the calculated harmonic emission over a range of photon energies E_{int}, given by $E_{int} \in [E_q - E_{fund}/2, E_q + E_{fund}/2]$. E_q and E_{fund} are the the photon energies of the target harmonic and fundamental field respectively.

Here we also see broad agreement with the match of the peak harmonic flux curve defined by eq. (6.2.15) to the optimal points for harmonic flux, but the SFA calculations show a less rapid drop in harmonic flux as a function of gas target length than were seen with the FOM. Crucially however we continue to see that, even at low peak intensity values, the peak harmonic flux follows the vertical side of the hyperbola.

These simulations required a factor of 2 more CPU nodes and used a comparable amount of memory, but were only run at 1/10 the sampling resolution in the propa-

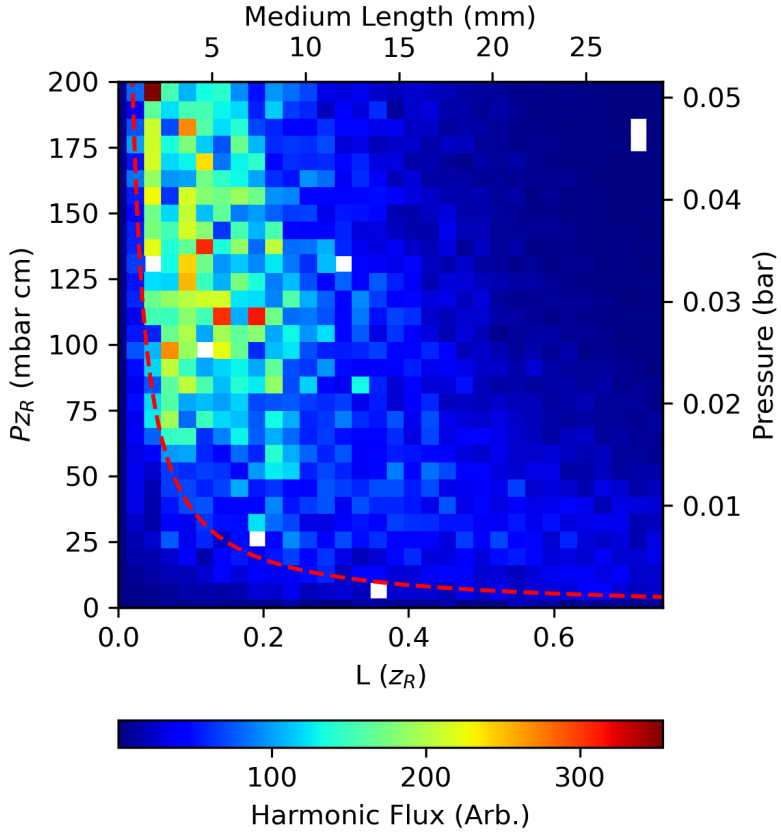


Figure 6.2.8: Harmonic flux calculated using the full HHG simulation code, with parameters matching the 150 $TWcm^{-2}$ plots shown in fig. 6.2.7. A good qualitative match can be seen between the FOM and HHG flux. White areas again indicate missing data points. There are two times fewer points in this calculated for this data set than the FOM plots above, and the spatial resolution in the z-axis is an order of magnitude lower while using the same amount of memory on the computing cluster.

gation direction (i.e. step sizes on the order of few-micron). While this is acceptable for these simulations as there is no substantial spatial reshaping of the focal spot, in the overdriven regime this would need to be increased as plasma will cause changes to the beam shape near the focus. This means that to achieve the same spatial resolution as the FOM calculations would require at least 10 times as much memory. Two times fewer data points were collected for the SFA data set, as the simulations took a factor of 2 longer to run. It is worth noting that the SFA simulations also take substantially longer when approaching the overdriven regime (increasing from a few

hours to around a day per simulation). On the other hand provisional tests with the FOM model appear only to increase runtime by around 10 - 20 % in these regimes, owing primarily to additional time taken in computing the laser propagation — an unavoidable common factor between the two models.

Further study with the full SFA calculations, using the same number of data points and equivalent propagation axis resolution, would provide important next steps to study the "goodness of fit" of the FOM by presenting a ratio of FOM to SFA-calculated HHG flux. This would be time intensive however, as it would require a substantial increase in requested resources from the computational cluster, also increasing queue times before accounting for the increased simulation time.

Instead we can examine the effectiveness of FOM model by investigating individual values of the pressure-length product, and comparing how the harmonic flux varies as a function of medium length. In fig. 6.2.9 we see a comparison of the computed HHG flux using the SFA and FOM models at 150 mbar cm and 35 mbar cm. These correspond to a region of higher and lower peak harmonic flux respectively as seen in the plots shown in fig. 6.2.7 and fig. 6.2.8 when varying along the density-length product axis. The plots here are normalised to the peak flux value seen for both the SFA and FOM models along the lines presented here.

We can see that while varying along the density-length product axis, the peak flux drops to around 40 % of its peak value for both of these calculations. Along the medium length axis, however, the FOM model appears to underestimate HHG flux from longer gas cells, with the harmonic flux values dropping rapidly to nearly zero for cell lengths around 0.3 times the Rayleigh length. As cells in this regime typically see no inherent "penalty" due to poor phase-matching, as we saw good phase matching across the entire propagated region in fig. 6.2.6, the author is led to believe that this is likely due either to an over-representation of either the reabsorption factor or harmonics emitted as a function of ionisation rate.

The first of these suggestions is supported by the fact that when the cell grows longer the calculated harmonics present at the end of the propagated distance drops dramatically if reabsorption is over-represented. Conversely, the second suggestion stems from the fact that if the ionisation-rate dependence of the FOM value was over-represented, the regions of high peak intensity would generate higher flux. As the harmonics are propagated to the end of the simulated region, these harmonics would be substantially more attenuated by reabsorption than in shorter cells. Further investigation here is important to better develop the model, however this could not be carried out within the timeline of the project, and we will instead return to comparison of the FOM to works in the literature.

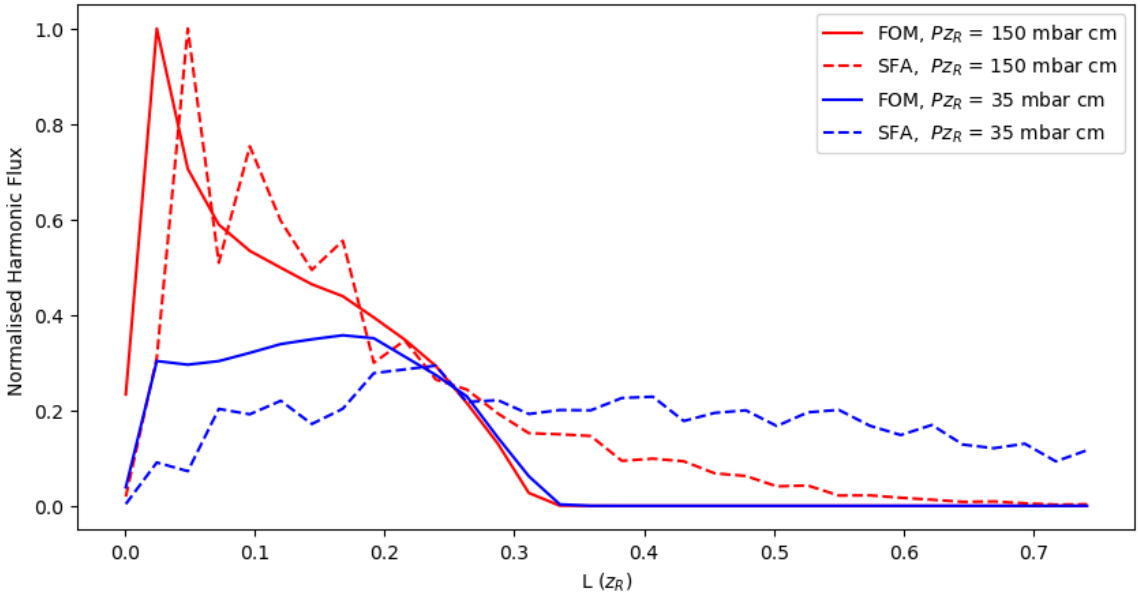


Figure 6.2.9: A comparison of the computed HHG flux using the SFA (dashed) and FOM (solid) models at 150 mbar cm and 35 mbar cm, with data taken from fig. 6.2.7 and fig. 6.2.8 respectively. These are normalised to the peak flux value seen for both the SFA and FOM models along the lines presented here, providing a normalised flux value for each model. The variation of the peak harmonic flux with density-length product appears to match well, falling to around 40% of the peak value. The variation with medium length however does not appear to match well, rising and falling far more sharply with the FOM than is seen using the SFA model.

The authors do not describe the particulars of the gas distribution used in the models in [37], and the observed discrepancy could come down to reabsorption in the tails of the medium in the targets modelled, as when comparing the anticipated harmonic flux seen in Figure 6.2.5 and described when discussing Figure 6.2.6.

For evidence of this one may look at the FOM plots for the highest flux half-cycles for a consistent set of parameters, expanding only the length of propagation region we are considering for the FOM. In Figure 6.2.10 we see the FOM maps calculated for resampled regions at 2, 5 and 10 times the length of the gas target L_t. The $10L_t$ plot has been spatially shifted for the calculation, as it was abundantly clear that there was no benefit to calculating the FOM from positions earlier in the propagation direction due to reabsorption of the harmonics.

The gas profiles here follow the structures shown in Figure 6.2.2. The particular experimental parameters for these plots are still a 12 fs pulse with a central wavelength of 810 nm and pulse energy of 75 μJ, a 100 μm focal spot diameter, and a gas cell peak pressure of 0.05 bar and diameter of 0.98 mm. This corresponds to a peak intensity of 150 $TWcm^{-2}$, matching the works from [37] with peak HHG efficiencies along the horizontal edge of the hyperbola. The absorption length and X-ray refractive index for these 35.2 eV harmonics for 1 bar of Ar at 810 nm was calculated using data from the CRXO database [44], with a calculated absorption length of 23.6 μm. This is further verified by examining a plot of harmonic build-up along the propagation axis from the full HHG simulations, also seen in fig. 6.2.10. Here we use a 4 mm long gas cell, again with a peak laser intensity of 150 $TWcm^{-2}$, and we see that the harmonic flux continues to increase beyond the end of the cell.

As the colour bars on the FOM plots in fig. 6.2.10 show harmonics over the same dynamic range (around e^{10}, or 4 orders of magnitude), we can see from the colour maps that the region of significance for the generated harmonics becomes longer as we reach the edge of the gas region. This clearly corresponds to the drop in local

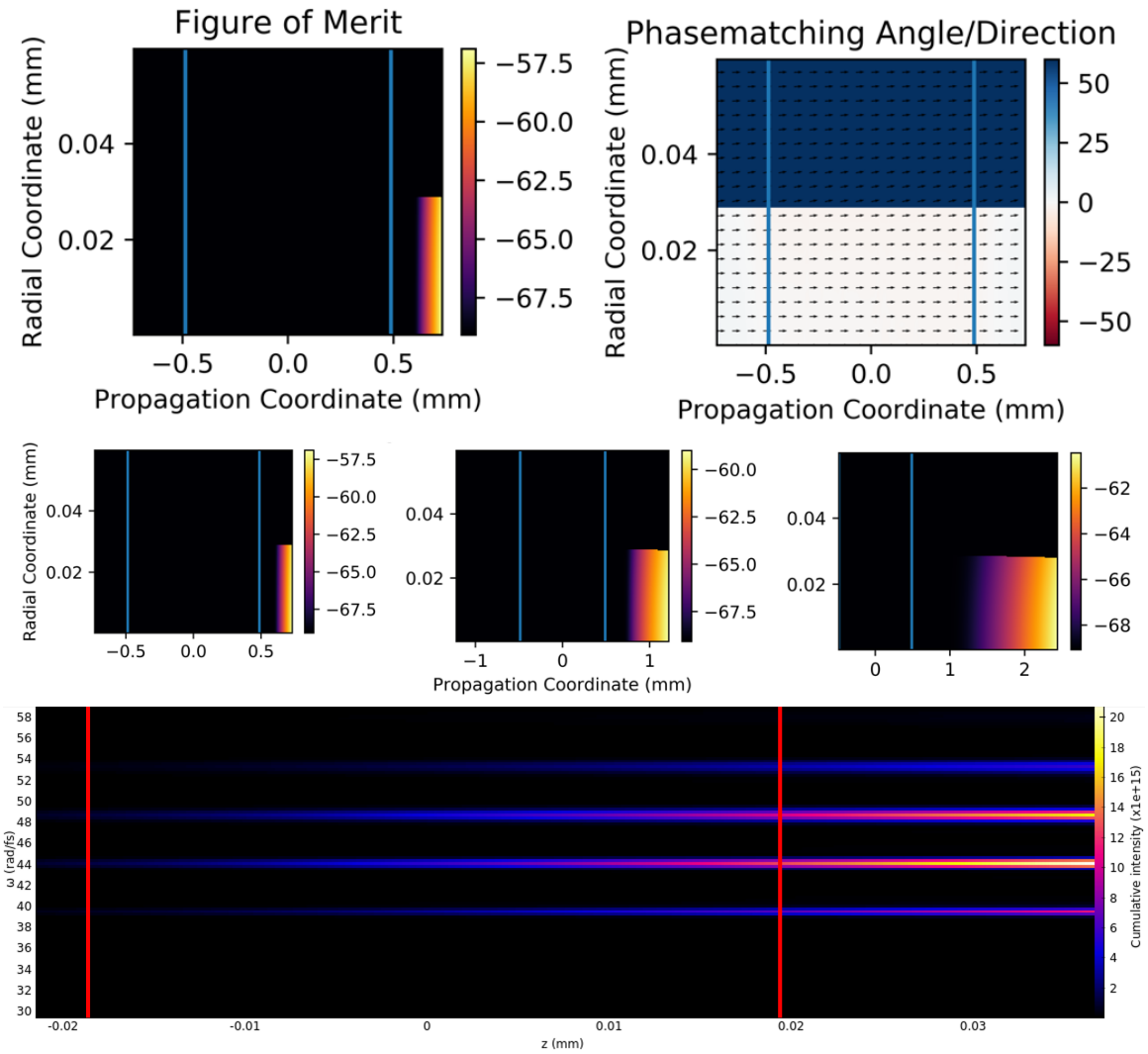


Figure 6.2.10: Above: The FOM and phase-matching diagnostic plots for 35.2 eV harmonics in argon, showing that while good phase-matching is achieved across the simulated region, the reabsorption in the wider gas region means that only harmonics at the edge of the target would provide any harmonic flux. Middle: The FOM diagnostic plots for resampled propagation regions at 2, 5 and 10 times the length of the gas target (left to right). The colour bars represent the log of the FOM values. Below: The harmonic build-up for the 19^{th} - 25^{th} harmonics along the propagation axis of the laser field. These harmonics are calculated for the centre of the laser field (i.e. $r = 0$), and the red lines indicate the edges of the gas target. As with the FOM plots, we see that the peak harmonic flux is achieved well beyond the edge of the cell.

gas pressure and reduced reabsorption in the propagation that follows. These plots also appear to reinforce the earlier suggestion that the FOM model underestimates harmonics in a longer cell by overestimating the reabsorption in the neutral gas. While the SFA plot at the bottom of fig. 6.2.10 similarly shows reaching a maximal harmonic flux beyond the edge of the gas cell, the harmonic emission around the centre of the cell shown is within an order of magnitude of the harmonics end of the cell. Given an absorption length of 23.6 μm at this harmonic energy, we would therefore expect only a drop of e^2 (or around 1 order of magnitude) flux decrease between the centre and end of the cell, leading to a difference of 2 orders of magnitude from the SFA model, compared to 4 in the FOM model.

In Figure 6.2.11 we see the compiled FOM calculations for the same resampled regions. While we still do not see the shift through the elbow of the hyperbola shown in Figure 6.2.7, we now see a "good" flux from a much wider range of cell lengths, but a repeated iteration that a higher pressure in a narrower gas target would be expected to yield higher photon flux. This point is very clear if we now extend our simulations to a regime that one might consider unfeasible. Instead of the 3-tiered gas distribution shown in Figure 6.2.2, we change to a much more rapidly decaying density profile, decaying directly down to 10^{-5} bar, as seen in Figure 6.2.12 profile. The gas pressure decay rate is kept at the same value of 105 μm. This is not feasible with any currently available experimental design, as the gas confinement naturally leads to rapidly expanding gas gets in the propagation directions. With this density profile however we see the movement of the anticipated harmonic flux through the elbow of the hyperbola and more parallel to the x-axis of the plot, as seen in Figure 6.2.13.

These plots highlight the importance of clear description of the gas phase targets used for works concerning HHG efficiency scaling, and further motivate the development of the variable length target described earlier. Without a clear mathematical model for the gas targets one is using one may struggle to properly optimise flux. In the low

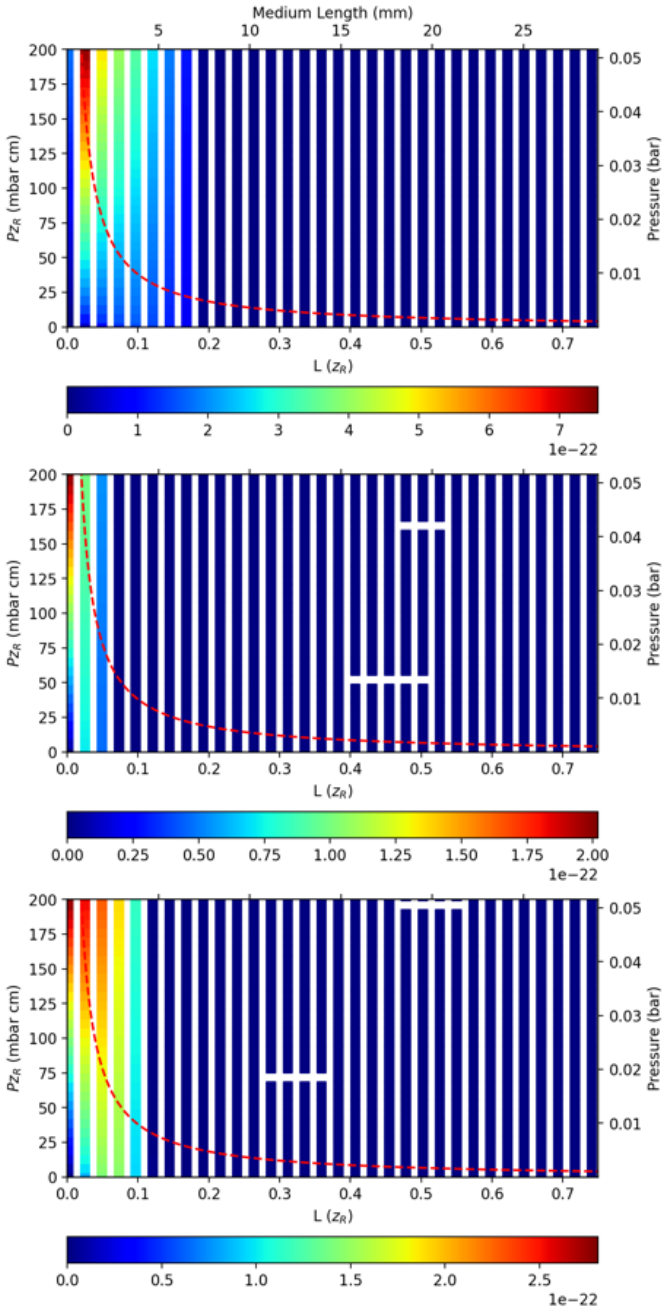


Figure 6.2.11: The calculated FOM values for resampled regions at 2, 5 and 10 times the length of the gas target. There is a clear broadening of the region in which higher generation efficiency is observed, but the curves continue to show a higher yield at higher backing pressures for the generating medium. These plots are scatter plots, and the white areas are simply a plotting artifact.

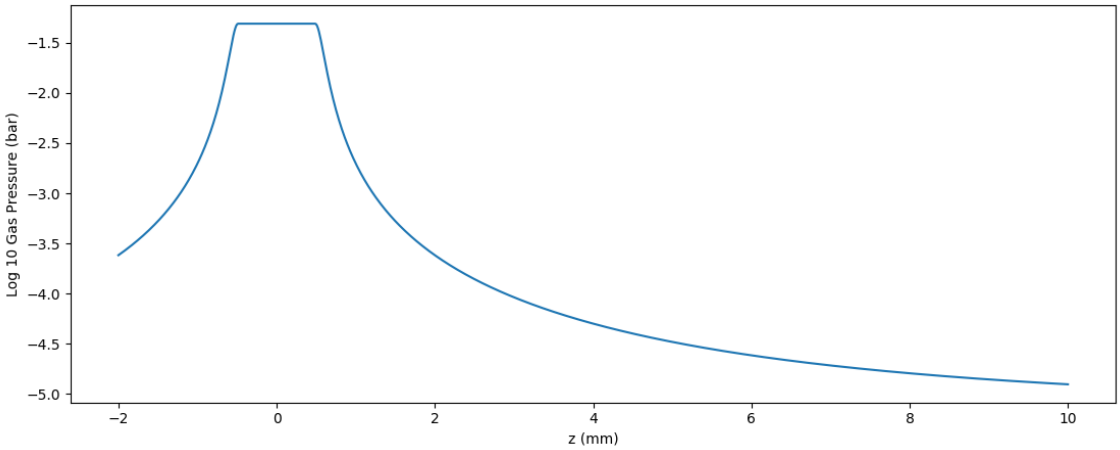


Figure 6.2.12: A more sharply decaying, if not strictly experimentally feasible, gas target profile for HHG.

photon energy range this is clearly caused by reabsorption in the diffuse gas medium, and for higher photon energy harmonics this will be driven by ionisation dynamics seen in Figure 6.2.3. The plots here also motivate an in-depth characterisation of the specific gas density profile of the variable-length gas target described earlier.

Overall, we find agreement with the work by Weissenbilder *at al.* regarding the hyperbolic curve proposed in their works outlining a pressure-length scaling regime in which HHG can be efficiently produced. The divergence from that work lies in the particular consideration of the gas targets used for harmonic generation and their impacts on measurable harmonic yield. The outcomes here provide a clear path for the next steps for this project. These first calculations provide a good starting point for experimental and computational exploration of the accuracy of the FOM models, and a combination of experimental study and further analytical consideration is needed to find which of the discrepancies lie in the FOM calculation itself, and which lie in differences in the gas target profiles between this work and others in the literature [141, 146]. To begin work in this vein, a comparison of the FOM calculations to a pre-existing SFA calculation show that a comparable variance of harmonic flux with density-length product is achieved, but that the dependence of the harmonic flux on gas target length is inconsistent between the two models, outlining a route for further

study. These avenues for progress will hopefully allow this figure of merit to provide a more unified and robust framework for understanding HHG in both the VUV and SXR regimes, and would mean the simulations could be used to calculate HHG in the overdriven regime using a 1.8 μm driving laser field matching our laboratory experiments to generate harmonics at the oxygen and nitrogen K-edges.

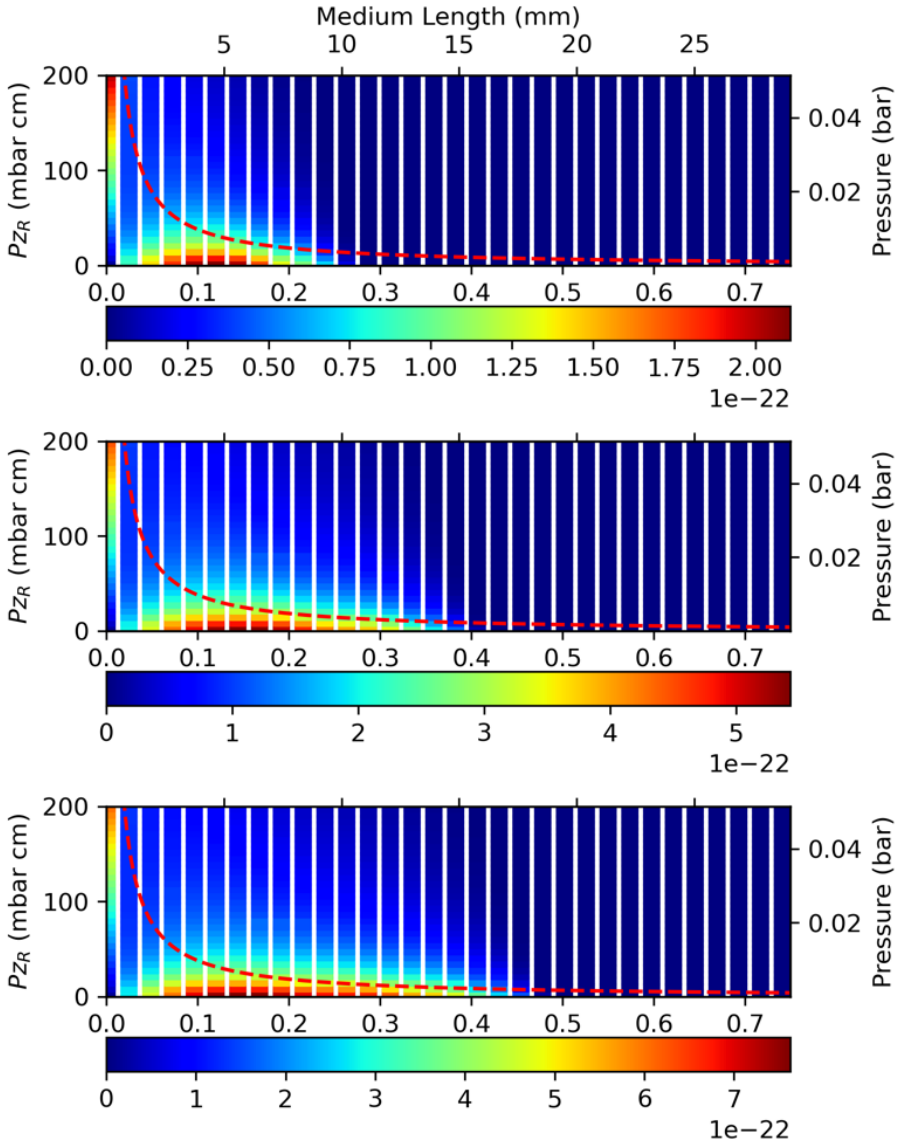


Figure 6.2.13: FOM calculations using the gas target with gas pressure decaying more rapidly to the vacuum. Here we now see the peak efficiency values for three different peak intensities (100, 130 and 150 $TWcm^{-2}$ from top to bottom) along the lower side of the efficiency hyperbola.

7 The Interaction of Liquid Jets and Intense Laser Fields

As previously discussed, VUV and X-ray flux through HHG scales quadratically with the number of emitters in the target region. Solid and liquid phase media typcially have a density on the order of 10^2 – 10^3 times higher than the few-bar gas pressures used for gas phase HHG. Solid phase HHG has seen a great deal of research over the past decade [52] with harmonics observed in crystalline and amorphous samples[147, 148].

While HHG from solid phase samples are limited in photon energy by the damage thresholds of generating media, their density and spatial confinement compared to gas targets mean harmonics can be generated from a large number of parent atoms or molecules without reabsorption in the spatial wings of a gas target. This also means that they are ideal for industrial and scientific applications, as the harmonic source needn't be replaced and they do not have the same requirement to be constantly pumped by vacuum pumps, and also means that compact devices could be constructed using these sources. The nozzles used by this group may need periodic replacement, but this can be on the scale of weeks of constant operation.

The liquid phase appears to offer both the sample stability and number density of the solid phase, and the shot-to-shot sample recovery of the gas phase, but it is substantially less explored. A small number of papers have so far been published on HHG from liquid targets [94, 149, 150], but the underlying mechanisms of their generation remains in question. The earliest studies on the matter involved focused on liquid droplets [149, 151] and targets in cylindrical jets [152]. Recent work has also been performed using liquid jets on the few- to hundred-micron thickness liquid jets [94, 150], but these used laser pulses with many cycles ($\geq$30 fs).

As was shown in Section 6, ionisation dynamics are a key factor when calculating harmonic yield. While the peak intensities, and hence peak photon energies, considered in these works have all remained low ($\leq$100 TWcm^{-2}), the high medium density means that even at these peak intensities the electron densities cause visible plasma plumes at the liquid surface. A good understanding of the interaction between the driving laser field and the liquid medium is needed as, if the pulse is substantially altered in its propagation through the target, the field driving the harmonics will not be well characterised. The ionisation dynamics here have importance beyond the HHG community, and would be of similar interest when investigating the machining of semiconductor surfaces or interactions between intense laser fields and biological and biochemical samples [46].

In order to study these topics further, the propagation and HHG code described in Section 6 was further developed by the author to accommodate harmonic generation in a liquid-equivalent density gas for comparative study with experimental results achieved both prior to and alongside this work [45, 46, 93, 153, 154]. In this chapter experimental work performed to measure liquid-phase HHG is presented, with which the author assisted but did not lead. Simulations using the code outlined in Section 6.2.1 with necessary modifications used to model and help understand the obtained experimental results are then presented. First the interaction of the laser pulse with the jet are be discussed, and then HHG emission from the bulk liquid. The code modifications included creating appropriate simulated interaction regions (e.g. the target sample densities, loss mechanisms through absorption and plasma reflection at the liquid surface) and modifying the preconditioning of the ODE solver to use appropriate step sizing and error tolerances for propagation through the medium as will be discussed later. Code was also written to process the simulation results to apply electron scattering curves to match experimental data.

7.1 Liquid-phase HHG: Experimental Background

To measure HHG from a liquid target a series of experiments was performed in which a 1 – 2 μm thickness liquid jet, created by flowing isopropanol backed by gaseous nitrogen through a 3d-printed nozzle made to an in-house design within a vacuum chamber pumped down to ≈10^{-4} mbar [45, 155]. The jet deteriorates after ≈10 mm, after which it was terminated in a conical collector which drew the liquid out of the chamber. A cold trap was used to collect and condense the liquid vapour to maintain a low vacuum pressure. This chamber was kept below 10^{-4} mbar using a combination of screw and turbomolecular pumps. While the jet was in operation a 1.8 μm laser with a duration of 13 fs, pulse energies of up to 500 μJ was incident on the jet's surface. The CEP was measured using a 2f-3f interferometer, set using a pair of fused silica wedges and actively stabilised using a motorised mirror in the TOPAS OPA, all as described in Section 4.

Using peak intensities on from 10 – 70 TWcm^{-2}, the system was driven to generate HHG up to 50 eV. The generation chamber was connected to a spectrometer chamber containing a slit, variable line spacing diffraction grating (Hitachi, 100 lines/mm) and microchannel plate detector (MCP, Photonis APD059M-01) imaged by a CCD camera (pixelfly PCO). This chamber was pumped down to ≈ 10^{-6} mbar using a combination of a scroll and turbomolecular pumps. A schematic image of this system can be seen in Figure 7.1.1. The harmonics generated by the system can be seen in Figure 7.1.2. To confirm that the harmonics were emitted from the liquid the jet was rotated perpendicular to the driving laser, and no harmonics were seen emitted from the vapour phase surrounding the jet. The jet was then scanned horizontally, as seen in Figure 7.1.3, and the harmonic flux dropped dramatically at the edges of the jet. At the edge of the jet one would naturally anticipate a drop in harmonics as the edge of the jet is curved into a rim by the surface tension of the flowing liquid. This is seen in Figure 7.1.1. Beyond the width of the jet however there will be vapour phase material as the jet evaporates into the vacuum chamber.

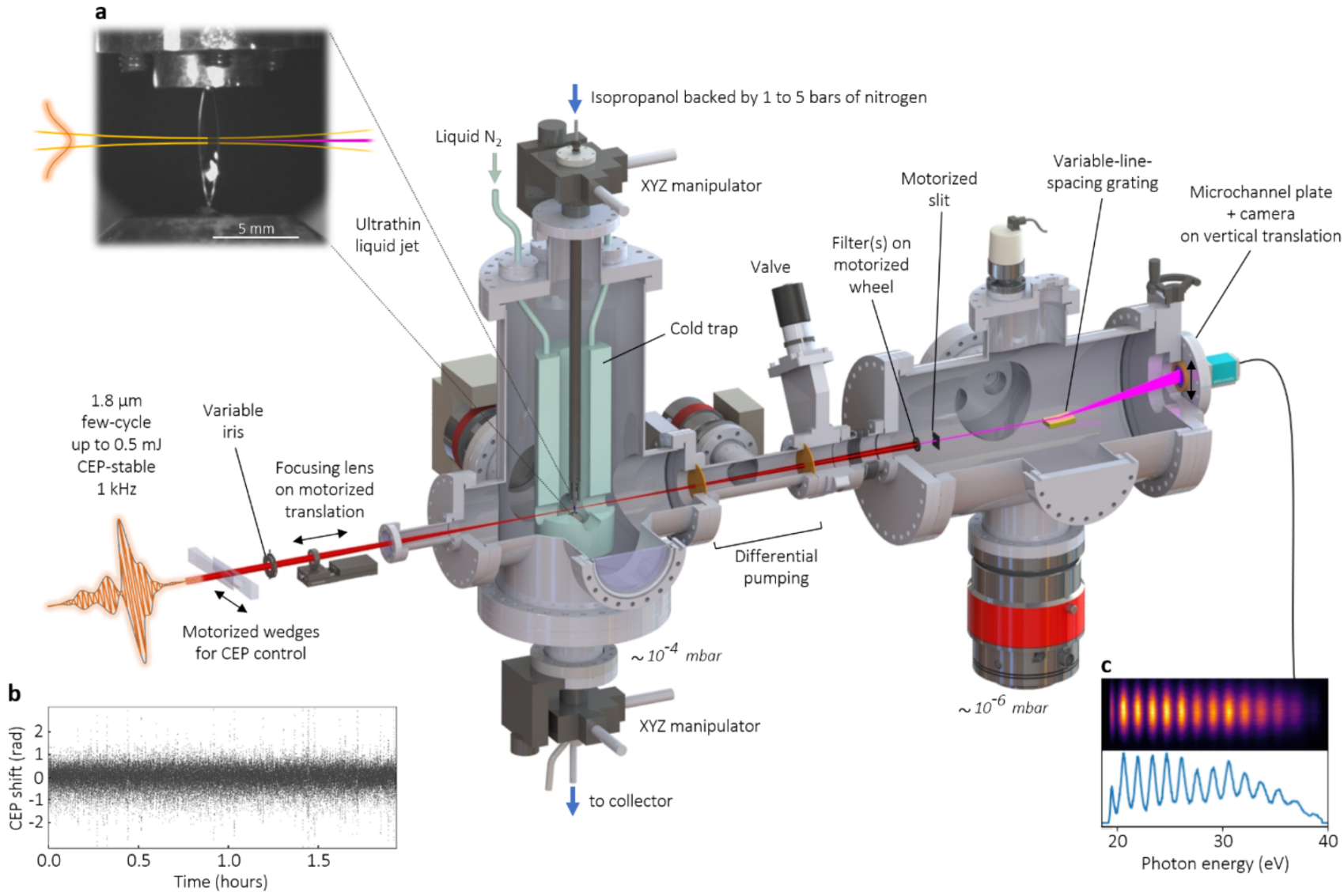


Figure 7.1.1: The apparatus used to generate HHG in the liquid phase in isopropanol. (a) shows an image of the optically flat liquid jet, (b) shows the CEP stability of the laser used to drive the harmonics, and (c) shows typical harmonics both spatially resolved (above) and integrated (below) from the system. As the path from the beam's entrance into the chamber to the MCP was fixed, a 3-axis translation stage and rotatable flange were used to ensure the jet could be moved onto the laser beam. Figure created by Clement Ferchaud, and reproduced with permission from [93] under CC BY-NC-SA 4.0.

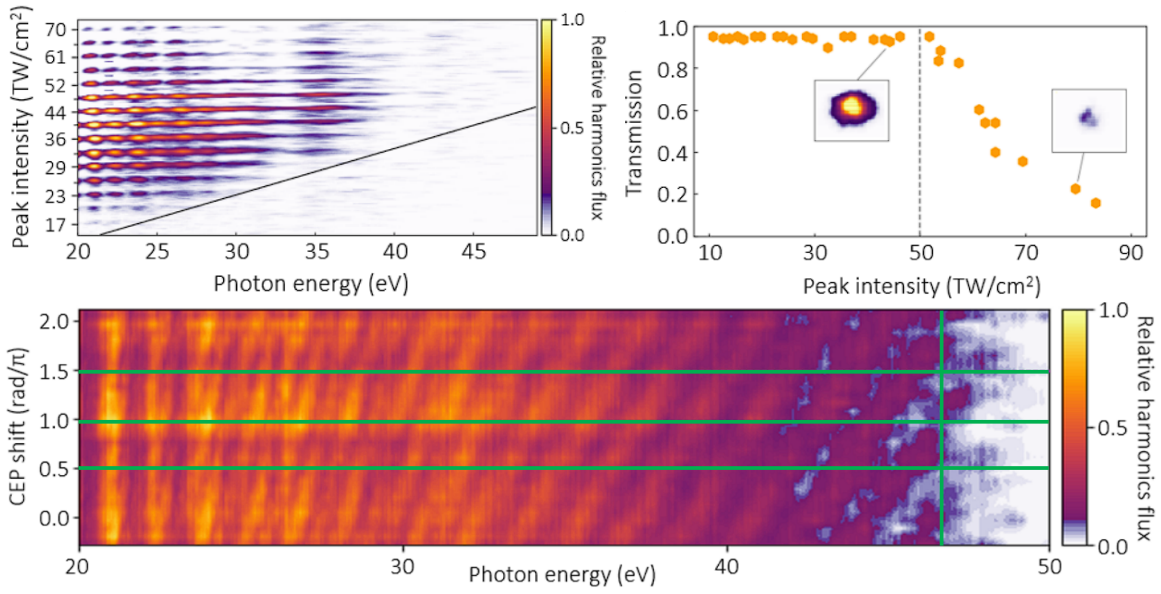


Figure 7.1.2: Harmonics generated from the IPA liquid jet using a 13 fs laser pulse. Top left: The normalised harmonic yield from the liquid jet, with the cut-off law in the gas phase for those peak intensities show by the black diagonal line. Top right: Transmitted pulse energy through the liquid jet. The point at which the critical plasma density is reached is denoted by the dashed vertical line. The inset beam profiles are that of the transmitted driving laser, set to the same exposure values. Below: a CEP scan of the driving laser field at 50 $TWcm^{-2}$ with a pulse duration of 10.8 fs. The solid green lines show the evolution of the spectrum with CEP at 0.5π intervals. A clear π-radian phase variance of the emitted harmonics can be seen Adapted with permission from [93] under CC BY-NC-SA 4.0.

Additionally, to study the effect of the vapour phase on the emitted harmonics, a vertical scan of the laser spot position on the jet was performed. Here the temperature of the jet decreased as it travelled through the vacuum, and so the vapour density decreased, as seen in Figure 7.1.3. The flux at positions with lower vapour pressure, and hence less absorption at higher photon energies, supports the conclusion that the harmonic generation occurs in the liquid phase of the jet, rather than in the surrounding vapour.

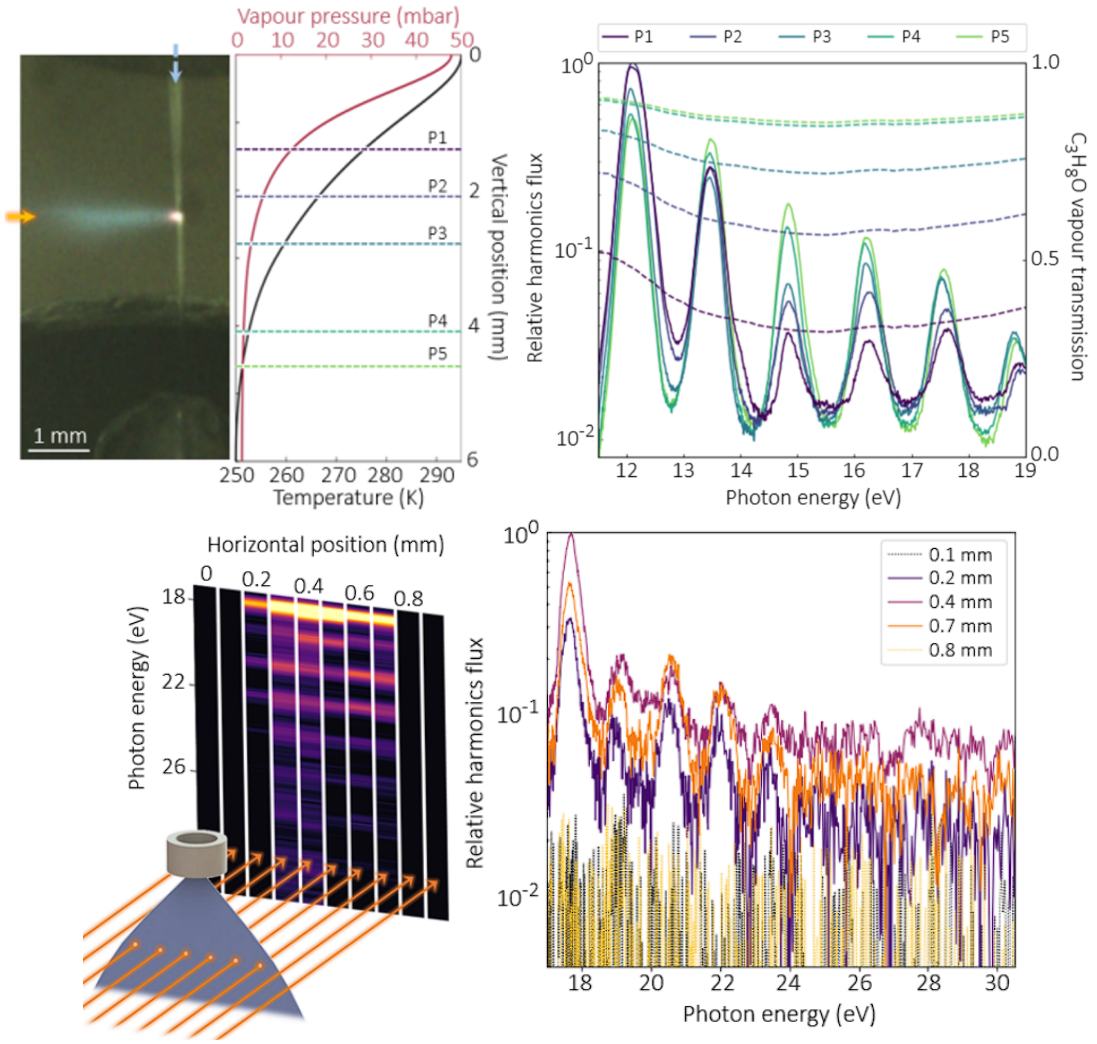


Figure 7.1.3: Plots showing the dependence of the HHG from the liquid target on the vertical (above) and lateral (below) position of the laser focal spot on the liquid jet's surface. Top Left: An image taken of the jet ≈1 ps after interaction with the driving laser, at a peak intensity above 50 $TWcm^{-2}$. The arrow indicates the propagation direction of the laser, and a plume can be seen ejected from the liquid's surface. Adjacent is a reference plot for the vertical extent of the jet, with the local vapour pressure and liquid temperature marked at a number of positions used for the vertical harmonic flux scan. Top Right: The results of the vertical harmonic flux scan. Bottom Left: A visualisation of the horizontal scan of the jet to diagnose harmonic flux in the vapour phase. Bottom Right: Line-outs of the flux from the system as the laser was scanned across the liquid jet. The harmonic flux drops sharply at the edges of the jet. Reproduced with permission from [93] under CC BY-NC-SA 4.0.

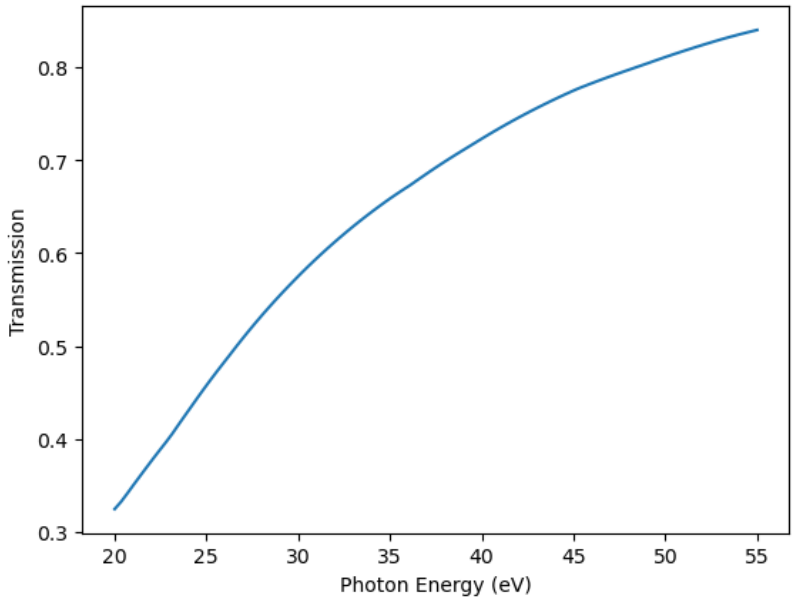


Figure 7.1.4: Transmission of 20 – 50 eV photons through 20 nm of isopropanol. Data from [44].

By considering the absorption lengths for 20 – 50 eV photons in isopropanol, we see that in the liquid phase the absorption length is on the order of 10's of nanometres and decrease for higher energy photons, and in Figure 7.1.4. This also suggests that the harmonic emission from the jet must have been within the final few-hundred nanometres of the liquid sheet, and motivates further study of the interaction at the front surface of the jet. If the harmonics recorded are all from the bulk liquid and these all happen close to the rear surface of the jet, then the limiting factor for recorded harmonics will be the peak intensity in the laser field that can reach that point, given losses at the front surface.

A good indicator of this lies in the sharp drop in the transmitted pulse at 50 $TWcm^{-2}$ seen in Figure 7.1.2, coupled with the observation of a plasma plume at the front surface of the jet, as seen in Figure 7.1.3. This suggests a large amount of absorbed energy at the surface, causing an expansion and ejection of plasma from the surface.

This line of reasoning is reinforced by pictures taken previously in the lab [154] using an ultrafast camera (Vision Research Phantom v7.3) with an exposure times of down to 2 µs and acquisition at up to 120 kHz. In Figure 7.1.5a) we seen a series of photos taken at 40 kHz, illuminated only by scattered light (i.e. not back-lit). These images suggest that the structure of the jet recovers from the incidence of the laser within 100 µs.

This is confirmed by the images in Figure 7.1.5b), which were taken at 100 kHz, with the jet back-lit by a triggered LED delivering a 100 µs bursts of illumination. Here we can track the descent of the hole in the surface of the liquid jet, and the speed of the hole can be calculated from these images at 20 ms^{-1}. This data is key to help characterise the timescales of the damage mechanisms for the jet, which we can use to further understand the interactions between the laser and jet.

7.2 The Interaction of Few-Cycle IR pulses with Thin Liquid Jets

The liquid jet modelled in the following sections are based on results established in the previous section, which was to be measured optically flat ($\lambda/20$ at 640 nm) with a width of 2 µm using monochromatic and white-light interferometry [46]. Using parameters from experiments performed in our laboratory, the driving laser modelled both here and in [93, 153] was a transform-limited, spatio-temporally Gaussian, 13 fs pulse with a focal spot diameter of 260 µm, and the isopropanol jet was modelled as a 293 bar ideal gas relative to STP. This pressure comes from comparing the number densities for an ideal gas and isopropanol at STP. To do this, we take the density ρ and molar mass of M_{mol} and say that the equivalent pressure for our medium, P_e is

$$P_e = \frac{\rho}{M_{mol}} \cdot \frac{N_A}{\rho_I} \tag{7.2.1}$$

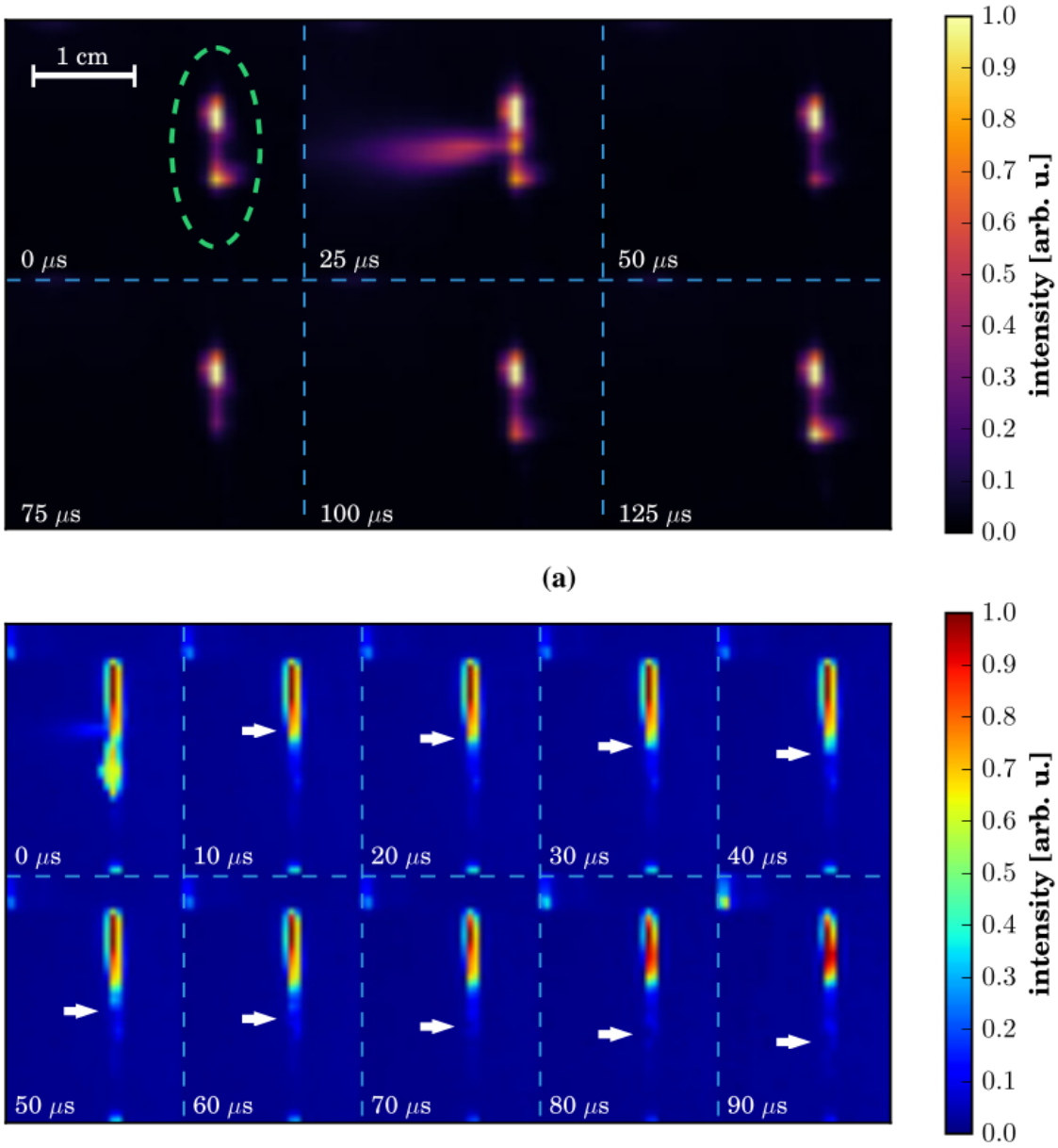


Figure 7.1.5: Images of the emission of the plasma plume after irradiation by the laser captured at 40 (a) and 100 kHz (b) FPS. At 40 kHz we see that the jet (circled in green) recovers from ablation within 125 µs. At 100 kHz, we can track the movement of the hole in the jets surface over 90 µs. These images provide the timescales for the recovery of the jet between laser shots. Reproduced from [154] under under CC BY-NC 4.0.

where N_A is Avogadro's number and ρ_I is the number density of an ideal gas. With a density of 786 kg/m^3 and molar mass of 60.1 g/Mol, this gives us a value of 293 bar for isopropanol.

Using the vapour pressure temperature dependence of isopropyl alcohol [156], we see that at 0 °C the vapour pressure is around 8 mbar, giving a pressure gradient of over 5 orders of magnitude between the liquid surface and the vapour. The vapour will also be rapidly extracted by the turbo pump on the chamber, meaning the pressure gradient from the effective 293 bar of the liquid phase to the sub-millibar pressures in the harmonic chamber renders the front and back faces of the jet an effective step function for our purposes, with negligible pressure tails in the beam path. This is verified in the horizontal scan in Figure 7.1.3.

To implement this high density target, the existing gas model shown in Figure 6.2.2 was modified to remove the intermediary region, fix the high pressure region to liquid-equivalent pressure and set the low pressure region to 8 mbar. This sharp drop is justified by considering the liquid jet boundary as a surface, so the step from the vapour to liquid phase is one of a critical boundary in the phase state of the medium. To encode this hard boundary into the propagation we set the decay length to be 1 nm, below the anticipated step size in the propagation.

High intensity ultrashort pulses in the condensed phase experience a number of loss mechanisms. While liquids do not exhibit long range structure and we therefore do not expect phonon-based losses, we would expect density-dependent loss mechanisms dominate over the usual multi-photon ionisation driven losses seen in the gas phase, which include plasma defocusing and ground state depletion. These interactions are largely classified as damage mechanisms in the jet and can be isolated by timescale as follows:

- Surface Ablation: This shot-to-shot damage mechanism occurs due to the build-up of plasma at the jet's surface. The flow rate of the jet, however, is maintained at $\approx 14\,\mathrm{ms}^{-1}$, and the focal spot diameter is on the order of $250\,\mu\mathrm{m}$. With these system parameters ablation, and any other shot-to-shot loss mechanism, would only set in at $\approx 50\,\mathrm{kHz}$ repetition rates. This is confirmed by being able to see the motion of the hole return of the shape of the jet inferred from Figure 7.1.5b) and a) respectively.

- Avalanche Ionisation: After the initial ionisation of molecules at the front of the jet, the liberated electrons can collide with further molecules while liberated from their parent atoms. Given the recombination of the electron can potentially release photons with multiple times the IP of the parent atom, these electrons can easily ionise multiple electrons and the avalanche effect could become significant in longer pulses. This is described by factoring an additional ionisation mechanism known as impact ionisation, with a rate $\alpha(I, n)$ given by [157]

$$\alpha(I, n) = \frac{2\omega}{c} \frac{\Im(\sqrt{\varepsilon})I}{\langle e_e \rangle + U}, \tag{7.2.2}$$

  where we are taking the imaginary part of the dielectric function ε ,and I and ω are the familiar descriptions of the laser intensity and laser frequency. U is the band gap energy, and $\langle e_e \rangle$ is the mean electron kinetic energy, which has been shown can be taken as $0.5U$ [158].

  The time-scales for this mechanism, however, prevent it from dominating our system, through an easily-understood scaling. The time taken for the ionisation of electrons is on the order of the cycle-time of the laser field. For these electrons to ionise further electrons in an "avalanche" will take multiple cycles of the field. Given that the driving laser is on the order of 13 fs, or 3-cycles, the avalanche cannot become dominant within the duration of the pulse. Feit et al. in [157] assert that, while one can consider these effects when calculating the ionisation

of a surface, "very short (less than 100 fs) pulses, MPI alone can almost produce the total density of electrons required for breakdown".

- Multiphoton Ionisation: Using the ADK formula from Equation 3.0.4, we can calculate the multiphoton ionisation rate as the laser field progresses through the medium. This ionisation occurs on the sub-cycle timescale, and is responsible for so-called intensity clamping, where the local ionisation causes spatial dispersion of the beam, reducing the peak intensity achieved in a sample and therefore the peak photon energies achieved in HHG [159].

Fortunately, as most of these are tied to pulse duration through their associated timescales, their effects are mitigated in our experimental apparatus through driving HHG with few cycle pulses. Only one of these mechanisms applies on the few-cycle scale, and so we will focus on instantaneous ionisation must clearly be the source of the laser transmission losses seen in Figure 7.1.2.

A number of other mechanisms could also be present, but were not considered for these works. The shot-to-shot ablation could cause shockwaves in the surface of the jet which might disrupt the flow. However no visual breakup of the jet was observed during operation, and the HHG and driving field could propagate to the detector, meaning this effect was not so substantial that it would prevent the effects observed. Between the timescales of avalanche ionisation and instantaneous ionisation listed above one might also observe X-ray self-emission in the plasma. This occurs as a result of liberated electrons scattering from ions and emitting photons through Bremsstrahlung radiation and as such is not coherent. While these X-rays may ionise the surrounding jet, a study of this is beyond the scope of this thesis.

While in the gas phase MPI losses typically amount to losses directly through ionisation or plasma defocusing at the intensity levels we using. In the liquid phase however the number of parent molecules, and hence the potential number of liberated

electrons, is 2 – 3 orders of magnitude higher, and so must provide more consideration to the effects at the jets surface. We recall from Equation 3.0.7 that the plasma frequency ω_p in a medium is given by

$$\omega_p = \sqrt{\frac{n_e e^2}{m_e \varepsilon_0}}, \tag{7.2.3}$$

where n_e is the number of ionised electrons, e and m_e are the electronic charge and mass respectively and ε_0 is the vacuum permittivity. Using the Drude model, this plasma frequency corresponds to a dielectric function ε_p given by

$$\varepsilon(\omega) = n_{Med}^2 - \frac{\omega_p^2}{\omega_0(\omega_0 + i\nu)}. \tag{7.2.4}$$

ω_0 is the laser frequency, n_{Med} is the complex refractive index of the medium, and ν is the electron scattering rate for the medium. In the solid phase, the scattering ν rate on the order of $1\,\mathrm{fs}^{-1}$[157], with a rate of $1 - 2\,\mathrm{fs}^{-1}$ previously measured for silica[160]. The rate for liquid water has been measured at around $0.33\,\mathrm{fs}^{-1}$ — around a third to a quarter the value for solids [157, 161]. This is perhaps unsurprising: fused silica and liquid IPA have approximately the same molar mass ($60\,\mathrm{g/mol}$), and so their number densities become simply a ratio of their densities — 2.203 and $0.786\,\mathrm{g/cm}^3$ for fused silica and IPA respectively — giving around a factor of 3.

When a critical plasma density has been reached at the surface of a material, one can see that the dielectric function becomes negative. We now take the Fresnel equation for reflectivity R of a surface at angle θ to the laser field at p-polarisation when

moving between an initial and secondary medium, of refractive indices n_1 and n_2 respectively:

$$R = \left| \frac{n_1\sqrt{1-(\frac{n1\sin\theta}{n2})^2} - n_2\cos\theta}{n_1\sqrt{1-(\frac{n_1\sin\theta}{n_2})^2} + n_2\cos\theta} \right|^2 . \tag{7.2.5}$$

The next step is the assumption that the laser, prior to interacting with the jet, propagating through such low pressures compared to the surface that it is in vacuum, i.e. $\varepsilon \approx \varepsilon_0$. We couple this with the knowledge that refractive index is related to a material's frequency dependant dielectric constant $\varepsilon(\omega)$ by $n = [(\varepsilon(\omega))/(\varepsilon_0)]^2$ to simplify Equation 7.2.5 to

$$R = \left| \frac{\sqrt{1-(\frac{\sin\theta}{\sqrt{\varepsilon_p}})^2} - \sqrt{\varepsilon_p}\cos\theta}{\sqrt{1-(\frac{\sin\theta}{\sqrt{\varepsilon_p}})^2} + \sqrt{\varepsilon_p}\cos\theta} \right|^2 . \tag{7.2.6}$$

From this see clearly that, when the dielectric function of the material is negative, its real parts' contribution to the reflectivity function is zero, and hence the material becomes completely reflective. Studies on this effect in water show have previously shown this on a flat liquid surface [162].

A photon of wavelength 1.8 µm has a mean photon energy, E_p, of 0.68 eV. Given the ionisation potential, I_p, of isopropanol is 10.3 eV it would take 15 photons to ionise a single electron from the ground state, represented most simply by an absorption per electron, A_e, given by

$$A_e = N_e\left(1 + \frac{I_p}{E_p}\right), \tag{7.2.7}$$

which, when integrated over the total ionisation of the jet, will give us the total absorption due to ionisation, A.

As the propagation section of the code was not designed to handle the liquid phase, calculations of reflection from plasma were not initially integrated into it. Indeed, the FME requires that the propagated field does not interact strongly in the backward direction, and the data seen in Figure 7.1.2 show losses of up to 80%. The modifications made to the code to account for reflection at the jets surface here are justifiable, however, by considering the nature of the system and reflected beam.

As the beam propagates through the front surface, the multiphoton ionisation in the earliest cycles of the pulse creates a sharp gradient in electron density as absorbed energy accumulates as plasma, and the resultant defocusing due to the plasma is already integrated into the code. Until this point we remain safely within the original use-case limit of the simulations and hence the FME.

Once sufficient electron densities are reached at the surface, the refractive index step function between the vacuum causes a reflection (as we previously established that the vapour pressure of isopropanol was very low and the strong vacuum pumping of the system rendered the local molecular density negligible), and once the critical electron density is reached the beam will be fully reflected. As there is no medium for the reflected and incoming portions of the beam to interact in, we can treat the reflected beam as we would any other loss, with the simple difference that this energy loss does not enter the medium as ionisation, and is simply removed from the simulation.

To do this, a plasma skin depth, δ_p is calculated using

$$\delta_p = c/\omega_p, \tag{7.2.8}$$

where c is the speed of light. As the simulations consider on the beam at normal incidence to the jets surface, we the calculate a reflection loss due to plasma at the surface, R_l,

$$R_l = \left| \frac{\sqrt{\varepsilon} - 1}{\sqrt{\varepsilon} + 1} \right|^2 . \tag{7.2.9}$$

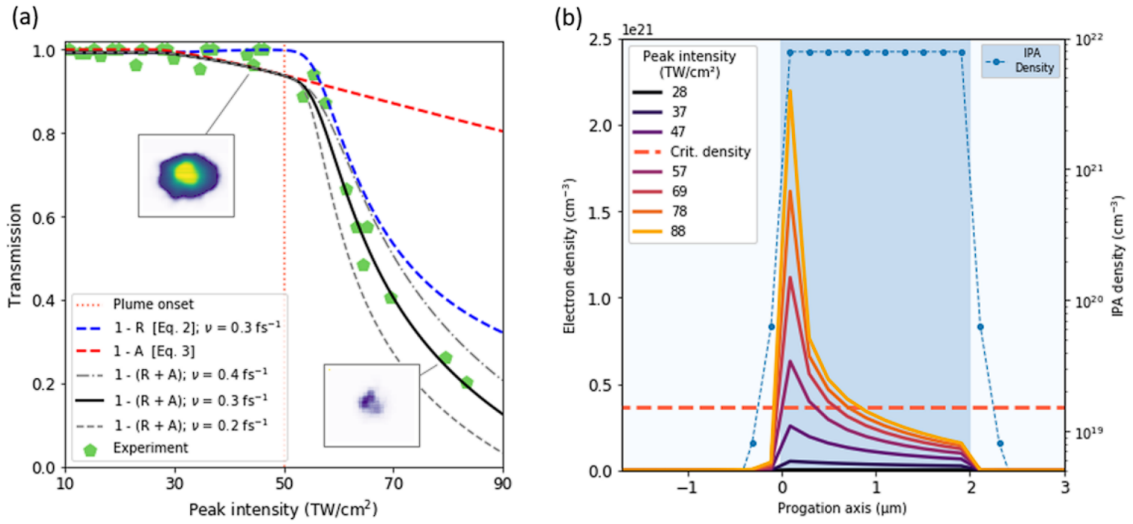


Figure 7.2.1: (a) Lines showing the simulated laser transmission, with the scattering rate ν fitted to the transmission of the experimental data. R and A here are the the reflection and absorption defined in Equation 7.2.6 and Equation 7.2.7 respectively. The fitting line for the scattering rate confirms the approximation that electron scattering in the liquid phase is roughly $\frac{1}{3}$ of that in the solid phase. The inset beam profile is that of the driving field as seen after transmission through the liquid jet. (b) A representation of the peak field intensity as the driving laser is propagated through the liquid jet, as produced by the simulations. We see a clear and sharp drop in intensity at the jet surface as the electron density exceeds the critical density at around 50 $\mathrm{TWcm^{-2}}$. Reproduced with permission from [153] under CC BY-NC 4.0.

We use use this to calculate the loss within the range of the plasma skin depth as the loss at each point in the propagation direction δ_R

$$\delta_R = \frac{R_l}{N} \exp\left(\frac{z - z_0}{\delta_p}\right) \tag{7.2.10}$$

where z_0 is the front surface of the jet, and N is a normalisation factor such that the integral over the reflection depth sums to R_l, given by $\frac{e}{(\delta_p(e-1))}$.

With this loss mechanism in place, we model the interaction of the laser with the jet, and find good agreement with the experimentally measured transmitted laser intensities, as seen in Figure 7.2.1 [153].

7.3 Liquid Phase HHG and the Scattering of Harmonic Generating Electrons

As previously discussed, in the liquid phase the number density compared to an ideal gas at STP is around 10^2 - 10^3 larger. While an ideal gas will have nearest-neighbour spacing on the order of 30 Å, and argon, commonly used in HHG, has a mean free path (the path a particle may travel before, on average, colliding with another particle) of 52 nm., the neighbour distances in isopropanol are on the order of around 10 Å.

As shown in Figure 7.1.2, experimental high harmonics are seen up to 50 eV. At these photon energies the electron trajectories lead to excursions that are on the few tens of Angstrom length scales, as seen in fig. 7.3.1, meaning that electrons are likely to scatter from neighbouring atoms. These scattering events will be different for each solvent molecule and electron energy dependent. Because the scattering probability increases substantially with trajectory time, long trajectories are expected to contribute minimally to the macroscopic harmonics emission.

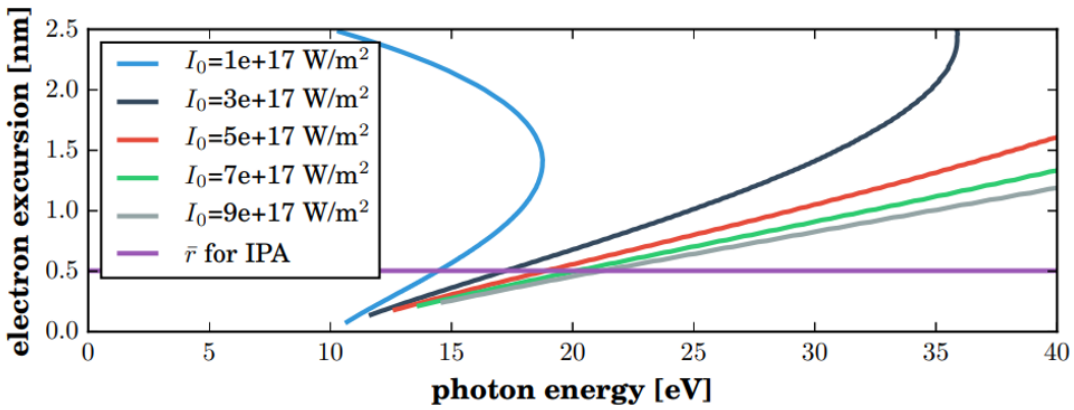


Figure 7.3.1: Electron excursion distances as a function of photon energy, as compared to the mean molecular spacing, $\bar{r}$, for IPA. Reproduced with permission from [154] under CC BY-NC 4.0.

A full quantum mechanical treatment for this system would require the inclusion of both "hard" and "soft" scattering of the electronic wavefunction. Hard scattering events cover when the wavepacket is dissipated and simply does not return to the parent molecule. Soft scattering events occur when a phase shift is induced by interaction with a surrounding molecule, but the return probability is non-zero. This will be considered further in Section 7.3.1 is beyond a simple integration into the SFA code, and therefore beyond the scope of this work.

For a first approximation of the system, a classical model is used. Both the harmonic-generating electron and the surrounding molecules are modelled as spherical with some size tied to its scattering cross-section. We then calculate a "no scattering" probability, which is the probability that the electron will propagate through the continuum and return without encountering any surrounding molecules. For simplicity, we will make the assumption that the IPA is a single, uniform density target. While this is not an approximation that holds well if considering the propagation of a single electron, the data from which we are able to draw scattering cross-section are in the gas or vapour phase, where electrons are launched at the targets at fixed kinetic energies. In these cases, rather than considering the shape of the molecule,

an overall scattering cross-section is divined from this interaction with the bulk gas. When using this data for our model we are, rather than considering the probability of a collision with a single molecule, treating the surrounding IPA as a uniformly distributed "bath" in which at any point there is a probability for collision. If we treat the medium as homogeneous and isotropic, the mean scattering cross section for the molecules in any orientation will tend towards this single scattering probability.

We calculate the return probability, that is the probability that the electron returns to the parent ion independent of standard HHG recombination probabilities, which are already included in the code, $p_{n.s.}$, using

$$p_{n.s.} = \prod_{i=1}^{N}(1 - p_i \Delta t) \quad \text{for} \quad N = \frac{t_{\text{rec}} - t_0}{\Delta t}. \tag{7.3.1}$$

t_0 and t_{rec} are the birth and recombination times of the electron trajectory, Δt are finite element time steps for the electron on its path, and p_i is defined by p_{scat}, the probability of scattering, through

$$p_i = p_{\text{scat}}(t_0 + i\Delta t) \tag{7.3.2}$$

Expanding $p_{n.s.}$ in orders of Δt, we get

$$p_{n.s.} = 1 + \sum_{i=1}^{N}\left(-\frac{1}{n!}\sum_{j=1}^{N} p_j \Delta t\right)^i = e^{-\langle n \rangle}, \tag{7.3.3}$$

where

$$\langle n \rangle = \sum_{j=1}^{N} p_j \Delta t \tag{7.3.4}$$

is the average number of collisions that would occur for the electron following its classical, scattering-free trajectory. For infinite N,

$$\langle n \rangle = \int_{t_0}^{t_{\text{rec}}} p_{\text{scat}}(t) dt\,. \tag{7.3.5}$$

For the classical collision model mentioned above we define p_{scat} as

$$p_{\text{scat}} = \rho_N A v(t) dt, \tag{7.3.6}$$

where ρ_N is the number density of the medium, A is the cross sectional area of the molecule, taken from empirical data [163], and $v(t)$ is the velocity of the electron at as a function over its trajectory. Using this we find the scattering probabilities in Figure 7.3.2.

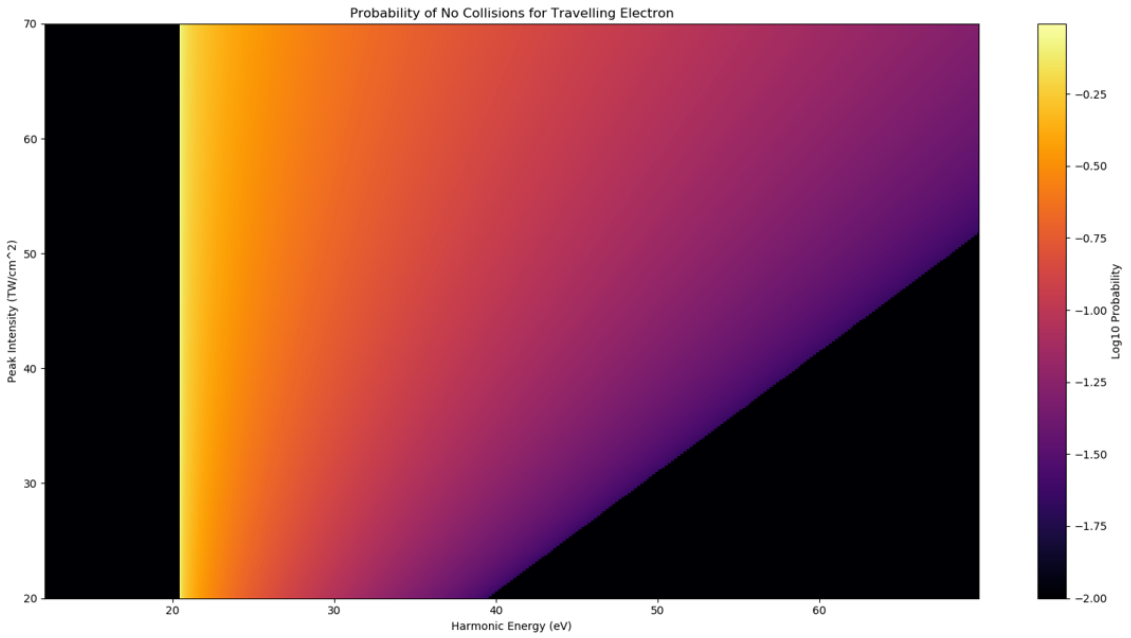


Figure 7.3.2: The probability of no collision for an electron of a given harmonic energy at given laser peak intensities, representing the likelihood a given electron with the return energy sufficient to generate a given harmonic with recombine with the parent molecule. The empirical scattering cross sections are taken from [163]. Given a sensitivity of 2 orders of magnitude on the CCD, return probabilities below 2 orders of magnitude are shown as black.

The limiting factor in these scattering models is now in the understanding of electron scattering on ultrafast timescales in the liquid phase. While there are scattering rates

available for molecules and clusters in the gas phase, literature on these cross sections in the liquid phase in the sub-keV energy range is limited, and it is known that simply scaling the density of the medium from gas to liquid phase in this context does not accurately reproduce liquid-phase electron scattering [164–167]. This is because gas phase models overestimate scattering in liquids due to the changes in the bond lengths, changes in the contributions of sub-shells to the total cross section, and charge screening and correlation effects will underestimate the mean free path for a propagating electron.

To attempt to account for this, a simple correction factor, k, is used to modify the magnitude of the cross section, with $k = 0$ representing no scattering whatsoever, $k = 1$ representing the the use of the unmodified vapour-phase cross section. Using the scattering probabilities as a damping for the harmonics emitted by a high density gas system we may retrieve k from the value which gives the best match between the simulated data and the experimentally obtained harmonic flux curves. Fitting the simulated harmonic yields we see an optimal correction factor of $k = 0.3$ as seen in Figure 7.3.3.

It is reasonable to say that we cannot fully diagnose the source of the changes in the cross section between phases, and that our elementary model is insufficient to precisely quantify the liquid phase cross section. We can however be certain that the model indicates an agreement that the vapour phase models are insufficient and need significant modification to agree well with both HHG and electron scattering in general in the liquid phase.

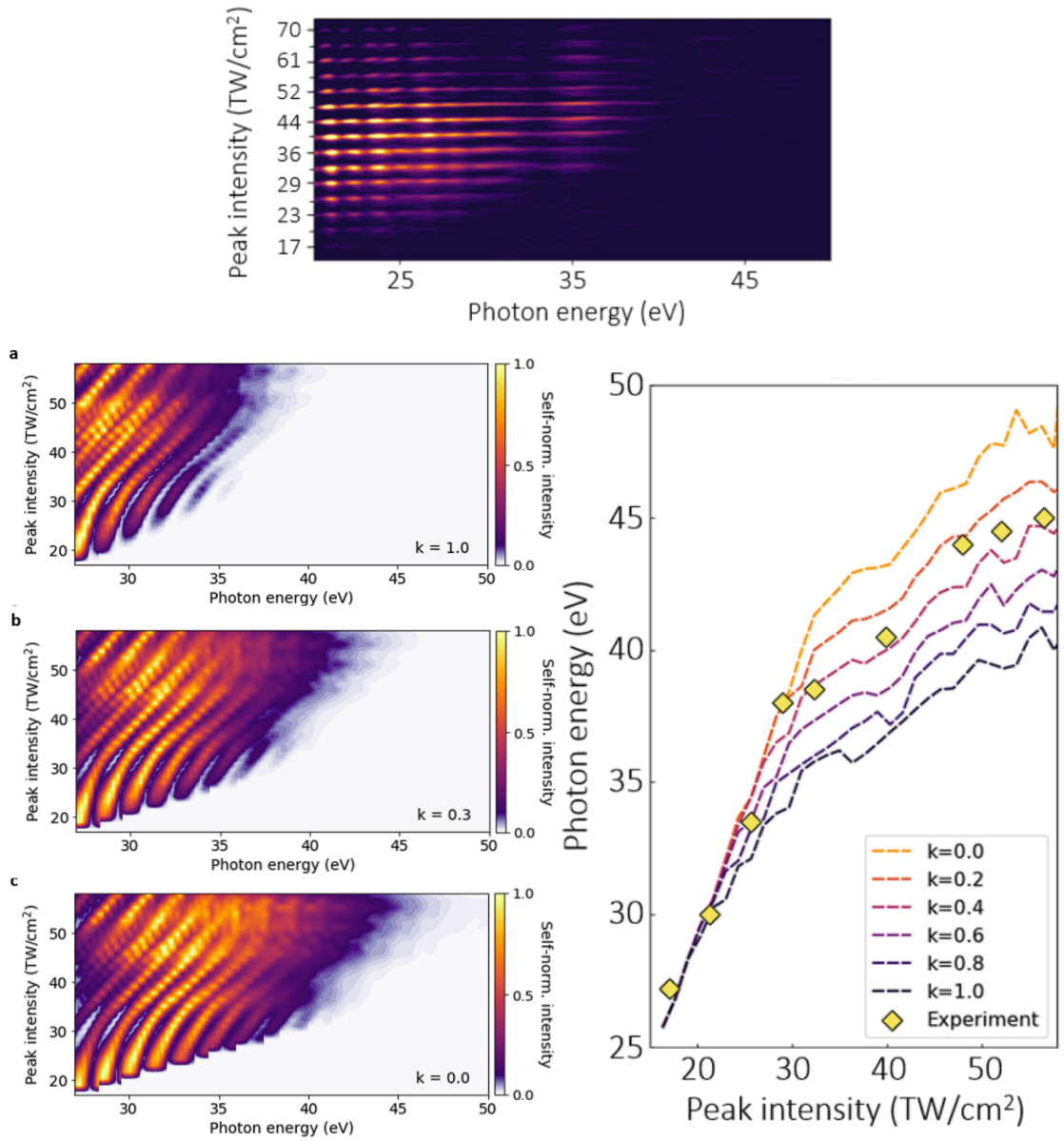


Figure 7.3.3: Above: Experimentally measured harmonics in IPA. Below: Simulated harmonic spectra in a 293 bar ideal gas, to match IPA. The 3 plots on the left show the simulated harmonic spectra with the fitting value k =0 (a), 0.3 (b) and 1 (c).The spectra are self-normalised for clarity and as the numerical values for harmonics flux are inexact. The diamonds on the right show the experimental cutoff harmonics against peak intensity, and the dashed lines represent the simulated values for these cutoffs with a range of values for k. We see the best fit for a value of k=0.3. Reproduced with permission from [93] under CC BY-NC-SA 4.0.

Particular care has to be taken with these simulations, and further optimisations are still required. Increasing the medium density to match a liquids is exceptionally computationally expensive as the non-linearity scales linearly with it. As a result the laser propagation simulation through a 4 μm thick target at liquid density requires an order of magnitude more memory and computation time than for a 1 mm gas phase target.

This stems from the fact that rapid spatial and spectral fluctuations appear due to the higher density of molecules. As a result the radial and longitudinal sampling must be significantly increased, and so the high nonlinearities create fixed lower bounds for resolution requirements.

The specific reasons for this become evident when we examine the split-step propagation method. When the pulse propagates, the pulse is divided into temporal and spectral components, within a bounded box and with a coarseness defined by the propagation and radial axis resolutions of the simulation respectively. As the pulse propagates through a medium, the nonlinearity of the medium and intensity of the pulse dictate the spectral broadening. At high nonlinearities and pulse energies, the pulse broadens very substantially, and the spectral intensity required for any given point on the spectrum to broaden is lower. If the spectral binning is too coarse, the intensities in the higher energy spectral bins become unphysically high, and this will mean that the pulse will continue to broaden drastically, potentially reaching the numerical boundary of the spectral range. If this occurs, as the pulse is Fourier transformed between the temporal and spectral domains, the pulse will "wrap around" and the simulation will experience an underflow error, with the highest frequency components spreading into the lowest.

For gas phase simulations, spatial sampling sizes can be on the order of a micron, as the cell size is on the order of hundreds of microns and third-order effects cause self-phase modulation on the order of microns. In the liquid phase however, the high

density means that the electron density is far higher as the beam still has an intensity sufficient to reach near-saturation of ionisation at the intensities needed for $\geq$50 eV (around 55 TWcm^{-2} with an 1800 nm driving laser, given the 10.3 V IP of IPA). As a result, for propagating in the liquid phase, iterative trials by the author found that the spatial sampling must be on the order of nanometers. These sampling rate limitations may well also lead to the shift in harmonic photon energies seen in Figure 7.3.3. Due a memory limitation on the computing nodes available, (240 GB) the spatio-temporal sampling rates for the laser propagation simulation could not be further increased. Work to further improve efficiency of the propagation stage of the simulation process may well aid to refine the numerical comparison to experimental results, as will be further discussed shortly. As a result, however, while we can confidently say that the envelopes of the harmonics, work to further refine these models is needed.

A recent study of HHG in the liquid phase suggested the loosely-ordered, short-range structure of liquids means a band structure model could be used to describe harmonics from a liquid jet [94]. In that work, 30 fs pulses at 1.5 µm and 1.2 mJ are used to drive HHG in liquid water and alcohols.

The most substantial difference between that work and those works shown in this thesis lies in the peak intensities used. The works presented for HHG in ethanol by Luu et al. show peak intensities of 0.9 – 1.4 VÅ^{-1}, corresponding to 106 – 259 TWcm^{-2}. At these peak intensities we might continue to observe harmonics, but long-range structures of the sample could not continue to exist due to extreme ionisation of the liquid at the surface of the jet. We posit that the harmonics observed in that study may well be due to the earlier half-cycles of the pulse strongly ionising the front surface, and the harmonics observed in the latter half cycles being reflected. This can be simply represented as seen in Figure 7.3.4.

While simulations could not be run to reflect this due to time and computational node availability, the CEP dependence seen in Figure 7.1.2 also shows the behaviour

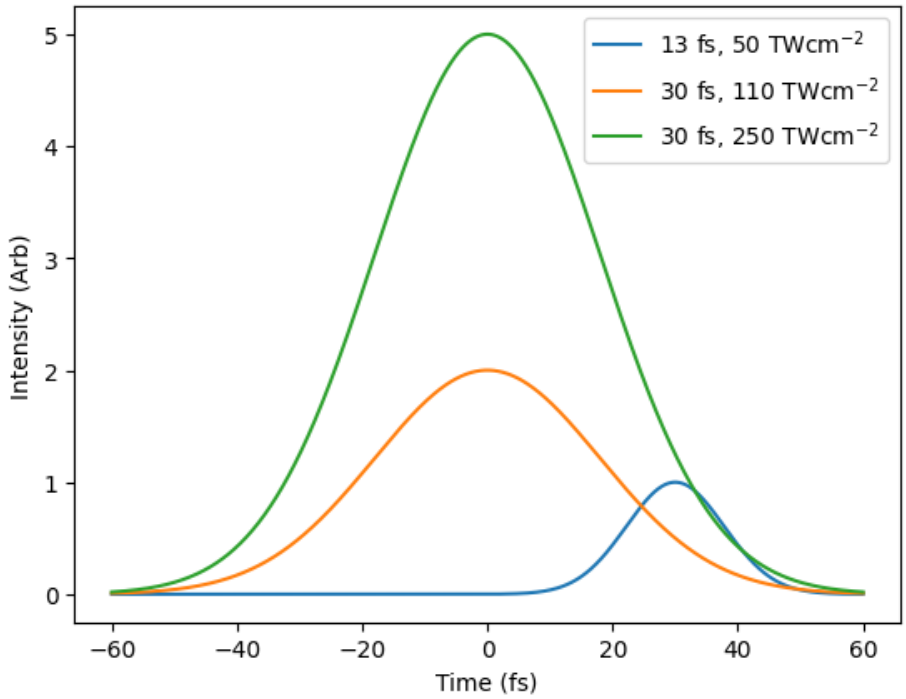


Figure 7.3.4: A comparison of the pulse envelopes used for this work compared to those stated in [94]. We see here that the rising edege of the pulse used in this work matches that of the higher intensity pulse of used by Luu et al.. The pulse used in this work has been temporally shifted, to make comparison of the rising edges of the pulses.

expected in a recombination-based model of HHG as described in the literature [168]. This is exhibited as a CEP invariance at the low energy harmonics and a strong dependence at cutoff energies as the instantaneous intensity is dictated by the CEP. In the solid phase, however, harmonics are either observed to all change with CEP, regardless of proximity to the cutoff, or not change at all [52]. Running simulations to reproduce these results would be a logical next step to further develop the picture provided by these models for HHG in the liquid phase.

7.3.1 Scope for Future Development

While the models are not yet complete, the initial simulations of HHG in liquid jets presented here offer some insight into the underlying mechanisms and highlights areas that need most development. Figure 7.3.3 shows good agreement between the $k = 0.3$

fitted curve for scattering, but we do not yet have a clear picture of what the physical origin for this is. Unlike the case of the electron scattering for calculation of electron scattering rates in Section 7.2, this reduction cannot simply be attributed to density considerations as in the change from solids to liquids. Rather, we must consider that gas phase models for low energy electron scattering overestimates the rates and fit the reduction parameter accordingly, stemming from screening, correlation, and exchange potentials [164–166].

In particular, recent works considering the difference in scattering cross-sections between liquid and gas phase argon and xenon [169] have also suggested a framework for calculating this scattering reduction factor compared to gas phase cross-sections in the literature [170]. They propose this reduction factor k can be calculated using the gas and liquid phase collision frequencies (ν_g and ν_l respectively) as

$$k = \frac{\nu_l}{\nu_g} \tag{7.3.7}$$

These scattering frequencies however require extensive theoretical analysis to calculate and are therefore beyond the scope of this thesis. The first steps in this however is to define a potential energy landscape and calculate the relevant structure factor. A 2-D slice of the such a potential energy surface can be seen in Figure 7.3.5. The spacing of the molecules was set using an intermolecular spacing of 0.5 nm [149, 154], and the potential landscape was calculated using a Lennard-Jones potential as this is a simple and well understood model for intermolecular pair potentials, given by

$$V_{LJ} = 4\varepsilon[\frac{\sigma}{r}^{12} - \frac{\sigma}{r}^{6}], \tag{7.3.8}$$

where ε is the maximal depth of any potential well, and sigma is the is the particle size, which we define as the Bohr radius for this simple calculation. This value is computer for each spatial point in the grid relative to each atom in each molecule.

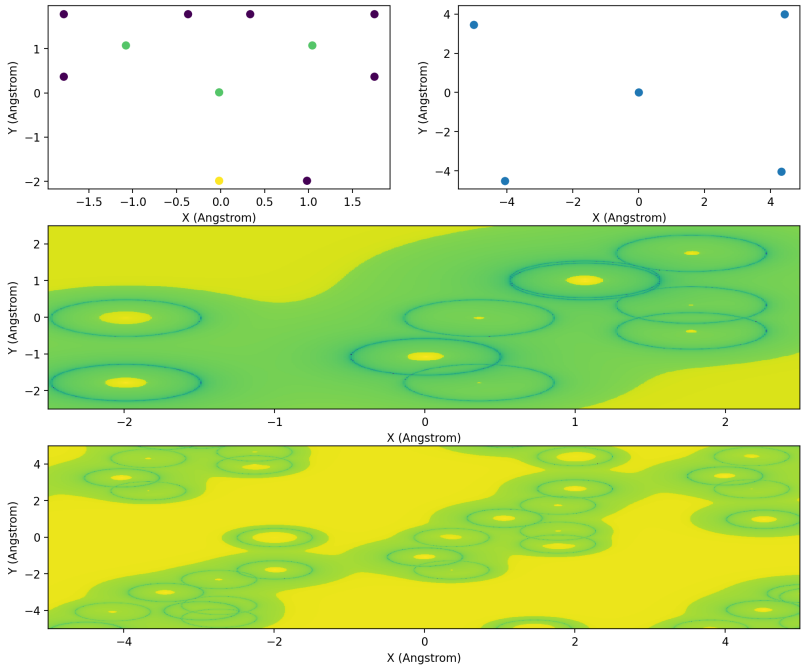


Figure 7.3.5: A 2D projection of a single isopropanol molecule (top left) a number of them scattered around a 5 Ågrid. The potential energy landscape by a freely propagating electron from a single IPA molecule can be seen (middle) alongside the landscape from the collection of molecules over a 10 Ågrid (bottom). The molecules are distributed using a Lennard-Jones potential. Each ring represents the boundary of the shell of an atom, with the distance determined by the Bohr radius.

Once these scattering cross-sections have been calculated, the next improvement would be a full description of scattering from atomic sites for a given electron velocity [149], in order to modify the dipole phase in the SFA calculation. This would require calculating not only the "hard" scattering events where the electron is completely scattered and HHG is guaranteed not to occur, but also a "soft" scattering events where a phase is accumulated by the electron but it may well return to the parent atom. This would likely be most impactful for electrons at higher velocities and therefore higher harmonic orders, where the electron excursion distance in the

classical model leads to larger scattering probabilities. Implementing this would allow the HHG code to total flux accurately, rather than having to apply the scattering curves and calculate re-absorption after the fact.

One way to provide greater depth to the datasets presented and highlight the differences between HHG in the gas and liquid phase would be to take similar measurements in a range of other solvents. By comparing HHG in jets of water, methanol and ethanol to our existing data in isopropanol, one could study the change in scattering rate with molecular configuration and sample density. A change in fit factor between the scattering rates in each liquid would allow us to refine the scattering modification coefficient compared to what an ab-initio calculation such as those presented in [169] and the effects of phases accumulated by the aforementioned soft scattering events.

Emission from condensed phase media also requires a different computational object structure to the current implementation of gasses in the code. Gas phase media in the current architecture of the simulation are constructed by importing the refractive index and molecular files from databases and imposing these on an ideal gas at STP. Simply increasing the pressure value of the ideal gas to match the density of an ideal gas to match liquid density is functional as a first approximation, but this means that the linear and nonlinear refractive indices of the material must be carefully calculated by extrapolating from the material, and the quantum numbers related to the ionisation of the material are added in the format required for atomic rather than molecular sources. Single molecule simulations are currently available in the repository of simulation code from previous works, but have only been implemented for single emitters [171], and not interaction volumes as is currently implemented for gasses.

In conclusion, we can infer from the comparison of the modelling to experimental data that the harmonic cutoff in the liquid phase do match well the recombination

methods of HHG seen in the gas phase. Further simulations to reproduce the CEP dependence of the cutoff harmonics in the medium could be performed to further solidify this agreement.

The combination of propagation simulations and specific considerations of the laser-induced plasma at the surface of the jet further provide reasoning to further reinforce the argument that only by using few-cycle laser pulses can one retrieve detail regarding HHG in the liquid phase before space-charge effects dominate the measured harmonic spectrum. Our results further show that vapour phase scattering cross sections for electrons in isopropanol appear to overestimate the damping one would anticipate for electrons propagating during HHG by a factor of 3.

The primary remaining discrepancy between the laboratory and in-silico experiments now lies in the shifting harmonic peaks in the simulated harmonic spectra. This may well originate from the blue-shifting of the laser field while propagating through plasma in the simulation, but seems more pronounced than any shift we see in the experimental data. While normally one would assume that this shift occurs from laser propagation through the plasma, in this case the level of ionisation appears to match experimental values well, and so this is not the case.

The first solution here would be to improve the numerical efficiency of the propagation simulation in the liquid phase to allow finer spectral resolution. This is because the extreme shifting may be due to the spectral binning of the field still being insufficiently fine to mitigate erroneous blue-shifting. This is a further architectural improvement in the code rather than scientific detail, but may also be useful for extending the code for simulating filamentation in liquids — another project currently being investigated in the group — and for improving the efficacy of future studies of ionisation and HHG in the liquid phase.

8 Discussion and Conclusions

8.1 Summary of Results

Experimentally, laser sources capable of generating tunable, few-fs, 0.5 – 3 μJ, *ultra-violet* (UV)-to-visible pulses in the 250 – 550 nm were built and tested by the author. These provide experimental capacity for a wide range of pump-probe experiments with high temporal resolution requirements, as shown in Section 5. Until recently, the use of a second or third harmonic crystal was needed to generate UV pump pulses, limiting the available wavelengths and temporal resolution, and this work should provide temporal resolution to the sub-5 fs regime. The spectral filtering and temporal characterisation methods for the UV pulses has also been outlined.

These UV pulses were generated using sub-15 fs 1350 nm pulses from an *optical parametric amplifier* (OPA) broadened using a tensioned *hollow core fibre* (HCF), compressed down from 65 fs using chirped mirrors. While the fibre tensioning method and gas cells used to achieve these results were provided by an external collaborator, a framework for building simple, cost effective laser broadening system in tensioned fibres has also been outlined. The methods for building this fibre can also be used to replace the existing HCF for broadening the 1800 nm OPA idler. This may provide additional energy for driving *high harmonic generation* (HHG) as >600 μJ pulses are needed to achieve well phase-matched *soft X-rays* (SXR) in the water window (280 – 520 eV) out to the nitrogen and oxygen K-edges as seen from the energy scaling in Section 6. By separating the pump and probe arms into two processes driven by separate but equally well temporally compressed arms of the same OPA, energy overhead for the HHG process has been reduced, while increasing the experimental capacity of the laboratory. Following the works shown in this thesis, temporal jitter between the HHG and RDW arms has been measured as 0.78 fs [172].

In parallel, a variable length cell has been constructed for generating experimentally optimised and reproducible HHG across a range of harmonic energies. The purpose of this source is both to test HHG scaling laws and to attempt to create target media to increase HHG flux for *transient absorption* (TA) experiments. The scanning range of the cell is 0.5 – 25 mm with a gas load of up to 8 bar. Simulations have been run to map the parameter space for HHG with the explicit aim of improving efficiency of HHG in the water window by harnessing transient phase-matching to improve harmonic yield without relying on low plasma density scaling laws to predict the harmonic flux. Initial results also show good agreement with proposed theoretical parabolic relationships between gas cell length and pressure for efficient HHG in recent literature for HHG in the gas phase [37]. Previous hypotheses from our group that few-bar gas pressures would be beneficial for HHG are supported where this work and [37] differ in when along this curve optimal HHG flux may be obtained.

Furthermore, both the interaction of high intensity laser spots with liquid jets and HHG in the liquid phase were modelled with the aim of reproducing experimental data to help understand the underlying mechanisms of both processes.

For the laser-jet interaction, insight has been gained into the interaction of intense few-cycle pulses with liquid surfaces. A scattering rate for electrons in liquid isopropanol of $0.3\,\mathrm{fs}^{-1}$ was found, roughly a third to a fifth of the scattering rate in solids as previously shown in literature [157, 161]. This provides a clear route to further confirmation of the propagation model by measuring directly the energy lost through reflection from the surface of the liquid jet.

We also find that the scattering rates for electrons undergoing HHG in the liquid phase neither match gas phase models well nor indicate the intrinsic structure of the solid phase. This was found by modelling recombination-picture HHG from an ideal gas target at pressures of 293 bar (equivalent to the density of liquid phase isopropanol at STP) and applying a scattering curve based on gas-phase electron

scattering cross sections from literature, with a fitting parameter k tuned to match the harmonic flux obtained experimentally. A value of $k = 0.3$ was found to give best matching between the simulated and experimental data. Using this reduced rate the simulated harmonic cutoffs from isopropanol match well those found in experiments, when factoring in losses due to ionisation at the jets surface. Further confirmation of this model may be obtained by modelling the CEP dependence of harmonics in the liquid phase and calculating more accurately the scattering cross sections for the low ($\leq 100\,\mathrm{eV}$) photons propagating in the liquid isopropanol medium during HHG.

8.2 Future Work

8.2.1 The Resonant Dispersive Wave System

There remain a number of routes available to further develop the fibre systems demonstrated in this thesis. Noble gasses with lower ionisation potentials could provide the opportunity to extend the phase matched wavelengths of the *resonant dispersive waves* (RDWs) to shorter wavelengths at higher gas pressures and therefore lower pulse energies, allowing shorter wavelength RDW production without the same limits on plasma defocusing. This provides a route to pump pulses for TA experiments in the 100 – 200 nm range.

At this point the transport optics will begin to provide a limitation, but if suitable dielectric mirrors can be found for the experiments in question then new studies in biomolecular and protein systems regarding photochemical reactions or photoprotection (the biochemical mechanisms by which damage due to excess light irradiation is mitigated) can be designed [173]. Since the conclusion of these works, the RDW pulses generated by this system have been used in commissioning experiments by providing sub-5 fs, 2 μJ, 270 nm pulses for studying photodissociation in dimethyl disulphide (DMDS).

8.2.2 The Variable Length Gas Cell

The path for the variable length gas cell for HHG, and the associated phase-matching and *figure of merit* (FOM) calculations, is clear. First the simulations must be performed with the 12 fs, few-hundred microjoule 1.8 μm laser pulses to predict harmonic emission in an experimental space matching that of the lab at Imperial College. Then scans of the cell length, focal spot position and size, and gas backing pressure should be performed and the FOM calculations compared with the harmonic yields obtained. If the efficiency predicted by the FOM matches experimental harmonic yields, we learn that we have created a modelling system which saves hours of simulation time for predicting harmonic fluxes over more onerous HHG calculations, and can quickly provide optimised experimental configurations for target SXR wavelengths. If there is a discrepancy, we are presented with an interesting study of scaling laws for HHG in the overdriven regime, and may begin shape the FOM calculations to represent the experimental data better. We may further find that the regressions for interpreting these FOM measurements require highly nonlinear shapes to improve accuracy, and this would provide information on the effects of plasma on HHG.

Once the HHG system has been characterised, these systems can initially be benchmarked in a UV-pump, X-ray probe experiment on a target recently performed in the lab, for example polythiophene [174]. As the HHG-driving arm is no longer being depleted to drive UV or visible pump pulse generation, the X-ray flux at the carbon-K edge should be improved compared to the original work. Compounded with the optimisation methods discussed in Section 6, this should lead to a substantial increase in TAS signal. In particular, recent experiments performed by other students in the lab have been limited by energy in the SXR probe when studying polythiophene [80, 174].

To compensate for this, the energy of the UV pump pulse needed to be increased, which accelerated the damage to the sample. As discussed in these works, by increas-

ing SXR flux the experiments could reduce the UV pump energy, allowing better signal to noise for experiments and reducing the need to compensate for sample damage effects.

Following this, experiments in the liquid phase should be tested, using $CaCl_2$ dissolved in ethanol. As seen in Section 1, the element L-edges in $CaCl_2$ bookend the region surrounding the carbon K-edge at 283 nm. The achieved signal-to-noise ratios at the calcium and chlorine edges will help establish the sensitivity limits for the system by varying the solute concentrations. Additionally, by optimising harmonics in the 400 eV range, one could also study cysteine by probing the nitrogen K-edge [175], whose biological relevance stems from its roles in human metabolism and whose excess formation is correlated with various diseases and neurodegenerative disorders.

Once this is completed, an *infrared* (IR) pulse from the original driving laser, likely the depleted 800 nm pump beam from the HE-TOPAS, may be spatially filtered and broadened in a HCF and compressed with chirped mirrors to the around the 15 fs. At this point, quantum control experiments, such the one proposed in [43], become possible.

8.2.3 Laser-Liquid Jet interactions and HHG

To further explore the interaction of intense laser pulses and liquids, follow-up studies on reflectivity from the jet of a second, independent pulse, such that the reflectivity and imparted phase from the surface can be characterised, can be performed. One could also use this surface to produce plasma mirror HHG [92]. This process would benefit from the fact that the target is self-refreshing and the jets surface is optically flat and measurable using interferometry, compared to solid targets where the optical flatness is defined by manufacture quality and refreshing the target would require raster scanning and replacement.

Study of the surface plasma from the jets surface and the resulting losses would allow for further study on the differences between ionisation for liquid and solid phase dielectrics. While calculating the volumetric loss of mass would be challenging, interferometric measures may provide more fruitful. To measure the ionisation on the femtosecond scale one could perform transient measurements using spectral phase interferometry techniques [176], which have previously used by our laboratory to measure ionisation in the gas phase [16]. This can provide diagnostic information the plasma density on the picosecond timescale to provide a complete picture for the evolution of the plasma at liquid jet surface [177]. To do this a weak pulse (defined such that it does not cause ionisation that would contaminate these measurements) is split into two, with a sub-picosecond delay (previous work in the group has used a 500 fs delay). The earlier of these two pulses precedes the pulse used to ionise the jet, and the second follows it. These two pulses are then recombined onto a spectrometer, with a spectral interference pattern arising from the delay between the pulses. The variation of the refractive index caused by the plasma (as discussed in Section 3) causes a phase shift that can be extracted from the spectral interference pattern. By using a higher frequency probe pulse for these studies — previously the fundamental Ti:Saph beam at 800 nm was used — one can also continue to observe these phase shifts even once the surface of the jet has become reflective to the driving pulse due to the plasma at the jet's surface.

If one were to study the effect of the laser ablation on the jet on a shot-to-shot timescale a new challenge is introduced. We already have information on the full recovery time of the jet as seen in Figure 7.1.5, and know that scatter from the ejected material vanishes after 50 µs. Unfortunately a 50 µs optical delay would require a delay line of 7.5 km, and instead an electronic delay would be needed. Instead, electronic delays would need to be used for such a measurement, which is not available in our laboratory. If one were to perform this experiment with one of the facility apparatus' available (e.g. the setup presented in [178]) it could also be performed at 100 kHz repetition rates. As 100 kHz equates to 10 µs delays, this would also allow

one to search for any shot-to-shot instability induced in the jet by the creation of the plasma plume.

Finally, there are a range of studies possible by attempting to further explore the scattering of low energy electrons in liquids. In the most academic case these results are key for pursuing high harmonic spectroscopy in the liquid phase. Understanding how a solutes' electrons will be affected by the surrounding solvent and therefore interfere with the structural information gathered from the technique is critical. The results in this thesis also add to the limited literature on scattering rates for sub-keV electrons and shine a further light on a gap in our current understanding of low energy electronic motion in the liquid phase. Further studies on liquid phase HHG spectra, particularly focused on wavelength scaling and electron scattering rates, in organic solvents could be performed to form a more complete picture in this regime.

8.3 Wider Implications

Beyond simply enabling the experiments listed in this thesis, the development of broadband, tunable UV sources provide exciting prospects for absorption spectroscopies in a region where few-fs resolution has not previously been available. *2D electronic spectroscopy* (2DES)[11], for example, provides insight into electronic correlation functions using UV-Visible pulses. By taking four identical pulses, using three to generate a transient grating signal in a material and interfering this transient grating with the fourth pulse an interference pattern is generated. Fourier transforming these interference fringes in the time domain provides frequency-space information about the electronic state changes in the system. These spectroscopies have been used to provide insights into photosynthesis [179], energy transfer, and the study of nanomaterials [180], with the key benefit that the mechanisms of state changes may be directly interpreted from experimental results, rather than extracted from implied transfers in one dimension as seen in pump-probe spectroscopies.

These signals, however, tend to be noise-limited by scattering and low signal peaks due to the nature of their fundamental experimental design. To compensate for this, they must be run at 10s to 100s of kHz repetition rates to maintain reasonable experimental time. Unfortunately, pulse-broadening at these repetition rates in the UV-Vis range beyond use of a commercial pulse shaper is not well explored in this spectral domain. While some work has been performed on fibre broadening systems for these experiments [181], the maturity of integration of these systems is still limited, and optimisation of broadening and coupling parameters could significantly enhance the experimental signals available. In particular, 2DES experiments cannot be run with high peak intensities due to limitations on exciton formation creating experimental noise [182, 183]. Access to higher pulse energies and spectral bandwidths than can be supported by current commercial pulse shapers allows use of larger focal spot sizes, increasing the level of experimental signal that can be extracted from a sample.

Developing models for intense laser interactions and low energy electron scattering in the liquid phase also has important implications for medical science. The scattering of electrons *in-vivo* is critical in ionising radiation therapies [184], as they contribute to dosimetry, radiobiology and medical nanotechnology. For intense laser fields the results add to the literature for laser surgeries, where explosive boiling or cell damage must be avoided. In particular, recent studies have focused on the interaction of intense, few-cycle lasers with whole blood and water [185], keratin-based membranes [186] and other biological tissues [187].

As previously discussed, the purpose of the development of these sources and models is to create robust sources for studying biologically relevant systems, for example cystiene or retinol. The scope that the availability of these sources and models provides for both further experimental apparatus development and development of both physical and biochemically relevant modelling, however, provides exciting opportunities for UV and X-ray spectroscopies.

9 Appendix

9.1 Elemental Edges

Data for commonly used K- and L- edges in the Imperial College Lab, taken from [188].

Element	Atomic Number	Atomic Weight	K Edge	L1 Edge	L2 Edge	L3 Edge
H	1	1.008	13.6	0	0	0
He	2	4.003	24.6	0	0	0
Li	3	6.941	54.8	0	0	0
C	6	12.011	283.8	0	6.4	6.4
N	7	14.007	401.6	0	9.2	9.2
O	8	15.999	532	23.7	7.1	7.1
F	9	18.998	685.4	31	8.6	8.6
Ne	10	20.18	866.9	45	18.3	18.3
Na	11	22.99	1072.1	63.3	31.1	31.1
Cl	17	35.453	2822.4	270.2	201.6	200.0
Ca	20	40.078	4038	437.8	350.0	346.4

References

[1] Margherita Maiuri, Marco Garavelli, and Giulio Cerullo. "Ultrafast Spectroscopy: State of the Art and Open Challenges". In: *Journal of the American Chemical Society* 142.1 (Jan. 2020), pp. 3–15. DOI: 10.1021/jacs.9b10533.

[2] Ahmed H. Zewail. "Femtochemistry: Recent Progress in Studies of Dynamics and Control of Reactions and Their Transition States". In: *The Journal of Physical Chemistry* 100.31 (Jan. 1996), pp. 12701–12724. DOI: 10.1021/jp960658s.

[3] A.M Rijs et al. "'Magnetic bottle' spectrometer as a versatile tool for laser photoelectron spectroscopy". In: *Journal of Electron Spectroscopy and Related Phenomena* 112.1-3 (Nov. 2000), pp. 151–162. DOI: 10.1016/S0368-2048(00)00209-7.

[4] Roland Wester. "Velocity map imaging of ion–molecule reactions". In: *Phys. Chem. Chem. Phys.* 16.2 (2014), pp. 396–405. DOI: 10.1039/C3CP53405G.

[5] Taran Driver et al. "Two-Dimensional Partial-Covariance Mass Spectrometry of Large Molecules Based on Fragment Correlations". In: *Physical Review X* 10.4 (Oct. 2020), p. 041004. DOI: 10.1103/PhysRevX.10.041004.

[6] G. Greczynski and L. Hultman. *X-ray photoelectron spectroscopy: Towards reliable binding energy referencing*. Jan. 2020. DOI: 10.1016/j.pmatsci.2019.100591.

[7] Jonathan A. Sobota, Yu He, and Zhi Xun Shen. "Angle-resolved photoemission studies of quantum materials". In: *Reviews of Modern Physics* 93.2 (June 2021), p. 025006. DOI: 10.1103/RevModPhys.93.025006.

[8] Sanjay M. Nilapwar et al. "Absorption spectroscopy". In: *Methods in Enzymology*. Vol. 500. Academic Press, Jan. 2011, pp. 59–75. DOI: 10.1016/B978-0-12-385118-5.00004-9.

[9] Yaron Paz. "Transient IR spectroscopy as a tool for studying photocatalytic materials". In: *Journal of Physics: Condensed Matter* 31.50 (Dec. 2019), p. 503004. DOI: 10.1088/1361-648X/ab3eda.

[10] Romain Geneaux et al. *Transient absorption spectroscopy using high harmonic generation: A review of ultrafast X-ray dynamics in molecules and solids*. May 2019. DOI: 10.1098/rsta.2017.0463.

[11] Tobias Brixner et al. "Phase-stabilized two-dimensional electronic spectroscopy". In: *Journal of Chemical Physics* 121.9 (2004), pp. 4221–4236. DOI: 10.1063/1.1776112.

[12] Charles A. Schmuttenmaer. "Exploring dynamics in the far-infrared with terahertz spectroscopy". In: *Chemical Reviews* 104.4 (Apr. 2004), pp. 1759–1779. DOI: 10.1021/cr020685g.

[13] P. B. Corkum. "Plasma perspective on strong field multiphoton ionization". In: *Physical Review Letters* 71.13 (Sept. 1993), pp. 1994–1997. DOI: 10.1103/PhysRevLett.71.1994.

[14] Jeffrey L. Krause, Kenneth J. Schafer, and Kenneth C. Kulander. "High-order harmonic generation from atoms and ions in the high intensity regime". In: *Physical Review Letters* 68.24 (June 1992), pp. 3535–3538. DOI: 10.1103/PhysRevLett.68.3535.

[15] M. Ferray et al. "Multiple-harmonic conversion of 1064 nm radiation in rare gases". In: *Journal of Physics B: Atomic, Molecular and Optical Physics* 21.3 (1988). DOI: 10.1088/0953-4075/21/3/001.

[16] Allan S. Johnson et al. "High-flux soft x-ray harmonic generation from ionization-shaped few-cycle laser pulses". In: *Science Advances* 4.5 (May 2018). DOI: 10.1126/sciadv.aar3761.

[17] Junko Yano and Vittal K. Yachandra. "X-ray absorption spectroscopy". In: *Photosynthesis Research* 102.2-3 (Dec. 2009), pp. 241–254. DOI: 10.1007/s11120-009-9473-8.

[18] R.W. Schoenlein. *New Science Opportunities Enabled By LCLS-II X-Ray Lasers*. Tech. rep. 2015, pp. 1–189.

[19] P. Emma et al. "First lasing and operation of an ångstrom-wavelength free-electron laser". In: *Nature Photonics* 4.9 (Sept. 2010), pp. 641–647. DOI: 10.1038/nphoton.2010.176.

[20] Christian Brahms and John C Travers. "Timing and energy stability of resonant dispersive wave emission in gas-filled hollow-core waveguides". In: *Journal of Physics: Photonics* 3.2 (Apr. 2021), p. 025004. DOI: 10.1088/2515-7647/abf238.

[21] Atia-tul-noor et al. "Sub-50 fs temporal resolution in an FEL-optical laser pump-probe experiment at FLASH2". In: *Optics Express* 32.4 (Feb. 2024), p. 6597. DOI: 10.1364/OE.513714.

[22] E. Lorek et al. "High-order harmonic generation using a high-repetition-rate turnkey laser". In: *Review of Scientific Instruments* 85.12 (Dec. 2014), p. 123106. DOI: 10.1063/1.4902819.

[23] John C. Travers et al. "High-energy pulse self-compression and ultraviolet generation through soliton dynamics in hollow capillary fibres". In: *Nature Photonics* 13.8 (Aug. 2019), pp. 547–554. DOI: 10.1038/s41566-019-0416-4.

[24] Anne-Lise Viotti et al. "Multi-pass cells for post-compression of ultrashort laser pulses". In: *Optica* 9.2 (Feb. 2022), p. 197. DOI: 10.1364/OPTICA.449225.

[25] Yi Wu, Fangjie Zhou, and Zenghu Chang. "Generation of 4.5mJ 2.5-μm pulses from a single stage Cr2+:ZnSe chirped-pulse amplifier". In: *Frontiers in Optics - Proceedings Frontiers in Optics + Laser Science APS/DLS*. 2019. DOI: 10.1364/FIO.2019.JW3A.47.

[26] Krishna Murari et al. "Ho:YLF amplifier with Ti:Sapphire frontend for pumping mid-infrared optical parametric amplifier". In: *Applied Physics Letters* 117.14 (Oct. 2020), p. 141102. DOI: 10.1063/5.0021438.

[27] Ming Zhong et al. "Retina, Retinol, Retinal and the Natural History of Vitamin A as a Light Sensor". In: *Nutrients* 4.12 (Dec. 2012), pp. 2069–2096. DOI: 10.3390/nu4122069.

[28] Sewon Kang et al. "Topical n-acetyl cysteine and genistein prevent ultraviolet-light-induced signaling that leads to photoaging in human skin in vivo". In: *Journal of Investigative Dermatology* 120.5 (May 2003), pp. 835–841. DOI: 10.1046/j.1523-1747.2003.12122.x.

[29] M. Ghotbi, M. Beutler, and F. Noack. "Generation of 25 μJ vacuum ultraviolet pulses with sub-50 fs duration by noncollinear four-wave mixing in argon". In: *Optics Letters* 35.20 (Oct. 2010), p. 3492. DOI: 10.1364/ol.35.003492.

[30] John C. Travers. "Optical solitons in hollow-core fibres". In: *Optics Communications* 555 (Mar. 2024), p. 130191. DOI: 10.1016/j.optcom.2023.130191.

[31] Rick Trebino et al. *Measuring ultrashort laser pulses in the time-frequency domain using frequency-resolved optical gating*. Tech. rep. 1997.

[32] Martin Dorner-Kirchner et al. "HHG at the Carbon K-Edge Directly Driven by SRS Red-Shifted Pulses from an Ytterbium Amplifier". In: *ACS Photonics* 10.1 (Jan. 2023), pp. 84–91. DOI: 10.1021/acsphotonics.2c01021.

[33] Allan Stewart Johnson. "Long and Short Wavelength Optical Sources for Attosecond Science". PhD thesis. Imperial College London, 2017.

[34] Nobuhisa Ishii et al. "Carrier-envelope phase-dependent high harmonic generation in the water window using few-cycle infrared pulses". In: *Nature Communications 2014 5:1* 5.1 (Feb. 2014), pp. 1–6. DOI: 10.1038/ncomms4331.

[35] Yuxi Fu et al. "High efficiency ultrafast water-window harmonic generation for single-shot soft X-ray spectroscopy". In: *Communications Physics* 3.1 (May 2020), p. 92. DOI: 10.1038/s42005-020-0355-x.

[36] Yoann Pertot et al. "Time-resolved x-ray absorption spectroscopy with a water window high-harmonic source". In: *Science* 355.6322 (2017), pp. 264–267. DOI: 10.1126/science.aah6114.

[37] R. Weissenbilder et al. "How to optimize high-order harmonic generation in gases". In: *Nature Reviews Physics* 4.11 (Oct. 2022), pp. 713–722. DOI: 10.1038/s42254-022-00522-7.

[38] Lou Barreau et al. "Efficient table-top dual-wavelength beamline for ultrafast transient absorption spectroscopy in the soft X-ray region". In: *Scientific Reports* 10.1 (Dec. 2020), pp. 1–9. DOI: 10.1038/s41598-020-62461-6.

[39] Chien-Jen Lai, Kyung-Han Hong, and Jonathas P Siqueira. "Water-window soft x-ray high-harmonic generation up to the nitrogen K-edge driven by a kHz, 2.1 μm OPCPA source Related content Multi-mJ mid-infrared kHz OPCPA

and Yb-doped pump lasers for tabletop coherent soft x-ray generation". In: *J. Phys. B: At. Mol. Opt. Phys* 49 (2016), p. 155601. DOI: 10.1088/0953-4075/49/15/155601.

[40] A. Comby et al. "Absolute gas density profiling in high-order harmonic generation". In: *Optics Express* 26.5 (Mar. 2018), p. 6001. DOI: 10.1364/OE.26.006001.

[41] Allan S. Johnson et al. "Apparatus for soft x-ray table-top high harmonic generation". In: *Review of Scientific Instruments* 89.8 (Aug. 2018). DOI: 10.1063/1.5041498.

[42] Yasuki Arasaki and Kazuo Takatsuka. "Optical conversion of conical intersection to avoided crossing". In: *Physical Chemistry Chemical Physics* 12.6 (Jan. 2010), pp. 1239–1242. DOI: 10.1039/b919504a.

[43] Thierry Tran et al. "The quantum-Ehrenfest method with the inclusion of an IR pulse: Application to electron dynamics of the allene radical cation". In: *Journal of Chemical Physics* 153.3 (July 2020), p. 031102. DOI: 10.1063/5.0015937.

[44] B. L. Henke, E. M. Gullikson, and J. C. Davis. "X-ray interactions: Photoabsorption, scattering, transmission, and reflection at E = 50-30, 000 eV, Z = 1-92". In: *Atomic Data and Nuclear Data Tables* 54.2 (July 1993), pp. 181–342. DOI: 10.1006/adnd.1993.1013.

[45] Gediminas Galinis et al. "Micrometer-thickness liquid sheet jets flowing in vacuum". In: *Review of Scientific Instruments* 88.8 (Aug. 2017), p. 83117. DOI: 10.1063/1.4990130.

[46] Jonathan C. T. Barnard et al. "Delivery of stable ultra-thin liquid sheets in vacuum for biochemical spectroscopy". In: *Frontiers in Molecular Biosciences* 9 (Nov. 2022), p. 1044610. DOI: 10.3389/fmolb.2022.1044610.

[47] G Fowles. *Introduction to modern optics*. Holt, Rinehart and Winston, 1975.

[48] G P Agrawal and Robert W Boyd. *Contemporary nonlinear optics*. 1992, xiv, 478 p. DOI: 10.1016/B978-0-12-145135-6.50011-1.

[49] Robert W. Boyd. "Nonlinear Optics". In: *Nonlinear Optics* (2008). DOI: 10.1201/9781420004694.ch5.

[50] Ofer Kfir et al. "Generation of bright phase-matched circularly-polarized extreme ultraviolet high harmonics". In: *Nature Photonics* 9.2 (Feb. 2015), pp. 99–105. DOI: 10.1038/nphoton.2014.293.

[51] Max Möller et al. "Dependence of high-order-harmonic-generation yield on driving-laser ellipticity". In: *Physical Review A - Atomic, Molecular, and Optical Physics* 86.1 (July 2012), p. 011401. DOI: 10.1103/PHYSREVA.86.011401/FIGURES/3/MEDIUM.

[52] Shambhu Ghimire and David A. Reis. "High-harmonic generation from solids". In: *Nature Physics* 15.1 (Jan. 2019), pp. 10–16. DOI: 10.1038/s41567-018-0315-5.

[53] Athanasios Lekosiotis et al. "Ultrafast circularly polarized pulses tunable from the vacuum to deep ultraviolet". In: *Optics Letters* 46.16 (Aug. 2021), p. 4057. DOI: 10.1364/OL.432228.

[54] Stéphane Schilt and Thomas Südmeyer. "Carrier-Envelope Offset Stabilized Ultrafast Diode-Pumped Solid-State Lasers". In: *Applied Sciences 2015, Vol. 5, Pages 787-816* 5.4 (Oct. 2015), pp. 787–816. DOI: 10.3390/APP5040787.

[55] R A Lewis. "A review of terahertz sources". In: *Journal of Physics D: Applied Physics* 47.37 (Sept. 2014), p. 374001. DOI: 10.1088/0022-3727/47/37/374001.

[56] R. Szipőcs and A. Kőházi-Kis. "Theory and design of chirped dielectric laser mirrors". In: *Applied Physics B: Lasers and Optics* 65.2 (Aug. 1997), pp. 115–135. DOI: 10.1007/s003400050258.

[57] Tamas Nagy, Peter Simon, and Laszlo Veisz. "High-energy few-cycle pulses: post-compression techniques". In: *Advances in Physics: X* 6.1 (Jan. 2021). DOI: 10.1080/23746149.2020.1845795.

[58] Eugene Hecht. *OPTICS FIFTH EDITION*. Reading, Mass: Addison-Wesley, 2002.

[59] Govind Agrawal. *Nonlinear Fiber Optics*. Elsevier, 2013. DOI: 10.1016/C2011-0-00045-5.

[60] E. A. J. Marcatili and R. A. Schmeltzer. "Hollow Metallic and Dielectric Waveguides for Long Distance Optical Transmission and Lasers". In: *Bell System Technical Journal* 43.4 (July 1964), pp. 1783–1809. DOI: 10.1002/j.1538-7305.1964.tb04108.x.

[61] Malte Christian Brahms. "Few-Femtosecond Deep-UV Pulses for Transient-Absorption Experiments". PhD thesis. Imperial College London, 2018.

[62] Gadi Fibich and Alexander L. Gaeta. "Critical power for self-focusing in bulk media and in hollow waveguides". In: *Optics Letters* 25.5 (Mar. 2000), p. 335. DOI: 10.1364/OL.25.000335.

[63] Ugaitz Elu et al. "Seven-octave high-brightness and carrier-envelope-phase-stable light source". In: *Nature Photonics* 15.4 (Dec. 2021), pp. 277–280. DOI: 10.1038/s41566-020-00735-1.

[64] Fedor Mitschke, Christoph Mahnke, and Alexander Hause. "Soliton Content of Fiber-Optic Light Pulses". In: *Applied Sciences* 7.6 (June 2017), p. 635. DOI: 10.3390/app7060635.

[65] J.N. Elgin, T. Brabec, and S.M.J. Kelly. "A perturbative theory of soliton propagation in the presence of third order dispersion". In: *Optics Communications* 114.3-4 (Feb. 1995), pp. 321–328. DOI: 10.1016/0030-4018(94)00602-Q.

[66] Dane R. Austin et al. "Role of tunnel ionization in high harmonic generation from substituted benzenes". In: *Faraday Discussions*. Vol. 194. 0. The Royal Society of Chemistry, Dec. 2016, pp. 349–368. DOI: 10.1039/c6fd00116e.

[67] A. V. Husakou and J. Herrmann. "Supercontinuum Generation of Higher-Order Solitons by Fission in Photonic Crystal Fibers". In: *Physical Review Letters* 87.20 (Oct. 2001), p. 203901. DOI: 10.1103/PhysRevLett.87.203901.

[68] Nail Akhmediev and Magnus Karlsson. "Cherenkov radiation emitted by solitons in optical fibers". In: *Physical Review A* 51.3 (Mar. 1995), pp. 2602–2607. DOI: 10.1103/PhysRevA.51.2602.

[69] John C. Travers et al. "Ultrafast nonlinear optics in gas-filled hollow-core photonic crystal fibers [Invited]". In: *Journal of the Optical Society of America B* 28.12 (Dec. 2011), A11. DOI: 10.1364/JOSAB.28.000A11.

[70] M. Erkintalo et al. "Cascaded phase matching and nonlinear symmetry breaking in fiber frequency combs". In: *Physical Review Letters* 109.22 (Nov. 2012), p. 223904. DOI: 10.1103/PHYSREVLETT.109.223904/FIGURES/3/MEDIUM.

[71] Arismar Cerqueira Sodre et al. "Highly efficient generation of broadband cascaded four-wave mixing products". In: *Optics Express* 16.4 (Feb. 2008), p. 2816. DOI: 10.1364/OE.16.002816.

[72] Christian Brahms and John C. Travers. *Luna.jl*. Dec. 2021. DOI: 10.5281/ZENODO.5797786. URL: https://zenodo.org/record/5797786.

[73] Maxim V. Ammosov, Nikolai B. Delone, and Vladimir P. Krainov. "Tunnel Ionization Of Complex Atoms And Atomic Ions In Electromagnetic Field". In: *Sov. Phys. JETP*. Ed. by John A. Alcock. Vol. 64. December 1986. Oct. 1986, p. 138. DOI: 10.1117/12.938695.

[74] A M Perelomov, V S Popov, and M.V. Terent'ev. "Ionization of atoms in an alternating electrical field". In: *Sov. Phys. JETP* 23.5 (1966), p. 924. DOI: 10.1016/0009-8981(77)90443-0.

[75] S F J Larochelle, A Talebpour, and S L Chin. "Coulomb effect in multiphoton ionization of rare-gas atoms". In: *J. Phys. B: At. Mol. Opt. Phys* 31 (1998), pp. 1215–1224.

[76] Carsten Bree, Ayhan Demircan, and Günter Steinmeyer. "Method for Computing the Nonlinear Refractive Index via Keldysh Theory". In: *IEEE Journal of Quantum Electronics* 46.4 (Apr. 2010), pp. 433–437. DOI: 10.1109/JQE.2009.2031599.

[77] Yehuda Benzion Band. *Light and matter : electromagnetism, optics, spectroscopy and lasers*. John Wiley, July 2006, p. 640.

[78] Wm M. Wood, C. W. Siders, and M. C. Downer. "Measurement of femtosecond ionization dynamics of atmospheric density gases by spectral blueshift-

ing". In: *Physical Review Letters* 67.25 (Dec. 1991), p. 3523. DOI: 10.1103/PhysRevLett.67.3523.

[79] K. C. Kulander, K. J. Schafer, and J. L. Krause. "Dynamics of Short-Pulse Excitation, Ionization and Harmonic Conversion". In: (1993), pp. 95–110. DOI: 10.1007/978-1-4615-7963-2{_}10.

[80] Douglas Garratt. "Time Resolved X-ray Absorption Spectroscopy in Poly (3-hexylthiophene)". PhD thesis. Imperial College London, 2020.

[81] Ferenc Krausz and Misha Ivanov. "Attosecond physics". In: *Reviews of Modern Physics* 81.1 (2009), pp. 163–234. DOI: 10.1103/RevModPhys.81.163.

[82] M. Lewenstein et al. "Theory of high-harmonic generation by low-frequency laser fields". In: *Physical Review A* 49.3 (Mar. 1994), pp. 2117–2132. DOI: 10.1103/PhysRevA.49.2117.

[83] Vladislav S Yakovlev et al. "Plasma perspective on strong field multiphoton ionization". In: *13. T. J. Mod. Opt* 3.23 (2007), pp. 441–450.

[84] K. Schiessl et al. "Quantum Path Interference in the Wavelength Dependence of High-Harmonic Generation". In: *Physical Review Letters* 99.25 (Dec. 2007), p. 253903. DOI: 10.1103/PhysRevLett.99.253903.

[85] A D Shiner et al. "Wavelength Scaling of High Harmonic Generation Efficiency". In: (). DOI: 10.1103/PhysRevLett.103.073902.

[86] Dane R. Austin and Jens Biegert. "Strong-field approximation for the wavelength scaling of high-harmonic generation". In: *Physical Review A - Atomic, Molecular, and Optical Physics* 86.2 (2012), p. 23813. DOI: 10.1103/PhysRevA.86.023813.

[87] E. L. Falcão-Filho et al. "Analytic scaling analysis of high harmonic generation conversion efficiency". In: *Optics Express* 17.13 (June 2009), p. 11217. DOI: 10.1364/OE.17.011217.

[88] Kasra Amini et al. "Symphony on strong field approximation". In: *Reports on Progress in Physics* 82.11 (Nov. 2019), p. 116001. DOI: 10.1088/1361-6633/ab2bb1.

[89] L. E. Chipperfield et al. “Tracking individual electron trajectories in a high harmonic spectrum”. In: *Optics Communications* 264.2 (Aug. 2006), pp. 494–501. DOI: 10.1016/j.optcom.2006.03.078.

[90] Dimitar Popmintchev et al. “Ultraviolet surprise: Efficient soft x-ray high-harmonic generation in multiply ionized plasmas”. In: *Science* 350.6265 (Dec. 2015), pp. 1225–1231. DOI: 10.1126/science.aac9755.

[91] A. McPherson et al. “Studies of multiphoton production of vacuum-ultraviolet radiation in the rare gases”. In: *Journal of the Optical Society of America B* 4.4 (1987), p. 595. DOI: 10.1364/josab.4.000595.

[92] Antonin Borot et al. “High-harmonic generation from plasma mirrors at kilohertz repetition rate”. In: *Optics Letters* 36.8 (Apr. 2011), p. 1461. DOI: 10.1364/OL.36.001461.

[93] Oliver Alexander et al. “Observation of recollision-based high-harmonic generation in liquid isopropanol and the role of electron scattering”. In: *Physical Review Research* 5.4 (Oct. 2023), p. 043030. DOI: 10.1103/PhysRevResearch.5.043030.

[94] Tran Trung Luu et al. “Extreme–ultraviolet high–harmonic generation in liquids”. In: *Nature Communications* 9.1 (Dec. 2018), p. 3723. DOI: 10.1038/s41467-018-06040-4.

[95] Shambhu Ghimire et al. “Strong-field and attosecond physics in solids”. In: *Journal of Physics B: Atomic, Molecular and Optical Physics* 47.20 (Oct. 2014), p. 204030. DOI: 10.1088/0953-4075/47/20/204030.

[96] M. Yeung et al. “Noncollinear Polarization Gating of Attosecond Pulse Trains in the Relativistic Regime”. In: *Physical Review Letters* 115.19 (Nov. 2015), p. 193903. DOI: 10.1103/PHYSREVLETT.115.193903/FIGURES/5/MEDIUM.

[97] Indranuj Dey et al. “Highly efficient broadband terahertz generation from ultrashort laser filamentation in liquids”. In: *Nature Communications* 8.1 (Oct. 2017), p. 1184. DOI: 10.1038/s41467-017-01382-x.

[98] Jie Li et al. “Attosecond science based on high harmonic generation from gases and solids”. In: *Nature Communications* 11.1 (June 2020), p. 2748. DOI: 10.1038/s41467-020-16480-6.

[99] Philippe Antoine, Anne L’Huillier, and Maciej Lewenstein. “Attosecond Pulse Trains Using High–Order Harmonics”. In: *Physical Review Letters* 77.7 (Aug. 1996), pp. 1234–1237. DOI: 10.1103/PhysRevLett.77.1234.

[100] Zenghu Chang, Paul B. Corkum, and Stephen R. Leone. “Attosecond optics and technology: progress to date and future prospects [Invited]”. In: *Journal of the Optical Society of America B* 33.6 (June 2016), p. 1081. DOI: 10.1364/JOSAB.33.001081.

[101] Philippe Balcou et al. “Generalized phase-matching conditions for high harmonics: The role of field-gradient forces”. In: *Physical Review A* 55.4 (Apr. 1997), pp. 3204–3210. DOI: 10.1103/PhysRevA.55.3204.

[102] Maciej Lewenstein, Pascal Salières, and Anne L’Huillier. “Phase of the atomic polarization in high-order harmonic generation”. In: *Physical Review A* 52.6 (Dec. 1995), pp. 4747–4754. DOI: 10.1103/PhysRevA.52.4747.

[103] E. Constant et al. “Optimizing High Harmonic Generation in Absorbing Gases: Model and Experiment”. In: *Physical Review Letters* 82.8 (Feb. 1999), pp. 1668–1671. DOI: 10.1103/PhysRevLett.82.1668.

[104] C. M. Heyl et al. “Scaling Nonlinear Optics in Gases”. In: *Optics InfoBase Conference Papers*. Vol. 3. 1. Optica Publishing Group, Jan. 2016, pp. 75–81. DOI: 10.1364/HILAS.2016.HS2B.4.

[105] *RedDragon - 50W — KMLabs*. URL: https://www.kmlabs.com/product/reddragon-50w/.

[106] A. C. DeFranzo and B. G. Pazol. “Index of refraction measurement on sapphire at low temperatures and visible wavelengths”. In: *Applied Optics* 32.13 (May 1993), p. 2224. DOI: 10.1364/AO.32.002224.

[107] Sterling Backus et al. “02-TW laser system at 1 kHz”. In: *Optics Letters* 22.16 (Aug. 1997), p. 1256. DOI: 10.1364/OL.22.001256.

[108] *Light Conversion: Optical Parametric Amplifiers for Ti:Sapphire Lasers*. URL: https://lightcon.com/product/topas-prime-high-energy-opa/#ufs.

[109] Andrius Baltuška, Takao Fuji, and Takayoshi Kobayashi. "Controlling the Carrier-Envelope Phase of Ultrashort Light Pulses with Optical Parametric Amplifiers". In: *Physical Review Letters* 88.13 (Mar. 2002), p. 133901. DOI: 10.1103/PhysRevLett.88.133901.

[110] U. Morgner et al. "Nonlinear Optics with Phase-Controlled Pulses in the Sub-Two-Cycle Regime". In: *Physical Review Letters* 86.24 (June 2001), pp. 5462–5465. DOI: 10.1103/PhysRevLett.86.5462.

[111] Th. Udem et al. "Measuring the frequency of light with a mode-locked laser". In: *The 15th Annual Meeting of the IEEE Lasers and Electro-Optics Society*. Vol. 1. IEEE, 2002, pp. 169–170. DOI: 10.1109/LEOS.2002.1133981.

[112] I. H. Malitson. "Interspecimen Comparison of the Refractive Index of Fused Silica*,†". In: *Journal of the Optical Society of America* 55.10 (Oct. 1965), p. 1205. DOI: 10.1364/JOSA.55.001205.

[113] Ian A. Walmsley and Christophe Dorrer. "Characterization of ultrashort electromagnetic pulses". In: *Advances in Optics and Photonics* 1.2 (Apr. 2009), p. 308. DOI: 10.1364/AOP.1.000308.

[114] Chris Iaconis, Matthew E. Anderson, and Ian A. Walmsley. "Spectral Phase Interferometry for Direct Electric Field Reconstruction of Ultrashort Optical Pulses". In: *Springer Series in Chemical Physics*. Vol. 63. 10. 1998, pp. 103–105. DOI: 10.1007/978-3-642-72289-9{_}31.

[115] Adam S Wyatt et al. "Sub-10 fs pulse characterization using spatially encoded arrangement for spectral phase interferometry for direct electric field reconstruction". In: (2006).

[116] Miguel Miranda et al. "Characterization of broadband few-cycle laser pulses with the d-scan technique". In: *Optics Express* 20.17 (Aug. 2012), p. 18732. DOI: 10.1364/OE.20.018732.

[117] Ocean Optics Inc. *USB2000+ Fiber Optic Gated Spectrometer Installation and Operation Manual*. 2010. URL: https://www.oceaninsight.com/globalassets/

catalog-blocks-and-images/manuals--instruction-ocean-optics/spectrometer/usb2000-operating-instructions1.pdf.

[118] D.J. Kane and R. Trebino. "Characterization of arbitrary femtosecond pulses using frequency-resolved optical gating". In: *IEEE Journal of Quantum Electronics* 29.2 (1993), pp. 571–579. DOI: 10.1109/3.199311.

[119] Christian Brahms, Federico Belli, and John C. Travers. "Resonant dispersive wave emission in hollow capillary fibers filled with pressure gradients". In: *Optics Letters* 45.16 (Aug. 2020), p. 4456. DOI: 10.1364/OL.398343.

[120] M. Nisoli, S. De Silvestri, and O. Svelto. "Generation of high energy 10 fs pulses by a new pulse compression technique". In: *Applied Physics Letters* 68.20 (May 1996), pp. 2793–2795. DOI: 10.1063/1.116609.

[121] Chris Leistner et al. "Shrinkage behavior of Araldite epoxy resin using Archimedes' principle". In: *Polymer Testing* 67 (May 2018), pp. 409–416. DOI: 10.1016/j.polymertesting.2018.03.031.

[122] Yasir Nawab et al. "Chemical shrinkage characterization techniques for thermoset resins and associated composites". In: *Journal of Materials Science* 48.16 (Aug. 2013), pp. 5387–5409. DOI: 10.1007/s10853-013-7333-6.

[123] A. Couairon et al. *Practitioner's guide to laser pulse propagation models and simulation*. Dec. 2011. DOI: 10.1140/epjst/e2011-01503-3. URL: https://link.springer.com/article/10.1140/epjst/e2011-01503-3.

[124] Crystran LTD. *The Design of Pressure Windows*. 2013. URL: https://www.crystran.co.uk/userfiles/files/design-of-pressure-windows.pdf.

[125] *Piezoelectric Deformable Mirror DMP40 Operation Manual*. 2021. URL: https://www.thorlabs.com/thorproduct.cfm?partnumber=DMP40/M-P01.

[126] G Vdovin et al. *LightPipes for Python*. URL: https://opticspy.github.io/lightpipes/.

[127] Ian H. Bell et al. "Pure and pseudo-pure fluid thermophysical property evaluation and the open-source thermophysical property library coolprop". In: *Industrial and Engineering Chemistry Research* 53.6 (Feb. 2014), pp. 2498–2508. DOI: 10.1021/ie4033999.

[128] Allan S. Johnson et al. “Attosecond soft X-ray high harmonic generation”. In: *Philosophical Transactions of the Royal Society A: Mathematical, Physical and Engineering Sciences* 377.2145 (May 2019), p. 20170468. DOI: 10.1098/rsta.2017.0468.

[129] C M Heyl et al. “Introduction to macroscopic power scaling principles for high-order harmonic generation”. In: *Journal of Physics B: Atomic, Molecular and Optical Physics* 50.1 (Jan. 2017), p. 013001. DOI: 10.1088/1361-6455/50/1/013001.

[130] C. Marceau et al. “Wavelength scaling of high harmonic generation for 267 nm, 400nm and 800nm driving laser pulses”. In: *Journal of Physics Communications* 1.1 (Sept. 2017), p. 015009. DOI: 10.1088/2399-6528/aa74f6.

[131] A. S. Johnson et al. “Measurement of sulfur L2,3 and carbon K edge XANES in a polythiophene film using a high harmonic supercontinuum”. In: *Structural Dynamics* 3.6 (Nov. 2016), p. 062603. DOI: 10.1063/1.4964821.

[132] James Grant-Jacob et al. “Gas jet structure influence on high harmonic generation”. In: *Optics Express* 19.10 (May 2011), p. 9801. DOI: 10.1364/oe.19.009801.

[133] Lana Neoričić et al. “4D spatio-temporal electric field characterization of ultrashort light pulses undergoing filamentation”. In: *Optics Express, Vol. 30, Issue 15, pp. 27938-27950* 30.15 (July 2022), pp. 27938–27950. DOI: 10.1364/OE.461388.

[134] S. Varoutis et al. “Rarefied gas flow through short tubes into vacuum”. In: *Journal of Vacuum Science & Technology A: Vacuum, Surfaces, and Films* 26.2 (Mar. 2008), pp. 228–238. DOI: 10.1116/1.2830639.

[135] Jialin Li et al. “Beam optimization in a 25 TW femtosecond laser system for high harmonic generation”. In: *Journal of Physics B: Atomic, Molecular and Optical Physics* 53.14 (2020). DOI: 10.1088/1361-6455/ab8e57.

[136] J R Sutherland et al. “High harmonic generation in a semi-infinite gas cell”. In: *Optics Express* 12.19 (Sept. 2004), p. 4430. DOI: 10.1364/opex.12.004430.

[137] F Brizuela et al. “Efficient high-order harmonic generation boosted by below-threshold harmonics”. In: *Scientific Reports* 3 (2013). DOI: 10.1038/srep01410.

[138] M. D. Feit and J. A. Fleck. “Beam nonparaxiality, filament formation, and beam breakup in the self-focusing of optical beams”. In: *Journal of the Optical Society of America B* 5.3 (Mar. 1988), p. 633. DOI: 10.1364/josab.5.000633.

[139] J. R. Dormand and P. J. Prince. “A family of embedded Runge-Kutta formulae”. In: *Journal of Computational and Applied Mathematics* 6.1 (Mar. 1980), pp. 19–26. DOI: 10.1016/0771-050X(80)90013-3.

[140] Jean Christophe Tremblay and Tucker Carrington. “Using preconditioned adaptive step size Runge-Kutta methods for solving the time-dependent Schrödinger equation”. In: *Journal of Chemical Physics* 121.23 (2004), pp. 11535–11541. DOI: 10.1063/1.1814103.

[141] Gabriel Tempea et al. “Self-phase-matched high harmonic generation”. In: *Physical Review Letters* 84.19 (May 2000), pp. 4329–4332. DOI: 10.1103/PhysRevLett.84.4329.

[142] Tenio Popmintchev et al. “Phase matching of high harmonic generation in the soft and hard X-ray regions of the spectrum”. In: *Proceedings of the National Academy of Sciences of the United States of America* 106.26 (2009), pp. 10516–10521. DOI: 10.1073/pnas.0903748106.

[143] Vladimir S Popov. “Tunnel and multiphoton ionization of atoms and ions in a strong laser field (Keldysh theory)”. In: *Physics-Uspekhi* 47.9 (Sept. 2004), p. 855. DOI: 10.1070/PU2004V047N09ABEH001812.

[144] Anne L’Huillier et al. “Calculations of high-order harmonic-generation processes in xenon at 1064 nm”. In: *Physical Review A* 46.5 (Sept. 1992), pp. 2778–2790. DOI: 10.1103/PhysRevA.46.2778.

[145] M. Geissler, G. Tempea, and T. Brabec. “Phase-matched high-order harmonic generation in the nonadiabatic limit”. In: *Physical Review A - Atomic, Molecular, and Optical Physics* 62.3 (Aug. 2000), p. 8. DOI: 10.1103/PhysRevA.62.033817.

[146] C Vozzi et al. “Phase-matching effects in the generation of high-energy photons by mid-infrared few-cycle laser pulses”. In: *New Journal of Physics* 13.7 (July 2011), p. 073003. DOI: 10.1088/1367-2630/13/7/073003.

[147] Shambhu Ghimire et al. “Observation of high-order harmonic generation in a bulk crystal”. In: *Nature Physics* 7.2 (Feb. 2011), pp. 138–141. DOI: 10.1038/nphys1847.

[148] Yong Sing You et al. “High-harmonic generation in amorphous solids”. In: *Nature Communications 2017 8:1* 8.1 (Sept. 2017), pp. 1–5. DOI: 10.1038/s41467-017-00989-4.

[149] Heiko G. Kurz et al. “Revealing the Microscopic Real-Space Excursion of a Laser-Driven Electron”. In: *Physical Review X* 6.3 (Aug. 2016), p. 031029. DOI: 10.1103/PhysRevX.6.031029.

[150] Anthony D DiChiara et al. “An investigation of harmonic generation in liquid media with a mid-infrared laser”. In: *Optics Express* 17.23 (Nov. 2009), p. 20959. DOI: 10.1364/oe.17.020959.

[151] A. Flettner et al. “High-harmonic generation and plasma radiation from water microdroplets”. In: *Applied Physics B* 77.8 (Dec. 2003), pp. 747–751. DOI: 10.1007/s00340-003-1329-x.

[152] P. Heissler et al. “Using the third state of matter: high harmonic generation from liquid targets”. In: *New Journal of Physics* 16.11 (Nov. 2014), p. 113045. DOI: 10.1088/1367-2630/16/11/113045.

[153] Clément Ferchaud et al. “Interaction of an intense few-cycle infrared laser pulse with an ultrathin transparent liquid sheet”. In: *Optics Express* 30.19 (Sept. 2022), p. 34684. DOI: 10.1364/OE.457470.

[154] Sebastian Jarosch. “High harmonic generation driven by few-cycle infrared fields in gases and liquids”. PhD thesis. Imperial College London, 2019.

[155] Jonathan Charles and Tobit Barnard. “X-ray generation from and spectroscopy of a thin liquid sheet”. PhD thesis. Imperial College London, 2021. DOI: 10.25560/92791.

[156] Daniel R. Stull. "Vapor Pressure of Pure Substances. Organic and Inorganic Compounds". In: *Industrial & Engineering Chemistry* 39.4 (Apr. 1947), pp. 517–540. DOI: 10.1021/ie50448a022.

[157] M. D. Feit, A. M. Komashko, and A. M. Rubenchik. "Ultra-short pulse laser interaction with transparent dielectrics". In: *Applied Physics A: Materials Science and Processing* 79.7 (2004), pp. 1657–1661. DOI: 10.1007/s00339-004-2683-1.

[158] B. C. Stuart et al. "Nanosecond-to-femtosecond laser-induced breakdown in dielectrics". In: *Physical Review B* 53.4 (Jan. 1996), pp. 1749–1761. DOI: 10.1103/PhysRevB.53.1749.

[159] S. C. Rae. "Ionization-induced defocusing of intense laser pulses in high-pressure gases". In: *Optics Communications* 97.1-2 (Mar. 1993), pp. 25–28. DOI: 10.1016/0030-4018(93)90611-8.

[160] Quan Sun et al. "Measurement of the collision time of dense electronic plasma induced by a femtosecond laser in fused silica". In: *Optics Letters* 30.3 (Feb. 2005), p. 320. DOI: 10.1364/OL.30.000320.

[161] A. Dubietis et al. "Measurement and calculation of nonlinear absorption associated with femtosecond filaments in water". In: *Applied Physics B* 84.3 (Sept. 2006), pp. 439–446. DOI: 10.1007/s00340-006-2249-3.

[162] M. Lebugle et al. "Absorption dynamics of a femtosecond laser pulse at the surface of dielectrics". In: *AIP Conference Proceedings*. Vol. 1464. 1. American Institute of PhysicsAIP, July 2012, pp. 91–101. DOI: 10.1063/1.4739863.

[163] M. H. F. Bettega et al. "Collisions of low-energy electrons with isopropanol". In: *Physical Review A* 84.4 (Oct. 2011), p. 042702. DOI: 10.1103/PhysRevA.84.042702.

[164] Thomas E Gartmann et al. "Electron scattering in large water clusters from photoelectron imaging with high harmonic radiation". In: *Physical Chemistry Chemical Physics* 20.24 (2018), pp. 16364–16371. DOI: 10.1039/c8cp02148a.

[165] Ruth Signorell. "Electron Scattering in Liquid Water and Amorphous Ice: A Striking Resemblance". In: *Physical Review Letters* 124.20 (2020). DOI: 10.1103/PhysRevLett.124.205501.

[166] Nidhi Sinha and Bobby Antony. "Mean Free Paths and Cross Sections for Electron Scattering from Liquid Water". In: *Journal of Physical Chemistry B* 125.21 (2021), pp. 5479–5488. DOI: 10.1021/acs.jpcb.0c10781.

[167] C. Champion. "Electron impact ionization of liquid and gaseous water: A single-center partial-wave approach". In: *Physics in Medicine and Biology* 55.1 (2010), pp. 11–32. DOI: 10.1088/0031-9155/55/1/002.

[168] P Rudawski et al. "A high-flux high-order harmonic source". In: *Review of Scientific Instruments* 84.7 (2013), p. 73103. DOI: 10.1063/1.4812266.

[169] G. J. Boyle et al. "Ab initio electron scattering cross-sections and transport in liquid xenon". In: *Journal of Physics D: Applied Physics* 49.35 (Aug. 2016), p. 355201. DOI: 10.1088/0022-3727/49/35/355201.

[170] M. C. Bordage et al. "Comparisons of sets of electron–neutral scattering cross sections and swarm parameters in noble gases: III. Krypton and xenon". In: *Journal of Physics D: Applied Physics* 46.33 (Aug. 2013), p. 334003. DOI: 10.1088/0022-3727/46/33/334003.

[171] Dane R. Austin et al. "Extracting sub-cycle electronic and nuclear dynamics from high harmonic spectra". In: *Scientific Reports 2021 11:1* 11.1 (Jan. 2021), pp. 1–8. DOI: 10.1038/s41598-021-82232-1.

[172] Jacob P. Lee et al. "Few-femtosecond soft X-ray transient absorption spectroscopy with tuneable DUV-Vis pump pulses". In: *Optica* 11.9 (Sept. 2024), p. 1320. DOI: 10.1364/OPTICA.530964.

[173] R. Borrego-Varillas et al. "Two-dimensional UV spectroscopy: a new insight into the structure and dynamics of biomolecules". In: *Chemical Science* 10.43 (Nov. 2019), pp. 9907–9921. DOI: 10.1039/C9SC03871J.

[174] D Garratt et al. "Direct observation of ultrafast exciton localization in an organic semiconductor with soft X-ray transient absorption spectroscopy". In: *Nature Communications* 13.1 (2022). DOI: 10.1038/s41467-022-31008-w.

[175] Sha Ding et al. “An excited state intramolecular proton transfer-based fluorescent probe with a large stokes shift for the turn-on detection of cysteine: a detailed theoretical exploration”. In: *ACS Omega* 5.31 (Aug. 2020), pp. 19695–19701. DOI: 10.1021/acsomega.0c02393.

[176] E. Frumker et al. “Spectral Wavefront Optical Reconstruction by Diffraction”. In: *Conference on Lasers and Electro-Optics 2010*. Washington, D.C.: OSA, May 2010, JThI1. DOI: 10.1364/CLEO.2010.JThI1.

[177] Y. B.S.R. Prasad et al. “Simple interferometer for space and time resolved density measurements of laser produced plasmas”. In: *Review of Scientific Instruments* 77.9 (Sept. 2006), p. 93106. DOI: 10.1063/1.2349596/353353.

[178] Gregory M. Greetham et al. “A 100 kHz Time-Resolved Multiple-Probe Femtosecond to Second Infrared Absorption Spectrometer”. In: *Applied Spectroscopy* 70.4 (Apr. 2016), pp. 645–653. DOI: 10.1177/0003702816631302.

[179] Roberta Moca, Stephen R Meech, and Ismael A Heisler. “Two-Dimensional Electronic Spectroscopy of Chlorophyll a: Solvent Dependent Spectral Evolution”. In: *Journal of Physical Chemistry B* 119.27 (2015), pp. 8623–8630. DOI: 10.1021/acs.jpcb.5b04339.

[180] Elisabetta Collini. “2D Electronic Spectroscopic Techniques for Quantum Technology Applications”. In: *The Journal of Physical Chemistry C* 125.24 (June 2021), pp. 13096–13108. DOI: 10.1021/acs.jpcc.1c02693.

[181] Colin Sonnichsen et al. “OPA-driven hollow-core fiber as a tunable, broadband source for coherent multidimensional spectroscopy”. In: *Optics Express* 29.18 (2021), p. 28352. DOI: 10.1364/oe.431988.

[182] Pavel Malý et al. “Separating single- from multi-particle dynamics in nonlinear spectroscopy”. In: *Nature* 616.7956 (Apr. 2023), pp. 280–287. DOI: 10.1038/s41586-023-05846-7.

[183] L. Valkunas et al. “Nonlinear annihilation of excitations in photosynthetic systems”. In: *Biophysical Journal* 69.3 (Sept. 1995), pp. 1117–1129. DOI: 10.1016/S0006-3495(95)79986-6.

[184] G. Massillon-JL. "Future directions on low-energy radiation dosimetry". In: *Scientific Reports* 11.1 (May 2021), pp. 1–10. DOI: 10.1038/s41598-021-90152-3.

[185] Alfred Vogel et al. "Femtosecond-laser-induced nanocavitation in water: Implications for optical breakdown threshold and cell surgery". In: *Physical Review Letters* 100.3 (2008). DOI: 10.1103/PhysRevLett.100.038102.

[186] L Hoffart et al. "Surface ablation of corneal stroma with few-cycle laser pulses at 800 nm". In: *Optics Express* 19.1 (Jan. 2011), p. 230. DOI: 10.1364/oe.19.000230.

[187] Javier Hernandez-Rueda et al. "Femtosecond laser-ablation of gel and water". In: *Optics Letters* 45.11 (June 2020), p. 3079. DOI: 10.1364/ol.390506.

[188] J A Bearden, A F Burr, and X-Ray Photoelectron Measurements. "Introduction. X-Ray Measurements of Wavelengths". In: *REVIEWS OF MODERN PHYSICS* 39.1 (1967).

9.2 Figure Permissions

American Physical Society
Reuse and Permissions License

05-Dec-2022

This license agreement between the American Physical Society ("APS") and Timur Avni ("You") consists of your license details and the terms and conditions provided by the American Physical Society and SciPris.

Licensed Content Information

License Number:	**RNP/22/DEC/060694**
License date:	05-Dec-2022
DOI:	10.1103/PhysRevLett.82.1668
Title:	Optimizing High Harmonic Generation in Absorbing Gases: Model and Experiment
Author:	E. Constant et al.
Publication:	Physical Review Letters
Publisher:	American Physical Society
Cost:	USD $ 0.00

Request Details

Does your reuse require significant modifications: No

Specify intended distribution locations:	Worldwide
Reuse Category:	Reuse in a thesis/dissertation
Requestor Type:	Student
Items for Reuse:	Figures/Tables
Number of Figure/Tables:	1
Figure/Tables Details:	Figure 1
Format for Reuse:	Print and Electronic
Total number of print copies:	Up to 1000

Information about New Publication:

University/Publisher:	Imperial College
Title of dissertation/thesis:	Coherent, Ultrashort IR, UV and X-Ray Sources for Ultrafast Spectroscopies
Author(s):	Timur Avni
Expected completion date:	Dec. 2022

License Requestor Information

Name:	Timur Avni
Affiliation:	Individual
Email Id:	timuravni@hotmail.co.uk
Country:	United Kingdom

American Physical Society
Reuse and Permissions License

TERMS AND CONDITIONS

The American Physical Society (APS) is pleased to grant the Requestor of this license a non-exclusive, non-transferable permission, limited to Print and Electronic format, provided all criteria outlined below are followed.

1. You must also obtain permission from at least one of the lead authors for each separate work, if you haven't done so already. The author's name and affiliation can be found on the first page of the published Article.
2. For electronic format permissions, Requestor agrees to provide a hyperlink from the reprinted APS material using the source material's DOI on the web page where the work appears. The hyperlink should use the standard DOI resolution URL, http://dx.doi.org/{DOI}. The hyperlink may be embedded in the copyright credit line.
3. For print format permissions, Requestor agrees to print the required copyright credit line on the first page where the material appears: "Reprinted (abstract/excerpt/figure) with permission from [(FULL REFERENCE CITATION) as follows: Author's Names, APS Journal Title, Volume Number, Page Number and Year of Publication.] Copyright (YEAR) by the American Physical Society."
4. Permission granted in this license is for a one-time use and does not include permission for any future editions, updates, databases, formats or other matters. Permission must be sought for any additional use.
5. Use of the material does not and must not imply any endorsement by APS.
6. APS does not imply, purport or intend to grant permission to reuse materials to which it does not hold copyright. It is the requestor's sole responsibility to ensure the licensed material is original to APS and does not contain the copyright of another entity, and that the copyright notice of the figure, photograph, cover or table does not indicate it was reprinted by APS with permission from another source.
7. The permission granted herein is personal to the Requestor for the use specified and is not transferable or assignable without express written permission of APS. This license may not be amended except in writing by APS.
8. You may not alter, edit or modify the material in any manner.
9. You may translate the materials only when translation rights have been granted.
10. APS is not responsible for any errors or omissions due to translation.
11. You may not use the material for promotional, sales, advertising or marketing purposes.
12. The foregoing license shall not take effect unless and until APS or its agent, Aptara, receives payment in full in accordance with Aptara Billing and Payment Terms and Conditions, which are incorporated herein by reference.
13. Should the terms of this license be violated at any time, APS or Aptara may revoke the license with no refund to you and seek relief to the fullest extent of the laws of the USA. Official written notice will be made using the contact information provided with the permission request. Failure to receive such notice will not nullify revocation of the permission.
14. APS reserves all rights not specifically granted herein.
15. This document, including the Aptara Billing and Payment Terms and Conditions, shall be the entire agreement between the parties relating to the subject matter hereof.

American Physical Society
Reuse and Permissions License

04-Dec-2022

This license agreement between the American Physical Society ("APS") and Timur Avni ("You") consists of your license details and the terms and conditions provided by the American Physical Society and SciPris.

Licensed Content Information

License Number:	**RNP/22/DEC/060658**
License date:	04-Dec-2022
DOI:	10.1103/RevModPhys.81.163
Title:	Attosecond physics
Author:	Ferenc Krausz and Misha Ivanov
Publication:	Reviews of Modern Physics
Publisher:	American Physical Society
Cost:	USD $ 0.00

Request Details

Does your reuse require significant modifications: No

Specify intended distribution locations:	Worldwide
Reuse Category:	Reuse in a thesis/dissertation
Requestor Type:	Student
Items for Reuse:	Figures/Tables
Number of Figure/Tables:	1
Figure/Tables Details:	Figure 20
Format for Reuse:	Print and Electronic
Total number of print copies:	Up to 1000

Information about New Publication:

University/Publisher:	
Title of dissertation/thesis:	Coherent, Ultrashort IR, UV and X-Ray Sources for Ultrafast Spectroscopies
Author(s):	Timur Avni
Expected completion date:	Dec. 2022

License Requestor Information

Name:	Timur Avni
Affiliation:	Individual
Email Id:	timuravni@hotmail.co.uk
Country:	United Kingdom

American Physical Society
Reuse and Permissions License

TERMS AND CONDITIONS

The American Physical Society (APS) is pleased to grant the Requestor of this license a non-exclusive, non-transferable permission, limited to Print and Electronic format, provided all criteria outlined below are followed.

1. You must also obtain permission from at least one of the lead authors for each separate work, if you haven't done so already. The author's name and affiliation can be found on the first page of the published Article.
2. For electronic format permissions, Requestor agrees to provide a hyperlink from the reprinted APS material using the source material's DOI on the web page where the work appears. The hyperlink should use the standard DOI resolution URL, http://dx.doi.org/{DOI}. The hyperlink may be embedded in the copyright credit line.
3. For print format permissions, Requestor agrees to print the required copyright credit line on the first page where the material appears: "Reprinted (abstract/excerpt/figure) with permission from [(FULL REFERENCE CITATION) as follows: Author's Names, APS Journal Title, Volume Number, Page Number and Year of Publication.] Copyright (YEAR) by the American Physical Society."
4. Permission granted in this license is for a one-time use and does not include permission for any future editions, updates, databases, formats or other matters. Permission must be sought for any additional use.
5. Use of the material does not and must not imply any endorsement by APS.
6. APS does not imply, purport or intend to grant permission to reuse materials to which it does not hold copyright. It is the requestor's sole responsibility to ensure the licensed material is original to APS and does not contain the copyright of another entity, and that the copyright notice of the figure, photograph, cover or table does not indicate it was reprinted by APS with permission from another source.
7. The permission granted herein is personal to the Requestor for the use specified and is not transferable or assignable without express written permission of APS. This license may not be amended except in writing by APS.
8. You may not alter, edit or modify the material in any manner.
9. You may translate the materials only when translation rights have been granted.
10. APS is not responsible for any errors or omissions due to translation.
11. You may not use the material for promotional, sales, advertising or marketing purposes.
12. The foregoing license shall not take effect unless and until APS or its agent, Aptara, receives payment in full in accordance with Aptara Billing and Payment Terms and Conditions, which are incorporated herein by reference.
13. Should the terms of this license be violated at any time, APS or Aptara may revoke the license with no refund to you and seek relief to the fullest extent of the laws of the USA. Official written notice will be made using the contact information provided with the permission request. Failure to receive such notice will not nullify revocation of the permission.
14. APS reserves all rights not specifically granted herein.
15. This document, including the Aptara Billing and Payment Terms and Conditions, shall be the entire agreement between the parties relating to the subject matter hereof.

CCC Marketplace

Order Confirmation

Thank you, your order has been placed. An email confirmation has been sent to you.

This is not an invoice. Please go to manage account to access your order history and invoices.

CUSTOMER INFORMATION

Payment by invoice: You can cancel your order until the invoice is generated by contacting customer service.

Billing Address

Timur Avni
[redacted]
United Kingdom
[redacted]

Customer Location

Timur Avni
[redacted]
United Kingdom

PO Number (optional)

N/A

Payment options

Invoice

ORDER CONFIRMATION

Confirmation Number: 1296888

Order Date: 04-Dec-2022

1. Philosophical Transactions of the Royal Society of London. Series A: Mathematical, Physical and Engineering Sciences

0.00 GBP

Order License ID	1296888-1	**Publisher**	ROYAL SOCIETY
ISSN	1471-2962	**Portion**	Image/photo/illustration
Type of Use	Republish in a thesis/dissertation		

LICENSED CONTENT

Publication Title	Philosophical Transactions of the Royal Society of London. Series A: Mathematical, Physical and Engineering Sciences	**Country**	United Kingdom of Great Britain and Northern Ireland
		Rightsholder	The Royal Society (U.K.)
		Publication Type	e-Journal

Author/Editor	Royal Society	**URL**	https://royalsociety.org/journals/
Date	01/01/1997		
Language	English		

REQUEST DETAILS

Portion Type	Image/photo/illustration	**Distribution**	Worldwide
Number of Images / Photos / Illustrations	2	**Translation**	Original language of publication
Format (select all that apply)	Print, Electronic	**Copies for the Disabled?**	No
Who Will Republish the Content?	Author of requested content	**Minor Editing Privileges?**	No
Duration of Use	Life of current and all future editions	**Incidental Promotional Use?**	No
Lifetime Unit Quantity	Up to 499	**Currency**	GBP
Rights Requested	Main product		

NEW WORK DETAILS

Title	Coherent, Ultrashort IR, UV and X-Ray Sources for Ultrafast Spectroscopies	**Institution Name**	Imperial College London
		Expected Presentation Date	2022-12-13
Instructor Name	Timur Avni		

ADDITIONAL DETAILS

Order Reference Number	PTotRSAFigs	**The Requesting Person/Organization to Appear on the License**	Timur Avni

REUSE CONTENT DETAILS

Title, Description or Numeric Reference of the Portion(s)	Figures 3 and 4	**Title of the Article/Chapter the Portion Is From**	Attosecond soft X-ray high harmonic generation
Editor of Portion(s)	Timur Avni	**Author of Portion(s)**	Royal Society
Volume of Serial or Monograph	Volume 377 Issue 2145	**Issue, if Republishing an Article From a Serial**	N/A
Page or Page Range of Portion	7-8	**Publication Date of Portion**	2022-12-13

RIGHTSHOLDER TERMS AND CONDITIONS

Out of Copyright - any journal requested with a Publication date older than 70 years.

Total Items: 1 **Total Due: 0.00 GBP**

Accepted: Marketplace Order General Terms and Conditions and any applicable Publisher Terms and Conditions

SPRINGER NATURE LICENSE
TERMS AND CONDITIONS

Dec 04, 2022

This Agreement between Timur Avni ("You") and Springer Nature ("Springer Nature") consists of your license details and the terms and conditions provided by Springer Nature and Copyright Clearance Center.

License Number	5442001186448
License date	Dec 04, 2022
Licensed Content Publisher	Springer Nature
Licensed Content Publication	Nature Reviews, Physics
Licensed Content Title	How to optimize high-order harmonic generation in gases
Licensed Content Author	R. Weissenbilder et al
Licensed Content Date	Oct 13, 2022
Type of Use	Thesis/Dissertation
Requestor type	academic/university or research institute
Format	print and electronic
Portion	figures/tables/illustrations
Number of figures/tables/illustrations	1
Will you be translating?	no
Circulation/distribution	1 - 29

Author of this Springer Nature content	no
Title	Coherent, Ultrashort IR, UV and X-Ray Sources for Ultrafast Spectroscopies
Institution name	Imperial College London
Expected presentation date	Dec 2022
Order reference number	wissenbilders1a
Portions	Supplementary Information Figure 1a
Requestor Location	Timur Avni [redacted] [redacted] United Kingdom Attn: Imperial College London
Total	0.00 GBP

Terms and Conditions

Springer Nature Customer Service Centre GmbH Terms and Conditions

The following terms and conditions ("Terms and Conditions") together with the terms specified in your [RightsLink] constitute the License ("License") between you as Licensee and Springer Nature Customer Service Centre GmbH as Licensor. By clicking 'accept' and completing the transaction for your use of the material ("Licensed Material"), you confirm your acceptance of and obligation to be bound by these Terms and Conditions.

1. Grant and Scope of License

1. 1. The Licensor grants you a personal, non-exclusive, non-transferable, non-sublicensable, revocable, world-wide License to reproduce, distribute, communicate to the public, make available, broadcast, electronically transmit or create derivative works using the Licensed Material for the purpose(s) specified in your RightsLink Licence Details only. Licenses are granted for the specific use requested in the order and for no other use, subject to these Terms and Conditions. You acknowledge and agree that the rights granted to you under this License do not include the right to modify, edit, translate, include in collective works, or create derivative works of the Licensed Material in whole or in part unless expressly stated in your RightsLink Licence Details. You may use the Licensed Material only as permitted under this Agreement and will not reproduce, distribute, display, perform, or otherwise use or exploit any Licensed Material in any way, in whole or in part, except as expressly

permitted by this License.

1. 2. You may only use the Licensed Content in the manner and to the extent permitted by these Terms and Conditions, by your RightsLink Licence Details and by any applicable laws.

1. 3. A separate license may be required for any additional use of the Licensed Material, e.g. where a license has been purchased for print use only, separate permission must be obtained for electronic re-use. Similarly, a License is only valid in the language selected and does not apply for editions in other languages unless additional translation rights have been granted separately in the License.

1. 4. Any content within the Licensed Material that is owned by third parties is expressly excluded from the License.

1. 5. Rights for additional reuses such as custom editions, computer/mobile applications, film or TV reuses and/or any other derivative rights requests require additional permission and may be subject to an additional fee. Please apply to journalpermissions@springernature.com or bookpermissions@springernature.com for these rights.

2. Reservation of Rights

Licensor reserves all rights not expressly granted to you under this License. You acknowledge and agree that nothing in this License limits or restricts Licensor's rights in or use of the Licensed Material in any way. Neither this License, nor any act, omission, or statement by Licensor or you, conveys any ownership right to you in any Licensed Material, or to any element or portion thereof. As between Licensor and you, Licensor owns and retains all right, title, and interest in and to the Licensed Material subject to the license granted in Section 1.1. Your permission to use the Licensed Material is expressly conditioned on you not impairing Licensor's or the applicable copyright owner's rights in the Licensed Material in any way.

3. Restrictions on use

3. 1. Minor editing privileges are allowed for adaptations for stylistic purposes or formatting purposes provided such alterations do not alter the original meaning or intention of the Licensed Material and the new figure(s) are still accurate and representative of the Licensed Material. Any other changes including but not limited to, cropping, adapting, and/or omitting material that affect the meaning, intention or moral rights of the author(s) are strictly prohibited.

3. 2. You must not use any Licensed Material as part of any design or trademark.

3. 3. Licensed Material may be used in Open Access Publications (OAP), but any such reuse must include a clear acknowledgment of this permission visible at the same time as the figures/tables/illustration or abstract and which must indicate that the Licensed Material is not part of the governing OA license but has been reproduced with permission. This may be indicated according to any standard referencing system but must include at a minimum 'Book/Journal title, Author, Journal Name (if applicable), Volume (if applicable), Publisher, Year, reproduced with permission from SNCSC'.

4. STM Permission Guidelines

4. 1. An alternative scope of license may apply to signatories of the STM Permissions Guidelines ("STM PG") as amended from time to time and made available at https://www.stm-assoc.org/intellectual-property/permissions/permissions-guidelines/.

4. 2. For content reuse requests that qualify for permission under the STM PG, and which may be updated from time to time, the STM PG supersede the terms and conditions contained in this License.

4. 3. If a License has been granted under the STM PG, but the STM PG no longer apply at the time of publication, further permission must be sought from the Rightsholder. Contact journalpermissions@springernature.com or bookpermissions@springernature.com for these rights.

5. Duration of License

5. 1. Unless otherwise indicated on your License, a License is valid from the date of purchase ("License Date") until the end of the relevant period in the below table:

Reuse in a medical communications project	Reuse up to distribution or time period indicated in License
Reuse in a dissertation/thesis	Lifetime of thesis
Reuse in a journal/magazine	Lifetime of journal/magazine
Reuse in a book/textbook	Lifetime of edition
Reuse on a website	1 year unless otherwise specified in the License
Reuse in a presentation/slide kit/poster	Lifetime of presentation/slide kit/poster. Note: publication whether electronic or in print of presentation/slide kit/poster may require further permission.
Reuse in conference proceedings	Lifetime of conference proceedings
Reuse in an annual report	Lifetime of annual report
Reuse in training/CME materials	Reuse up to distribution or time period indicated in License
Reuse in newsmedia	Lifetime of newsmedia
Reuse in coursepack/classroom materials	Reuse up to distribution and/or time period indicated in license

6. Acknowledgement

6. 1. The Licensor's permission must be acknowledged next to the Licensed Material in print. In electronic form, this acknowledgement must be visible at the same time as the figures/tables/illustrations or abstract and must be hyperlinked to the journal/book's homepage.

6. 2. Acknowledgement may be provided according to any standard referencing system and at a minimum should include "Author, Article/Book Title, Journal name/Book imprint, volume, page number, year, Springer Nature".

7. Reuse in a dissertation or thesis

7. 1. Where 'reuse in a dissertation/thesis' has been selected, the following terms apply: Print rights of the Version of Record are provided for; electronic rights for use only on institutional repository as defined by the Sherpa guideline

(www.sherpa.ac.uk/romeo/) and only up to what is required by the awarding institution.

7. 2. For theses published under an ISBN or ISSN, separate permission is required. Please contact journalpermissions@springernature.com or bookpermissions@springernature.com for these rights.

7. 3. Authors must properly cite the published manuscript in their thesis according to current citation standards and include the following acknowledgement: '*Reproduced with permission from Springer Nature*'.

8. License Fee

You must pay the fee set forth in the License Agreement (the "License Fees"). All amounts payable by you under this License are exclusive of any sales, use, withholding, value added or similar taxes, government fees or levies or other assessments. Collection and/or remittance of such taxes to the relevant tax authority shall be the responsibility of the party who has the legal obligation to do so.

9. Warranty

9. 1. The Licensor warrants that it has, to the best of its knowledge, the rights to license reuse of the Licensed Material. **You are solely responsible for ensuring that the material you wish to license is original to the Licensor and does not carry the copyright of another entity or third party (as credited in the published version).** If the credit line on any part of the Licensed Material indicates that it was reprinted or adapted with permission from another source, then you should seek additional permission from that source to reuse the material.

9. 2. EXCEPT FOR THE EXPRESS WARRANTY STATED HEREIN AND TO THE EXTENT PERMITTED BY APPLICABLE LAW, LICENSOR PROVIDES THE LICENSED MATERIAL "AS IS" AND MAKES NO OTHER REPRESENTATION OR WARRANTY. LICENSOR EXPRESSLY DISCLAIMS ANY LIABILITY FOR ANY CLAIM ARISING FROM OR OUT OF THE CONTENT, INCLUDING BUT NOT LIMITED TO ANY ERRORS, INACCURACIES, OMISSIONS, OR DEFECTS CONTAINED THEREIN, AND ANY IMPLIED OR EXPRESS WARRANTY AS TO MERCHANTABILITY OR FITNESS FOR A PARTICULAR PURPOSE. IN NO EVENT SHALL LICENSOR BE LIABLE TO YOU OR ANY OTHER PARTY OR ANY OTHER PERSON OR FOR ANY SPECIAL, CONSEQUENTIAL, INCIDENTAL, INDIRECT, PUNITIVE, OR EXEMPLARY DAMAGES, HOWEVER CAUSED, ARISING OUT OF OR IN CONNECTION WITH THE DOWNLOADING, VIEWING OR USE OF THE LICENSED MATERIAL REGARDLESS OF THE FORM OF ACTION, WHETHER FOR BREACH OF CONTRACT, BREACH OF WARRANTY, TORT, NEGLIGENCE, INFRINGEMENT OR OTHERWISE (INCLUDING, WITHOUT LIMITATION, DAMAGES BASED ON LOSS OF PROFITS, DATA, FILES, USE, BUSINESS OPPORTUNITY OR CLAIMS OF THIRD PARTIES), AND WHETHER OR NOT THE PARTY HAS BEEN ADVISED OF THE POSSIBILITY OF SUCH DAMAGES. THIS LIMITATION APPLIES NOTWITHSTANDING ANY FAILURE OF ESSENTIAL PURPOSE OF ANY LIMITED REMEDY PROVIDED HEREIN.

10. Termination and Cancellation

10. 1. The License and all rights granted hereunder will continue until the end of the applicable period shown in Clause 5.1 above. Thereafter, this license will be terminated and all rights granted hereunder will cease.

10. 2. Licensor reserves the right to terminate the License in the event that payment is not received in full or if you breach the terms of this License.

11. General

11. 1. The License and the rights and obligations of the parties hereto shall be construed, interpreted and determined in accordance with the laws of the Federal Republic of Germany without reference to the stipulations of the CISG (United Nations Convention on Contracts for the International Sale of Goods) or to Germany´s choice-of-law principle.

11. 2. The parties acknowledge and agree that any controversies and disputes arising out of this License shall be decided exclusively by the courts of or having jurisdiction for Heidelberg, Germany, as far as legally permissible.

11. 3. This License is solely for Licensor's and Licensee's benefit. It is not for the benefit of any other person or entity.

Questions? For questions on Copyright Clearance Center accounts or website issues please contact springernaturesupport@copyright.com or +1-855-239-3415 (toll free in the US) or +1-978-646-2777. For questions on Springer Nature licensing please visit https://www.springernature.com/gp/partners/rights-permissions-third-party-distribution

Other Conditions:

Version 1.4 - Dec 2022

Questions? customercare@copyright.com or +1-855-239-3415 (toll free in the US) or +1-978-646-2777.

AIP PUBLISHING LICENSE
TERMS AND CONDITIONS

Mar 01, 2024

This Agreement between Timur Avni ("You") and AIP Publishing ("AIP Publishing") consists of your license details and the terms and conditions provided by AIP Publishing and Copyright Clearance Center.

License Number	5740160592332
License date	Mar 01, 2024
Licensed Content Publisher	AIP Publishing
Licensed Content Publication	Review of Scientific Instruments
Licensed Content Title	Apparatus for soft x-ray table-top high harmonic generation
Licensed Content Author	Johnson, Allan S.; Wood, David
Licensed Content Date	Aug 21, 2018
Licensed Content Volume	89
Licensed Content Issue	8
Type of Use	Thesis/Dissertation
Requestor type	Student
Format	Print and electronic
Portion	Figure/Table
Number of figures/tables	3

Will you be translating?	No
Title of new work	Coherent, Ultrashort IR, UV and X-Ray Sources for Ultrafast Spectroscopies
Institution name	Imperial College London
Expected presentation date	Jun 2024
Order reference number	29235872
Portions	Figures
Requestor Location	Timur Avni [redacted] [redacted] United Kingdom Attn: Imperial College London
Total	0.00 GBP

Terms and Conditions

AIP Publishing -- Terms and Conditions: Permissions Uses

AIP Publishing hereby grants to you the non-exclusive right and license to use and/or distribute the Material according to the use specified in your order, on a one-time basis, for the specified term, with a maximum distribution equal to the number that you have ordered. Any links or other content accompanying the Material are not the subject of this license.

1. You agree to include the following copyright and permission notice with the reproduction of the Material:"Reprinted from [FULL CITATION], with the permission of AIP Publishing." For an article, the credit line and permission notice must be printed on the first page of the article or book chapter. For photographs, covers, or tables, the notice may appear with the Material, in a footnote, or in the reference list.
2. If you have licensed reuse of a figure, photograph, cover, or table, it is your responsibility to ensure that the material is original to AIP Publishing and does not contain the copyright of another entity, and that the copyright notice of the figure, photograph, cover, or table does not indicate that it was reprinted by AIP Publishing, with permission, from another source. Under no circumstances does AIP Publishing purport or intend to grant permission to reuse material to which it does not hold appropriate rights.
   You may not alter or modify the Material in any manner. You may translate the

Material into another language only if you have licensed translation rights. You may not use the Material for promotional purposes.

3. The foregoing license shall not take effect unless and until AIP Publishing or its agent, Copyright Clearance Center, receives the Payment in accordance with Copyright Clearance Center Billing and Payment Terms and Conditions, which are incorporated herein by reference.
4. AIP Publishing or Copyright Clearance Center may, within two business days of granting this license, revoke the license for any reason whatsoever, with a full refund payable to you. Should you violate the terms of this license at any time, AIP Publishing, or Copyright Clearance Center may revoke the license with no refund to you. Notice of such revocation will be made using the contact information provided by you. Failure to receive such notice will not nullify the revocation.
5. AIP Publishing makes no representations or warranties with respect to the Material. You agree to indemnify and hold harmless AIP Publishing, and their officers, directors, employees or agents from and against any and all claims arising out of your use of the Material other than as specifically authorized herein.
6. The permission granted herein is personal to you and is not transferable or assignable without the prior written permission of AIP Publishing. This license may not be amended except in a writing signed by the party to be charged.
7. If purchase orders, acknowledgments or check endorsements are issued on any forms containing terms and conditions which are inconsistent with these provisions, such inconsistent terms and conditions shall be of no force and effect. This document, including the CCC Billing and Payment Terms and Conditions, shall be the entire agreement between the parties relating to the subject matter hereof.

This Agreement shall be governed by and construed in accordance with the laws of the State of New York. Both parties hereby submit to the jurisdiction of the courts of New York County for purposes of resolving any disputes that may arise hereunder.

V1.2

Questions? customercare@copyright.com.